

# **Noninvasive Thrombolysis using Microtripsy**

**by**

**Xi Zhang**

A dissertation submitted in partial fulfillment  
of the requirements for the degree of  
Doctor of Philosophy  
(Biomedical Engineering)  
in the University of Michigan  
2016

Doctoral Committee:

Associate Professor Zhen Xu, Chair  
Professor Charles A. Cain  
Professor J. Brian Fowlkes  
Associate Professor Hitinder S. Gurm  
Assistant Professor Gabe E. Owens

© Xi Zhang 2016

## **Acknowledgements**

I want to take this opportunity to express my sincere gratitude to my adviser, Dr. Zhen Xu, for her continuous support, guidance and encouragement. Zhen gave me tremendous helps in both my research and my life. She trusted me and my abilities from the very beginning and guided me through the difficulties I faced throughout my research. I really appreciate all the time and efforts she spent in helping me with my papers, abstracts and presentations. It is truly my luck to have Zhen as my adviser for the past five years. I would also like to thank my dissertation committee members: Drs. Charles Cain, Gabe Owens, Hitinder Gurm and Brian Fowlkes. It is a great honor for me to have them in my committee and to have opportunities to work with them. They are always willing to share their professional knowledge with me and provide constructive comments and ideas on my papers and projects. I have been impressed by Charles' knowledge, passion and extremely creative thinking and I have benefited a lot from the conversations and meetings with him. Gabe never hesitated to offer his helps for my experiments. Without the clinical knowledge and tricks he taught me and the support he gave me, it was impossible for me to complete my studies. As a cardiologist, Hitinder provided me with essential guidance and support using his professional experience and knowledge. Brian helped me a lot to shape my goals and research plans and kept encouraging me to move forward on the way.

I want to thank all the other members of the histotripsy group. It is a group of great people, who are brilliant, passionate and always willing to share and help. Because of the people, the lab is not just a place to work but a warm harbor for explorers to inspire and encourage each

other. I would like to thank the faculties and staffs I worked together with, especially Dr. Tim Hall and Kimberly Ives. Tim is another adviser of mine and he gave me tremendous helps and encouragements, especially at those tough moments. I could never forget the encouraging words he said to me after my first presentation, which motivated me all the way through. Kimberly Ives unconditionally supported all my animal experiments. Her professional experience contributed essentially to the success of my studies. I would also like to thank all the graduate students and post-docs worked together with me in the lab: Yohan Kim, Ryan Miller, Eli Vlasisavljevic, Alex Duryea, Kuang-Wei Lin, Jonathan Sukovich, Steven Allen, Rajiv Devanagondi, Simone Park, Tzu-Yin Wang, Yige Li, Hedieh Tamaddoni, Jonathan Macoskey, Jonathan Lundt, and Tyler Gerhardson. We worked hard together and we had fun together. Yohan got me started in the lab and taught me everything I needed to know at the beginning. He is a friend, a brother and a teacher to me. I appreciate his patience and kindness when answering every question I asked and his company in the lab during holidays. Ryan and I spent a lot of days and nights together doing experiments in the water tanks. He showed me the way to open the door to research and he inspired me from multiple aspects, which was helpful for my following studies. Eli is always willing to share his experience and knowledge with me. He is super active in both research and life and I am continuously inspired by him. I also want to thank Adam for his outstanding works, which laid a solid foundation for my research and pointed the direction I could move further along.

I want to thank the administrative staffs at the Biomedical Engineering Department, especially to Kathleen McCrumb, Maria Steele, Pat Metzler, Chuck Nicholas and Therese Kummer. Kathy helped me with tons of purchases and reimbursements over the past few years and never had any complaints. She is always nice to talk to and will help me with any of my

problems. Maria is the one I would directly go to if I have any administrative questions and she never disappointed me. Chuck is always there to help when I got questions and troubles about the computers and internet.

At the end, I want to express my deepest love and thanks to my parents and my wife. My parents showed me the best examples of how hard work, integrity and kindness can build a happy and wealthy life from scratch. Their words and deeds taught me what to do and what spirit to hold when facing different situations in life. Their unconditional love is always with me and encourages me to explore and chase the true, the good and the beautiful. I feel very sorry about the limited time I spent together with my parents during the last five years. But I am sure they recognize my motivation behind my dissertation work and they will be proud of what I have dedicated into. My wife has sacrificed so much for me over the past few years. We went through a long-distance relationship for the first two years of my PhD time and because of her understanding and devotion we made it at the end. I greatly appreciate her company. She made my life much brighter, happier and richer. She is the warmest light in my heart, which shows me the way home and also keeps me moving forward fearlessly.

## Table of Contents

<b>Acknowledgements.....</b>	<b>ii</b>
<b>List of Figures.....</b>	<b>xiii</b>
<b>List of Tables .....</b>	<b>xxvii</b>
<b>Abstract .....</b>	<b>xxix</b>
<b>Chapter 1 Introduction .....</b>	<b>1</b>
1.1 Thrombosis .....	1
1.2 Sonothrombolysis.....	2
1.3 Histotripsy Thrombolysis .....	3
1.4 Microtripsy .....	5
1.5 Bubble-induced Color Doppler.....	5
1.6 Outline of This Dissertation .....	6
1.7 References .....	9
<b>Chapter 2 Development of Histotripsy Thrombolysis System.....</b>	<b>13</b>
2.1 Introduction.....	13
2.2 Therapy Transducer Development.....	13

2.2.1	Initial Prototype.....	14
2.2.2	Final Design.....	16
2.3	Ultrasound Imaging.....	18
2.3.1	Ultrasound Imaging System.....	18
2.3.2	Custom Ultrasound Imaging Probe.....	19
2.4	Positioning System.....	20
2.5	System Integration.....	21
2.6	Software Development.....	22
2.7	Summary.....	26
2.8	Appendix.....	27
2.9	References.....	27
<b>Chapter 3 Noninvasive Thrombolysis using Histotripsy beyond the “Intrinsic” Threshold</b>		
<b>(Microtripsy).....29</b>		
3.1	Introduction.....	29
3.2	Material and Methods.....	32
3.2.1	Flow Model.....	32
3.2.2	Vessel Phantom.....	33
3.2.3	Clot Formation.....	34
3.2.4	Microtripsy Thrombolysis System.....	34
3.2.5	Treatments.....	36

3.2.6	Cavitation.....	38
3.2.7	Flow Channel Quantification.....	39
3.2.8	Restored Flow Measurement.....	39
3.2.9	Debris Particle Measurements.....	40
3.2.10	Statistics.....	41
3.3	Results.....	41
3.3.1	Cavitation.....	41
3.3.2	Flow Channel.....	42
3.3.3	Restored Flow Rate.....	45
3.3.4	Debris Particle Measurements.....	46
3.4	Discussion.....	48
3.4.1	Cavitation.....	48
3.4.2	Elimination of Vessel Damage.....	49
3.4.3	Accuracy of Cavitation Cloud Size Estimation.....	49
3.4.4	Predictions of Flow Channel Sizes.....	50
3.4.5	Channel Size Controls.....	51
3.4.6	Restored Flow Rate.....	52
3.4.7	Treatment Time Optimization.....	53
3.4.8	Comparison of Different Scan Intervals.....	53
3.4.9	Debris.....	54



3.5	Conclusion .....	55
3.6	References .....	56
<b>Chapter 4 Noninvasive Thrombolysis using Microtripsy: A Parameter Study .....</b>		<b>60</b>
4.1	Introduction.....	60
4.2	Methods and Materials .....	63
4.2.1	Flow Model.....	63
4.2.2	Vessel Phantom.....	64
4.2.3	Clot Formation.....	65
4.2.4	Microtripsy Thrombolysis System .....	66
4.2.5	Treatments .....	67
4.2.6	Cavitation Monitor .....	69
4.2.7	Flow Channel Quantification .....	71
4.2.8	Restored Flow Measurements .....	72
4.2.9	Debris Particle Size Measurements.....	72
4.2.10	Statistics Analysis.....	73
4.3	Results .....	73
4.3.1	Cavitation.....	73
4.3.2	Flow Channel .....	75
4.3.3	Restored Flow Rate .....	80
4.3.4	Debris Size Distribution .....	81

4.4	Discussion.....	83
4.4.1	Cavitation.....	83
4.4.2	Flow Channels.....	84
4.4.3	Debris.....	85
4.4.4	Choice of Treatment PRF .....	86
4.4.5	Future Work.....	88
4.5	Conclusion.....	88
4.6	References .....	89
<b>Chapter 5 Histotripsy Thrombolysis on Retracted Clots .....</b>		<b>94</b>
5.1	Introduction.....	94
5.2	Materials and Methods .....	97
5.2.1	Flow Model.....	97
5.2.2	Retracted Clot Formation .....	99
5.2.3	Therapy System.....	101
5.2.4	Pre-treatment Planning.....	102
5.2.5	Treatment Strategies.....	103
5.2.6	Elasticity and Porosity Measurements.....	108
5.2.7	Flow Channel Measurement .....	108
5.2.8	Restored Flow Measurement .....	109
5.2.9	Debris Measurement.....	110

5.3	Results .....	110
5.3.1	Elasticity and Porosity of Retracted and Unretracted Clot .....	110
5.3.2	Comparison with Unretracted Clot .....	112
5.3.3	Single-focus Treatments .....	113
5.3.4	Comparison of Three Strategies .....	114
5.3.5	Restored Flow .....	116
5.3.6	Debris .....	117
5.4	Discussion .....	119
5.5	Conclusion .....	123
5.6	References .....	124
<b>Chapter 6 Real-time Feedback of Histotripsy Thrombolysis Using Bubble-induced Color Doppler .....</b>		<b>130</b>
6.1	Introduction .....	130
6.2	Materials and Methods .....	132
6.2.1	Investigation of Bubble-induced Motion .....	132
6.2.2	Correlation of BCD Feedback and Histotripsy Thrombolysis .....	137
6.2.3	Validation of BCD Feedback in <i>In Vitro</i> Clots .....	141
6.2.4	Real-time Monitoring of Histotripsy Thrombolysis using BCD Feedback ...	145
6.3	Results .....	146
6.3.1	Investigation of Bubble-induced Motion .....	146

6.3.2	Correlation of BCD Feedback and Histotripsy Thrombolysis.....	150
6.3.3	Validation of BCD Feedback in <i>In Vitro</i> Clots.....	154
6.3.4	Real-time Monitoring of Histotripsy Thrombolysis using BCD Feedback.....	155
6.4	Discussion.....	157
6.5	Conclusion.....	160
6.6	References .....	161
<b>Chapter 7</b>	<b>Noninvasive Thrombolysis using Microtripsy in a Porcine Deep Vein Thrombosis Model .....</b>	<b>166</b>
7.1	Introduction.....	166
7.2	Materials and Methods .....	168
7.2.1	Animal Preparation and Thrombus Formation .....	168
7.2.2	Microtripsy Thrombolysis System and Setup.....	169
7.2.3	Pre-treatment Planning .....	171
7.2.4	Treatments .....	172
7.2.5	Measurements and Evaluations.....	173
7.2.5	Statistical Analysis .....	174
7.3	Results .....	174
7.3.1	Thrombus .....	174
7.3.2	Cavitation.....	176
7.3.3	Recanalization.....	176

7.3.4	Blood .....	179
7.3.5	Gross and Histology Evaluation.....	180
7.3.5	Animal Behavior and Symptom Monitoring .....	181
7.4	Discussion.....	181
7.5	References .....	186
<b>Chapter 8 Summary and Future Work.....</b>		<b>188</b>
8.1	Summary.....	188
8.2	Future Work.....	190
8.2.1	Further Investigation of Bubble-induced Color Doppler Feedback.....	191
8.2.2	Microtripsy PRF Study.....	192
8.2.3	Retracted Clots in the Porcine DVT Model.....	193
8.2.4	Further Investigation of Multi-pass Treatment Strategy .....	194
8.3	References .....	194

## List of Figures

<b>Figure 2.1:</b> Initial prototyping of histotripsy thrombolysis transducer. <b>(a)</b> CAD design and <b>(b)</b> the final transducer with a linear ultrasound-imaging probe inserted.....	15
<b>Figure 2.2:</b> Pressure profiles of the initial prototype along the three axes and the focal pressure waveform measured by a fiber optical hydrophone.....	15
<b>Figure 2.3:</b> Final histotripsy thrombolysis transducer. <b>(a)</b> CAD design. <b>(b)</b> Transducer front surface. <b>(c)</b> Element design. <b>(d)</b> Focal length illustration.....	16
<b>Figure 2.4:</b> Pressure calibration of the clinical histotripsy thrombolysis transducer. <b>(a)–(c)</b> Pressure profiles along the three axes. <b>(d)</b> Estimated focal pressure waveform by summing the three sub-group waveforms.....	17
<b>Figure 2.5:</b> <b>(a)</b> Pressure profiles along the lateral direction at multiple steered locations. <b>(b)</b> Overlapped 2D pressure fields on the lateral-elevational plane at multiple steered locations.....	17
<b>Figure 2.6:</b> Commercial SonixTouch <sup>®</sup> ultrasound imaging system.....	18
<b>Figure 2.7:</b> Ultrasound imaging probe with a rectangular customized housing.....	19
<b>Figure 2.8:</b> The positioning system. The compact motorized positioner is installed on the top of the mechanical arm.....	20
<b>Figure 2.9:</b> The compact motorized positioner can be controlled by joy sticks and software commands through a programmable logic controller.....	21
<b>Figure 2.10:</b> Integrated histotripsy thrombolysis system.....	22

<b>Figure 2.11:</b> Schematic structure of control software. ....	23
<b>Figure 2.12:</b> The user interface of the engineering version of the control software. Real-time ultrasound images are shown on the left of the window. Two operation tabs are displayed on the right, including a pre-treatment planning tab (Top) and a treatment tab (Bottom). ....	25
<b>Figure 2.13:</b> The treatment version of the control software: the primary display screen (Left) and the touch screen (Right). ....	26
<b>Figure 2.14:</b> Control panel with a touch screen and physical buttons and knobs, with different touch screen interfaces shown. There are tabs: one for imaging setting, one for pre-treatment planning and one for treatment. Detailed operation instructions are listed on the left of each tab. ....	26
<b>Figure 3.1:</b> Schematic diagram of the flow model.....	32
<b>Figure 3.2:</b> The vessel phantom is held by a plastic frame and connected in line with the flow model using tubing fittings. A 35% stenosis is located at the outlet side of the vessel phantom to fix the clot formed aside so that it does not slip under pressure. A clot is formed on the side of the stenosis as shown in the figure. (ID = Inner Diameter).....	33
<b>Figure 3.3:</b> Integrated microtripsy thrombolysis system. It consists of an ultrasound imaging system, a microtripsy therapy system and a motorized positioning system.....	35
<b>Figure 3.4:</b> 1 MHz 18-element microtripsy transducer with an ultrasound imaging probe at the center. With the imaging probe fixed in both lateral and elevational directions, the imaging plane is automatically aligned with the treatment focus of the therapy transducer. (A = Axial, L = Lateral, E = Elevational). ....	36

**Figure 3.5:** Pressure waveform of a microtripsy pulse. Since peak negative pressure larger than 20 MPa cannot be directly measured, this estimated waveform was linearly summed from the directly-measured waveforms of 6 separate element groups.....37

**Figure 3.6:** Schematic illustration of the treatment strategy. After a fixed number of microtripsy pulses are applied at one location along the treatment path, the therapy transducer is moved with a pre-set scan interval to the next location and repeats. ....38

**Figure 3.7:** Cavitation bubble clouds during treatments. **(a)** Using 30 MPa P(-)<sub>LS</sub>. **(b)** Using 36 MPa P(-)<sub>LS</sub>. Ultrasound was propagated from the top to the bottom of the images. ....42

**Figure 3.8:** Ultrasound images of a treated clot in the vessel phantom. **(a)** Before treatment. The vertical arrow locates the stenosis is. **(b)** Flow channel presence after treatment. **(c)** Color flow presence after treatment. Glass beads (Part# 10089; TSI, Shoreview, MN, USA) were mixed in the perfusion saline after the treatment to obtain this color Doppler image. Flow is from the right to the left of the images. ....43

**Figure 3.9:** Representative ultrasound images of flow channel generated from the 4 treatment groups. The generated flow channels show as the hypoechoic zones inside clots (block arrow). Reduced echogenicity is found at one side of the flow channels with 0.7 mm SI (line arrow), where the tail of the cavitation cloud was. Ultrasound was propagated from the top to the bottom of the images. ....43

**Figure 3.10:** Illustrations of the cross sections of the flow channels for the 4 treatment groups. Fitted ellipse is determined by  $D_{major}$  and  $D_{minor}$  from Table 3.2. Equivalent circle is determined by  $D_{circle}$  from Table 3.2. ....45



**Figure 3.11:** Restored flow rates of the 4 treatment groups. Treatments associated with creation of larger cross-sectional area opening were associated with larger flow rates. The flow rates in the control group were measured under the same pressure as the treatment groups but without blockage in vessel phantom. For both P(-)<sub>LS</sub> used, statistical analysis (one-sided t-tests) showed significant flow rate increase as the SI decreased ( $P < 0.0001$ ). And with the SI of 0.3 mm, the flow rate increase from the low P(-)<sub>LS</sub> groups to the high P(-)<sub>LS</sub> groups was also statistically significant ( $P < 0.0001$ ).....46

**Figure 3.12:** Filter weight increases after treatment.....47

**Figure 3.13:** Debris particle distributions are normalized by the maximal value of the 4 treatment groups.....47

**Figure 3.14:** Cross-sectional ultrasound images of cavitation bubble clouds in the vessel phantom. The vessel phantom was filled with saline. Vessel wall is indicated by line arrow and bubble cloud is indicated by block arrow. Left: Using shock scattering mechanism (5-cycle pulses). Right: Using intrinsic threshold mechanism (microtripsy, 1-cycle pulse). The same peak negative pressure was applied in both cases.....49

**Figure 3.15:** Example microscopic images of debris fluid smear from one treatment. **(a)** 10 times magnification. White arrow points to a large debris particle (~40 μm). **(b)** 40 times magnification. Most of individual particles are around 4 μm. ....55

**Figure 4.1:** Schematic diagram of the flow model.....64

**Figure 4.2:** The vessel phantom is held by a 3D-printed frame and can be connected in line with the flow model using tubing fittings. A 35% stenosis is located in the vessel phantom to fix the clot formed to one side so that it does not slip under pressure. The inner diameter is 4.2 mm on

the left of the stenosis and 6.5 mm on the right. A clot is formed on the right side of the stenosis as shown in the figure.....65

**Figure 4.3:** Integrated microtripsy thrombolysis system. It consists of an ultrasound imaging system, a microtripsy therapy system, and a motorized positioning system. The insert shows the therapy transducer with a linear imaging probe embedded at the center. ....67

**Figure 4.4:** Pressure waveform of a microtripsy pulse. Because peak negative pressure larger than 20 MPa cannot be directly measured, this estimated waveform was linearly summed from the directly measured waveforms of 6 separate element groups (3 adjacent elements per group). .....69

**Figure 4.5:** Control waveform of cavitation monitor. The two bursts in the figure are the reflected signals from the front vessel wall (left) and rear vessel wall (right), respectively. The corresponding temporal zones of the Front Vessel Region (FVR) and Vessel Lumen Region (VLR) can be determined by these two reflections.....71

**Figure 4.6:** Ultrasound images of vessel lumen during treatment. Left: Focal cavitation at the center of the vessel lumen only (block arrow). Right: Focal cavitation (block arrow) with weak pre-focal cavitation (line arrow). .....74

**Figure 4.7:** The waveforms of cavitation monitor during treatment. Left: Focal cavitation only. Right: Pre-focal cavitation and focal cavitation together. The vertical dashed lines divide the Front Vessel Region (FVR) and the Vessel Lumen Region (VLR). .....75

**Figure 4.8:** Representative high-resolution ultrasound images of flow channel generated from each treatment parameter combination. The generated flow channels show as the hypoechoic zones inside clots. Ultrasound propagated from the top to the bottom of the images. ....76

**Figure 4.9:** The cross-sectional area ( $A_{\text{cross}}$ ) of generated flow channel using each treatment PRF was shown as a function of dose. ( $N = 6 \times 67$ ).....76

**Figure 4.10:** The axial location ( $L_{\text{axial}}$ ) of generated flow channel using each treatment PRF was shown as a function of dose. ( $N = 6 \times 67$ ). .....78

**Figure 4.11:** The ratio ( $R_D$ ) of the major diameter over the minor diameter of generated flow channel using each treatment PRF was shown as a function of dose. ( $N = 6 \times 67$ ). .....79

**Figure 4.12:** The width of boundary transition zone ( $W_{\text{bound}}$ ) of generated flow channel using each treatment PRF was shown as a function of dose. ( $N = 6 \times 67$ ). .....80

**Figure 4.13:** Restored flow rates of each treatment parameter combination. Treatments associated with creation of larger cross-sectional area opening were associated with larger flow rates. ( $N = 6$ ). .....81

**Figure 4.14:** A representative distribution of debris particles from 2 to 300  $\mu\text{m}$ . It is normalized to 1.....82

**Figure 5.1:** Schematic diagram of the *in vitro* flow model. ....98

**Figure 5.2:** The vessel phantom was held by a 3D-printed frame and could be easily connected in line with the flow model using tubing fittings. A 35% stenosis in the vessel phantom was used to stabilize the clot so that it did not slip under pressure. The inner diameter was 4.2 mm on the downstream side of the stenosis and 6.5 mm on the upstream side. A clot was inserted to the upstream side of the stenosis as shown in the figure. ....99

**Figure 5.3:** A clot was retracted in a hydrophilic glass tube after 7 days in 4°C incubation. The serum extruded from the clot can be clearly distinguished. ....100

**Figure 5.4:** The integrated microtripsy thrombolysis system is shown in the left picture. It consists of an ultrasound imaging system, a microtripsy therapy system, and a motorized positioning system. The ultrasound therapy transducer is shown in the middle. A linear imaging probe was embedded at the center of the therapy transducer. The arrangement of the 18 elements in the therapy transducer is illustrated in the right picture. (A = Axial, L = Lateral and E = Elevational)..... 102

**Figure 5.5:** Pressure waveform of a microtripsy pulse. Because peak negative pressure larger than 20 MPa cannot be directly measured, this waveform was estimated by linearly summing the directly-measured waveforms from 6 separate element groups (3 adjacent elements per group) and the peak negative pressure was 36 MPa. .... 104

**Figure 5.6:** Schematic diagrams of the three treatment strategies in the vessel phantom, with the solid lines outlined the inner vessel lumen. The ellipses in the vessel lumen represent the treatment foci. A illustrates the single-focus strategy. B and C illustrate the 3 foci and 5 foci multi-focus strategies, respectively. D and E illustrate the 1+2 foci and 2+3 foci dual-pass strategies, respectively. In D and E, the gray foci were treated in the first treatment pass and the white foci were treated in the second treatment pass. (SI = Scan Interval, Sp = Separation between foci). .... 107

**Figure 5.7:** One long retracted clot separated from the serum before being cut into 2-cm segments. .... 111

**Figure 5.8:** Representative histology sections of retracted (left) and unretracted (right) clots showing a cross section (a, b) and 4x magnification (c, d). Stain: Hematoxylin and Eosin. .... 111

**Figure 5.9:** Representative ultrasound images of the cross sections of the flow channels generated using the single-focus strategy in one unretracted clot (left) and one retracted clot

(right). The exact same treatment parameters (30 MPa P(-)LS , 0.3 mm Scan Interval and 100 pulses per treatment location) were used in both cases. The generated flow channels show as the hypoechoic zones inside clots (indicated by the block arrow in the left image). Therapeutic ultrasound propagated from the top to the bottom of the images. .... 112

**Figure 5.10:** Representative ultrasound images of the cross sections of the flow channels generated using the single-focus strategy with different doses. The last image shows the flow channel generated with a reduced scan interval (0.15 mm). The generated flow channels show as the hypoechoic zones inside clots (block arrows). Therapeutic ultrasound propagated from the top to the bottom of the images. .... 113

**Figure 5.11:** The mean cross-sectional area (Across) of the flow channels generated using the single-focus strategy with different doses. The last bar shows the flow channel generated with a reduced scan interval (SI = 0.15 mm). (N = 4 × 200). .... 114

**Figure 5.12:** Representative ultrasound images of the cross sections of the flow channels generated using the single-focus strategy (left column), the multi-focus strategy (middle column) and the dual-pass strategy (right column). The treatment times were 3.3 min/cm in the upper row and 5.5 min/cm in the lower row. The generated flow channels show as the hypoechoic zones inside the clot. Therapeutic ultrasound propagated from the top to the bottom of the images. ... 115

**Figure 5.13:** The mean cross-sectional area (Across) of the flow channels generated using the three strategies under the two treatment times (3.3 min/cm and 5.5 min/cm). (N = 4 × 200). ... 116

**Figure 5.14:** Restored flow rates of the three strategies under the two treatment times (3.3 min/cm and 5.5 min/cm). (N = 4). .... 117

**Figure 5.15:** The mean distributions of debris particles (3 to 10  $\mu\text{m}$ ) generated using the single-focus and dual-pass strategies ( $N = 4 \times 9$ ). The volumes of the fluids collected from the restored flows were recorded in all the treatments. And the volumes used for Coulter Counter measurements were recorded as well. With this information, the number of the debris particles was first converted to unit volume (mL) for each treatment. Then the mean distributions for each treatment strategy were calculated and normalized by the maximal peak among the mean distributions. .... 118

**Figure 6.1:** Transparent fibrin clot embedded in agarose hydrogel. The clot was molded to be rectangular in shape. A ruler segment was placed under the clot to show the transparency. .... 133

**Figure 6.2:** A schematic illustration of the experimental setup. A 6-element 1.5-MHz histotripsy transducer was placed facing down in a water tank filled with degassed water. The transducer was driven by a high-voltage amplifier that was connected to a field-programmable gated-array (FPGA) development board specifically programmed for controlling the firing of the transducer. A 5-MHz ultrasound imaging probe was inserted in the central hole of the histotripsy transducer and connected to Verasonics<sup>®</sup> ultrasound imaging system to image at the transducer focus. A high-speed camera and a continuous-wave light source were placed on the two sides outside the water tank. The FPGA controller sent triggers to the Verasonics<sup>®</sup> system and the high-speed camera to synchronize them with therapy pulses. The therapy focus was positioned within the transparent fibrin clot phantom. The central plane of the clot plate, the ultrasound imaging plane and the focal plane of the camera were aligned to overlap with each other. .... 134

**Figure 6.3:** A representative pressure waveform of the 6-element 1.5-MHz histotripsy transducer taken at the highest pressure (peak negative) level that could be directly measured by the fiber optical hydrophone. .... 135

**Figure 6.4:** Three-layer fibrin clot embedded in agarose hydrogel. **(a)** A picture of a three-layer fibrin clot phantom from top view. **(b)** A schematic of the phantom from side view. .... 139

**Figure 6.5:** Representative lesion formation of a treated spot in a soft three-layer fibrin clot. The lesions at different stages (pulse 0, 50, 100, 200, 300 and 1000) are shown here. These images were taken in the axial-lateral plane of the transducer, and the histotripsy pulses propagated from the top to the bottom of the field..... 140

**Figure 6.6:** The illustration of the slope detection algorithm. The lesion progression data shown here is from one treated sample. The slopes over three representative time windows are indicated. The highest change rate appears at the beginning of the treatment around the first time window (slope 1) and the saturation starts to occur around the second time window (slope 2). 141

**Figure 6.7:** RBC fibrin clot. The separation between the two adjacent tick marks on the scale ruler is 1 mm. .... 142

**Figure 6.8:** **(a)** A schematic illustration of the *in vitro* experiment setup. An 18-element 1.25-MHz histotripsy transducer was placed facing up in a tank filled with the degassed water. The transducer was driven by a high-voltage amplifier which was connected by an FPGA controller. A 5-MHz ultrasound imaging probe was positioned opposite to the transducer, aligned rigidly to the treatment focus and connected to the Verasonics<sup>®</sup> ultrasound imaging system. The FPGA controller sent triggers to the Verasonics<sup>®</sup> system to synchronize them with therapy pulses. Vessel phantom was placed between the transducer and the ultrasound imaging probe. **(b)** A picture of the vessel phantom. **(c)** Strategy of recanalization treatment. Each ellipse represents a treatment focal spot and after the completion of each spot treatment, the focus will move to the adjacent location with a 0.7 mm separation. .... 143

**Figure 6.9:** A representative pressure waveform of the 1.25-MHz histotripsy transducer taken at the highest pressure (peak negative) level which can be directly measured by the fiber optical hydrophone. .... 144

**Figure 6.10:** Representative PIV estimations overlaid with the corresponding optical images taken after the 100<sup>th</sup> histotripsy pulse. These images were taken in the axial-lateral plane of the transducer, and the histotripsy pulses propagated from the top to the bottom of the field. At 0.2 ms after the pulse, the cavitation bubbles show and no coherent motion is detected. At 0.5 ms, coherent motion is forming and pushing away from the transducer in the majority of the focal area proximal to the transducer and another stream of coherent motion at the distal side is moving towards the transducer. At 1.5 ms, the coherent motion at the proximal side is rebounding back and the coherent motion at the distal side is rebounding away. The motions repeat at 5 ms and 7.5 ms as in 0.5 and 1.5 ms. .... 147

**Figure 6.11:** Representative full profiles of mean axial velocity at the focal zone. **(a)** PIV estimation (only the proximal side). **(b)** BCD estimation. Positive values indicate motion towards the therapy transducer and negative values indicate motion away from the transducer. The horizontal axis shows the number of applied pulses and the vertical axis shows the delay from each histotripsy pulse. .... 149

**Figure 6.12:** The times of peak rebound velocity ( $t_{PRV}$ ) and peak second rebound velocity ( $t_{PRV2}$ ) estimated by PIV and BCD as a function of the number of the applied histotripsy pulses from one of the treated locations. The lower curves represent  $t_{PRV}$  and the upper curves represent  $t_{PRV2}$ . .... 149

**Figure 6.13:** Comparison between BCD feedback and histotripsy thrombolysis from a representative treated spot in a soft fibrin clot. **(a)** The progression curve of lesion area is



compared with the time of peak rebound velocity ( $t_{PRV}$ ) from its BCD feedback. **(b)** The progression curve of lesion area is compared with the mean velocity of the focal zone at 2ms delay ( $V_{f,2ms}$ ) from its BCD feedback. **(c)** The Pearson linear correlation between the progressions of lesion area and  $t_{PRV}$ . **(d)** The Pearson linear correlation between the progressions of lesion area and  $V_{f,2ms}$ . The detected saturation doses were also illustrated.....151

**Figure 6.14:** Comparison between BCD feedback and histotripsy thrombolysis from a representative treated spot in a hard fibrin clot. **(a)** The progression curve of lesion area is compared with the time of peak rebound time ( $t_{PRV}$ ) from its BCD feedback. **(b)** The progression curve of lesion area is compared with the mean velocity of the focal zone at 1ms delay ( $V_{f,1ms}$ ) from its BCD feedback. **(c)** The Pearson linear correlation between the progressions of lesion area and  $t_{PRV}$ . **(d)** The Pearson linear correlation between the progressions of lesion area and  $V_{f,1ms}$ . The detected saturation doses were also illustrated.....151

**Figure 6.15:** The saturation doses of lesion progression, and its corresponding  $t_{PRV}$  and  $V_{f,delay}$ . 50 spots were collected in total, 30 of which were in soft fibrin clots and 20 were in hard fibrin clots. The 20 spots from the hard fibrin clots are all on the top of the ones from soft fibrin clots. ....153

**Figure 6.16:** Comparison between the change of the fractionated debris volume and  $V_{f,0.5ms}$  from the BCD feedback. ....154

**Figure 6.17:** The debris distributions after histotripsy treatments with different doses. The 1000-pulse, 1500-pulse and 3000-pulse lines almost overlap with each other. The debris volume of the 500-pulse one (dashed line) is a little lower than the three higher-dose groups. The size of the majority of the fractionated debris is smaller than 6 um in all cases. ....155

**Figure 6.18:** (a) Real-time  $V_{f,2ms}$  of BCD feedback from one treated spot. (b) The real-time calculated change rate of  $V_{f,2ms}$ . (c) The corresponding progression of the lesion area. The vertical dashed line indicates the saturation dose real-time detected by the BCD feedback and the vertical solid line indicates the true saturation dose of the lesion progression, which represents the treatment completion. ....156

**Figure 6.19:** Representative full profiles of mean axial velocity of PIV estimation. (a) Proximal side (three fourths of the whole focal zone). (b) Distal side. Although the motions at the two sides are different, the changing trends appear the same. To the left of the dashed line (around 300 pulses) is the rapid changing stage and to the right of the dashed line is the stable stage. ..158

**Figure 7.1:** The integrated microtripsy thrombolysis system. It consists of an ultrasound imaging system, a microtripsy therapy system, and a motorized positioning system. A linear imaging probe was embedded at the center of the therapy transducer. The therapy transducer is mounted on the top of the positioning system. Treatment is controlled using touch screen interface and physical buttons on the control panel. ....170

**Figure 7.2:** Schematic experimental setup (Left) and a picture of the actual setup during one thrombolysis treatment (Right). ....171

**Figure 7.3:** Illustration of the dual-pass treatment. Each ellipse represents a focal zone with the number of the treatment pass. The gray foci were treated in the first treatment pass and the white foci were treated in the second treatment pass. ....172

**Figure 7.4:** Partially and fully occlusive thrombi (Arrow) formed in femoral veins. FV: Femoral Vein; FA: Femoral Artery. ....175

**Figure 7.5:** Representative US B-mode images (first row) and color Doppler images (second row) taken before and right after microtripsy thrombolysis treatment in an acute pig. (a)-(d): Longitudinal sections of the femoral vein. (e)-(h): Cross sections of the femoral veins (indicated by the block arrows)..... 176

**Figure 7.6:** Representative US B-mode images (first row) and color Doppler images (second row) taken before, right after and two weeks after microtripsy thrombolysis treatment in a subacute pig. Blood flow was increased after two weeks of recovery compared to that right after the treatment. Since a relatively smaller velocity scale was chosen to be consistent throughout all the color Doppler images, velocity aliasing occurred on the two-week color Doppler image (g) with an increased blood flow..... 177

**Figure 7.7:** Quantification of flow channel generated by microtripsy. On the left is the ultrasound image taken before treatment. On the right is the ultrasound image taken at the exact same location right after treatment. Green lines indicate the boundaries of the thrombi and red lines indicate the vessel lumen..... 178

**Figure 7.8:** Histology of Femoral Veins. (a)-(d): Right after a free-flow treatment. (e)-(h): Two weeks after a thrombolysis treatment..... 181

## List of Tables

<b>Table 3.1:</b> Treatment plan.....	38
<b>Table 3.2:</b> Quantifications of the flow channels (Mean $\pm$ Standard Deviation) .....	44
<b>Table 3.3:</b> Number percentage of debris particles.....	48
<b>Table 3.4:</b> Observed debris particles larger than 100 $\mu\text{m}$ .....	48
<b>Table 3.5:</b> Comparisons among the diameters of the flow channel, -6dB focal zone of the therapy transducer, supra-threshold estimations of focal region, and cavitation cloud diameters. Two-sided t-tests were performed to compare the diameters of flow channel with the other three. Superscript mark “ * ” indicates that this group is statistically significantly different from the flow channel diameter group. Superscript mark “ $\circ$ ” indicates there is no statistically significant difference between this group and the flow channel diameter group. ....	51
<b>Table 4.1:</b> The percentages of detected pre-focal and focal cavitation. ....	75
<b>Table 4.2:</b> Average number of particles $>100 \mu\text{m}$ over 6 treatments for each parameter set. ....	83
<b>Table 4.3:</b> Largest particle size $<300 \mu\text{m}$ . ....	83
<b>Table 4.4:</b> Particles larger than 300 $\mu\text{m}$ . The underline indicates they are from the same treatment.....	83
<b>Table 5.1:</b> Treatment Plan .....	106

<b>Table 5.2:</b> Summary of the generated debris larger than 100 $\mu\text{m}$ using the single-focus and dual-pass strategies .....	119
<b>Table 6.1:</b> The saturation doses (Mean $\pm$ SD) .....	153
<b>Table 6.2:</b> The differences between the BCD detected saturation doses and the corresponding lesion saturation doses.....	153
<b>Table 6.3:</b> The Pearson correlation coefficients (Mean $\pm$ SD) between the BCD progression curves and their corresponding lesion progression curves .....	154
<b>Table 7.1:</b> Summary of Thrombus Formations and Treatment Outcomes .....	175
<b>Table 7.2:</b> Blood Contents Change. “*” indicates significant difference.....	179

## Abstract

Thrombosis refers to blood clot formation and when pathological, is the cause of many vascular diseases. For example, deep vein thrombosis (DVT), which affects three million Americans per year, is the formation of clots in the deep veins of the legs. Current clinical treatments include thrombolytic drugs and catheter-based surgical procedures. Both methods have significant drawbacks, such as excessive bleeding, invasiveness, and long treatment time. Ultrasound has been combined with thrombolytic drugs and/or microbubbles to enhance drug delivery. However, these methods are still quite slow and share the drawbacks of thrombolytic drugs.

Histotripsy is a tissue ablation method that mechanically fractionates soft tissue via well-controlled acoustic cavitation generated by microsecond-long, high-pressure ultrasound pulses. The initial feasibility and safety of using histotripsy as a noninvasive, drug-free, and image-guided thrombolysis technique has been demonstrated both *in vitro* and *in vivo*. The *in vitro* studies showed that histotripsy fractionated blood clots into debris smaller than red blood cells at a speed an order of magnitude faster than any clinical method. The *in vivo* studies in a porcine deep vein thrombosis model showed histotripsy could restore blood flow and decrease thrombus burden with real-time guidance of ultrasound imaging.

The overriding goal of this dissertation is clinical translation of histotripsy thrombolysis. First, an integrated image-guided histotripsy thrombolysis system suitable for clinical DVT treatment are designed and constructed. Second, the recently discovered technical innovations,

microtripsy and bubble-induced color Doppler (BCD), are investigated for histotripsy thrombolysis application to further improve treatment efficacy. Microtripsy is a new histotripsy approach and uses an intrinsic threshold mechanism to generate more reproducible and predictable cavitation via a single ultrasound pulse, which can minimize vessel damage by confining cavitation within vessel lumen and eliminate cavitation on vessel wall. Within 7 minutes, 2-cm long whole blood clots were recanalized by microtripsy *in vitro* with flow channel opening up to 60%, restored flow up to 500 mL/min and 99.9% of clot debris smaller than 10  $\mu\text{m}$ . BCD is developed to monitor tissue motion induced by histotripsy pulses and investigated as a real-time quantitative feedback for histotripsy thrombolysis. The results show the potential of using BCD feedback to quantitatively monitor clot fractionation and accurately predicting its completion in real-time. Finally, a comprehensive pre-clinical study in a large animal DVT model is conducted to validate the safety and efficacy of this clinically designed system incorporating these technical innovations. In 13 out of the 14 treatments, a through channel was generated with 50% opening in average, and blood flows were successfully restored or significantly improved. The average treatment time was 16.6 minutes per cm-long clot. Only mild intravascular hemolysis was induced during microtripsy treatments and no damage was observed on vessel walls after two weeks of recovery. It is our hope that this dissertation work will establish a foundation for the translation of this noninvasive thrombolysis technology into relevant clinical applications.

# Chapter 1

## Introduction

This dissertation focuses on the research, development and clinical translation of noninvasive thrombolysis using histotripsy, which uses focused ultrasound to mechanically break down target blood clots in human vascular system via well-controlled acoustic cavitation. The dissertation work is conducted in three steps: 1) An integrated, portable histotripsy thrombolysis system, consisting of a histotripsy therapy system, an ultrasound imaging system, and a motorized positioning system, is designed and constructed for clinical use. 2) Two technical innovations, microtripsy and bubble-induced color Doppler, are developed and investigated for histotripsy thrombolysis application. 3) A comprehensive pre-clinical study in an *in vivo* porcine DVT model is conducted to validate the safety and efficacy of microtripsy thrombolysis using the clinically-designed system. This chapter will first give a brief background of thrombosis diseases and current treatments, followed by an introduction of ultrasound-mediated thrombolysis methods. Histotripsy technology and previous histotripsy thrombolysis work are then discussed. Backgrounds of the two technical innovations, microtripsy and bubble-induced color Doppler, are also covered. Lastly, this chapter is concluded with an outline of this dissertation providing an overview of the following chapters.

### 1.1 Thrombosis

Thrombosis is the formation of a blood clot in the cardiovascular system that prevents blood from circulating. Arterial thrombosis in the cerebral vasculature leads to ischemic stroke,



which is a leading cause of disability and death in the United States [1]. The most common form of venous thrombosis is deep vein thrombosis (DVT), which occurs predominantly in the legs and can sometimes lead to lethal pulmonary embolism (PE). DVT/PE (also called venous thromboembolism) affects over 300,000 people and causes deaths of 60,000 to 100,000 each year in the United States [2]. Other common thrombosis diseases include myocardial infarction, superficial vein thrombosis, and peripheral artery thrombosis, each of which poses a significant clinical problem.

Anticoagulant medicines are the most common treatment for thrombosis. Severely symptomatic patients may require thrombolytic treatments instead of simply taking oral anticoagulant drugs. Current thrombolytic treatments include thrombolytic drugs and catheter-based surgical procedures. Thrombolytic drugs such as tissue plasminogen activator (tPA) dissolves the blood clot by breaking down the cross-linked fibrin structures that solidify the clot [3]. Systemic administration of thrombolytic drugs has limited effectiveness with long treatment time (several hours to days) and is associated with a high risk of major bleeding [4]. Catheter-based devices are used for localized treatment to the target clot, including catheter-directed delivery of thrombolytic drugs [5] and mechanical thrombectomy [6]. Catheter-based procedures are more effective than thrombolytic drugs, but they are invasive and carry an increased risk of bleeding, vessel damage, and infection [7].

## **1.2 Sonothrombolysis**

Ultrasound has been a promising technique for promoting clot breakdown for several decades. Significant efforts have been focused on enhancing the efficacy of thrombolytic drugs with low intensity ultrasound [8-11]. Pfaffenberger *et al.* showed that continuous wave ultrasound significantly enhanced rt-PA mediated thrombolysis: in a travelling wave field

thrombolysis was augmented by  $49.0 \pm 14.7\%$  and in a standing wave field by  $34.8 \pm 7.3\%$ . Holland *et al.* further showed that both pulsed and continuous wave ultrasound enhanced rt-PA thrombolysis in a porcine whole blood clot model *in vitro*. Several clinical trials have been conducted for acute ischemic stroke and the results are promising [12-14]. In nine reported clinical trials, complete recanalization rates were higher in patients receiving combination of transcranial Doppler with tPA 37.2% (95% CI, 26.5%-47.9%) compared with patients treated with tPA alone 17.2% (95% CI, 9.5%-24.9%). Ultrasound combined with microbubbles has also been demonstrated to successfully break down clot in the presence or absence of thrombolytic drugs [15-17]. In a study conducted by Datta *et al.*, a commercial contrast agent, Definity®, was used to promote and sustain the nucleation of cavitation during pulsed ultrasound exposure at 120 kHz to enhance thrombolysis along with tPA and it was showed that stable cavitation activity plays an important role in enhancement of thrombolysis [15]. Another study concluded that sonothrombolysis using only microbubbles is also effective [17]. High-intensity focused ultrasound (HIFU) has been investigated as a stand-alone method for thrombolysis both *in vitro* and *in vivo* [18-20]. Wright *et al.* investigated the ability of HIFU for thrombolysis [20]. In their *in vitro* flow bypass experiments, 99.2% clot erosion with 1.1% of debris above 0.5mm in size was achieved using HIFU. In their *in vivo* study where clots were initialized in femoral veins of rabbits, partial flow restoration in 6 out of 10 clots was achieved by 1ms pulse with only 1 out of 10 showing evidence of bleeding.

### **1.3 Histotripsy Thrombolysis**

Histotripsy is a noninvasive non-thermal tissue ablation technology that mechanically fractionates soft tissue through well-controlled acoustic cavitation generated by ultrasound. Using high pressure (>10 MPa), microsecond-long ultrasound pulses generated outside human

body and focused into target tissue, histotripsy generates a cloud of cavitation microbubbles using pre-existing gas nuclei in the tissue within the focal region [21-25]. The rapid expansion and collapse of the cavitation bubble clouds induce high strain to the target tissue, which tears the cell and the extracellular matrix apart and result in tissue fractionation. Histotripsy can be used to create controlled tissue erosion at a fluid-tissue interface [23, 26, 27] or generate localized well-demarcated tissue fractionation inside bulk tissue [28-30]. Histotripsy is a platform therapeutic ultrasound technology and has potentials for clinical applications where noninvasive tissue removal is desired. Previous studies have demonstrated the feasibilities of using histotripsy to treat several diseases, such as benign prostatic hyperplasia [31, 32], congenital heart disease [23, 33] and liver cancer [30].

The feasibility of using histotripsy as a noninvasive, drug-free, and image-guided thrombolysis technique has been demonstrated previously. An *in vitro* study showed that histotripsy can completely break down large clots (140-300 mg) within 5 min with none detected larger than 100  $\mu\text{m}$  [34] and an *in vivo* study in a porcine deep vein thrombosis model, showed histotripsy therapy can re-establish blood flow and decrease thrombus burden at a speed an order of magnitude faster than any current methods [35]. In these studies, multi-cycle (usually  $\geq 5$  cycles) ultrasound pulses, often with peak negative pressure below 20 MPa and peak positive pressure above 50 MPa, were used to generate the cavitation bubble cloud via a shock scattering mechanism. Individual microbubbles are formed from pre-existing gas nuclei in the tissue in the initial 1-2 cycles. The high amplitude positive shock is scattered from these individual bubbles, and the inverted shockwave interferes with negative cycles in the incident wave, resulting in very high negative pressures and producing a layer of dense bubbles [25]. Using the shock scattering approach, the cavitation cloud is less-confined and tends to be generated in contact with vessel

wall, resulting in potential vessel damage from histotripsy treatment. Even though no vessel penetration was observed in the previous *in vivo* porcine study, denudation of endothelium was found in isolated locations of the vein wall. This damage type is considered reversible, but there is a concern that cavitation may also damage vein valves resulting in irreversible functional damage.

#### **1.4 Microtripsy**

A new mechanism has been discovered recently to initiate cavitation cloud using an ultrasound pulse of  $\leq 2$  cycles length with very high peak negative pressure, which is enabled by the latest breakthrough in transducer amplifier electronics [36]. Cavitation cloud is formed when the peak negative pressure directly exceeds a distinctive “intrinsic threshold” of the medium (27 MPa for blood clots) [24]. Using this intrinsic threshold mechanism, microscopic and precise lesions smaller than the diffraction limit (half of the acoustic wavelength) have been generated by allowing only a small fraction of the focal region to exceed the intrinsic threshold, hence termed “microtripsy” [37]. The location and size of the cavitation cloud generated using the intrinsic threshold mechanism is more reproducible and predictable than the shock scattering mechanism. Using microtripsy for thrombolysis application, cavitation cloud can be generated reliably and entirely within vessel lumen, without contacting the vessel wall and reducing the risk of damaging the vein valves or endothelium. The microtripsy approach (both mechanism and hardware) and the use of microtripsy for thrombolysis treatment provide a novel innovative advantage that is likely to significantly enhance clinical safety of histotripsy thrombolysis.

#### **1.5 Bubble-induced Color Doppler**

Standard ultrasound B-mode imaging is used to visualize cavitation during histotripsy treatments, but it is difficult to provide quantitative feedback. A bubble-induced color Doppler

(BCD) method has been developed for real-time quantitative monitoring of the progress of bulk tissue fractionation by histotripsy [38]. When a cavitation cloud is generated by a histotripsy pulse, a substantial motion is induced in the focal zone and observable on color Doppler synchronized with the histotripsy pulse. After a brief chaotic motion (within 500  $\mu$ s) following the cloud collapse, a coherent motion was observed first away from the transducer and then towards the transducer (lasting for up to 20 ms). The time profile of the resulting velocity of the coherent motion expands as target tissue is fractionated and saturates when the target tissue is completely liquefied. Similarly, the averaged velocity within a specific time window of the coherent motion increases with increasing degree of fractionation, and saturates when the target tissue is completely liquefied. The concurrent occurrence of this saturation point and the complete fractionation has been observed consistently across different tissue types. The surrounding tissue conditions (i.e. vessel/tissue boundaries and tissue-blood interface) are more complicated in thrombolysis application than in bulk tissue fractionation, which leads to different histotripsy-induced motions and makes BCD monitoring for histotripsy thrombolysis more challenging. A specific BCD algorithm needs to be developed for histotripsy thrombolysis to detect the BCD saturation point in real-time, as a reliable indication for complete clot liquefaction. The bubble-induced color Doppler feedback and the algorithm development to pinpoint the complete clot fractionation in real-time is critical to maximize the treatment efficacy for thrombolysis treatment and other histotripsy applications.

## **1.6 Outline of This Dissertation**

This dissertation is organized into eight chapters, documenting the details of our work on the research, development and clinical translation of histotripsy thrombolysis. A brief summary of each chapter follows.

The present chapter gives an overall introduction of my dissertation. The focus of this dissertation work is first introduced. The necessary backgrounds of this work, including thrombosis diseases, histotripsy technology and previous histotripsy thrombolysis work, and relevant technical innovations, are then presented.

Chapter 2 describes in detail the development of the integrated, portable histotripsy thrombolysis system. The system consists of three subsystems: a histotripsy therapy system, an ultrasound imaging system and a motorized positioning system. It was developed with built-in capabilities for microtriopsy and bubble-induced color Doppler. Therapy transducers, with an ultrasound imaging probe embedded inside, are developed specifically for thrombolysis application. Compact motorized positioner is designed and built onto a mechanical arm for flexible therapy transducer positioning. Integrated control software is also developed to implement complex treatment strategies.

Chapter 3 demonstrates the feasibility of using microtriopsy approach for thrombolysis in an *in vitro* flow model. Blood clots made from bovine blood are formed in a flow model and treated using microtriopsy pulses by scanning the cavitation focus through target clots. Cavitation bubble clouds are consistently generated in the center of the vessel lumen without contacting the vessel wall. Flow channels are successfully generated through the clots with a diameter up to 60% of the vessel diameter. The debris particles were small with over 99.9% < 10  $\mu\text{m}$  and the largest at 153  $\mu\text{m}$ .

Chapter 4 extends the feasibility study of microtriopsy thrombolysis presented in Chapter 3, investigating the effects of pulse repetition frequency (PRF) and dose (number of pulses) on thrombolysis treatments. Microtriopsy treatments using different PRFs (5, 50, and 100 Hz) and doses (20, 50, and 100 pulses) were performed on blood clots in an *in vitro* flow model. The

results shows that a high PRF (50 or 100 Hz) may be a better clinical choice for microtripsy thrombolysis due to the larger resulting flow channel, shorter treatment time, and smaller debris particles.

Chapter 5 further investigates the treatment efficacies of microtripsy thrombolysis on different clot types. Unretracted and retracted clots are prepared *in vitro* and treated using microtripsy pulses. Three treatment strategies are developed and applied during treatments in retracted clots. It is demonstrated that microtripsy can successfully generate a flow channel through retracted clots but with reduced treatment efficacy compared to unretracted clots. This work also shows that the treatment strategies incorporating the electronic focal steering can significantly increase the size of recanalized flow channels in retracted clots.

Chapter 6 investigates the potential of bubble-induced color Doppler (BCD) to quantitatively monitor microtripsy thrombolysis in real-time. Bubble-induced motion after each ultrasound pulse is first cross-validated using BCD and optical particle image velocimetry (PIV). Then a strong correlation is demonstrated to exist between the degree of histotripsy clot fractionation and BCD feedback, regardless clot types. Finally, a real-time algorithm is developed and verified to reliably detect the completion of histotripsy fractionation using BCD feedback. This work provides a quantitative method to monitor histotripsy thrombolysis and other histotripsy-mediated treatments.

Chapter 7 validates the efficacy and safety of microtripsy thrombolysis through a comprehensive pre-clinical study in a porcine DVT model. Microtripsy thrombolysis treatments are conducted in 14 pigs, of which acute clots are induced in femoral veins. Results show that blood flow is restored or significantly increased after treatment in 13 pigs and only minor hemolysis and microscopic hemorrhage outside vessel wall are observed. This work further

demonstrates the potential of microtripsy thrombolysis for fast, precise, and effective clot recanalization, minimizing risks of vessel damage and hemolysis.

Chapter 8 summarizes the findings and contributions of this dissertation work, and discuss future work that will be necessary to push this noninvasive thrombolysis technology further towards clinical use.

## 1.7 References

- [1] D. Mozaffarian, *et al.*, "Executive Summary: Heart Disease and Stroke Statistics—2015 Update A Report From the American Heart Association," *Circulation*, vol. 131, pp. 434-441, 2015.
- [2] M. G. Beckman, *et al.*, "Venous thromboembolism: a public health concern," *American journal of preventive medicine*, vol. 38, pp. S495-S501, 2010.
- [3] D. Collen, *et al.*, "Thrombolytic therapy," *Annual review of medicine*, vol. 39, pp. 405-423, 1988.
- [4] H. S. Friedman, *et al.*, "Tissue plasminogen activator for acute ischemic stroke," *N Engl J Med*, vol. 334, p. 1405, 1996.
- [5] M. W. Mewissen, *et al.*, "Catheter-directed Thrombolysis for Lower Extremity Deep Venous Thrombosis: Report of a National Multicenter Registry 1," *Radiology*, vol. 211, pp. 39-49, 1999.
- [6] H. S. Kim, *et al.*, "Catheter-directed thrombolysis with percutaneous rheolytic thrombectomy versus thrombolysis alone in upper and lower extremity deep vein thrombosis," *Cardiovascular and interventional radiology*, vol. 29, pp. 1003-1007, 2006.
- [7] M. J. Sharafuddin, *et al.*, "Endovascular management of venous thrombotic and occlusive diseases of the lower extremities," *Journal of vascular and interventional radiology*, vol. 14, pp. 405-423, 2003.
- [8] S. Pfaffenberger, *et al.*, "2MHz ultrasound enhances t-PA-mediated thrombolysis: comparison of continuous versus pulsed ultrasound and standing versus travelling acoustic waves," *THROMBOSIS AND HAEMOSTASIS-STUTTGART-*, vol. 89, pp. 583-589, 2003.
- [9] C. K. Holland, *et al.*, "Ultrasound-enhanced tissue plasminogen activator thrombolysis in an *in vitro* porcine clot model," *Thrombosis research*, vol. 121, pp. 663-673, 2008.



- [10] K. E. Hitchcock, *et al.*, "Ultrasound-Enhanced rt-PA Thrombolysis in an *ex vivo* Porcine Carotid Artery Model," *Ultrasound in medicine & biology*, vol. 37, pp. 1240-1251, 2011.
- [11] J. Larsson, *et al.*, "Ultrasound enhanced thrombolysis in experimental retinal vein occlusion in the rabbit," *British journal of ophthalmology*, vol. 82, pp. 1438-1440, 1998.
- [12] A. V. Alexandrov, *et al.*, "Ultrasound-enhanced systemic thrombolysis for acute ischemic stroke," *New England Journal of Medicine*, vol. 351, pp. 2170-2178, 2004.
- [13] C. A. Molina, *et al.*, "Transcranial ultrasound in clinical sonothrombolysis (TUCSON) trial," *Annals of neurology*, vol. 66, pp. 28-38, 2009.
- [14] G. Tsivgoulis, *et al.*, "Safety and efficacy of ultrasound-enhanced thrombolysis a comprehensive review and meta-analysis of randomized and nonrandomized studies," *Stroke*, vol. 41, pp. 280-287, 2010.
- [15] S. Datta, *et al.*, "Ultrasound-Enhanced Thrombolysis Using Definity<sup>®</sup> as a Cavitation Nucleation Agent," *Ultrasound in medicine & biology*, vol. 34, pp. 1421-1433, 2008.
- [16] A. T. Brown, *et al.*, "Microbubbles improve sonothrombolysis *in vitro* and decrease hemorrhage *in vivo* in a rabbit stroke model," *Investigative radiology*, vol. 46, 2011.
- [17] W. C. Culp, *et al.*, "Successful microbubble sonothrombolysis without tissue-type plasminogen activator in a rabbit model of acute ischemic stroke," *Stroke*, vol. 42, pp. 2280-2285, 2011.
- [18] U. Rosenschein, *et al.*, "Ultrasound Imaging–Guided Noninvasive Ultrasound Thrombolysis Preclinical Results," *Circulation*, vol. 102, pp. 238-245, 2000.
- [19] A. Burgess, *et al.*, "High-intensity focused ultrasound (HIFU) for dissolution of clots in a rabbit model of embolic stroke," *PloS one*, vol. 7, p. e42311, 2012.
- [20] C. Wright, *et al.*, "*In vitro* and *in vivo* high intensity focused ultrasound thrombolysis," *Investigative radiology*, vol. 47, p. 217, 2012.
- [21] Z. Xu, *et al.*, "Effects of acoustic parameters on bubble cloud dynamics in ultrasound tissue erosion (histotripsy)," *The Journal of the Acoustical Society of America*, vol. 122, pp. 229-236, 2007.
- [22] Z. Xu, *et al.*, "Evolution of bubble clouds induced by pulsed cavitation ultrasound therapy-histotripsy," *Ultrasonics, Ferroelectrics and Frequency Control, IEEE Transactions on*, vol. 55, pp. 1122-1132, 2008.

- [23] Z. Xu, *et al.*, "Noninvasive creation of an atrial septal defect by histotripsy in a canine model," *Circulation*, vol. 121, pp. 742-749, 2010.
- [24] A. D. Maxwell, *et al.*, "Probability of cavitation for single ultrasound pulses applied to tissues and tissue-mimicking materials," *Ultrasound in medicine & biology*, vol. 39, pp. 449-465, 2013.
- [25] A. D. Maxwell, *et al.*, "Cavitation clouds created by shock scattering from bubbles during histotripsy," *The Journal of the Acoustical Society of America*, vol. 130, pp. 1888-1898, 2011.
- [26] Z. Xu, *et al.*, "Controlled ultrasound tissue erosion," *Ultrasonics, Ferroelectrics, and Frequency Control*, IEEE Transactions on, vol. 51, pp. 726-736, 2004.
- [27] G. E. Owens, *et al.*, "Therapeutic ultrasound to noninvasively create intracardiac communications in an intact animal model," *Catheterization and Cardiovascular Interventions*, vol. 77, pp. 580-588, 2011.
- [28] J. E. Parsons, *et al.*, "Pulsed cavitation ultrasound therapy for controlled tissue homogenization," *Ultrasound Med Biol*, vol. 32, pp. 115-29, Jan 2006.
- [29] W. W. Roberts, "Focused ultrasound ablation of renal and prostate cancer: current technology and future directions," *Urol Oncol*, vol. 23, pp. 367-71, Sep-Oct 2005.
- [30] E. Vlaisavljevich, *et al.*, "Image-guided non-invasive ultrasound liver ablation using histotripsy: Feasibility study in an *in vivo* porcine model," *Ultrasound in medicine & biology*, vol. 39, pp. 1398-1409, 2013.
- [31] A. M. Lake, *et al.*, "Histotripsy: minimally invasive technology for prostatic tissue ablation in an *in vivo* canine model," *Urology*, vol. 72, pp. 682-686, 2008.
- [32] T. L. Hall, *et al.*, "Histotripsy for the treatment of BPH: evaluation in a chronic canine model," in *Ultrasonics Symposium, 2008. IUS 2008. IEEE, 2008*, pp. 765-767.
- [33] G. E. Owens, *et al.*, "Intermediate-term effects of intracardiac communications created noninvasively by therapeutic ultrasound (histotripsy) in a porcine model," *Pediatric cardiology*, vol. 33, pp. 83-89, 2012.
- [34] A. D. Maxwell, *et al.*, "Noninvasive thrombolysis using pulsed ultrasound cavitation therapy–histotripsy," *Ultrasound in medicine & biology*, vol. 35, pp. 1982-1994, 2009.
- [35] A. D. Maxwell, *et al.*, "Noninvasive treatment of deep venous thrombosis using pulsed ultrasound cavitation therapy (histotripsy) in a porcine model," *Journal of Vascular and Interventional Radiology*, vol. 22, pp. 369-377, 2011.

- [36] Y. Kim, et al., "Rapid prototyping fabrication of focused ultrasound transducers," IEEE transactions on ultrasonics, ferroelectrics, and frequency control, vol. 61, pp. 1559-1574, 2014.
- [37] K.-W. Lin, *et al.*, "Histotripsy beyond the "Intrinsic" Cavitation Threshold using Very Short Ultrasound Pulses:"Microtripsy"," IEEE transactions on ultrasonics, ferroelectrics, and frequency control, vol. 61, p. 251, 2014.
- [38] R. M. Miller, *et al.*, "Investigation of the mechanism of ARFI-based Color Doppler feedback of histotripsy tissue fractionation," in Ultrasonics Symposium (IUS), 2013 IEEE International, 2013, pp. 934-937.

## **Chapter 2**

### **Development of Histotripsy Thrombolysis System**

#### **2.1 Introduction**

The development of an integrated, portable histotripsy thrombolysis system is described in detail in this chapter. This system is designed specifically for clinical use and incorporates all the necessary hardware components for microtripsy and BCD implementations. It serves as a platform where new functionalities, new treatment parameters and strategies can be implemented and tested, and also serves as an integrated therapy device for clinical validations. The system consists of three subsystems: a histotripsy therapy system, an ultrasound imaging system, and a motorized positioning system. The whole system is built based on a commercial ultrasound imaging system. A multi-degree-of-freedom mechanical arm is installed into the cart of the imaging system. A histotripsy transducer with an ultrasound imaging probe embedded inside is mounted onto a compact motorized 3-dimensional positioner which is installed at the top of the mechanical arm. Ultrasound images from the embedded imaging probe are displayed in real-time on a 15-inch screen. Treatment is controlled and managed through a control panel which includes a touch screen, a pair of joysticks and several physical buttons and knobs. Two versions of control software are developed: one for engineering tuning and testing, and one for clinical use.

#### **2.2 Therapy Transducer Development**

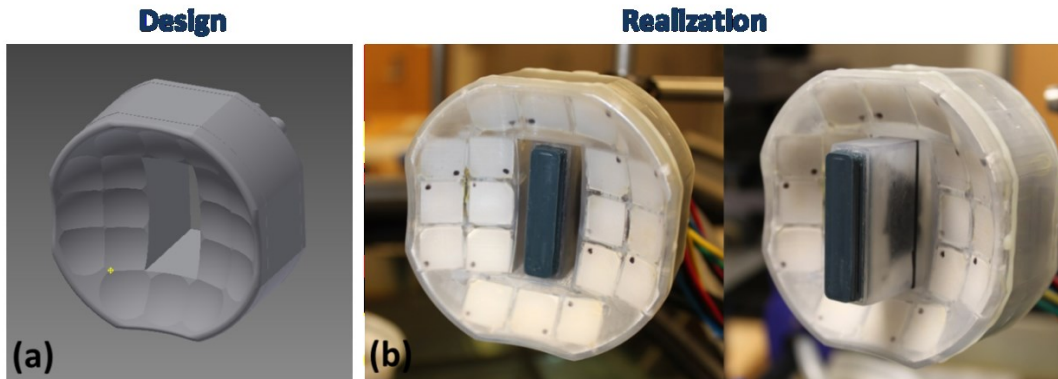
### 2.2.1 Initial Prototype

Therapy transducers for thrombolysis application were designed following the four criteria. 1) The transducer focal zone needs to be sufficiently small to be entirely contained within the femoral vein. 2) The transducer focal distance will be longer than the maximum overlying tissue depth but sufficiently short to minimize the distance between the transducer surface and the skin. 3) The surface area of the transducer will be within the available acoustic window but sufficiently large to obtain high focal pressure required for microtripsy. 4) The center frequency will be determined by attenuation from the overlying tissue, the maximum surface pressure of the transducer, the desired focal size, and acoustic saturation.

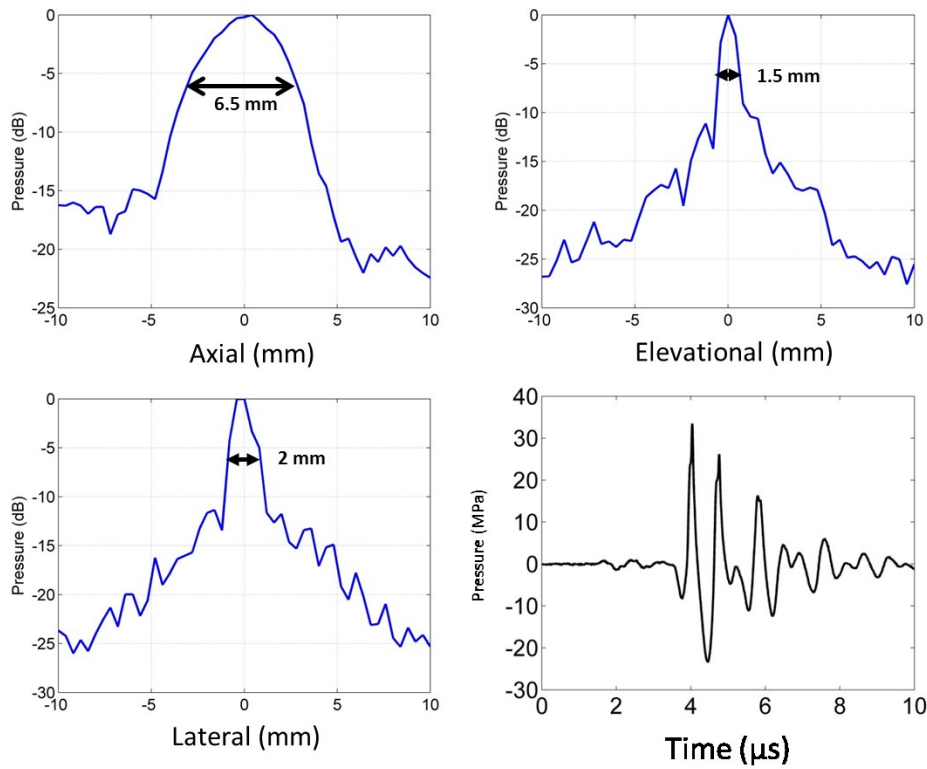
Based on these criteria and our initial DVT patient data, an initial prototype of histotripsy thrombolysis transducer was designed using the initial ultrasound imaging data collected from DVT patients and constructed using the SLA method developed in our lab [1]. This 1.25-MHz transducer has 18 square piezoelectric elements (1.5-cm x 1.5-cm), with an 8 cm (laterally) x 8.3 cm (elevationally) aperture size and a 6-cm focal length (**Figure 2.1**). A 4.8-cm x 2.2-cm rectangular central hole allows the insertion of a linear ultrasound imaging probe to guide and monitor the treatment. This design provides a 4 cm working distance (from the front transducer edge to the focus) that can cover the full range of overlying tissue, while minimizing the standoff distance between the surface of the therapy and imaging transducers and the patient skin.

The transducer was calibrated using a fiber-optic probe hydrophone (FOPH) adapted from a previously published design [2]. The  $-6$  dB focal beam volume of the transducer was measured to be 6.5 mm (axially) x 2 mm (laterally) x 1.5 mm (elevationally) at a peak negative pressure of 15MPa, which is sufficiently small to limit the entire cavitation cloud within the femoral vein of both humans and pigs (5 ~ 21.7 mm) [3, 4]. The pressure profiles on the three

axes and the focal waveform are shown in **Figure 2.2**. By summing the pressure outputs of 3 sub-groups of the elements, the maximal focal peak negative pressure was estimated to be 48 MPa in free field and 36 MPa through 5 cm of soft tissue by taking acoustic attenuation into account.



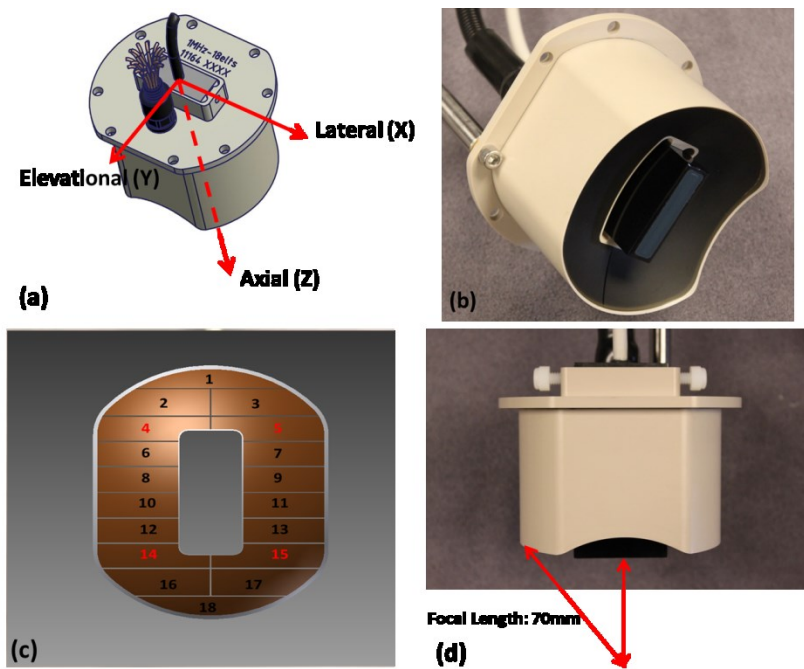
**Figure 2.1:** Initial prototyping of histotripsy thrombolysis transducer. **(a)** CAD design and **(b)** the final transducer with a linear ultrasound-imaging probe inserted.



**Figure 2.2:** Pressure profiles of the initial prototype along the three axes and the focal pressure waveform measured by a fiber optical hydrophone.

### 2.2.2 Final Design

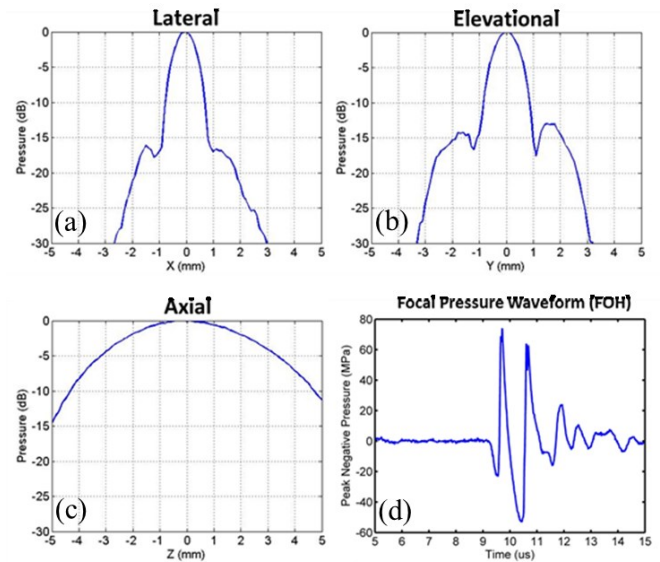
After verifying the prototyping transducer in *in vitro* experiments, a final version of the clinically designed histotripsy thrombolysis transducer was designed and contracted to an experienced transducer company (Imasonic, France). The transducer has an effective 9.8-cm (laterally) x 8-cm (elevationally) aperture size, a 7-cm focal length and 5-cm working distance (**Figure 2.3**). The rectangular central hole for ultrasound imaging probe is 6-cm (lateral) x 2.4-cm (elevationally). It contains 18 strip elements along the elevational direction (**Figure 2.3(c)**), which allows electrical steering of the focus along the lateral direction.



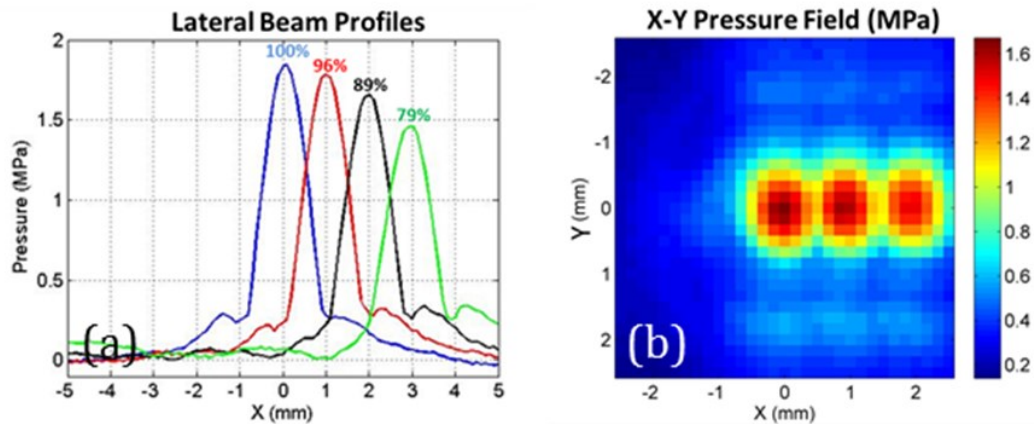
**Figure 2.3:** Final histotripsy thrombolysis transducer. (a) CAD design. (b) Transducer front surface. (c) Element design. (d) Focal length illustration.

The  $-6$  dB focal beam volume of the transducer was measured to be 6.5 mm (axially) x 2 mm (laterally) x 1.5 mm (elevationally) at a peak negative pressure of 15MPa (**Figure 2.4(a)-(c)**). The pressure profiles at multiple steered locations along the lateral direction and their

corresponding 2D pressure fields are shown in **Figure 2.5**. By summing the pressure outputs of 3 sub-groups (6 contiguous elements in each group), the peak negative pressure at the geometry focus was estimated to be over 45 MPa in free field and 34 MPa through 5 cm of soft tissue by taking acoustic attenuation into account. The pressure only drops around 10% at the steered location 2 mm away from the geometry focus, which means the cavitation region can be widened to 5mm along the lateral axis.



**Figure 2.4:** Pressure calibration of the clinical histotripsy thrombolysis transducer. (a)–(c) Pressure profiles along the three axes. (d) Estimated focal pressure waveform by summing the three sub-group waveforms.



**Figure 2.5:** (a) Pressure profiles along the lateral direction at multiple steered locations. (b) Overlapped 2D pressure fields on the lateral-elevational plane at multiple steered locations.



## 2.3 Ultrasound Imaging

### 2.3.1 Ultrasound Imaging System

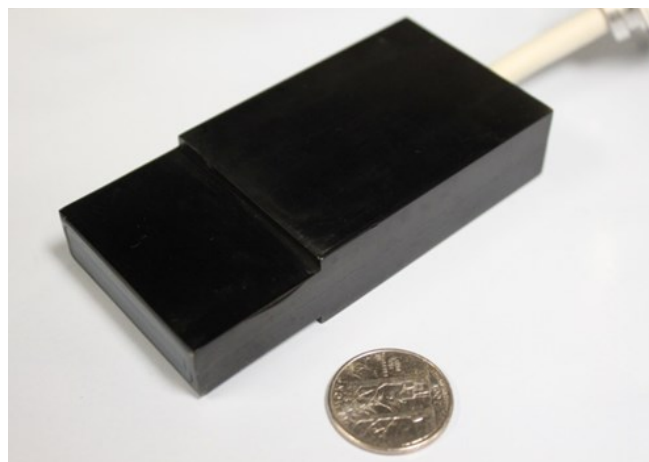
A commercial ultrasound imaging system (SonixTouch; Analogic Ultrasound, Vancouver, Canada) is deployed as the base of the histotripsy thrombolysis system (**Figure 2.6**). It is a FDA-approved diagnostic ultrasound system packaged with an Ultrasound Research Interface (URI). The URI module has the ability to run special research tools for performing tasks such as transducer prototyping, low-level ultrasound beam sequencing control, and development of commercial ultrasound applications running on its platform. It has 256 transmit channels and 64 receive channels, with 80 MHz transmit delays calculation clock and 40 MHz receive sampling clock. This system accepts a wide range of ultrasound imaging probes: linear, phased, curve linear, 2D, high frequency (40 MHz) and so on. Full ranges of C++ software development kits (SDKs) are provided by the manufacturer from very low level of US transmit/receive control to the high level of remote control and custom application development. The cart of this imaging system is extended to hold our therapy transducer amplifier and motor drivers inside.



**Figure 2.6:** Commercial SonixTouch<sup>®</sup> ultrasound imaging system.

### 2.3.2 Custom Ultrasound Imaging Probe

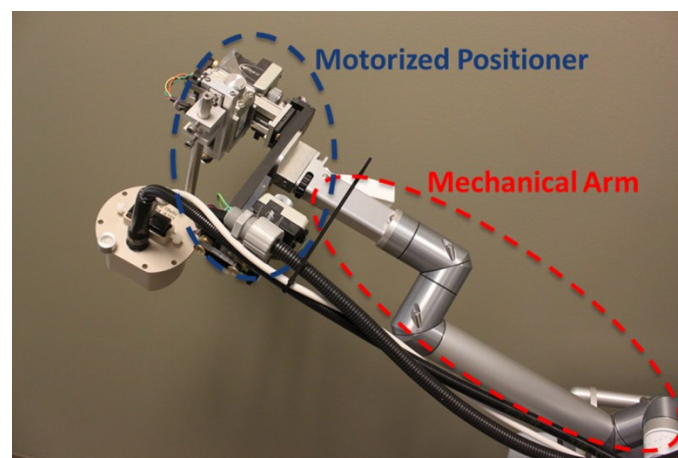
The histotripsy thrombolysis treatment is guided by real-time ultrasound imaging feedback using a linear array imaging probe (7.5 MHz center frequency). It has 128 elements and compatible with the ultrasound imaging system. A rectangular customized housing is designed to minimize its volume and ease the insertion to the central hole of the therapy transducer (**Figure 2.7**). The imaging probe and its housing were constructed by Vermon, Inc. (France). The imaging probe can be inserted through the center hole of the therapy transducer (**Figure 2.3**) and only has one degree of freedom to move along the axial axis of the therapy transducer. The imaging probe can be moved close to the patient's skin to avoid degradation of imaging quality. A simple locking structure is designed on the back of the therapy transducer to allow holding and releasing the imaging probe. By locking the imaging probe position coaxially with the therapy transducer, the imaging plane will be always aligned with the therapy plane. It is connected to the ultrasound imaging system and real-time ultrasound images from this probe are displayed on the imaging system.



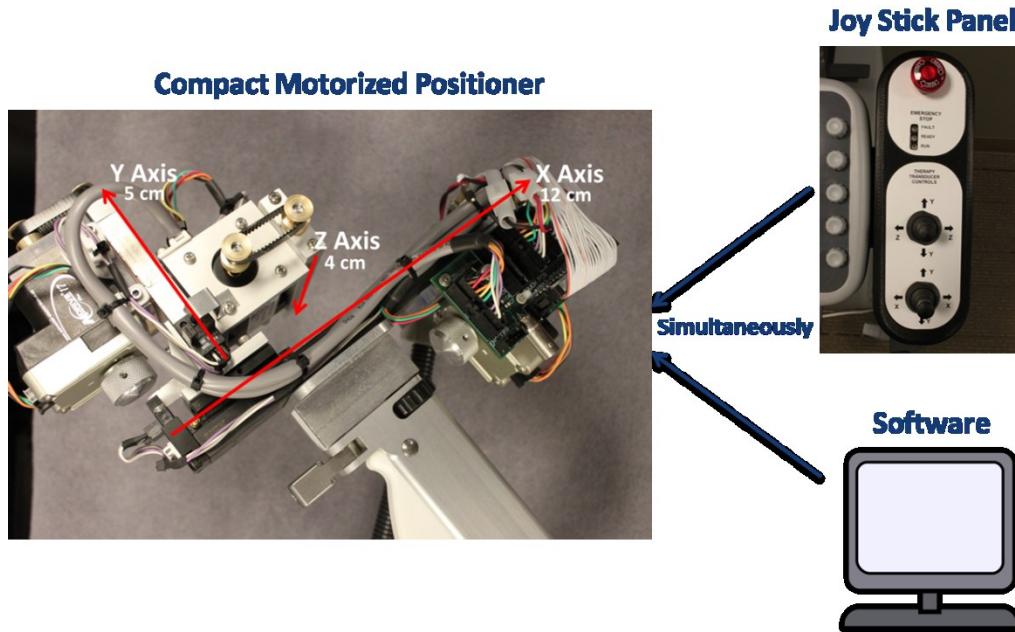
**Figure 2.7:** Ultrasound imaging probe with a rectangular customized housing.

## 2.4 Positioning System

The positioning system includes two parts: a multi-degree-of-freedom mechanical arm and a compact motorized 3-dimensional positioner. The mechanical arm is purchased from DK Technologies (Barum, Germany). With a press/release lock, the arm can be moved and positioned anywhere within a range of 0.5 m (**Figure 2.8**). The compact motorized 3-dimensional positioner is developed in house for finer position adjustment. It is assembled using three linear stages to form three perpendicular moving axes. A step motor is installed at the end of each linear stage. The three motors are driven by a programmable logic controller and the whole positioner can be controlled physically through the joy sticks installed on the cart and virtually through software (**Figure 2.9**). This positioner provides a step size of 20  $\mu\text{m}$ , a moving range of 12, 5, and 4 cm in x, y, and z direction respectively. Using this positioning system, the therapy transducer can be easily positioned in a large range and precisely adjusted to align with the targets.



**Figure 2.8:** The positioning system. The compact motorized positioner is installed on the top of the mechanical arm.



**Figure 2.9:** The compact motorized positioner can be controlled by joy sticks and software commands through a programmable logic controller.

## 2.5 System Integration

The histotripsy thrombolysis system is integrated based on the ultrasound imaging machine (**Figure 2.10**). The positioning system is installed on the extended cart of the imaging system and the motors are connected to the programmable logic controller placed inside of the extended cart. The joy sticks and an emergency button are installed on the right of the original control panel of the imaging system and connected to the same programmable logic controller. The therapy transducer with the embedded imaging probe is mounted onto the compact motorized positioner and connected to its amplifier placed inside the cart. The imaging probe is connected directly to the imaging system.

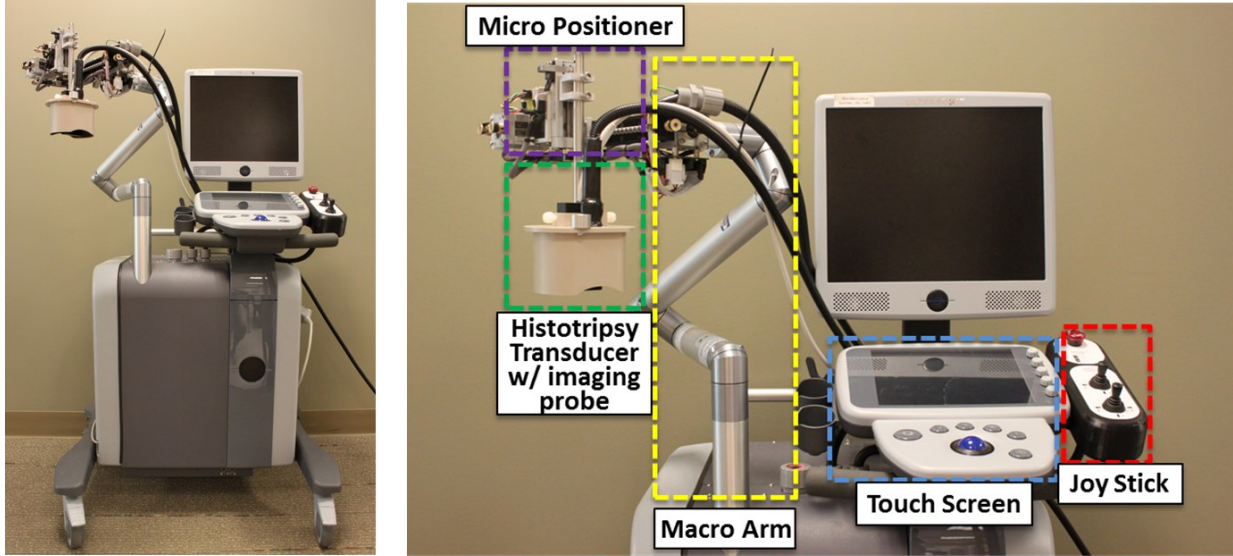


Figure 2.10: Integrated histotripsy thrombolysis system.

## 2.6 Software Development

Integrated software with a clinician-friendly interface is developed to control the therapy, imaging, and positioning systems together, and to implement complex therapy and monitoring algorithms. Systemic integration is very important to connect the therapy and positioning control and imaging feedback. Control needs to be determined and adjusted by the feedback for desired effects to be achieved. Two versions of control software are developed using C++ and Qt framework: one for engineering testing and tuning, and one for treatment use. The software applications are designed according to the practical experiences on *in vivo* animal thrombolysis treatments we conducted and the discussions with two clinicians.

The two software versions share a similar structure as shown in **Figure 2.11**. Individual C++ classes to control ultrasound imaging, histotripsy therapy and positioning are developed and tested first and then integrated into one entity. Each C++ class is like a virtual machine including all the basic functions of the corresponding subsystem. For the therapy, it is able to set all the treatment parameters (PRF, charging time, steering focuses, dose, etc.), treating sequences and

operation management. For positioning, it can move the transducer simultaneously along all three axes and read current positions from their driver. For the imaging, it can synchronize the imaging with the therapy to avoid interference between imaging pulses and therapy pulses. All the imaging parameters can be set and all the imaging data can be accessed by the corresponding C++ class. A user interface class is developed to serve as a main class to hold and connect the three sub-system classes and also to be responsible to interact with the users, such as responses to user's inputs and display information on the screen.

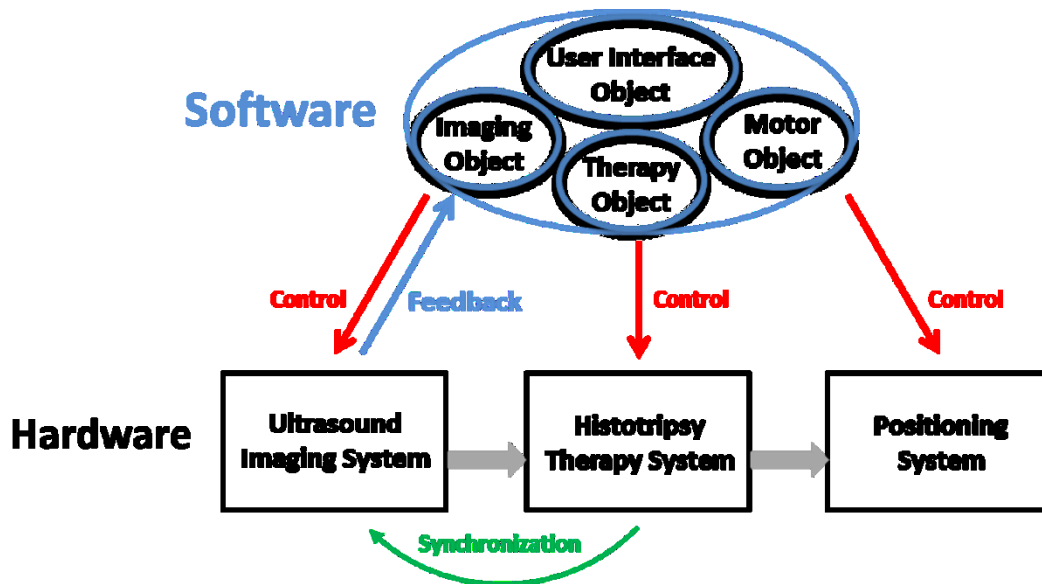
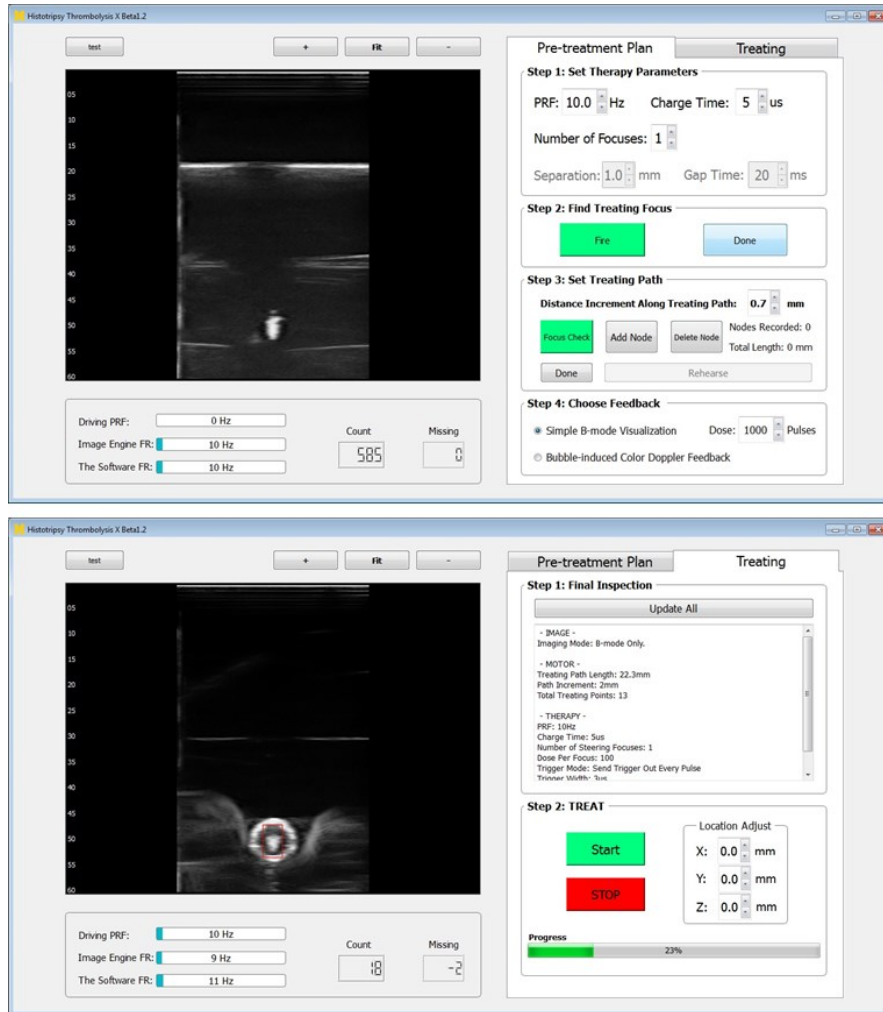


Figure 2.11: Schematic structure of control software.

The major differences between the two software versions are the user interface design and the imaging SDK used. As discussed in 2.3.1, the imaging system provides different SDKs to control the imaging functionalities. For the engineering version, a remote control SDK (called Ulterius) is used to send commands to the commercial built-in software and receive image data from it. It requires a separate computer to communicate with the imaging system. All the operations are conducted on the separate computer using a mouse. For the clinical version, a more basic SDK (called Porta) is used to directly develop our own imaging modality without

using the built-in software. The programming is more complicated but at the same time more flexible. The treatment software is run directly on the imaging system and no separate computer is needed. With this version, user interface are designed specifically for clinicians and only touch screen and physical buttons are used for user inputs.

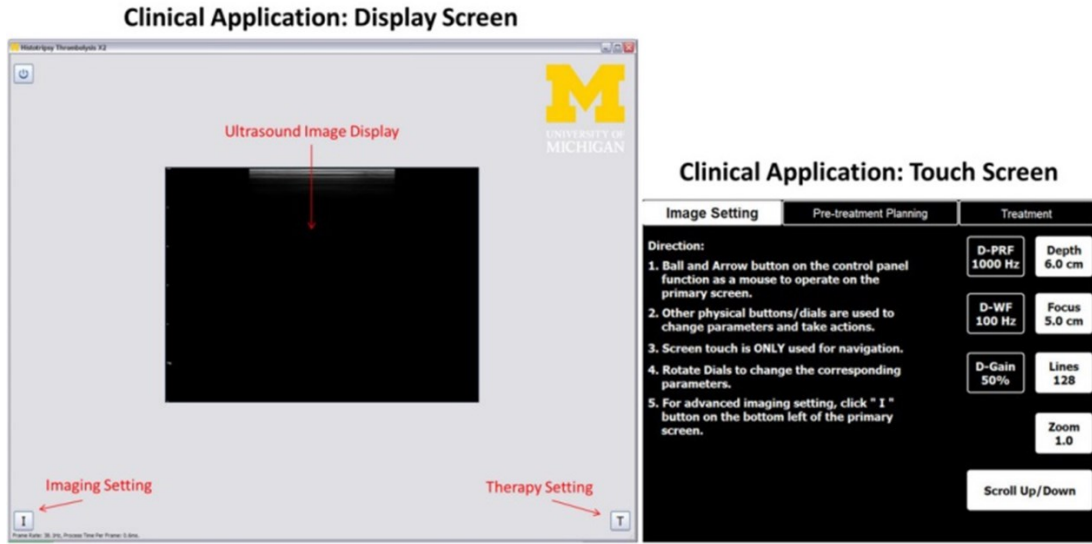
The engineering version of the control software is developed for engineering and research purposes. The parameters and settings can be easily changed and different algorithms can be easily tested. The user interface of the engineering version is displayed in **Figure 2.12**. On the left part of the UI, real-time ultrasound images and performance information are displayed. On the right side, pre-treatment planning and treatment configurations can be set with step by step guidance. For pre-treatment planning, the treatment focus need to be first marked on the real-time images. The software will then allow the operating clinician to align the focus with the clot inside vessel and plan the scanning path along the length of the clot. To verify the targeting accuracy, a small number of pulses will be applied to produce a hyperechoic zone to ensure several positions on the scanning path will be on or in the clot within the vessel. After the path verification, preset treatment parameters will be confirmed or new treating strategy can be specified. After the pre-treatment plan is specified, B-mode image or the bubble-induced color Doppler feedback (Chapter 6) will be chosen to monitor the treatment. Before starting treatment, all the settings can be updated and reviewed by the operator to avoid mistakes. During treatment, emergency stop is enabled to avoid adverse results and the scanning path can be adjusted real-time.



**Figure 2.12:** The user interface of the engineering version of the control software. Real-time ultrasound images are shown on the left of the window. Two operation tabs are displayed on the right, including a pre-treatment planning tab (Top) and a treatment tab (Bottom).

The treatment software version is developed to simplify the operations for clinicians, who will eventually conduct the treatments instead of engineers. Our plan is to use the engineering version to test, tune and optimize the treatment parameters and settings and then set the optimal values in the clinical version. In this clinical version, the operation flow remains the same as the engineering version but with different user interfaces. The 15-inch screen on the therapy system is used purely for display (**Figure 2.13**). Only the touch screen, the surrounding physical buttons and joysticks are used for user inputs (**Figure 2.14**). There are imaging setting tab, pre-treatment planning tab, and treatment tab in the touch screen interface.





**Figure 2.13:** The treatment version of the control software: the primary display screen (Left) and the touch screen (Right).



**Figure 2.14:** Control panel with a touch screen and physical buttons and knobs, with different touch screen interfaces shown. There are tabs: one for imaging setting, one for pre-treatment planning and one for treatment. Detailed operation instructions are listed on the left of each tab.

## 2.7 Summary

The development of an integrated, portable thrombolysis system is discussed in this chapter. Major efforts have been put into the therapy transducer design and development and the software development. Using this system as a platform, the studies and experiments in the following chapters was able to be conducted to investigate new therapy and imaging methods

and further improve the efficacy and safety of microtripsy thrombolysis. Such a clinically designed integrated system is an important milestone to advance the clinical translation of this new exciting noninvasive thrombolysis technology. This integrated system is used for the studies performed in Chapters 3-7. A list of the system components is attached in Appendix below.

## **2.8 Appendix**

- (1) One Ultrasonix (SonixTouch) system with one mechanical arm and one compact motorized positioner.
- (2) One Imasonic 18-element ultrasound transducer with one 3-board amplifier and one FPGA chip.
- (3) One L11-5 Ultrasonix imaging probe (made by Vermon) with custom housing (black color).
- (4) Four regular Ultrasonix imaging probes: L40, PA7, C7, L14.
- (5) One HP® laptop.
- (6) Three cables: one cable for FPGA communication, one USB-Serial cable for positioner PLC communication and one Ethernet cable for Ultrasonix-laptop communication.
- (7) Two software applications: one for engineering (requires laptop) and one for clinical use.

## **2.9 References**

- [1] Y. Kim, *et al.*, "Rapid prototyping fabrication of focused ultrasound transducers," *Ultrasonics, Ferroelectrics, and Frequency Control*, IEEE Transactions on, vol. 61, pp. 1559-1574, 2014.
- [2] J. E. Parsons, *et al.*, "Cost-effective assembly of a basic fiber-optic hydrophone for measurement of high-amplitude therapeutic ultrasound fields," *The Journal of the Acoustical Society of America*, vol. 119, pp. 1432-1440, 2006.
- [3] B. Hertzberg, *et al.*, "Sonographic assessment of lower limb vein diameters: implications for the diagnosis and characterization of deep venous thrombosis," *AJR. American journal of roentgenology*, vol. 168, pp. 1253-1257, 1997.

- [4] A. D. Maxwell, et al., "Noninvasive treatment of deep venous thrombosis using pulsed ultrasound cavitation therapy (histotripsy) in a porcine model," *Journal of vascular and interventional radiology*, vol. 22, pp. 369-377, 2011.

## Chapter 3

### Noninvasive Thrombolysis using Histotripsy beyond the “Intrinsic” Threshold (Microtripsy)

This chapter has been published in *IEEE Transactions on Ultrasonics, Ferroelectrics, and Frequency Control*. 2015; 62(7):1342-1355. © IEEE. Reprinted, with permission, from [1].

#### 3.1 Introduction

Thrombosis is the formation of a blood clot inside an artery or vein. Arterial obstruction via thrombosis in the cerebral vasculature leads to stroke, which is the fifth leading cause of death in the United States [2]. Deep vein thrombosis, or DVT, affects 300,000 people a year in the United States. Occurring mostly in the legs, it is the most common form of venous thrombosis. The current gold standard of thrombolytic treatment involves the infusion of thrombolytic drugs such as tissue plasminogen activator (tPA) [3, 4]. However, administration of thrombolytic drugs systemically has limited effectiveness requiring long treatment time (several hours to days) and is associated with increased risks of major bleeding [5]. Other treatment options are catheter-based endovascular procedures that are site-specific but more invasive and associated with bleeding, vascular damage, and infections [6-9].

Ultrasound has been a promising technique for promoting clot breakdown for several decades. Significant efforts have focused on enhancing the efficacy of thrombolytic drugs with low intensity ultrasound [10-13]. Several clinical trials have been conducted and the results are promising [14-16]. Ultrasound combined with microbubbles has also been demonstrated to successfully break down clot in the presence or absence of thrombolytic drugs [17-19]. Another

approach using high-intensity focused ultrasound (HIFU) alone for thrombolysis has been investigated *in vitro* and *in vivo* [20-22].

Histotripsy fractionates soft tissue by well-controlled acoustic cavitation using microsecond-long, high-intensity and focused ultrasound pulses [23-25]. The feasibility of using histotripsy as a noninvasive, drug-free, and image-guided thrombolysis technique has been demonstrated previously. *In vitro* studies show that histotripsy can completely break down large clots (140-300 mg) within 5 min with none detected larger than 100  $\mu\text{m}$  [26] and *in vivo* studies in a porcine deep vein thrombosis model, showed histotripsy therapy can re-establish blood flow and decrease thrombus burden. However, vascular damage was still observed in some treatments, as cavitation is not entirely confined in the vessel lumen and sometimes occurs in contact with vessel wall [27].

In our previous histotripsy thrombolysis studies [26, 27], a shock scattering mechanism was used to generate the cavitation bubble cloud, which employs multi-cycle pulses, often with the peak negative pressure below 20 MPa and the peak positive pressure above 50 MPa [28]. Individual sparse microbubbles are first formed and expanded in the initial 1-2 cycles. The high amplitude positive shock is scattered from these individual bubbles, and the inverted shockwave interferes with negative cycles in the incident wave, resulting in very high negative pressures and producing a layer of dense bubbles. Using the shock-scattering mechanism for thrombolysis, the initial bubbles are preferentially generated on the vessel walls where the weak nuclei tend to reside, potentially subjecting the vessel wall to high stress. In our *in vivo* study [27], no vessel penetration was observed, however, denudation of endothelium was found in isolated locations of the vein wall. Endothelial injury occurs with all interventional devices and is generally

considered reversible, but damage to the vein valve may result in irreversible functional damage, leading to chronic venous insufficiency associated with severe morbidity [29].

To avoid cavitation damage to the vessel wall, we have recently discovered a new mechanism to initiate a cavitation cloud via a single pulse of  $< 2$  cycles with only one high negative pressure phase. When the peak negative pressure directly exceeds a distinctive “intrinsic threshold” for the medium (27 MPa for blood clots) [30, 31], a cavitation cloud is formed matching the volume exceeding the threshold. Using this intrinsic threshold mechanism and a very short acoustic pulse ( $< 2$  cycles) to prevent shock-scattering, the volume of the histotripsy-induced cavitation cloud and lesion corresponded well to the volume of the focal regions above the intrinsic cavitation threshold. Because the supra-threshold portion of the negative half cycle can be precisely controlled, lesions considerably smaller than a wavelength are easily produced, hence the term Microtripsy [31].

We hypothesize that microtripsy can accurately generate and confine cavitation in the vessel lumen, without contacting the vessel wall, which results in accurate recanalization within the clot and potentially eliminating vessel damage. In this chapter, microtripsy thrombolysis experiments were conducted in an *in vitro* flow model of DVT. Microtripsy was used to generate the cavitation cloud within the clot formed inside a vessel-mimicking phantom. The cavitation cloud was scanned through the clot to create a flow channel to restore blood flow. Two different scan intervals (SI) and two different peak negative pressures (P-) of applied microtripsy pulses were used to create different flow channels. The goal of this study is to show the potential of using this new microtripsy thrombolysis method to avoid the contact of cavitation with the vessel wall and thus realize accurate and effective clot recanalization, meanwhile eliminating the risk of vessel damage.

## 3.2 Material and Methods

### 3.2.1 Flow Model

An *in vitro* flow model, similar to that described by Spengos *et al.* [32], was developed to mimic the condition of occlusive deep vein thrombosis where no flow is present but pressure is still applied on the clot. As shown in **Figure 3.1**, the flow model consisted of a reservoir, a pressure sensor, a vessel phantom, a filter set, and a fluid collector. All the components were connected with silicone tubing (Masterflex L/S 17; Cole-Parmer, Vernon Hills, IL, USA). The reservoir stored saline for perfusion and was placed above the vessel phantom to apply a constant pressure of 3.7 mm Hg, which was measured by the pressure sensor (MG-9V; SSI Technologies, Janesville, WI, USA). The 3.7 mm Hg was chosen according to reported femoral vein pressure [33, 34]. The vessel phantom was placed horizontally and its inlet and outlet are at the same height. The upstream pressure measured by the sensor at the inlet side equaled the pressure drop across the clot in this model. When a channel was created through the clot by the microtripsy treatment, the flow was restored through the clot inside the vessel phantom due to the pressure applied. The restored flow of saline and clot debris particles from the treatment was then passed through a filter set, and the filtered saline was collected for further particle analysis of the remaining debris particles.

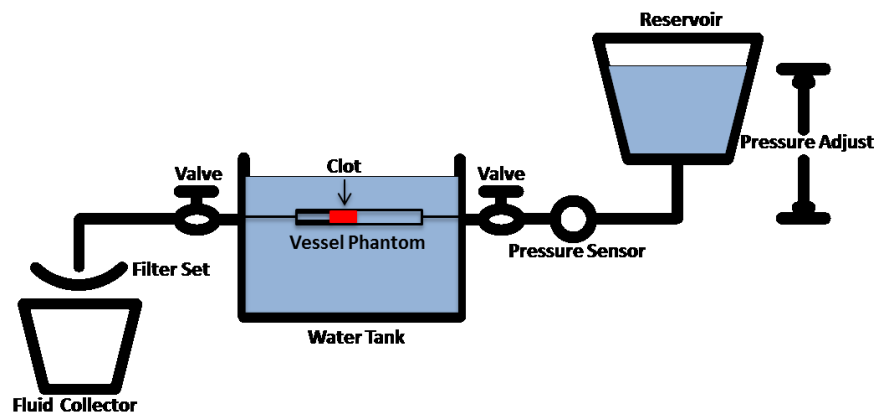
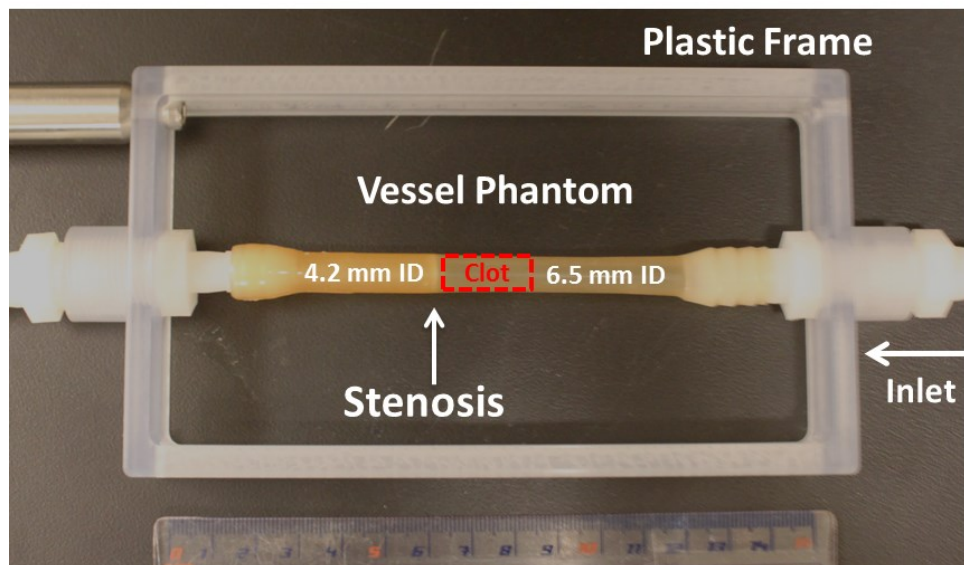


Figure 3.1: Schematic diagram of the flow model.

### 3.2.2 Vessel Phantom

The vessel phantom was developed to mimic a femoral vein in the leg (**Figure 3.2**). It was made from urethane polymer (Urethane RTV Mold-Making System; Tap Plastics Inc., San Leandro, CA, USA), which has a similar acoustic property to human tissue [35]. Urethane (liquid) was first degassed to get rid of bubbles and then poured carefully into a mold similar to that described by Park *et al.* [36]. After solidification of the urethane, it was removed from the mold. The final vessel phantom had a 6.5 mm inner diameter and an 8 mm outer diameter. The 6.5 mm inner diameter was chosen according to the reported DVT vein diameters (5 ~ 21.7 mm) [37]. On one side of the vessel phantom, the inner lumen was narrowed to 4.2 mm (35% stenosis) so that clot can be formed and stabilized by the stenosis to avoid slipping under pressure. The vessel phantom was held by a plastic frame with tube fittings at the two ends to connect the vessel lumen in-line with the rest of the flow model [36].



**Figure 3.2:** The vessel phantom is held by a plastic frame and connected in line with the flow model using tubing fittings. A 35% stenosis is located at the outlet side of the vessel phantom to fix the clot formed aside so that it does not slip under pressure. A clot is formed on the side of the stenosis as shown in the figure. (ID = Inner Diameter)



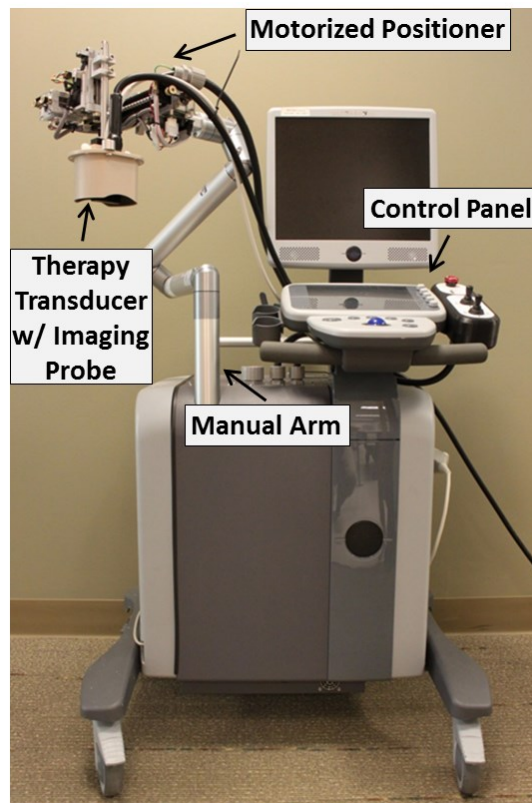
### 3.2.3 Clot Formation

Fresh bovine blood was collected from a local abattoir. Blood from 8 animals was used in this study. Before use, bovine blood was degassed to avoid formation of large stable gas bubble in the clot. A citrate-phosphate-dextrose (CPD) solution (#C7165; Sigma-Aldrich Co., St. Louis, MO, USA) was immediately mixed with bovine blood as an anti-coagulant at a ratio of 1 mL CPD per 9 mL blood. The blood sample was stored at 4°C and used within 72 hours. To stimulate the clotting cascade, calcium chloride (#21107; Sigma-Aldrich Co., St. Louis, MO, USA) was mixed with bovine blood to a final concentration of 20mM/L. To form clot inside the vessel phantom, the stimulated blood was poured into the vertically-placed vessel phantom with the stenosis sealed by a balloon catheter. After staying in 37 °C water bath for 2 hours, a clot with a length of 2 cm was matured and cross-linked with the vessel interior and stenosis. The balloon catheter was then removed and the vessel phantom was connected back into the flow model with the stenosis end of the clot distal to the pressure reservoir.

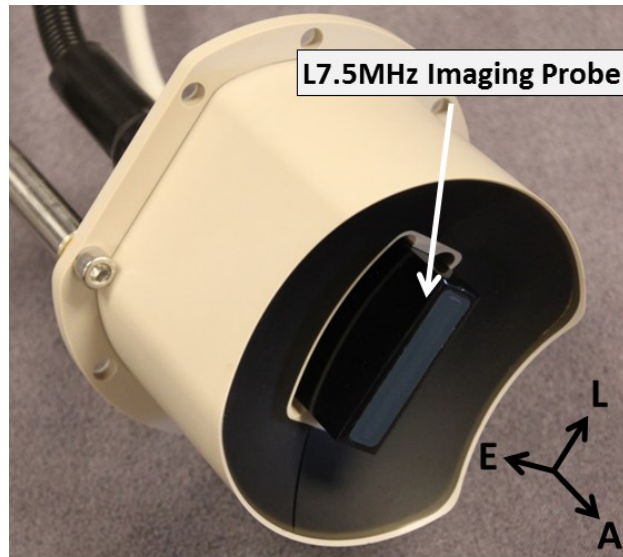
### 3.2.4 Microtripsy Thrombolysis System

Thrombolysis treatment was conducted by an integrated image-guided microtripsy thrombolysis system (**Figure 3.3**) developed in our laboratory. The system integrated three sub-systems: therapy system, ultrasound imaging system and positioning system. A 1-MHz 18-element microtripsy thrombolysis transducer was designed in our laboratory based on the anatomy of DVT patients and manufactured by Imasonic (S.A., Besancon, France) (**Figure 3.4**). The transducer has an effective 9.8 cm (lateral) x 8 cm (elevational) aperture and a 7 cm focal distance. The focal beam volume (-6 dB) of the transducer was measured to be 6.5 mm (axial) x 1.3 mm (lateral) x 1.5 mm (elevational) at a peak negative pressure of 15 MPa using a fiber-optic probe hydrophone (FOPH) [38]. An ultrasound imaging probe with rectangular custom housing

(L7.5MHz; Vermon, France) was inserted into the rectangular central hole of the transducer to guide and monitor microtripsy thrombolysis therapy. Ultrasound imaging was provided by SonixTouch<sup>®</sup> system (Analogic Ultrasound, Vancouver, Canada). The therapy transducer was mounted on a motorized 3-dimension micro-positioner, which had a range of 10 cm x 5 cm x 4 cm. A manual arm to which the micro-positioner was attached gave a range radius of about 1 meter for pre-treatment positioning. Control software was developed to manage and coordinate the therapy, imaging, and positioning systems.



**Figure 3.3:** Integrated microtripsy thrombolysis system. It consists of an ultrasound imaging system, a microtripsy therapy system and a motorized positioning system.



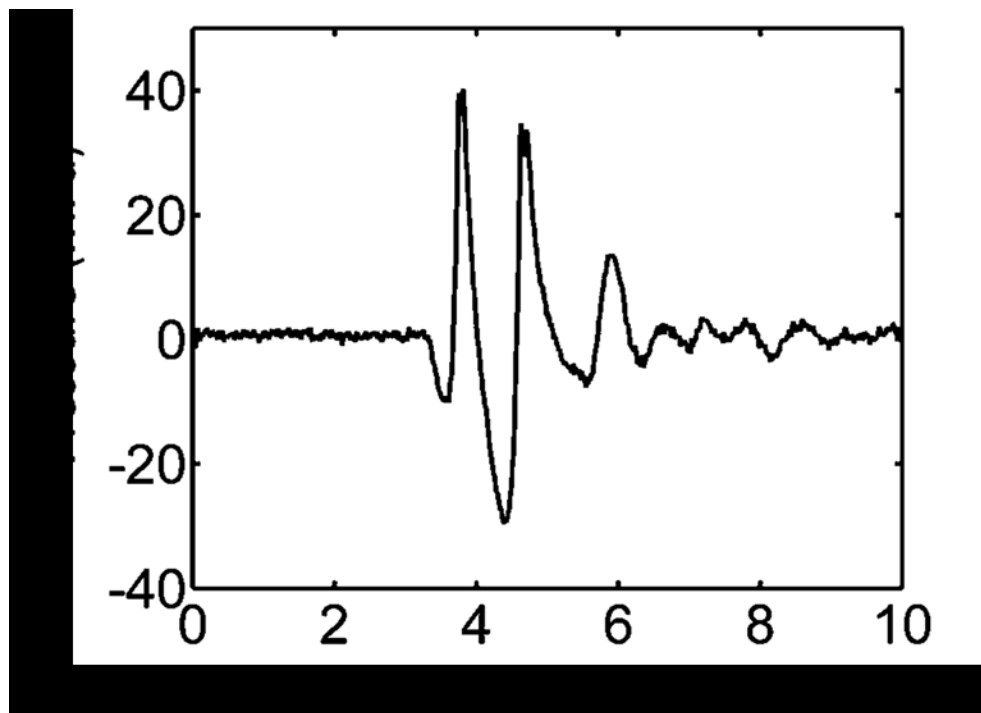
**Figure 3.4:** 1 MHz 18-element microtripsy transducer with an ultrasound imaging probe at the center. With the imaging probe fixed in both lateral and elevational directions, the imaging plane is automatically aligned with the treatment focus of the therapy transducer. (A = Axial, L = Lateral, E = Elevational).

### 3.2.5 Treatments

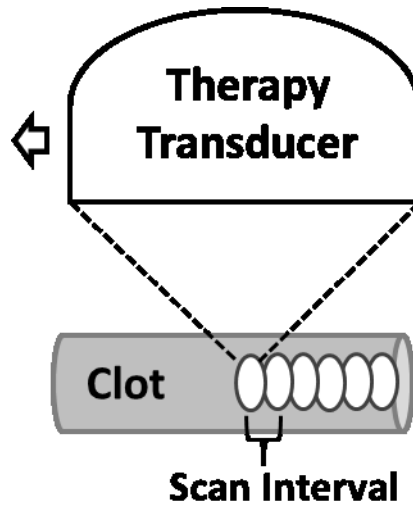
Before treatment, the vessel phantom connected to the flow model was occluded by a clot formed inside. The vessel phantom with the clot was placed in a water tank filled with degassed water. The therapy transducer was placed above the vessel phantom facing down. The treatment focus was first calibrated by marking the hyperechoic cavitation region on the real-time ultrasound images. With the treatment focus aligned at the center of the vessel lumen, a treatment path from one end to the other end of the clot was determined by registering key position coordinates along the clot using the real-time ultrasound images and micro-positioner.

During treatment, the microtripsy thrombolysis system applied a fixed number of pulses at each location along the treatment path with a pulse repetition frequency (PRF) of 50 Hz. An example of microtripsy waveform is shown in **Figure 3.5**. The therapy transducer was moved with a pre-set interval to scan the treatment focus to next location along the path (**Figure 3.6**). Four groups of treatments were conducted using two scan intervals and two peak negative

pressures (**Table 3.1**). Peak negative pressure larger than 20 MPa can't be directly measured and therefore was estimated by linear summation ( $P(-)_{LS}$ ) of P- outputs from 6 separate groups of transducer elements (3 elements per group). According to the predication of treatment focal region using the area where the applied negative pressure exceeds the intrinsic threshold in the clot (27 MPa) [30, 31], peak negative pressures of 30 MPa and 36 MPa were chosen to give reasonable axial lengths of focal region to fit within the 6.5-mm vessel lumen. Scan intervals of 0.7 mm and 0.3 mm were chosen as the half and quarter of the mean elevational width (-6dB) of the predicted focal regions, respectively. To ensure complete clot homogenization for sufficient treatment, 1000 histotripsy pulses were applied per scan location for the treatment groups with 0.7 mm scan interval ( $SI_{0.7mm}$ ) and 300 pulses for the groups with 0.3 mm scan interval ( $SI_{0.3mm}$ ). Ultrasound video was taken throughout each treatment. The total treatment time to scan through a 2-cm clot was 10 min for SI of 0.7 mm and 7 min for SI of 0.3 mm.



**Figure 3.5:** Pressure waveform of a microtripsy pulse. Since peak negative pressure larger than 20 MPa cannot be directly measured, this estimated waveform was linearly summed from the directly-measured waveforms of 6 separate element groups.



**Figure 3.6:** Schematic illustration of the treatment strategy. After a fixed number of microtripsy pulses are applied at one location along the treatment path, the therapy transducer is moved with a pre-set scan interval to the next location and repeats.

**Table 3.1:** Treatment plan

	Scan Interval	$P(-)_{LS}$	Dose Per Location	Number of Treated Clots		
				Debris Analysis Method 1	Debris Analysis Method 2	Total
Group A	0.7 mm	30 MPa	1000 pulses	6	/	6
Group B	0.7 mm	36 MPa	1000 pulses	6	/	6
Group C	0.3 mm	30 MPa	300 pulses	6	6	12
Group D	0.3 mm	36 MPa	300 pulses	6	6	12

### 3.2.6 Cavitation

Cavitation generated by microtripsy was monitored with B-mode ultrasound imaging during the treatment. Since cavitation bubble could appear as a dynamic hyperechoic region on the ultrasound images, the intensity variance between the ultrasound images within the vessel lumen was used to quantify the cavitation region. Cavitation cloud size was quantified using the ultrasound video taken during the treatments with 0.3 mm SI. For each treatment, 1000 pairs of ultrasound images were randomly extracted from the video and an average cavitation region was

generated. An ellipse was fitted into the cavitation region using a function provided by Matlab (MathWorks, Natick, MA, USA) to calculate its major and minor diameters.

### **3.2.7 Flow Channel Quantification**

To quantitatively evaluate the flow channel generated through the clot by the microtripsy thrombolysis treatment, each treated clot was scanned using a 20MHz linear ultrasound image probe (Analogic Ultrasound, Vancouver, Canada). Mounted on the micro-positioner, the imaging probe was placed right above the vessel phantom and its imaging plane was aligned perpendicular to the central axis of the vessel phantom. High quality B-mode images of cross sections of each treated clot were captured every 0.3 mm along the vessel. Since the fractionated clot region was hypoechoic when the flow was restored, we applied a contrast threshold compared to surrounding intact clot to detect the cross section of the flow channel on ultrasound image. The cross area ( $A_{\text{cross}}$ ) of the flow channel was calculated and an ellipse was fitted into the flow channel region using the same method as that for quantifying cavitation region to obtain its major and minor diameters ( $D_{\text{major}}$  and  $D_{\text{minor}}$ ). The mean  $A_{\text{cross}}$ ,  $D_{\text{major}}$  and  $D_{\text{minor}}$  over all valid scan images of each treated clot were used to characterize the generated channel. Diameter of circle ( $D_{\text{circle}}$ ) with equivalent area of  $A_{\text{cross}}$  and opening percentage ( $P_{\text{open}} = D_{\text{circle}}/D_{\text{vessel}}$ ) were also derived to assess potential clinical effectiveness.

### **3.2.8 Restored Flow Measurement**

Restored flow rate is one critical index for clinical effectiveness of current thrombolysis treatments. In our *in vitro* treatments, restored flow rate was measured to evaluate microtripsy thrombolysis effectiveness. The flow channel creation was determined when fluid came out from the vessel phantom to the reservoir. After the first 150 mL of restored fluid was collected for debris analysis, the flow was turned off using a valve in line with the flow system. The system

pressure was adjusted back to 3.7 mm Hg and a measuring beaker was placed under the downstream outlet. The flow was turned on again, and the saline through the treated clot was collected by the beaker for a period of 30 seconds. The restored volume flow rate was then calculated as the volume of the saline collected divided by the time. Owing to the brevity of the time period and the small change in reservoir volume, pressure was assumed to be constant over this time period. A control measurement with no blockage in the circulation system was also conducted to compare with restored flow rate.

### **3.2.9 Debris Particle Measurements**

There is a concern that clot debris particles generated by microtripsy thrombolysis may embolise and occlude downstream vessels. To address this issue, two different methods were utilized to measure and analyze the debris particles. First, a filter weight and Coulter Counter combination method was adopted in 24 clot treatments (six per treatment group for all parameters). The restored flow of saline with suspended debris particles was serially filtered through three filters with pore sizes of 1000, 500 and 100  $\mu\text{m}$ . The dry weight of each filter was measured prior to each treatment. After treatment, the filters were dried in room temperature over 48 hours and reweighed. Because of potential weight increase introduced by sodium chloride crystals formation on the filters, a control group ( $N = 10$ ) was measured in the same way with only saline filtered through. The filtered, collected fluid with debris particles smaller than 100  $\mu\text{m}$  were suspended in the fluid was analyzed using a Coulter Counter (Multisizer 3; Beckman Coulter, Brea, CA, USA). The measurable size range was 2-60  $\mu\text{m}$  by using a 100- $\mu\text{m}$  aperture tube [39]. Second, a microscopic inspection and Coulter Counter combination method was adopted in another 12 clot treatments (6 per treatment group with 0.3mm SI). Clot debris suspended in the restored flow was filtered by only one filter with a pore size of 300  $\mu\text{m}$ .

Macroscopic inspection was conducted to check if there was any debris particle trapped on the 300  $\mu\text{m}$  filter. High-resolution optical images were taken of the filter paper before and after each treatment and the number of distinguishable particles was counted and recorded. The filtered, collected fluid debris particles through the 300  $\mu\text{m}$  filter suspended in the fluid was analyzed using the Coulter Counter. The measurable size range was 2-300  $\mu\text{m}$  by using two aperture tubes (100  $\mu\text{m}$  and 560  $\mu\text{m}$ ).

### 3.2.10 Statistics

All statistical comparisons in this study were performed using a student's t-test. P-values  $<0.01$  were considered significant. Numerical data are expressed as mean  $\pm$  standard deviation. Error bars on graphs represent standard deviation.

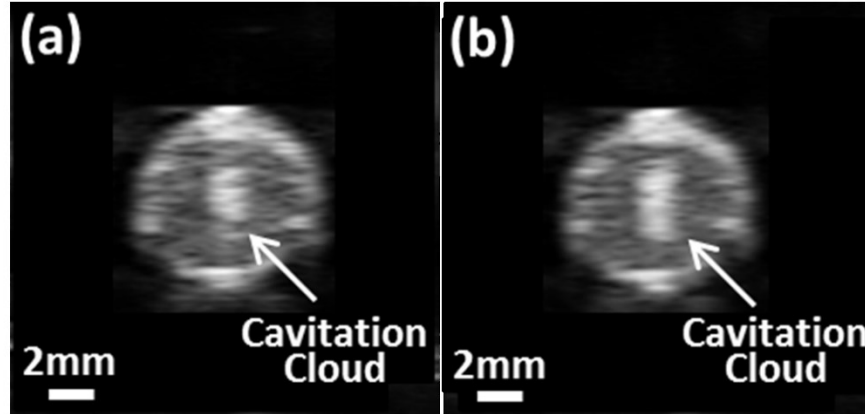
## 3.3 Results

### 3.3.1 Cavitation

For all experiments, cavitation was monitored by ultrasound imaging during the microtripsy thrombolysis treatment. The cavitation bubble cloud was clearly distinguished as a dynamic hyperechoic region on the B-mode images and presented an elliptical shape with its major axis along the ultrasound propagation direction. Using this 6.5-mm diameter vessel phantom, no cavitation was observed on either external or internal sides of the vessel walls during treatment. In the treatment groups with the low  $P(-)_{LS}$ , the bubble cloud was well-confined and consistently maintained in the center of the vessel lumen without contact with the internal vessel wall (**Figure 3.7a**). In the treatment groups with the high  $P(-)_{LS}$ , the bubble cloud was still well-confined but enlarged due to the increased P- (**Figure 3.7b**). Among all the treatments with the 30 MPa  $P(-)_{LS}$  and 0.3 mm SI, the major and minor diameters of the cavitation region were estimated as  $3.41 \pm 0.54$  mm and  $1.95 \pm 0.37$  mm, respectively. And with



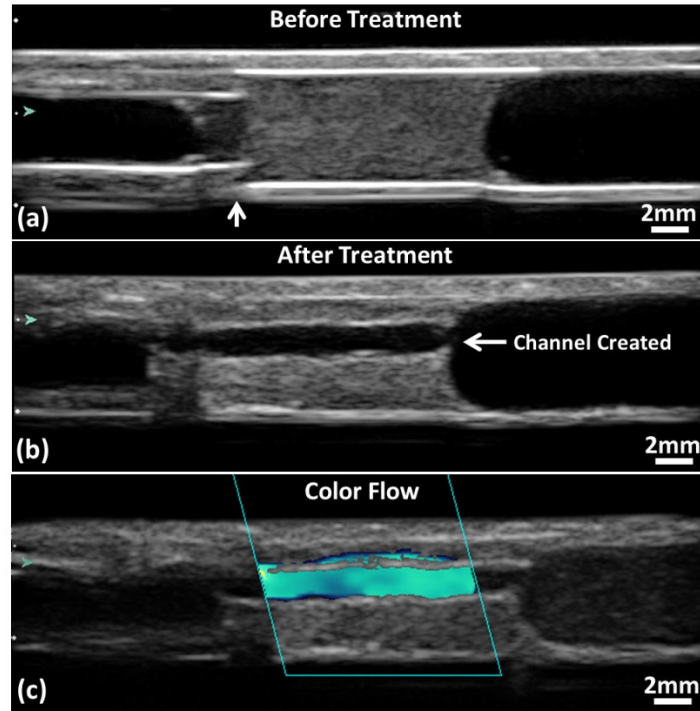
the 36 MPa P(-)<sub>LS</sub> and 0.3 mm SI, the major and minor diameters of the cavitation region were estimated as  $4.53 \pm 0.65$  mm and  $2.12 \pm 0.35$  mm, respectively.



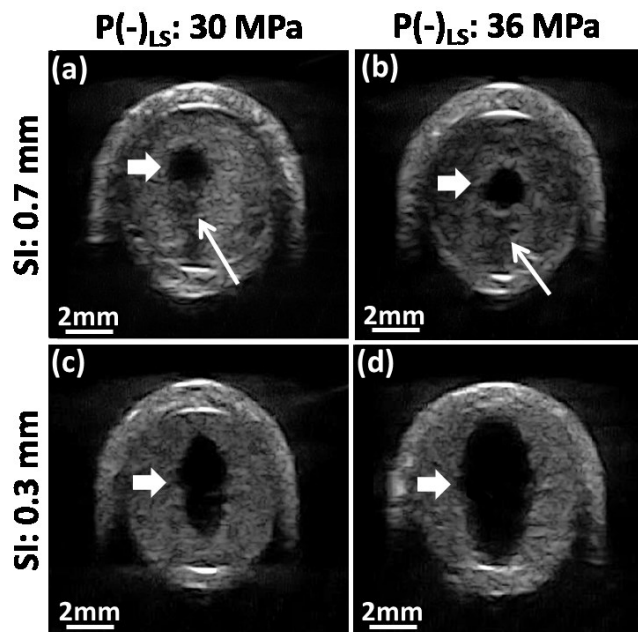
**Figure 3.7:** Cavitation bubble clouds during treatments. (a) Using 30 MPa P(-)<sub>LS</sub>. (b) Using 36 MPa P(-)<sub>LS</sub>. Ultrasound was propagated from the top to the bottom of the images.

### 3.3.2 Flow Channel

A flow channel was successfully generated through the clot after all microtripsy thrombolysis treatments (**Figure 3.8**). The channels were measured using the ultrasound images. Within each treatment, the flow channel was well confined inside the clots without contact with internal vessel wall. The cross sections of the generated flow channel at different scan positions across the clot were consistent. The boundaries of the channel from surrounding intact clots were sharp and clear. Representative cross-sectional images of flow channels generated were shown in **Figure 3.9**. For the treatment groups with the scan interval of 0.7 mm (SI<sub>0.7mm</sub>), the cross-sectional shape of the channels was closer to a circle, and there were small areas with reduced brightness (probably limited fractionation) on one side of the channel contour which corresponded to the tail of the bubble cloud. For the treatment groups with the scan interval of 0.3 mm (SI<sub>0.3mm</sub>), the cross-sectional shape of the channels was generally larger and more like an ellipse with its major axis along the ultrasound propagation direction (i.e. the axial direction of the therapy transducer). No area with reduced brightness near the channel contour was observed.



**Figure 3.8:** Ultrasound images of a treated clot in the vessel phantom. (a) Before treatment. The vertical arrow locates the stenosis is. (b) Flow channel presence after treatment. (c) Color flow presence after treatment. Glass beads (Part# 10089; TSI, Shoreview, MN, USA) were mixed in the perfusion saline after the treatment to obtain this color Doppler image. Flow is from the right to the left of the images.



**Figure 3.9:** Representative ultrasound images of flow channel generated from the 4 treatment groups. The generated flow channels show as the hypoechoic zones inside clots (block arrow). Reduced echogenicity is found at one side of the flow channels with 0.7 mm SI (line arrow), where the tail of the cavitation cloud was. Ultrasound was propagated from the top to the bottom of the images.


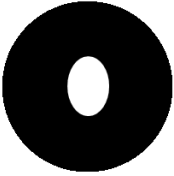
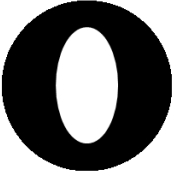
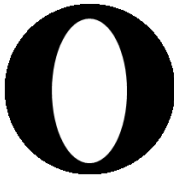



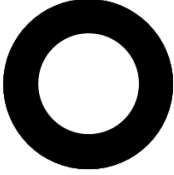
Quantitative results characterizing the channel size in each treatment group are shown in **Table 3.2**. For easier comparison, cartoon illustrating the cross section of the generated channel inside of the vessel lumen in proportion to the actual sizes from **Table 3.2** is also shown in **Figure 3.10**. Using the same  $P(-)_{LS}$ , the mean  $A_{cross}$  of the flow channel generated with  $SI_{0.3mm}$  was over three times larger than that generated with  $SI_{0.7mm}$ . One-sided t-tests were performed between Group A and C (30 MPa  $P(-)_{LS}$ ), and Group B and D (36 MPa  $P(-)_{LS}$ ). Both showed significant increases of  $A_{cross}$  by reducing SI from 0.7 mm to 0.3 mm (both  $P < 0.0001$ ). The mean equivalent opening  $P_{open}$  in the  $SI_{0.3mm}$  groups was above 48%, which was about twice of that in the  $SI_{0.7mm}$  groups. The ratio of  $D_{minor}$  to  $D_{major}$  for the  $SI_{0.7mm}$  groups was over 67% whereas that for the  $SI_{0.3mm}$  groups was approximately 50%. Within the groups using the same scan interval, the mean  $A_{cross}$  of the flow channel generated with 36 MPa  $P(-)_{LS}$  was larger than that generated with 30 MPa  $P(-)_{LS}$ . By applying one-sided t-test on Group C and D (0.3 mm SI), it showed the increase of  $A_{cross}$  with increased  $P(-)_{LS}$  was also statistically significant ( $P < 0.0001$ ). The ratio of  $D_{minor}$  to  $D_{major}$  stayed almost the same between the low  $P(-)_{LS}$  and high  $P(-)_{LS}$  groups. The biggest  $D_{major}$  (5.52 mm) was found in the group with 0.3 mm scan interval and high  $P(-)_{LS}$ , whereas the smallest  $D_{major}$  (1.22 mm) was seen in the group with 0.7mm scan interval and low  $P(-)_{LS}$ .

**Table 3.2:** Quantifications of the flow channels (Mean  $\pm$  Standard Deviation)

SI	0.7 mm		0.3 mm	
	30MPa	36MPa	30MPa	36MPa
$A_{cross}$ (mm <sup>2</sup> )	1.79 $\pm$ 0.60	2.46 $\pm$ 0.93	6.33 $\pm$ 1.65	11.15 $\pm$ 1.22
$D_{major}$ (mm)	1.85 $\pm$ 0.41	2.15 $\pm$ 0.51	4.04 $\pm$ 0.49	5.46 $\pm$ 0.36
$D_{minor}$ (mm)	1.25 $\pm$ 0.16	1.50 $\pm$ 0.24	2.03 $\pm$ 0.32	2.77 $\pm$ 0.18
$D_{circle}$ (mm)*	1.51 $\pm$ 0.23	1.77 $\pm$ 0.30	2.84 $\pm$ 0.35	3.77 $\pm$ 0.20
$P_{open}$ **	23 $\pm$ 3%	27 $\pm$ 4%	44 $\pm$ 5%	58% $\pm$ 3%

\*  $D_{circle}$  is the diameter of circle has the same area as the cross-sectional area ( $A_{cross}$ ) of flow channel.

\*\*  $P_{open} = D_{circle}/D_{vessel}$  is the opening percentage of flow channel regarding to the 6.5 mm vessel lumen.

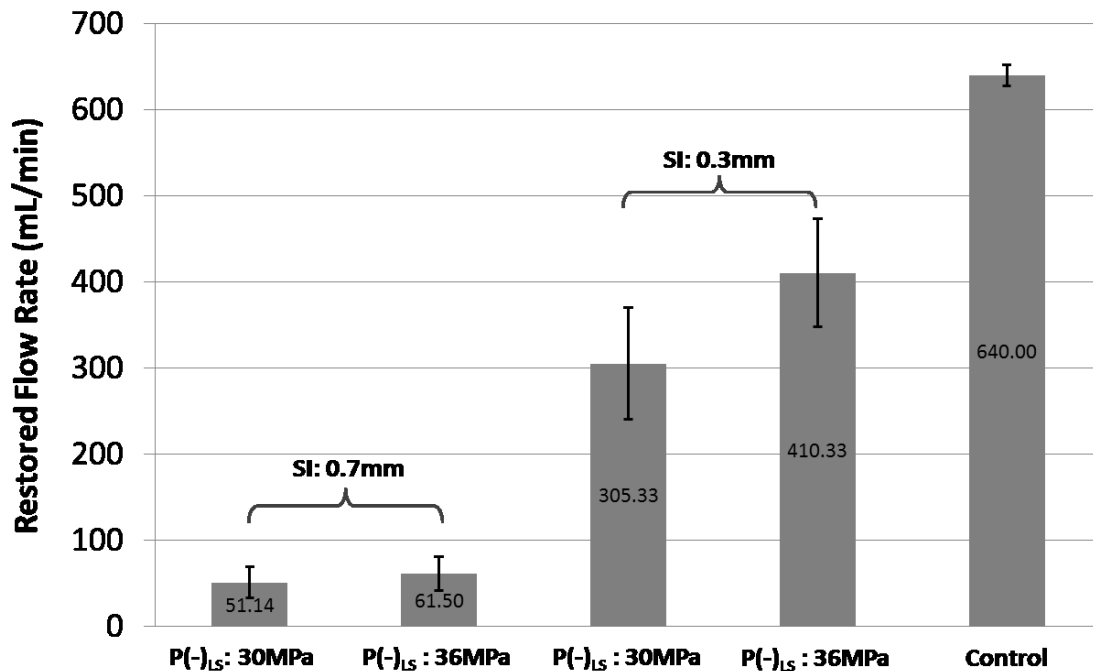
SI	0.7 mm		0.3 mm	
P(-) <sub>LS</sub>	30MPa	36MPa	30MPa	36MPa
Fitted Ellipse				
Equivalent Circle				

**Figure 3.10:** Illustrations of the cross sections of the flow channels for the 4 treatment groups. Fitted ellipse is determined by  $D_{\text{major}}$  and  $D_{\text{minor}}$  from Table 3.2. Equivalent circle is determined by  $D_{\text{circle}}$  from Table 3.2.

### 3.3.3 Restored Flow Rate

No flow was observed on Color Doppler and no fluid was collected by the fluid collector prior to any treatment. Flow was successfully restored after each microtripsy thrombolysis treatment. Representative color Doppler flow images are shown in Figure 3.8c. As expected, the path and the volume of the flow matched well with the generated channel. Flow rate was measured after each treatment (**Figure 3.11**). With a constant pressure, larger channel would be expected to permit higher flow rate, which is confirmed by these flow rate results. One-sided t-tests were performed to compare the restored flow rates between different treatment groups. For both P(-)<sub>LS</sub> used, significant flow rate increase (from about 50 mL/min to above 300 mL/min) was observed as the SI decreased ( $P < 0.0001$ ). And with the SI of 0.3 mm, the flow increase from the low P(-)<sub>LS</sub> groups to the high P(-)<sub>LS</sub> groups was also statistically significant ( $P < 0.0001$ ). The lowest flow rate was 30 mL/min in one of the treatments with 0.7 mm scan interval and low P(-)<sub>LS</sub>. The highest flow rate was 520 mL/min in one of the treatments with 0.3 mm scan interval and high P(-)<sub>LS</sub>. Within the SI<sub>0.3mm</sub> treatment groups, the lowest flow rate was

240mL/min. The flow model with no blockage had a maximal flow rate of 640 mL/min under the pressure of 3.7 mm Hg.

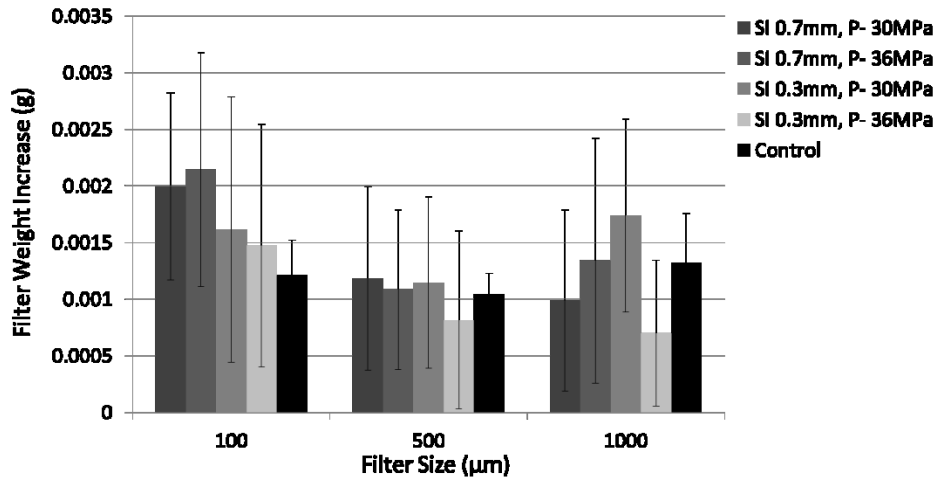


**Figure 3.11:** Restored flow rates of the 4 treatment groups. Treatments associated with creation of larger cross-sectional area opening were associated with larger flow rates. The flow rates in the control group were measured under the same pressure as the treatment groups but without blockage in vessel phantom. For both P(-)<sub>LS</sub> used, statistical analysis (one-sided t-tests) showed significant flow rate increase as the SI decreased ( $P < 0.0001$ ). And with the SI of 0.3 mm, the flow rate increase from the low P(-)<sub>LS</sub> groups to the high P(-)<sub>LS</sub> groups was also statistically significant ( $P < 0.0001$ ).

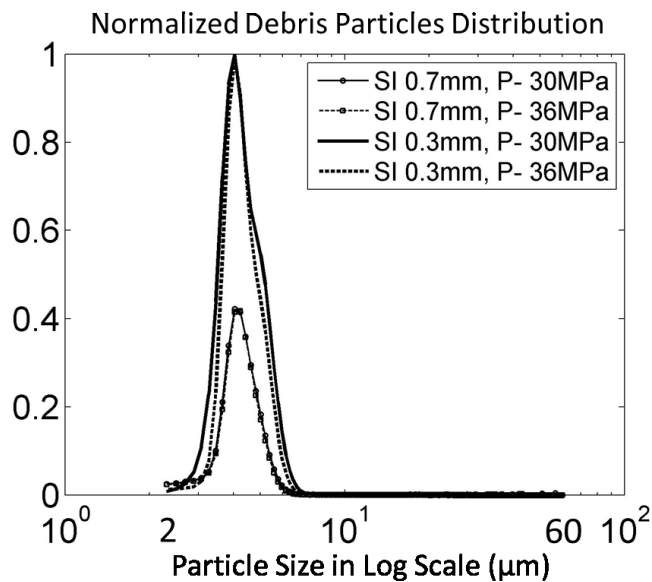
### 3.3.4 Debris Particle Measurements

In the 24 treatments using the filter weight and Coulter Counter combination method, the mean weight change of each filter size in each treatment group was shown versus the control group in **Figure 3.12**. Over all the treatments and all the filter sizes, the filter's dry weight increased by a mean of 1.4 mg with a standard deviation of 1.0 mg. For the control group, the filter's dry weight changed by a mean of 1.1 mg with a standard deviation of 0.4 mg. T-test was performed between the control group and each treatment group for each filter size. No significant difference was found for any filter size between control and any of the treatment groups. Smaller

debris particles (2 to 60  $\mu\text{m}$ ) suspended in the filtered fluid were analyzed using a Coulter Counter. In all the treatments, over 99.9 % of the debris particles were smaller than 10  $\mu\text{m}$  and centered around 4  $\mu\text{m}$ . Normalized debris particle distribution ranging from 2 to 60  $\mu\text{m}$  was plotted vs. debris particle size for each treatment group in **Figure 3.13**. The absolute number of debris particles increased over 2 times from the SI<sub>0.7mm</sub> group to SI<sub>0.3mm</sub> group but didn't change much between the two P- groups.



**Figure 3.12:** Filter weight increases after treatment.



**Figure 3.13:** Debris particle distributions are normalized by the maximal value of the 4 treatment groups.

For the 12 treatments using the microscopic inspection and Coulter Counter combination method, no debris particle pieces  $\geq 300 \mu\text{m}$  were observed by microscopic inspection on the filters of any treatment. **Table 3.3** shows the number percentage of the debris particles ranging from  $2 \mu\text{m}$  to  $300 \mu\text{m}$  for each of the two treatment groups. Over 99.9 % of the debris particles were smaller than  $10 \mu\text{m}$ , with the largest particle at  $153 \mu\text{m}$ . The debris particles became orders of magnitude less as the size increased from  $10 \mu\text{m}$  to  $100 \mu\text{m}$ . The total number of debris particles ranging from  $100 \mu\text{m}$  to  $300 \mu\text{m}$  observed for each of the 12 treatments with the maximum debris size was listed in **Table 3.4**.

**Table 3.3:** Number percentage of debris particles

Debris Diameter( $\mu\text{m}$ )	2-10	10-30	30-60	60-100	100-300	>300
SI 0.3mm, P(-) <sub>LS</sub> 30MPa	99.89%	0.11%	<0.001%	<0.0001%	<0.0001%	None
SI 0.3mm, P(-) <sub>LS</sub> 36MPa	99.96%	0.04%	<0.001%	<0.0001%	<0.0001%	None

**Table 3.4:** Observed debris particles larger than  $100 \mu\text{m}$

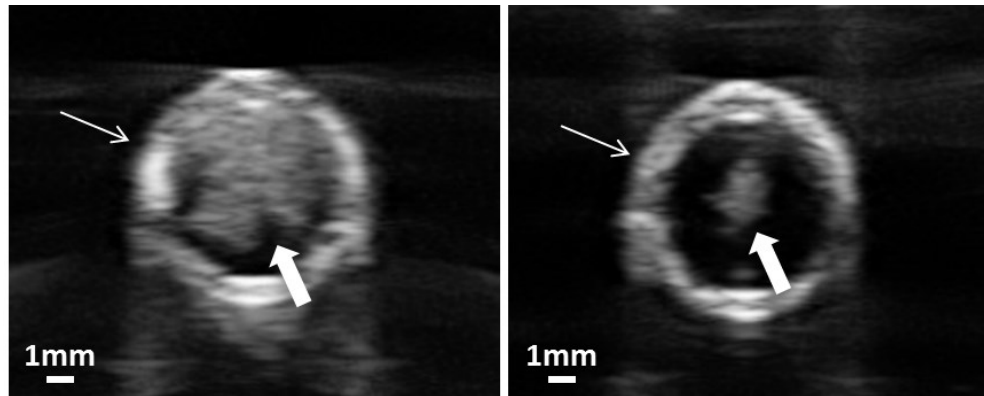
Group	SI 0.3mm, P(-) <sub>LS</sub> 30MPa						SI 0.3mm, P(-) <sub>LS</sub> 36MPa					
	1	2	3	4	5	6	7	8	9	10	11	12
Clot No.												
No. of Particles	1	0	0	0	0	2	0	6	3	0	2	0
Max. Diameter ( $\mu\text{m}$ )	114	/	/	/	/	132	/	139	153	/	116	/

## 3.4 Discussion

### 3.4.1 Cavitation

As expected, the cavitation bubble cloud was completely confined inside the targeted clot within the vessel lumen. No cavitation bubble cloud was in contact with the vessel wall on ultrasound imaging. Ultrasound images of cavitation bubble clouds in the vessel phantom, generated by shock scattering and intrinsic threshold mechanism respectively, are compared in

**Figure 3.14.** By using microtripsy via a single-cycle length pulse, shocking scattering was limited to avoid bubble cloud elongation and unexpected cavitation on vessel wall surface. As cavitation by intrinsic threshold mechanism was less affected by surrounding interfaces, microtripsy may become a better option for thrombolysis application by avoiding any cavitation on surrounding vessel walls.



**Figure 3.14:** Cross-sectional ultrasound images of cavitation bubble clouds in the vessel phantom. The vessel phantom was filled with saline. Vessel wall is indicated by line arrow and bubble cloud is indicated by block arrow. Left: Using shock scattering mechanism (5-cycle pulses). Right: Using intrinsic threshold mechanism (microtripsy, 1-cycle pulse). The same peak negative pressure was applied in both cases.

### 3.4.2 Elimination of Vessel Damage

As shown previously [26], cavitation was strongly correlated with clot fractionation. So the well-confined cavitation within the vessel lumen resulted in accurate clot recanalization. On the high-resolution B-mode images, the generated channels were confined in the clots within the vessel lumen and showed clear boundaries from the surrounding intact clot. The intact clots attached to the vessel wall didn't show any speckle reduction suggesting no clot fractionation, which confirmed that no cavitation occurred near vessel walls.

### 3.4.3 Accuracy of Cavitation Cloud Size Estimation

Caution must be paid before trusting the estimation of cavitation cloud size. First, the hyperechoic region visualized on the b-mode images may not be the original cavitation bubble



cloud itself but the bubble nuclei after cavitation bubble collapse. It took more than 2ms to collect acoustic signals to form a b-mode image, whereas cavitation bubble collapses within several hundred microseconds. Second, since the bubble nuclei after collapse are dynamic, the size and shape of this hyperechoic region may change with the time delay and imaging parameters we used to look at it after each pulse. Third, with lesion developing during treatment, the change in both location and size of the hyperechoic region may also cause error in this averaging-based estimation.

#### **3.4.4 Predictions of Flow Channel Sizes**

**Table 3.5** below lists the diameters of the flow channel, -6dB focal zone of the therapy transducer, supra-threshold estimations of focal region, and cavitation cloud diameters. The supra-threshold method estimates the treatment region by the area where the applied negative pressure exceeds the intrinsic threshold in the clot (27MPa) [30, 31]. Two-sided t-tests were performed to compare the diameters of flow channel with the other three categories. First, the flow channels generated by microtripsy were significantly smaller in the axial direction compared to the -6dB focal zone of the therapy transducer. Second, the supra-threshold estimations were statistically significantly different from the flow channel sizes. Compared to a better match between this supra-threshold estimation and the lesion size showed by Lin *et al.* [31], the mismatch observed in this study was probably related to cavitation memory effect by using a much higher PRF (50 Hz) compared to 1 Hz used by Lin *et al.* As Wang *et al.* [40] demonstrated that at the 50 Hz PRF, residual bubbles from previous pulses persisted and moved between pulses functioning as cavitation nuclei for subsequent pulses, which may effectively change the cavitation zone. Third, there is no significant difference between the major and minor diameters of cavitation cloud and those of flow channel in the 30 MPa P(-)<sub>LS</sub> case, suggesting

that the cavitation zone visualized by B-mode ultrasound image could provide a good predication of the flow channel sizes. The B-mode visualization of the cavitation cloud in this study was not optimized. Further investigation will be conducted to optimize the imaging parameters and address the issues discussed in the last section so that this technique may be used to predict flow channel sizes accurately and reliably.

**Table 3.5:** Comparisons among the diameters of the flow channel, -6dB focal zone of the therapy transducer, supra-threshold estimations of focal region, and cavitation cloud diameters. Two-sided t-tests were performed to compare the diameters of flow channel with the other three. Superscript mark “ \* ” indicates that this group is statistically significantly different from the flow channel diameter group. Superscript mark “ ° ” indicates there is no statistically significant difference between this group and the flow channel diameter group.

	P(-) <sub>LS</sub>	Flow Channel Diameter	-6dB Focal Zone	Supra-threshold Estimation	Cavitation Cloud Diameter
<b>Major Diameter</b>	<b>30 MPa</b>	4.04 ± 0.49 mm	6.5 mm*	3.70 mm*	3.41 ± 0.54 mm <sup>°</sup>
	<b>36 MPa</b>	5.46 ± 0.36 mm	6.5 mm*	5.30 mm*	4.53 ± 0.65 mm*
<b>Minor Diameter</b>	<b>30 MPa</b>	2.03 ± 0.32 mm	1.3 mm*	1.10 mm*	1.95 ± 0.37 mm <sup>°</sup>
	<b>36 MPa</b>	2.77 ± 0.18 mm	1.3 mm*	1.45 mm*	2.12 ± 0.35 mm*

### 3.4.5 Channel Size Controls

It is clinically desirable to generate a sufficiently large channel to maximize the restored flow while minimizing the vessel damage. The capability of microtripsy to finely control the cavitation size by adjusting P- will potentially allow the formation of flow channel with different sizes for individual patients with different vein diameters, but still confined with the vessel lumen without damaging the vessel wall. In clinical situations the exact P- delivered at the target inside body can't be directly measured. As the cavitation cloud can be directly seen on the real-time images using ultrasound imaging, the applied microtripsy P- can be adjusted to achieve a

desired size of the cavitation cloud based on the imaging feedback while ensuring that the cavitation is well confined within the vessel lumen without contacting the vessel wall. This approach is supported by the match between the flow channel sizes and the cavitation cloud sizes measured by B-mode ultrasound image. As such the control of flow channel size may be realized via microtripsy in clinical situations.

Although increasing P- allows enlarging the diameters ( $D_{\text{major}}$  and  $D_{\text{minor}}$ ) of channel, to avoid potential vessel damage the maximal  $D_{\text{major}}$  is limited by the inner diameter of vessel. As the single focal zone shape is elliptical with the short axis significantly smaller than diameter of the vessel lumen, the cross sectional area of the flow channel can also be increased by steering the focus along the short axis (laterally) to create multiple lesions within one cross sectional plane. Our transducer is capable of electrically steering the focus laterally within a few millimeters to further enlarge channel and improve effectiveness of recanalization. As microtripsy utilizes extremely short, single-cycle pulses with long waiting time, the focus can be electrically scanned to other locations between pulses, thus the lateral steering strategy to achieve a larger, more circular flow channel can be implemented without increasing treatment time.

### **3.4.6 Restored Flow Rate**

With our current *in vitro* setting (6.5 mm diameter and 3.7 mm Hg pressure), the restored flow rate could reach up to 500 mL/min. Compared to the control flow rate (640 mL/min) where the same pressure was applied but no blockage presented in the flow system, our treatment restored up to 78 %. In clinical situations, the normal blood flow rate in femoral vein ranges from 268 mL/min to 721 mL/min [37, 41] assuming a mean velocity of 13.88 cm/s. Compared to these clinical data, our 500mL/min recanalization rate suggests the potential of microtripsy to significantly improve blood circulation after treatment of DVT.

### **3.4.7 Treatment Time Optimization**

In this study the 2cm-long clots could be recanalized within 7 minutes. The treatment efficiency can be further improved with optimization of acoustic parameters. Three acoustic parameters can be optimized to improve the treatment efficiency, including peak negative pressure, dose of histotripsy pulses per location, and pulse repetition frequency. This study shows that the flow channel size and flow rate restored by microtripsy are higher with higher P-. The dose of 300 pulses per location used in this study was chosen empirically to ensure complete clot fractionation and is probably overdosed. As the clot properties can vary across patients and even an individual clot can be heterogeneous, we are investigating a new feedback method that can indicate the complete clot fractionation in real-time, which will allow us to adaptively apply the optimal dose at each treatment location during treatment [42, 43]. The treatment time can be further reduced by increasing the PRF, however higher PRF may increase the risk of heating the overlying tissue and lower treatment efficiency by introducing cavitation memory effect [40]. Further parameter study is warranted to identify the microtripsy parameter set that can rapidly and accurately create a desired flow channel through the clot without damaging the vessel wall or overheating the overlying tissue.

### **3.4.8 Comparison of Different Scan Intervals**

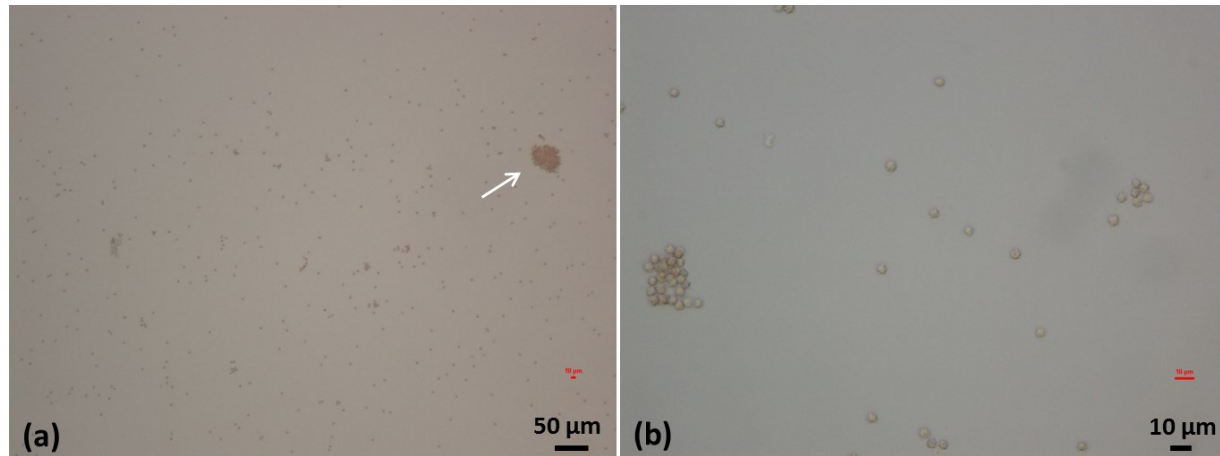
The flow channel size also depends on the scan interval. There was noticeable difference of channel sizes and shapes between the treatment groups with the 0.7 mm and 0.3 mm scan intervals. The lesion volume at an individual focus generated by microtripsy is a raindrop shape with a main circular lesion and a smaller tail. The channels generated from the  $SI_{0.3\text{mm}}$  group were larger and had elliptical shapes, which matched the volume and shape of the individual focal volume, while the channel generated in the  $SI_{0.7\text{mm}}$  group was more circular with a smaller

opening. This difference was because the 0.7 mm interval was larger than the size of the tail, resulting in incomplete fractionated clot at the tail-end between the lesions at adjacent locations and a smaller opening. When the scan interval was equal or smaller than the tail (i.e. the 0.3 mm interval), raindrop shaped channels with larger opening was generated. Although smaller scan interval will results in more treatment locations on the path, the dose per location can be accordingly reduced due to more overlapping volume. As shown in this study, the smaller scan interval (0.3 mm) with the reduced dose per location (300 pulses) produced a larger flow channel with a faster treatment time (7 min for  $SI_{0.3mm}$  vs. 10 min for  $SI_{0.7mm}$ ).

### **3.4.9 Debris**

Sonothrombolysis studies have not seen clot debris large enough to cause significant embolism. Although debris particles generated in previous histotripsy studies were no greater than 100  $\mu\text{m}$  and also unlikely to cause hazardous emboli, we wanted to confirm the new microtripsy parameters would produce debris in line with that observed previously [26, 27]. We used two methods to measure the debris particle size distribution. Using the filter weight and Coulter Counter combination method, weight increases of the dried filters before and after recanalization treatments were observed, but no significant difference was found between these increases and those in the control group and no debris particles were directly visualized on any of the filters. The filter weight increase may be due to sodium chloride crystal dried from residual saline on the filter. Changes of environmental humidity and temperature may also play a role in increasing the filter weight. The macroscopic inspection and Coulter Counter method was also used to characterize debris particles, which was expected to be more sensitive and accurate than the filter weight method. Debris particles larger than 100  $\mu\text{m}$  were uncommonly observed and the largest debris particle was only 153  $\mu\text{m}$ . The results using this method are also supported by

microscopic images of debris fluid smear [44] (**Figure 3.15**). Most of the particles appear to be red blood cells (RBC) or RBC fragments and the larger particles were clusters of RBCs. Particles of this size range are unlikely to form hazardous emboli, as 100  $\mu\text{m}$  mechanical filters have been successful at preventing embolization in catheter-based thrombolysis procedures [45].



**Figure 3.15:** Example microscopic images of debris fluid smear from one treatment. **(a)** 10 times magnification. White arrow points to a large debris particle ( $\sim 40 \mu\text{m}$ ). **(b)** 40 times magnification. Most of individual particles are around  $4 \mu\text{m}$ .

### 3.5 Conclusion

Histotripsy has been previously demonstrated to be a promising non-invasive and drug-free thrombolysis strategy with the advantages of fast treatment and real-time image guidance. However, histotripsy using conventional shock-scattering approach may generate cavitation on the vessel wall, leading to potential vessel damage. In this chapter, a new histotripsy approach, Microtripsy, was shown to precisely and consistently confine the cavitation within the vessel lumen, avoiding any contact with the vessel wall to prevent vessel damage. Microtripsy accurately generated flow channels inside the vessel phantom with 6.5-mm inner diameter, which is at the lower end of the reported DVT vein diameter range [37]. The flow channel

created by microtripsy formed opening up to 60 % of the vessel lumen size and restored flow up to 500 mL/min. The 2cm-long clot was recanalized within 7 min and the generated channel could be enlarged by increasing the peak negative pressures of microtripsy pulses. The debris particles generated by microtripsy were measured with over 99.9% smaller than 10  $\mu\text{m}$  and the largest particle at 153  $\mu\text{m}$ , which are unlikely to form hazardous emboli. Future work will focus on optimizing acoustic parameters of microtripsy to further enhance treatment safety and efficiency.

### 3.6 References

- [1] X. Zhang, *et al.*, "Noninvasive thrombolysis using histotripsy beyond the intrinsic threshold (microtripsy)," *Ultrasonics, Ferroelectrics, and Frequency Control, IEEE Transactions on*, vol. 62, pp. 1342-1355, 2015.
- [2] D. Mozaffarian, *et al.*, "Executive Summary: Heart Disease and Stroke Statistics—2015 Update A Report From the American Heart Association," *Circulation*, vol. 131, pp. 434-441, 2015.
- [3] H. P. Adams, *et al.*, "Guidelines for thrombolytic therapy for acute stroke: a supplement to the guidelines for the management of patients with acute ischemic stroke a statement for healthcare professionals from a special writing group of the stroke council, American heart association," *Circulation*, vol. 94, pp. 1167-1174, 1996.
- [4] S. M. Bates and J. S. Ginsberg, "Treatment of deep-vein thrombosis," *New England Journal of Medicine*, vol. 351, pp. 268-277, 2004.
- [5] H. S. Friedman, *et al.*, "Tissue plasminogen activator for acute ischemic stroke," *N Engl J Med*, vol. 334, p. 1405, 1996.
- [6] K. Kasirajan, *et al.*, "Percutaneous AngioJet thrombectomy in the management of extensive deep venous thrombosis," *Journal of Vascular and Interventional Radiology*, vol. 12, pp. 179-185, 2001.
- [7] H. S. Kim, *et al.*, "Catheter-directed thrombolysis with percutaneous rheolytic thrombectomy versus thrombolysis alone in upper and lower extremity deep vein thrombosis," *Cardiovascular and interventional radiology*, vol. 29, pp. 1003-1007, 2006.
- [8] W. S. Smith, *et al.*, "Safety and efficacy of mechanical embolectomy in acute ischemic stroke results of the MERCI trial," *Stroke*, vol. 36, pp. 1432-1438, 2005.
- [9] W. S. Smith, *et al.*, "Mechanical thrombectomy for acute ischemic stroke final results of the multi MERCI trial," *Stroke*, vol. 39, pp. 1205-1212, 2008.

- [10] S. Pfaffenberger, *et al.*, "2MHz ultrasound enhances t-PA-mediated thrombolysis: comparison of continuous versus pulsed ultrasound and standing versus travelling acoustic waves," *THROMBOSIS AND HAEMOSTASIS-STUTTGART*, vol. 89, pp. 583-589, 2003.
- [11] C. K. Holland, *et al.*, "Ultrasound-enhanced tissue plasminogen activator thrombolysis in an *in vitro* porcine clot model," *Thrombosis research*, vol. 121, pp. 663-673, 2008.
- [12] K. E. Hitchcock, *et al.*, "Ultrasound-Enhanced rt-PA Thrombolysis in an *ex vivo* Porcine Carotid Artery Model," *Ultrasound in medicine & biology*, vol. 37, pp. 1240-1251, 2011.
- [13] J. Larsson, *et al.*, "Ultrasound enhanced thrombolysis in experimental retinal vein occlusion in the rabbit," *British journal of ophthalmology*, vol. 82, pp. 1438-1440, 1998.
- [14] A. V. Alexandrov, *et al.*, "Ultrasound-enhanced systemic thrombolysis for acute ischemic stroke," *New England Journal of Medicine*, vol. 351, pp. 2170-2178, 2004.
- [15] C. A. Molina, *et al.*, "Transcranial ultrasound in clinical sonothrombolysis (TUCSON) trial," *Annals of neurology*, vol. 66, pp. 28-38, 2009.
- [16] G. Tsivgoulis, *et al.*, "Safety and efficacy of ultrasound-enhanced thrombolysis a comprehensive review and meta-analysis of randomized and nonrandomized studies," *Stroke*, vol. 41, pp. 280-287, 2010.
- [17] S. Datta, *et al.*, "Ultrasound-Enhanced Thrombolysis Using Definity<sup>®</sup> as a Cavitation Nucleation Agent," *Ultrasound in medicine & biology*, vol. 34, pp. 1421-1433, 2008.
- [18] A. T. Brown, *et al.*, "Microbubbles improve sonothrombolysis *in vitro* and decrease hemorrhage *in vivo* in a rabbit stroke model," *Investigative radiology*, vol. 46, 2011.
- [19] W. C. Culp, *et al.*, "Successful microbubble sonothrombolysis without tissue-type plasminogen activator in a rabbit model of acute ischemic stroke," *Stroke*, vol. 42, pp. 2280-2285, 2011.
- [20] U. Rosenschein, *et al.*, "Ultrasound Imaging-Guided Noninvasive Ultrasound Thrombolysis Preclinical Results," *Circulation*, vol. 102, pp. 238-245, 2000.
- [21] A. Burgess, *et al.*, "High-intensity focused ultrasound (HIFU) for dissolution of clots in a rabbit model of embolic stroke," *PloS one*, vol. 7, p. e42311, 2012.
- [22] C. Wright, *et al.*, "*In vitro* and *in vivo* high intensity focused ultrasound thrombolysis," *Investigative radiology*, vol. 47, p. 217, 2012.



- [23] Z. Xu, *et al.*, "Effects of acoustic parameters on bubble cloud dynamics in ultrasound tissue erosion (histotripsy)," *The Journal of the Acoustical Society of America*, vol. 122, pp. 229-236, 2007.
- [24] Z. Xu, *et al.*, "Evolution of bubble clouds induced by pulsed cavitation ultrasound therapy-histotripsy," *Ultrasonics, Ferroelectrics and Frequency Control, IEEE Transactions on*, vol. 55, pp. 1122-1132, 2008.
- [25] Z. Xu, *et al.*, "Noninvasive creation of an atrial septal defect by histotripsy in a canine model," *Circulation*, vol. 121, pp. 742-749, 2010.
- [26] A. D. Maxwell, *et al.*, "Noninvasive thrombolysis using pulsed ultrasound cavitation therapy-histotripsy," *Ultrasound in medicine & biology*, vol. 35, pp. 1982-1994, 2009.
- [27] A. D. Maxwell, *et al.*, "Noninvasive treatment of deep venous thrombosis using pulsed ultrasound cavitation therapy (histotripsy) in a porcine model," *Journal of Vascular and Interventional Radiology*, vol. 22, pp. 369-377, 2011.
- [28] A. D. Maxwell, *et al.*, "Cavitation clouds created by shock scattering from bubbles during histotripsy," *The Journal of the Acoustical Society of America*, vol. 130, pp. 1888-1898, 2011.
- [29] R. T. Eberhardt and J. D. Raffetto, "Chronic venous insufficiency," *Circulation*, vol. 111, pp. 2398-2409, 2005.
- [30] A. D. Maxwell, *et al.*, "Probability of cavitation for single ultrasound pulses applied to tissues and tissue-mimicking materials," *Ultrasound in medicine & biology*, vol. 39, pp. 449-465, 2013.
- [31] K.-W. Lin, *et al.*, "Histotripsy beyond the "Intrinsic" Cavitation Threshold using Very Short Ultrasound Pulses: "Microtripsy"," *IEEE transactions on ultrasonics, ferroelectrics, and frequency control*, vol. 61, p. 251, 2014.
- [32] K. Spengos, *et al.*, "Acceleration of thrombolysis with ultrasound through the cranium in a flow model," *Ultrasound in medicine & biology*, vol. 26, pp. 889-895, 2000.
- [33] U. Albrechtsson, *et al.*, "Femoral vein pressure measurements for evaluation of venous function in patients with postthrombotic iliac veins," *Cardiovascular and interventional radiology*, vol. 4, pp. 43-50, 1981.
- [34] D. Negus and F. Cockett, "Femoral vein pressures in post-phlebotic iliac vein obstruction," *British Journal of Surgery*, vol. 54, pp. 522-525, 1967.
- [35] J. Browne, *et al.*, "Assessment of the acoustic properties of common tissue-mimicking test phantoms," *Ultrasound in medicine & biology*, vol. 29, pp. 1053-1060, 2003.

- [36] S. Park, *et al.*, "Non-Invasive Embolus Trap Using Histotripsy—An Acoustic Parameter Study," *Ultrasound in medicine & biology*, vol. 39, pp. 611-619, 2013.
- [37] B. Hertzberg, *et al.*, "Sonographic assessment of lower limb vein diameters: implications for the diagnosis and characterization of deep venous thrombosis," *AJR. American journal of roentgenology*, vol. 168, pp. 1253-1257, 1997.
- [38] J. E. Parsons, *et al.*, "Cost-effective assembly of a basic fiber-optic hydrophone for measurement of high-amplitude therapeutic ultrasound fields," *The Journal of the Acoustical Society of America*, vol. 119, pp. 1432-1440, 2006.
- [39] B. Coulter, "Coulter Counter Multisizer 3 User's Manual," *Hiialeah, FL*, 2000.
- [40] T.-Y. Wang, *et al.*, "An efficient treatment strategy for histotripsy by removing cavitation memory," *Ultrasound in medicine & biology*, vol. 38, pp. 753-766, 2012.
- [41] A. Fronek, *et al.*, "Common femoral vein dimensions and hemodynamics including Valsalva response as a function of sex, age, and ethnicity in a population study," *Journal of vascular surgery*, vol. 33, pp. 1050-1056, 2001.
- [42] R. M. Miller, *et al.*, "Investigation of the mechanism of ARFI-based Color Doppler feedback of histotripsy tissue fractionation," in *Ultrasonics Symposium (IUS), 2013 IEEE International*, 2013, pp. 934-937.
- [43] X. Zhang, *et al.*, "Real-Time Feedback of Histotripsy Thrombolysis Using Bubble-Induced Color Doppler," *Ultrasound in medicine & biology*, 2015.
- [44] M. H. Ross, *et al.*, "Histology: a text and atlas with cell and molecular biology," 2003.
- [45] M. K. Eskandari, "Cerebral embolic protection," in *Seminars in vascular surgery*, 2005, pp. 95-100.

## Chapter 4

### Noninvasive Thrombolysis using Microtripsy: A Parameter Study

This chapter has been published in *IEEE Transactions on Ultrasonics, Ferroelectrics, and Frequency Control*. 2015; 62(12):2092-2105. © IEEE. Reprinted, with permission, from [1].

#### 4.1 Introduction

Thrombosis is the formation of a blood clot inside an artery or vein, blocking blood flow in the circulatory system. Arterial obstruction via thrombosis in the cerebral vasculature leads to stroke, which is a leading cause of disability and death in the United States [2]. The most common form of venous thrombosis is deep vein thrombosis (DVT), which occurs usually in the legs and can lead to pulmonary embolism (PE). DVT/PE (also called venous thromboembolism) affects over 300,000 people each year in the United States and causes deaths of 60,000 to 100,000 [3]. Severely symptomatic patients may require thrombolytic treatments instead of simply taking anticoagulant medicines. The current standard thrombolytic treatment involves the infusion of thrombolytic drugs such as tissue plasminogen activator (tPA) [4, 5]. Administration of thrombolytic drugs systemically has limited effectiveness with long treatment time (several hours to days) and is associated with a high risk of major bleeding [6]. Catheter-directed thrombolysis has the advantage over systematic thrombolysis by means of local application at the thrombosis site, but it is invasive and still carries the risks of bleeding, vascular damage, and infections [7, 8].

Ultrasound has been shown to enhance or induce thrombolysis for several decades [9]. Significant efforts have been focused on enhancing the efficacy of thrombolytic drugs with

ultrasound [10-15], with several clinical trials showing promising results [16-18]. In addition, ultrasound combined with microbubble contrast agents has been demonstrated to successfully augment clot dissolution in the presence or absence of thrombolytic drugs [19-21]. Ultrasound has also been investigated as an independent thrombolysis method under approaches utilizing acoustic cavitation [22-27].

Histotripsy is non-thermal ablation method that mechanically fractionates soft tissue through well-controlled acoustic cavitation generated by microsecond-long, high-pressure ultrasound pulses [28-30]. The feasibility of using histotripsy as a noninvasive, drug-free, and image-guided thrombolysis technique was first demonstrated *in vitro* and *in vivo* by Maxwell *et al.* [25, 26]. In those studies, multi-cycle (usually  $\geq 5$  cycle) ultrasound pulses were used to generate the cavitation bubble cloud via a shock scattering mechanism [31]. Using the shock scattering approach, the cavitation cloud is less-confined and tends to be generated in contact with vessel wall where the weak nuclei reside, resulting in potential vessel damage from histotripsy treatment. A new histotripsy approach, termed microtripsy, has been recently investigated for thrombolysis application to improve treatment precision and avoid potential vessel damage [27]. Microtripsy uses an intrinsic threshold mechanism where a cavitation cloud is initiated via a single ultrasound pulse with only one high negative pressure phase. When the peak negative pressure directly exceeds a distinctive “intrinsic threshold” for the medium (27 MPa for blood clots), a cavitation cloud is formed within the focal region exceeding the threshold [32, 33]. The location and size of the cavitation cloud generated using the intrinsic threshold mechanism is more reproducible and predictable than the shock scattering mechanism. Our microtripsy thrombolysis study showed that, cavitation can be precisely generated and

confined in the vessel lumen without contacting vessel wall, allowing for a precise flow channel to be created within the clot while minimizing the risk of vessel damage [27].

In our previous microtripsy thrombolysis study, the pulse repetition frequency (PRF) of applied ultrasound pulses was fixed to 50 Hz and the treatment dose (i.e. the number of ultrasound pulses applied at each treatment location) was chosen to be more than sufficient for complete clot fractionation. A higher PRF is expected to result in a shorter treatment time. However, a previous study suggested that higher PRF (>10 Hz) introduced cavitation memory effects where residual bubble nuclei from collapse of transient cavities from the previous pulse might become cavitation sites for subsequent cavitation events. As a result, the cavitation might reoccur at the same locations from pulse to pulse and the per-pulse fractionation efficiency could be lowered [34]. In the case for thrombolysis, the cavitation memory effects may result in an incomplete flow channel and different distributions of clot debris particles. Also, there was a concern that using 1-2 cycles pulses with a high PRF (>10Hz) may still result in pre-focal cavitation on the vessel wall. The pre-focal cavitation on the vessel wall can potentially damage the vessel and weaken the focal cavitation within vessel lumen by shielding the ultrasound energy propagation to the treatment focus. Finally, when high PRF are utilized, residual bubble nuclei from cavitation memory effects may shift the location of cavitation towards the ultrasound transducer [35]. In such a situation, to avoid damage to the interior vessel wall, the treatment focus within vessel lumen would need to be relocated prior to treatment to compensate for the potential shift.

This chapter explores the influence of treatment PRFs on microtripsy thrombolysis and to address the above concerns with high treatment PRFs. Microtripsy thrombolysis treatments using different PRFs were performed on blood clots in an *in vitro* flow model. As the number of pulses

necessary to completely fractionate the clot may vary with different PRF, we also tested different treatment doses (i.e., number of pulses) for each PRF. During each treatment, cavitation was monitored in real-time to detect any pre-focal cavitation incident. After treatments, the flow channels generated were characterized by 3D-scans using a high-frequency ultrasound imaging probe. Pre-focal cavitation, the size and shape of generated flow channel, and the relative location of flow channel with respected to the treatment focus were quantified. The size distribution of generated clot debris particles was also measured. By comparing these results between different treatment PRFs as a function of dose, an optimized treatment PRF was selected for future microtripsy thrombolysis studies.

## **4.2 Methods and Materials**

### **4.2.1 Flow Model**

An *in vitro* flow model, similar to that described by Spengos *et al.* [36], was designed to mimic occlusive deep vein thrombosis where no blood flow is present but pressure is still applied on the clot. As shown in **Figure 4.1**, the flow model consisted of a reservoir, a pressure sensor, a vessel phantom, a filter, and a fluid collector. All the components were connected with silicone tubing (Masterflex L/S 17; Cole-Parmer, Vernon Hills, IL, USA). The reservoir was placed above the vessel phantom and filled with saline to perfuse the system using gravity-driven pressure. The vessel phantom was mounted horizontally inside a tank filled with degassed water. The height difference between the saline level in the reservoir and the vessel phantom was adjusted to apply a constant pressure of 3.7 mm Hg, which was measured by the pressure sensor (MG-9V; SSI Technologies, Janesville, WI, USA). The 3.7 mm Hg was chosen according to reported femoral vein pressure [37, 38]. The valves remained open all the time during each treatment. Flow was restored when a channel was created through the clot by microtripsy

treatment. The restored flow, together with clot debris particles generated from the treatment, was passed through the filter and the filtered fluid was collected for further small particle analysis.

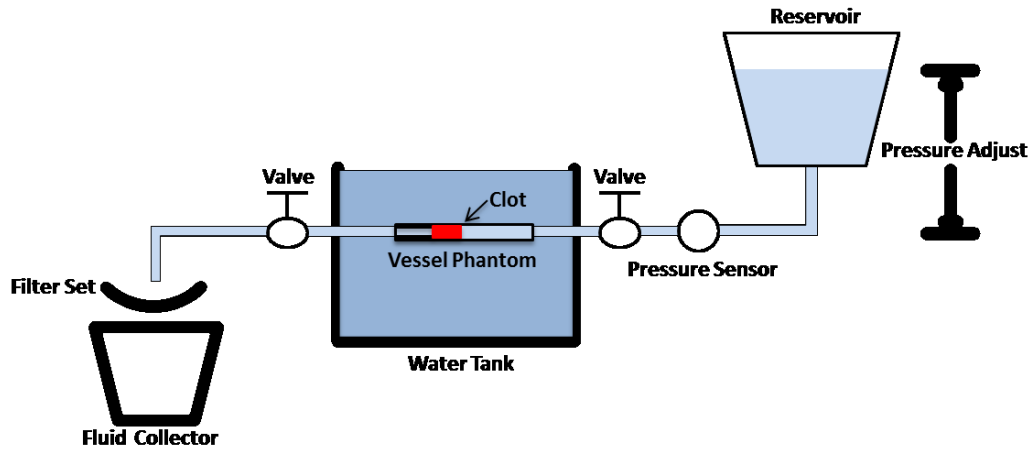
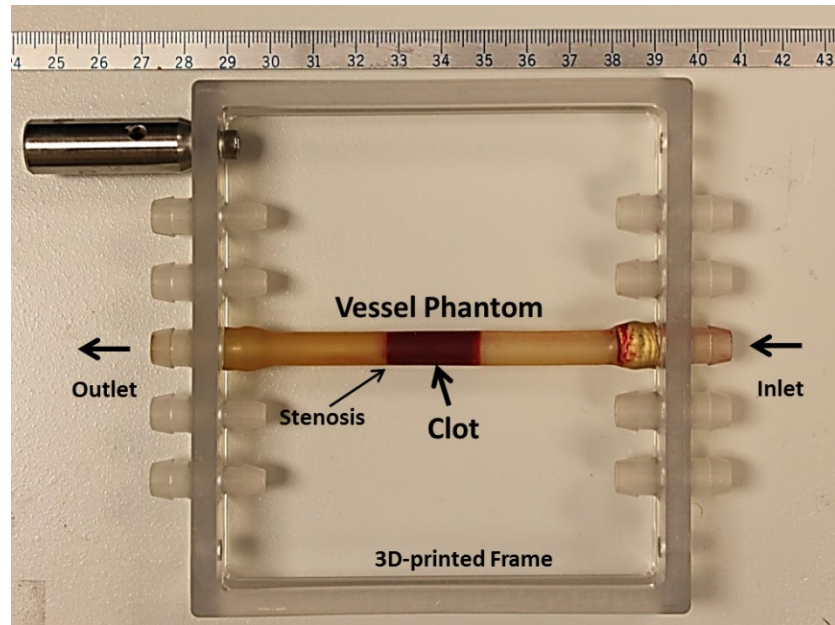


Figure 4.1: Schematic diagram of the flow model.

#### 4.2.2 Vessel Phantom

The vessel phantom was developed to mimic a human femoral vein (**Figure 4.2**). The phantom was made from urethane polymer (Urethane RTV Mold-Making System; Tap Plastics Inc., San Leandro, CA, USA), which has similar acoustic properties to human tissue [39]. Two parts of urethane (liquid) were first mixed at a 1:1 ratio and degassed in a vacuum chamber to remove bubbles. The mixture was then poured carefully into a 3D-printed mold. The mold includes two components: a hollow tube with an 8 mm inner diameter and a rod in the center of the hollow tube. To make a stenosis in the vessel phantom, the rod was made with a 6.5 mm diameter on one side and a 4.2 mm diameter on the other side. After solidification of the urethane (~ 24 hours), the vessel phantom was removed from the mold. The vessel phantom had an 8 mm outer diameter, a 6.5 mm inner diameter on one side, a 35% stenosis and a 4.2 mm inner diameter on the other side. The 6.5 mm inner diameter was chosen according to reported DVT vein diameters (5 to 21.7 mm) [40]. The stenosis in this *in vitro* setup provided additional

stabilization of the formed clot by preventing slipping under pressure. The vessel phantom was held by a 3D-printed frame with tube fittings at the two ends to connect the vessel in-line with the rest of the flow model [41].



**Figure 4.2:** The vessel phantom is held by a 3D-printed frame and can be connected in line with the flow model using tubing fittings. A 35% stenosis is located in the vessel phantom to fix the clot formed to one side so that it does not slip under pressure. The inner diameter is 4.2 mm on the left of the stenosis and 6.5 mm on the right. A clot is formed on the right side of the stenosis as shown in the figure.

### 4.2.3 Clot Formation

Fresh bovine blood was collected from a local abattoir. A citrate-phosphate-dextrose (CPD) solution (#C7165; Sigma-Aldrich Co., St. Louis, MO, USA) was immediately mixed with fresh bovine blood as an anti-coagulant at a ratio of 1 mL CPD per 9 mL blood. The blood sample was stored at 4°C and used within 72 hours. Before use, bovine blood was warmed up to the normal cow body temperature (38.6 °C). To stimulate the clotting cascade, calcium chloride (#21107; Sigma-Aldrich Co., St. Louis, MO, USA) was injected into bovine blood to a final concentration of 20 mM/L. To form clot inside the vessel phantom, the stimulated blood was poured into the vertically-placed vessel phantom with the stenosis sealed by a balloon catheter.

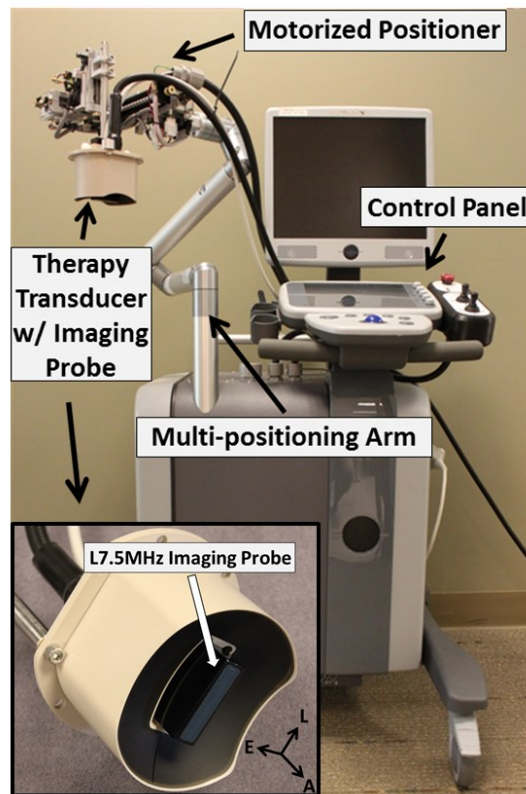


Any visible bubble was removed. After 2 hours in a water bath at 38.6 °C, the clot was matured and cross-linked with the vessel interior and stenosis. The balloon catheter was then removed and the vessel phantom was connected back into the flow model with the stenosis end of the clot distal to the pressure reservoir. The connecting tubes were carefully refilled with saline. All the clots in this study were made with a length of 2 cm.

#### **4.2.4 Microtripsy Thrombolysis System**

An integrated pre-clinical system for image-guided microtripsy thrombolysis was developed in our laboratory and used for all the treatments in this study (**Figure 4.3**). It includes three subsystems: microtripsy therapy, ultrasound imaging and positioning system. The therapy subsystem used a 1 MHz 18-element microtripsy transducer that was designed based on the anatomy of DVT patients and manufactured by Imasonic (S.A., Besancon, France) (**Figure 4.3**). The transducer had an effective 9.8 cm (lateral) x 8 cm (elevational) aperture and a 7 cm focal length. It was driven by a pulse amplifier developed in our lab to generate very short (< 2 cycles), high intense ultrasound pulses. The focal beam volume (-6 dB) of the transducer was measured to be 6.5 mm (axial) x 1.3 mm (lateral) x 1.5 mm (elevational) at a peak negative pressure of 15 MPa using a fiber-optic probe hydrophone (FOPH) [42]. The imaging subsystem was developed based on a SonixTouch® imaging machine (Analogic Ultrasound, Vancouver, Canada). An ultrasound probe with custom rectangular housing (L7.5MHz; Vermon, France) was inserted into the rectangular central hole of the therapy transducer to guide and monitor microtripsy thrombolysis treatment. Software development kits were provided by the SonixTouch® manufacturer to allow custom application developments. The positioning subsystem included a multi-positioning arm and a compact motorized positioner on the arm. The therapy transducer was mounted on the compact positioner. With 6 degrees of freedom and a

range around 1 meter, the multi-positioning arm can be manually moved and hold using a press/release lock for coarse target localization. With 3 degrees of freedom and a range of 10 cm x 5 cm x 4 cm, the motorized positioner was controlled by both software and joy sticks for finer localization. Control software was developed to manage and coordinate the therapy, imaging, and positioning systems.



**Figure 4.3:** Integrated microthrombolysis system. It consists of an ultrasound imaging system, a microthrombolysis therapy system, and a motorized positioning system. The insert shows the therapy transducer with a linear imaging probe embedded at the center.

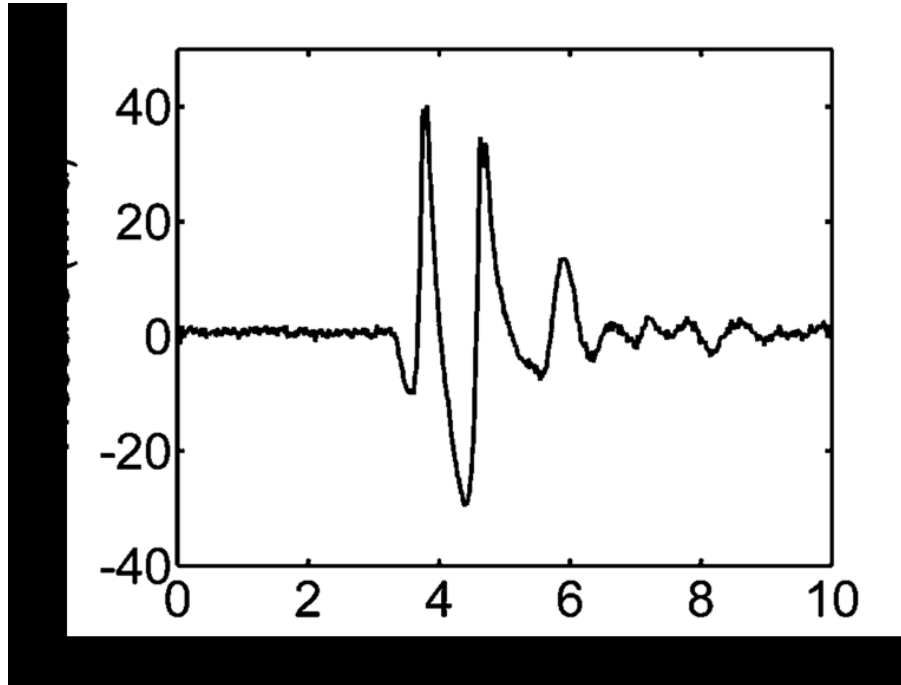
#### 4.2.5 Treatments

The vessel phantom with an occlusive clot inside was connected to the flow model and placed in a tank filled with degassed water. Using the multi-positioning arm, the therapy transducer was manually placed above the vessel phantom and its lateral axis was oriented

perpendicular to the vessel phantom so that the cross section of vessel was imaged during treatment. Pre-treatment planning was performed to determine the treatment path prior to each microtripsy clot treatment following three steps. First, cavitation was generated in empty water field and the center of the hyperechoic cavitation region was marked as the treatment focus on the ultrasound imaging window. Second, guided by the real-time ultrasound images, the transducer was moved using the motorized positioner to align the treatment focus at the center of vessel lumen. The transducer was then adjusted to move the treatment focus from one end of the clot to the other end. Several locations (spaced around 3 mm) from one end of the clot (close to the pressure reservoir) to the other end were recorded by the control software. Third, after these locations were registered, the control software linearly interpolated these key locations into a scan path of denser treatment locations with an interval of 0.3 mm.

For one treatment, the microtripsy thrombolysis system applied a fixed number of microtripsy pulses (dose) at each location with a fixed pulse repetition frequency (PRF) and then moved automatically to next location on the treatment path. A peak negative pressure of 30 MPa was used for microtripsy pulses throughout this study, as this pressure level was right above the intrinsic threshold and was shown to create precise flow channels in our previous microtripsy thrombolysis study. An example of microtripsy waveform is shown in **Figure 4.4**. Peak negative pressure larger than 20 MPa can't be directly measured and therefore was estimated by linear summation ( $P(-)_{LS}$ ) of direct P- outputs from 3 separate groups of transducer elements (6 elements per group). In this parameter study, three different PRFs (5, 50, and 100 Hz) combined with three treatment doses (20, 50, and 100 pulses) were examined. A maximal dose of 100 pulses was chosen to ensure the generated flow channel was confined within the clot. Six clots were treated with each of the parameter combinations. Real-time ultrasound images for treatment

monitoring were recorded as a video throughout each treatment. Imaging with a central frequency of 7.5 MHz was synchronized with the microtripsy pulses. The depth of the image was 6 cm and the cavitation focus was located in the center at a depth of 5 cm. There were 128 scan lines for each image. When a microtripsy pulse was fired, it scanned from left to right line by line (100  $\mu$ s per line). There was a delay of  $\sim$ 6.4 ms to image the cavitation after a pulse fire.



**Figure 4.4:** Pressure waveform of a microtripsy pulse. Because peak negative pressure larger than 20 MPa cannot be directly measured, this estimated waveform was linearly summed from the directly measured waveforms of 6 separate element groups (3 adjacent elements per group).

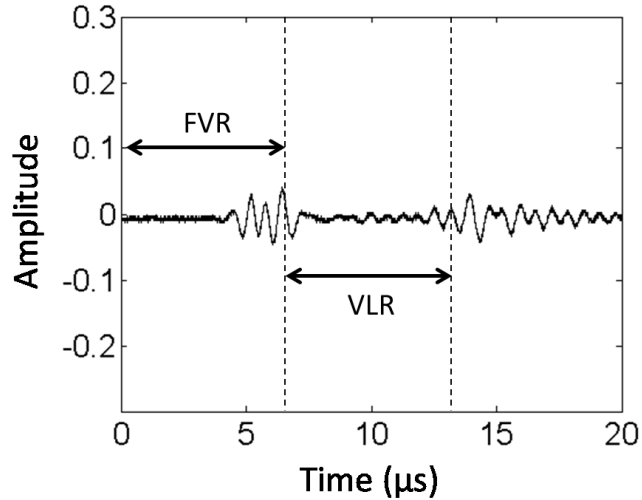
#### 4.2.6 Cavitation Monitor

Ultrasound image video taken during each treatment provided qualitative visualization of cavitation. Adopted from the previous studies [31, 43, 44], an acoustic cavitation detection method was also used to monitor cavitation in this study. One element in the therapy transducer was employed for both transmitting microtripsy pulse and receiving the backscattered signals of the microtripsy pulse from cavitation bubbles as well as emissions from bubble collapse. The element was connected to an oscilloscope (Lecroy372c, Teledyne LeCroy Inc., Chestnut Ridge,

New York, USA) through a high-voltage probe (PPE2kV, Teledyne LeCroy Inc., Chestnut Ridge, New York, USA). The oscilloscope was set in a sequential mode and synchronized with microtripsy pulses to digitize the received cavitation signals. Starting at 87  $\mu$ s after a microtripsy pulse was generated by the transducer, a 20  $\mu$ s long waveform of the backscatter signals of the therapy pulse from the cavitation bubble cloud was acquired with a sampling rate of 250 MHz. The 87  $\mu$ s delay time was chosen based on the round-trip travel time of ultrasound propagation to and from the cavitation focus. The 20  $\mu$ s time window was selected to cover the whole vessel region on the ultrasound propagation path. Before each treatment, a control waveform containing acoustic reflections only from vessel walls was acquired using a microtripsy pulse with a P- of 20 MPa (below the intrinsic threshold for cavitation). During each treatment, 300 treatment waveforms containing both vessel reflections and backscatter signals from cavitation were collected.

The primary purpose of monitoring cavitation in this study was to detect whether there was pre-focal cavitation on vessel walls when using different treatment PRFs. The control waveform was scaled by the ratio of the P- of the therapy pulses over 20MPa (control) to better estimate the reflected acoustic signal from vessel walls during treatment. Using the control waveform, the time windows corresponding to front vessel wall region (proximal to therapy transducer) and vessel lumen region were determined in each treatment waveform (**Figure 4.5**). When cavitation occurred, the signal amplitude at the corresponding temporal location on the treatment waveform was greatly increased as the incident therapy pulse was backscattered from cavitation bubbles. Cavitation was detected when the peak amplitude of the backscatter signal exceeds a threshold for each region, which was set as twice the peak amplitude of the scaled control waveform in that region. The percentages of pre-focal cavitation occurrence on front

vessel wall and focal cavitation occurrence in vessel lumen were calculated for each treatment (the number of pulses when cavitation was detected/total number of measured pulses).



**Figure 4.5:** Control waveform of cavitation monitor. The two bursts in the figure are the reflected signals from the front vessel wall (left) and rear vessel wall (right), respectively. The corresponding temporal zones of the Front Vessel Region (FVR) and Vessel Lumen Region (VLR) can be determined by these two reflections.

#### 4.2.7 Flow Channel Quantification

To quantitatively evaluate flow channels generated by microtripsy with different PRFs and doses, each treated clot was scanned using a 20 MHz high-resolution ultrasound probe. The probe was separately mounted onto the motorized positioner after each treatment. With the imaging plane perpendicular to the vessel central axis, the probe was moved by the positioner from one end to the other end of the clot taking one cross-sectional image every 0.3 mm along the vessel. 67 scan images were collected from each treated clot. Since the fractionated clot region appeared hypoechoic (very low brightness on image) when flow was restored, whereas intact clot region was hyperechoic (high brightness on image), we applied a brightness threshold to detect the cross section of flow channel on each scan image. Inside the vessel lumen on each scan image, the area with pixel intensity less than 20 (0-255 overall range) was thresholded out as the cross section of the flow channel. The value of 20 was selected according to the intensity

histogram of the scan images. To quantify the size and shape of the flow channel, the cross area ( $A_{\text{cross}}$ ) of the flow channel region was calculated and an ellipse was fitted into the flow channel region to estimate its major and minor diameters ( $D_{\text{major}}$  and  $D_{\text{minor}}$ ) using a function provided by Matlab (MathWorks, Natick, MA, USA). To evaluate the influence of different PRFs and doses on flow channel location inside of clot, the axial location of flow channel ( $L_{\text{axial}}$ ) was calculated as the distance from the center of the flow channel (actual treatment location) to the center of vessel lumen (intended target) along the axial direction (i.e. ultrasound propagation direction). The sharpness of channel boundary transitioning from unfractionated area to fractionated area was also quantified by measuring the width of boundary transition zone ( $W_{\text{bound}}$ ), which was detected as the area with the pixel intensity higher than 20 but less than 30 outside the completely fractionated lesion. The mean  $A_{\text{cross}}$ ,  $D_{\text{major}}$ ,  $D_{\text{minor}}$ ,  $L_{\text{axial}}$  and  $W_{\text{bound}}$  over all valid scan images of treated clots using the same PRF and dose were used to characterize the flow channel under this parameter combination.

#### **4.2.8 Restored Flow Measurements**

Restored flow rate was measured to evaluate microtripsy thrombolysis effectiveness under this *in vitro* environment. After the flow channel was created, the volume of downstream saline in the fluid collector within 30 seconds was measured. The restored volume flow rate was then calculated as the volume of the saline collected divided by the time. Owing to the brevity of the time period and the small change in reservoir volume, pressure was assumed to be constant over this time period. A control measurement with no blockage in the flow system was also conducted to compare with restored flow rate.

#### **4.2.9 Debris Particle Size Measurements**

There is a concern that clot debris particles generated by microthrombolysis may embolise to occlude downstream vessels or seed clotting elsewhere to create a new thrombus. To address this issue, a method combining macroscopic inspection and Coulter Counter analysis were utilized to measure clot debris particles generated during microthrombolysis treatment. When flow was restored in each treatment, clot debris was flushed by the restored flow and filtered by a filter sheet with a pore size of 300  $\mu\text{m}$ . Macroscopic inspection was conducted to check if there was any debris particle trapped on the 300  $\mu\text{m}$  filter. High-resolution optical images were taken of the filter sheet before and after each treatment and the number of distinguishable particles larger than 300  $\mu\text{m}$  was counted and the size of individual large debris particles were measured. The filtered fluid with suspended debris particles smaller than 300  $\mu\text{m}$  was analyzed using a Coulter Counter (Multisizer 3; Beckman Coulter, Brea, CA, USA). With this Coulter Counter, the measurable range of particles was from 2 to 60  $\mu\text{m}$  using a 100- $\mu\text{m}$  aperture tube and from 60 to 300  $\mu\text{m}$  using a 560- $\mu\text{m}$  aperture tube [45]. The measurements using these two aperture tubes were combined to generate a distribution of particles from 2 to 300  $\mu\text{m}$ .

#### **4.2.10 Statistics Analysis**

All statistical comparisons in this study were performed using Student's t-test. P-values < 0.05 were considered significant. Numerical data are expressed as mean  $\pm$  standard deviation. Error bars on graphs represent standard deviation.

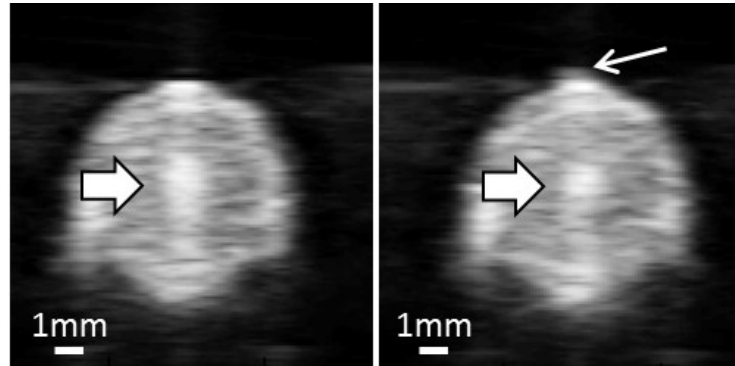
### **4.3 Results**

#### **4.3.1 Cavitation**

Cavitation bubble clouds appeared as a dynamic hyperechoic region on real-time ultrasound images providing both location information and approximate size of cavitation bubble. According to the ultrasound videos taken during the treatments, no pre-focal cavitation



on front vessel wall was observed when using either 5 Hz or 50 Hz treatment PRF. Although pre-focal cavitation was observed with higher treatment PRF (100 Hz), it happened infrequently and appeared small, weak, and sparse (**Figure 4.6**). Focal cavitation was still present even when the pre-focal cavitation occurred (**Figure 4.6**). In all the treatments, focal cavitation was well confined in the vessel lumen with no contact to the interior vessel wall (Figure 4.6).

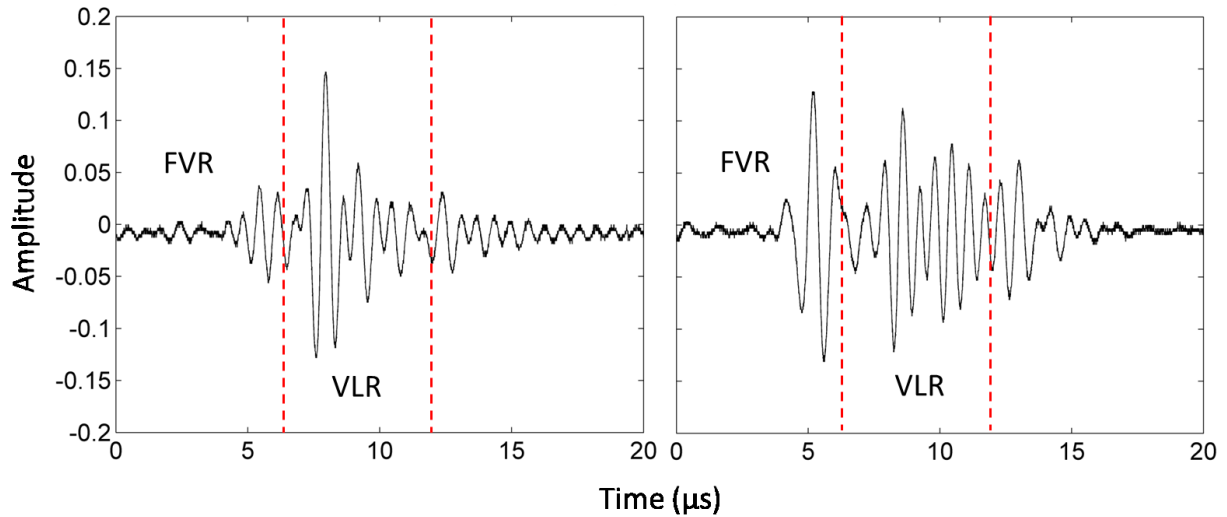


**Figure 4.6:** Ultrasound images of vessel lumen during treatment. Left: Focal cavitation at the center of the vessel lumen only (block arrow). Right: Focal cavitation (block arrow) with weak pre-focal cavitation (line arrow).

Quantitative results were obtained using the acoustic cavitation detection method. The percentages of detected pre-focal and focal cavitation incidents during the treatments are shown in **Table 4.1**. Representative waveforms captured during treatment are also plotted in **Figure 4.7**. No pre-focal cavitation was detected when using 5 Hz treatment PRF. Pre-focal cavitation was rarely detected when using 50 Hz PRF (1.20%) and occasionally detected when using 100 Hz PRF (5.43%). Focal cavitation occurred persistently regardless of treatment PRF and whether pre-focal cavitation happened or not. These results matched well with our qualitative observations from ultrasound imaging.

**Table 4.1:** The percentages of detected pre-focal and focal cavitation.

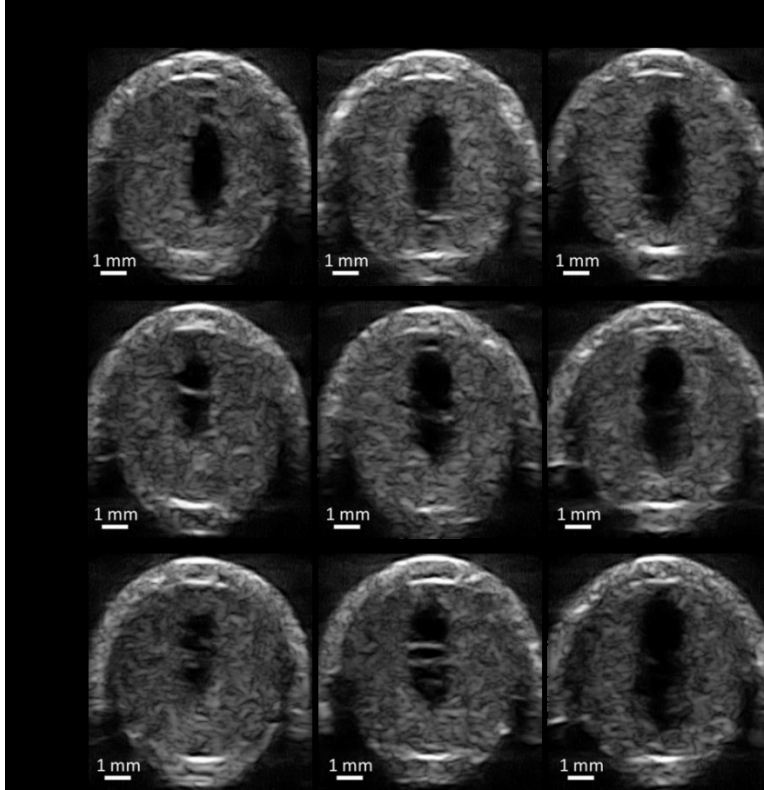
N = 18	Pre-focal Cavitation	Focal Cavitation
5 Hz	$0.00 \pm 0.00\%$	100%
50 Hz	$1.20 \pm 0.51\%$	100%
100 Hz	$5.43 \pm 1.82\%$	100%



**Figure 4.7:** The waveforms of cavitation monitor during treatment. Left: Focal cavitation only. Right: Pre-focal cavitation and focal cavitation together. The vertical dashed lines divide the Front Vessel Region (FVR) and the Vessel Lumen Region (VLR).

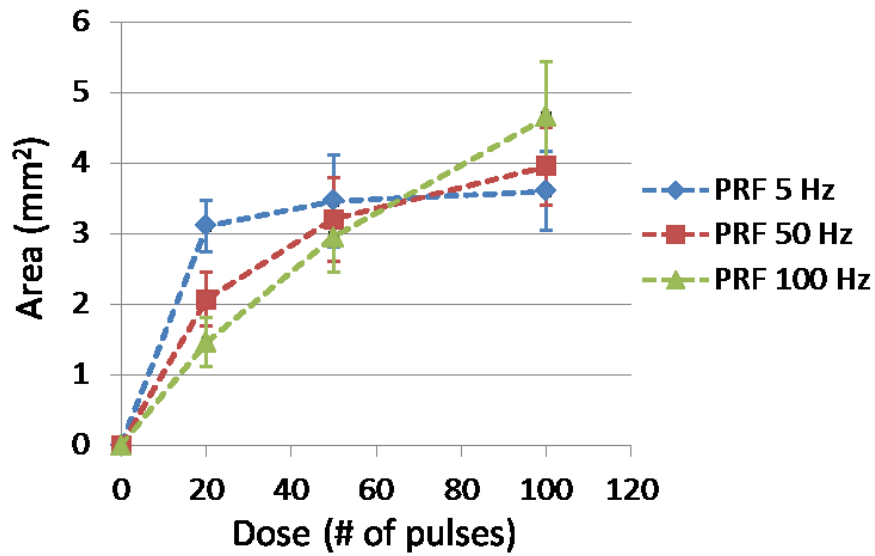
### 4.3.2 Flow Channel

Flow channels generated using different treatment PRFs and doses were thoroughly scanned using the high-resolution ultrasound imaging probe. Representative cross-sectional images of the flow channels after the microtripsy treatments are shown in **Figure 4.8**. The differences of the flow channels generated using different treatment PRFs were analyzed from the following four aspects: size, location, shape, and boundary sharpness.



**Figure 4.8:** Representative high-resolution ultrasound images of flow channel generated from each treatment parameter combination. The generated flow channels show as the hypochoic zones inside clots. Ultrasound propagated from the top to the bottom of the images.

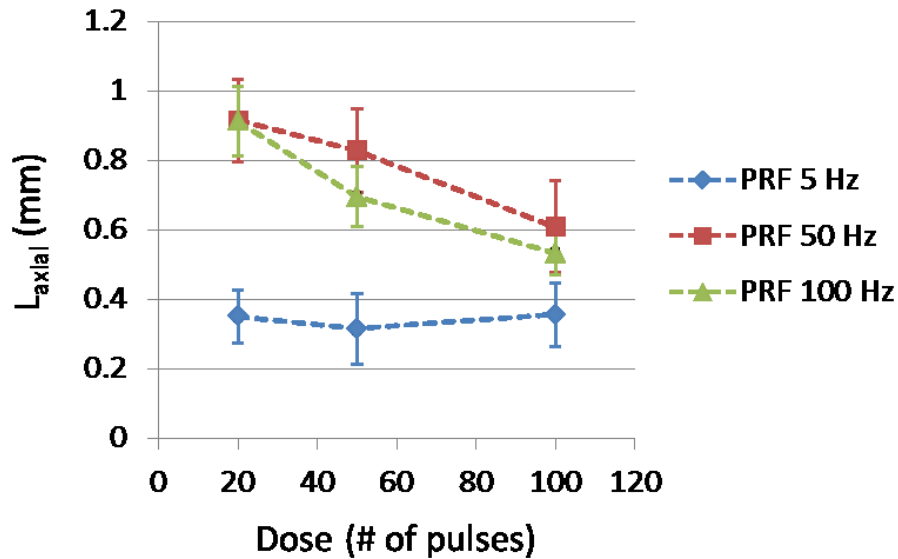
**- Size**



**Figure 4.9:** The cross-sectional area ( $A_{\text{cross}}$ ) of generated flow channel using each treatment PRF was shown as a function of dose. ( $N = 6 \times 67$ ).

The flow channel size was quantified as the cross area ( $A_{\text{cross}}$ ) of the flow channels on ultrasound scan images. The mean  $A_{\text{cross}}$  and its standard deviation using each treatment PRF was shown as a function of dose in **Figure 4.9**. With a final dose of 100 pulses, the mean  $A_{\text{cross}}$  of flow channel generated using 5, 50 and 100 Hz PRF were 3.60, 3.96 and 4.65 mm<sup>2</sup> respectively. One-sided t-tests showed that the final flow channel generated using 100 Hz PRF was significantly larger than those using 50 Hz ( $P<0.001$ ) and 5Hz ( $P<0.001$ ). Flow channel developments as a function of dose showed different trends when using different PRFs. The rate of increase in **Figure 4.9** illustrated the per-pulse efficiency of clot fractionation. The highest rate of increase at the beginning of treatment was observed for 5 Hz PRF, which indicated better per-pulse fractionation efficiency than those using 50 and 100 Hz PRF. After 20 pulses, the rate of increase almost plateaued. For 50 Hz PRF, a slower rate of increase was observed compared to 5 Hz PRF but faster than 100 Hz before 20 pulses. As more pulses were applied, the rate of increase gradually decreased but it did not reach complete saturation within 100 pulses. The lowest rate of increase at the start of the treatment was observed for 100 Hz PRF. However, as the treatment continued, the rate of increase remained almost linear all the way up to 100 pulses. By fitting 5-degree polynomials into the developing curves of flow channel in **Figure 4.9**, it was estimated to take 28, 73 and 89 pulses to reach 90% of flow channel size generated by 100 pulses for 5, 50 and 100 Hz PRF respectively. These trends suggested that higher treatment PRF had lower per-pulse fractionation efficiency (rate of increase) but longer growth “period” before saturation. 100 Hz PRF were 20 times faster than 5Hz PRF to reach the same dose, which indicates the higher PRF had a much higher temporal fractionation rate.

## - Location

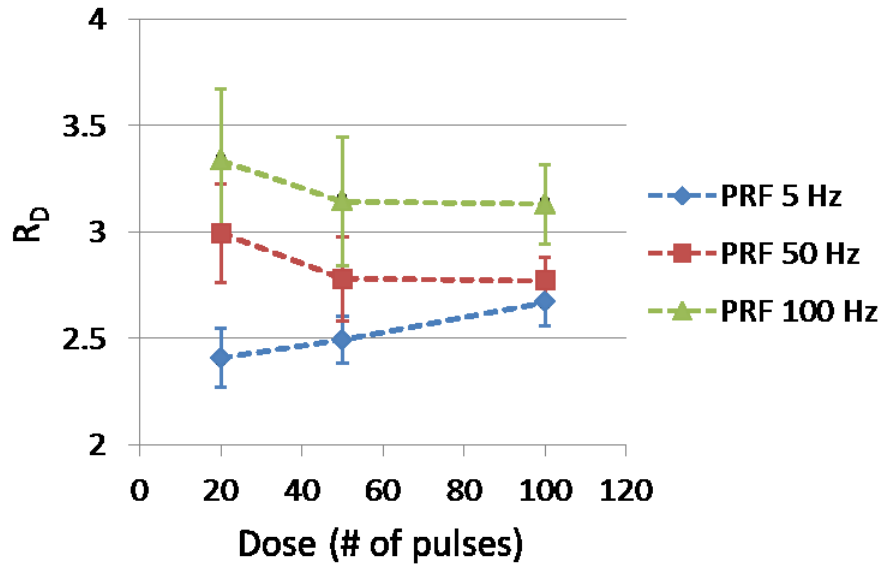


**Figure 4.10:** The axial location ( $L_{axial}$ ) of generated flow channel using each treatment PRF was shown as a function of dose. ( $N = 6 \times 67$ ).

The relative location of the flow channels generated by different PRFs were evaluated using channel axial location ( $L_{axial}$ ), which was defined as the axial distance from the cross-sectional center of flow channel (actual treatment location) to the cross-sectional center of the vessel lumen (intended target). For all the treatments, the center of the treatment focus was rigidly placed at the center of the vessel lumen. The mean  $L_{axial}$  of flow channel generated by each treatment PRF is shown in **Figure 4.10** as a function of treatment dose. For 5 Hz PRF, the center of the generated flow channel remained around 0.35 mm above the vessel center. For 50 and 100 Hz PRF, the flow channels were first generated approximately 0.9 mm above the vessel center (closer to the therapy transducer). As more pulses were applied, the centers of flow channels were shifted back towards the vessel center and finally stayed at around 0.6 mm above the vessel center. As shown in **Figure 4.8**, the flow channels generated by 5 Hz PRF were enlarged symmetrically with increasing the number of pulses while retaining the center location,

whereas the flow channels generated by 50 and 100 Hz PRF showed an asymmetric growth and their center locations shifted along the direction of ultrasound propagation.

### - Shape

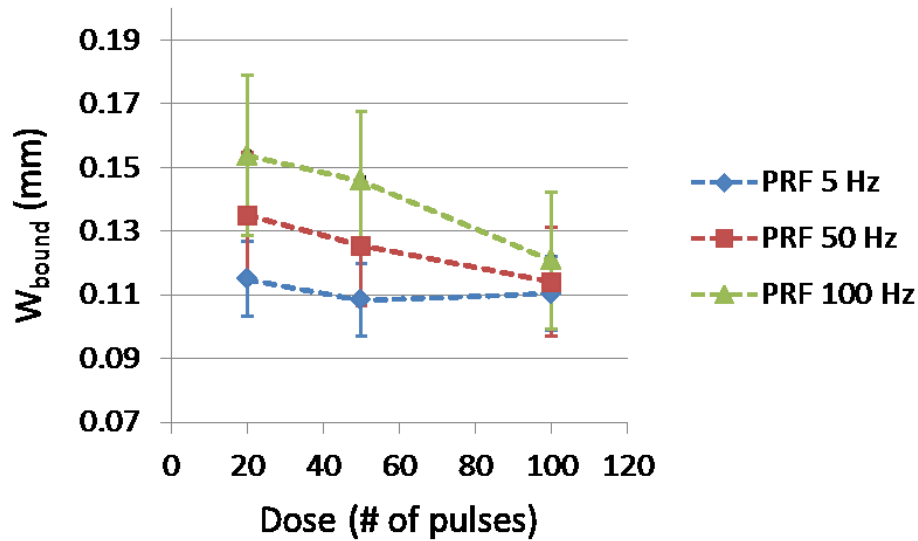


**Figure 4.11:** The ratio ( $R_D$ ) of the major diameter over the minor diameter of generated flow channel using each treatment PRF was shown as a function of dose. ( $N = 6 \times 67$ ).

The shape of flow channels created using different treatment PRFs were quantified as the ratio ( $R_D$ ) of major diameter ( $D_{\text{major}}$ ) over minor diameter ( $D_{\text{minor}}$ ) of the cross sections of flow channels. The mean  $R_D$  of each treatment PRF is shown in **Figure 4.11** as a function of treatment dose. A  $R_D$  value of 1 indicates a circular shape and higher  $R_D$  indicates a narrower cross section of flow channel. Overall, higher treatment PRF created narrower flow channels (higher  $R_D$ ). At the beginning of treatment, 50 Hz and 100 Hz PRF had a  $R_D$  of 3.33 and 2.99, respectively, whereas 5 Hz PRF had a  $R_D$  smaller than 2.5.  $R_D$  at 50 and 100 Hz PRF decreased by 5.7% and 7.2 % respectively as the dose increased from 20 to 50 pulses and remained almost the same afterwards. However  $R_D$  at 5 Hz PRF increased by 3.6% from 20 to 50 pulses and continued increasing by 7.0% from 50 to 100 pulses. After 100 pulses,  $R_D$  was 2.66, 2.77, and 3.13 for PRF

of 5, 50, and 100 Hz, respectively, which indicated a more elongated elliptical flow channel at a higher PRF.

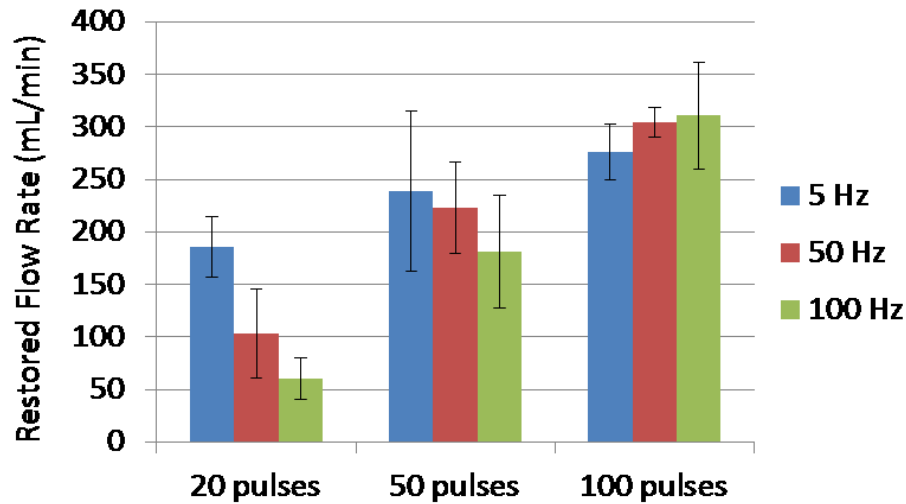
### - Boundary Sharpness



**Figure 4.12:** The width of boundary transition zone ( $W_{\text{bound}}$ ) of generated flow channel using each treatment PRF was shown as a function of dose. ( $N = 6 \times 67$ ).

The boundary sharpness of flow channels generated using different treatment PRFs were quantified as the width of boundary transition zone containing partially fractionated region outside the completely fractionated flow channel ( $W_{\text{bound}}$ ). The mean  $W_{\text{bound}}$  of each treatment PRF is shown in **Figure 4.12** as a function of treatment dose. As shown, when using 5 Hz PRF,  $W_{\text{bound}}$  remained at approximately 0.11 mm as more pulses applied. In the cases of 50 and 100 Hz PRF with small dose (20 pulses),  $W_{\text{bound}}$  was larger ( $0.135 \pm 0.020$  mm for 50 Hz PRF and  $0.154 \pm 0.025$  mm for 100 Hz PRF). As the dose increased all the way to 100 pulses,  $W_{\text{bound}}$  using 50 and 100 Hz PRF was decreased to a level close to that at 5 Hz PRF.

### 4.3.3 Restored Flow Rate



**Figure 4.13:** Restored flow rates of each treatment parameter combination. Treatments associated with creation of larger cross-sectional area opening were associated with larger flow rates. (N = 6).

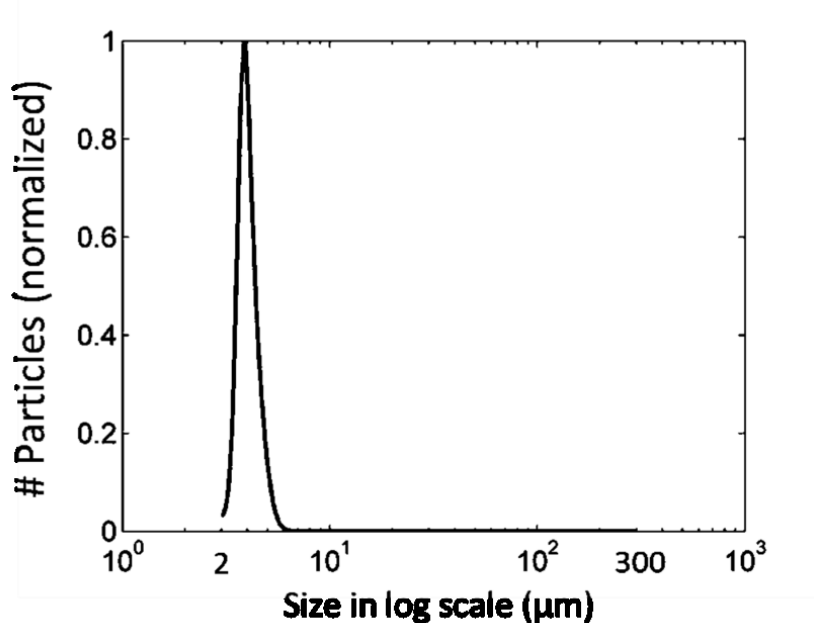
Prior to any treatment, no flow was observed on color Doppler imaging. After each microthrombolysis treatment, flow was successfully restored even with the minimal dose (20 pulses). The restored flow rate was measured after each treatment. With the constant pressure (3.7 mm Hg) applied, larger channel would be expected to permit higher flow rate, which is confirmed by the flow rate results shown in **Figure 4.13**. With 20 pulses, 5 Hz PRF had the highest flow rate (185mL/min) whereas for 100 Hz PRF it was only 60 mL/min. However, with a final dose of 100 pulses, both 50 and 100 Hz PRF achieved a mean flow rate over 300 mL/min, higher than that of 5 Hz PRF (276 mL/min). As a reference, the flow model with no blockage had a flow rate of 640 mL/min under the same pressure.

#### 4.3.4 Debris Size Distribution

According to the Coulter Counter measurements, all the treatments shared a very similar debris particle distribution from 2 to 300  $\mu\text{m}$ , regardless of the treatment PRF and dose used. A representative distribution of debris particles is shown in **Figure 4.14**. It was normally distributed with an expectation of 4.2  $\mu\text{m}$  and over 99.9 % of the debris particles were smaller than 10  $\mu\text{m}$ . The debris particles became orders of magnitude less as their size increased from 10



$\mu\text{m}$  to  $100\ \mu\text{m}$ . Detailed results of debris particles larger than  $100\ \mu\text{m}$  are presented as follows. The average number of debris particles from  $100$  to  $300\ \mu\text{m}$  from treatments using different PRFs and doses were shown in **Table 4.2**. Very few particles larger than  $100\ \mu\text{m}$  were observed after each treatment and there was no significant difference between different treatment PRFs and doses. The largest sizes of debris particles smaller than  $300\ \mu\text{m}$  from different treatments were shown in **Table 4.3**. The largest particle to pass through the  $300\ \mu\text{m}$  filter was  $236\ \mu\text{m}$ , which was generated from a treatment with  $100\ \text{Hz}$  PRF and  $50$  pulses dose. The total number of debris particles trapped on the  $300\ \mu\text{m}$  filter sheets, together with their sizes, is shown in **Table 4.4**. No particle  $> 300\ \mu\text{m}$  was trapped in 20 out of the 28 clot treatments. In 7 out of the 28 treatments, there was only one particle  $> 300\ \mu\text{m}$  trapped per treatment. And in only one treatment, there were two particles trapped together. The large particles ( $400$ ,  $570$  and  $630\ \mu\text{m}$ ) all appeared in treatments using  $5\ \text{Hz}$  PRF.



**Figure 4.14:** A representative distribution of debris particles from  $2$  to  $300\ \mu\text{m}$ . It is normalized to 1.

**Table 4.2:** Average number of particles >100  $\mu\text{m}$  over 6 treatments for each parameter set.

	<b>20 Pulses</b>	<b>50 Pulses</b>	<b>100 Pulses</b>
<b>PRF 5 Hz</b>	0 $\pm$ 0	7.0 $\pm$ 4.2	2.3 $\pm$ 2.6
<b>PRF 50 Hz</b>	7.0 $\pm$ 3.3	3.3 $\pm$ 2.9	3.3 $\pm$ 3.9
<b>PRF 100 Hz</b>	5.3 $\pm$ 4.3	14.0 $\pm$ 5.8	4.7 $\pm$ 4.4

**Table 4.3:** Largest particle size <300  $\mu\text{m}$ .

	<b>20 Pulses</b>	<b>50 Pulses</b>	<b>100 Pulses</b>
<b>PRF 5 Hz</b>	93 $\mu\text{m}$	128 $\mu\text{m}$	110 $\mu\text{m}$
<b>PRF 50 Hz</b>	148 $\mu\text{m}$	102 $\mu\text{m}$	104 $\mu\text{m}$
<b>PRF 100 Hz</b>	126 $\mu\text{m}$	236 $\mu\text{m}$	114 $\mu\text{m}$

**Table 4.4:** Particles larger than 300  $\mu\text{m}$ . The underline indicates they are from the same treatment.

	<b>20 Pulses</b>	<b>50 Pulses</b>	<b>100 Pulses</b>
<b>PRF 5 Hz</b>	1 (307 $\mu\text{m}$ )	1 (630 $\mu\text{m}$ )	<b>2</b> (570, 400 $\mu\text{m}$ )
<b>PRF 50 Hz</b>	0	0	<b>1</b> (300 $\mu\text{m}$ )
<b>PRF 100 Hz</b>	0	<b>1</b> (312 $\mu\text{m}$ )	<b>3</b> (300, <u>310</u> , <u>305</u> $\mu\text{m}$ )

## 4.4 Discussion

### 4.4.1 Cavitation

For all PRFs, focal cavitation was generated within the vessel lumen without contacting the vessel wall. No pre-focal cavitation was observed at 5 Hz PRF. As treatment PRF was increased to 50 and 100 Hz, instances of pre-focal cavitation were observed to occur on the front vessel wall during the treatments. However, because of the low frequency of occurrence (< 6%) and sparse bubble appearance, the pre-focal cavitation is expected to have limited impact on treatment efficacy and is unlikely to cause clinically relevant damage to exterior vessel wall, which has previously been showed to be resistant to cavitation damage [46]. However, further *in vivo* evaluation is necessary to validate this hypothesis. The cause of the pre-focal cavitation with higher PRF is potentially associated with both the water-vessel interface and cavitation memory.

In our experimental setup, the water-vessel interface was about 4 mm from the treatment focus in the vessel lumen closer to the ultrasound transducer. Bubble nuclei tend to reside on this interface and a previous study suggested the cavitation threshold was lowered at the tissue-fluid interface [47]. With higher PRF, residual bubble nuclei from cavitation persisted on the interface between microtripsy pulses due to cavitation memory and made the cavitation generation on the interface easier by acting as seeds for subsequent pulses. So with the enhancement by cavitation memory effects using higher PRF [48-50], pre-focal cavitation was manifested at the vessel interface.

In this chapter, we used the acoustic signals received from one transmit element to detect cavitation incidents. This method served well to detect whether a cavitation incident occur on the front vessel wall and/or in the vessel lumen, but the location of cavitation could not be accurately extracted. Potentially the accuracy and sensitivity of cavitation detection can be further improved by using one or more separate ultrasound transducers with higher frequency.

#### **4.4.2 Flow Channels**

With different treatment PRFs, the location, size, and shape of created flow channels varied, and the progression of the flow channel generation also changed. At 5 Hz PRF, the flow channel was generated consistently at the target focal location in the vessel lumen. Using high PRFs (50 and 100 Hz), the lesion was first generated at the front of the focal region in the vessel (close to the front vessel wall and the transducer) and then developed back towards the vessel center away from the transducer where the treatment focus was originally placed. The reason why at higher PRF the lesion started closer to the transducer and grew asymmetrically away from the transducer is potentially related to the cavitation memory effects. At the beginning of treatment, residual bubble nuclei were formed from the first few pulses and trapped all over the

focal region in the clot. With a high PRF, a subsequent ultrasound pulse arrived before the complete dissolution of residual bubble nuclei produced from the previous pulse. The nuclei proximal to the transducer acted as seeds to cause onsite cavitation, which absorbed and shielded the incident acoustic energy from propagating further towards the treatment focus, resulting in a cavitation cloud at the front of the treatment focal region. As more pulses were applied, the clot at the front of the focal region was fractionated, creating a small liquefied clot zone and a fluid-tissue interface. Then the clot was gradually eroded from the liquefied region and grew away from the transducer towards the vessel center. Using low PRF (5 Hz), the lesion was first generated at the vessel center and then enlarged radially. In this case, residual bubble nuclei were probably dissolved before the subsequent ultrasound pulse, minimizing the cavitation memory effects.

Per-pulse fractionation efficiencies were also different between these treatment PRFs, which can be potentially explained by the same rationale above based on the cavitation memory effects. At the beginning of fractionation, 5 Hz PRF showed better per-pulse fractionation efficiency probably because the cavitation was intrinsically generated covering the entire focal region in the vessel center without memory effects. As clot in the focal region was quickly fractionated using 5 Hz PRF, the per-pulse fractionation efficiency decreased significantly after 20 pulses because less and less clot volume could be broken down in the focal region. But for 50 and 100 Hz PRF, since a small lesion was generated on the proximal side and the clot was then gradually eroded from the lesion and expanded away from the transducer, the lesion size still grew significantly after 20 pulses.

#### **4.4.3 Debris**

Only a few (less than 20 average) debris particles  $> 100 \mu\text{m}$  were observed per treatment in this study. Only a total of nine debris particles  $> 300 \mu\text{m}$  were observed in 8 out of the 28 treatments. From Table 4.4, we can see the largest particles ( $570 \mu\text{m}$ ,  $630 \mu\text{m}$ ) were observed when using 5 Hz PRF. This may be associated with the low temporal fractionation rate of 5 Hz PRF. At the end of recanalization, when fractionating the last clot segment, flow started to restore. Due to the slow fractionation of 5 Hz PRF, large clot pieces might be swept away before fractionated into smaller pieces. In contrast, since high treatment PRF has a much higher temporal fractionation rate, large clot pieces at the end of treatment might be fractionated down quickly before major flow was restored.

Our previous study using a PRF of 50 Hz and an increased dose of 300 pulses showed no debris particles  $> 300 \mu\text{m}$  and less 100- $\mu\text{m}$ -level particles, which indicates increasing treatment dose can probably eliminate large debris particles [27]. The debris observed in this study can be considered as the worst possible case. Even with this worst case, the generated debris shouldn't cause any severe embolism in lung in the DVT application. First, the largest particle observed overall was only  $630 \mu\text{m}$ . According to the morphometry of pulmonary arterial system reported by Singhal *et al.* [51], 500- $\mu\text{m}$ -level particles may only obstruct one arteriole of order 9 which supplies only 0.016% of total capillary beds. Second, the number of debris particles larger than  $100 \mu\text{m}$  from one treatment was very small (less than 20), which wouldn't be expected to cause massive pulmonary embolism. Third, mechanical thrombectomy treatments generate clot particles up to  $1000 \mu\text{m}$  with no severe embolism reported from human patient treatments [52-54].

#### **4.4.4 Choice of Treatment PRF**

Even though 5 Hz PRF avoids the pre-focal cavitation formation, it generates cavitation consistently at the geometric focal region, and has better per-pulse fractionation efficiency at the treatment beginning, overall, 50 or 100 Hz PRF may be a better choice for microtripsy thrombolysis to use clinically due to the larger flow channels, smaller debris particles, and much higher temporal fractionation rate. Compared to 5Hz PRF, the higher PRFs in this study created larger flow channels after 100 pulse dose, and the maximal size of debris particles was smaller. The higher PRFs have a higher temporal fractionation rate and can shorten treatment time significantly. Assuming a dose of 300 pulses is used in clinical situation to minimize the debris particle size, it takes only about 15 minutes for microtripsy to recanalize a 10-cm long clot using 100 Hz PRF compared to hours for 5Hz PRF. Reduced treatment time can be a very competitive advantage over the current thrombolysis treatments. We also see less large debris particles  $>300\ \mu\text{m}$  generated using higher PRF. With this observed trend, it is reasonable to consider even higher PRF which may achieve the same or better results with shorter treatment time. The reason why we didn't get a chance to try PRF  $> 100\ \text{Hz}$  was the limitation of the therapy transducer. Since it was outputting a very high acoustic pressure, we were worried about damaging the transducer's piezoelectric elements by heating with higher PRF.

Despite these favorable results of using 50 and 100 Hz PRF, further investigation is still needed to evaluate the risk of potential vessel damages. It should be noted that sparse and infrequent pre-focal cavitation was observed on the vessel wall using 50 or 100Hz PRF. We were not able to evaluate this risk using this vessel phantom but future *in vivo* experiments may provide us a more detailed answer regarding this concern. In addition, using a higher PRF, the cavitation started closer to the transducer and grew away from the transducer, and the lesion center did not align exactly with the center of the geometric focal zone. Though with imaging

feedback we can take that into account in the pre-treatment planning to ensure the focal cavitation zone is completely confined within the vessel lumen, further *in vivo* evaluation of this offset is needed.

#### **4.4.5 Future Work**

Freshly formed clots were used in this study to mimic acute thrombosis. Literature shows that chronic retracted clots are more resistant to sonothrombolysis treatments [55, 56]. We plan to evaluate the efficacy and safety of the microtripsy thrombolysis on retracted clots. In addition, we are currently investigating a new real-time imaging feedback (Bubble-induced Color Doppler [57, 58]) for histotripsy thrombolysis treatment, and we plan to incorporate this feedback with microtripsy thrombolysis to adaptively deliver the optimal dose at each treatment location during treatment. Finally, *in vivo* studies will be conducted to validate the feasibility, safety and efficacy of microtripsy thrombolysis in a porcine deep vein thrombosis model [26, 59]. Since there may be a difference in cavitation behavior between *in vitro* and *in vivo* settings, we want to confirm what we observed in this *in vitro* study still applies *in vivo*.

#### **4.5 Conclusion**

This chapter investigated the effects of PRF (5, 50, and 100 Hz) on microtripsy thrombolysis. The results demonstrated that focal cavitation was always well-confined in the vessel lumen without contacting the vessel wall regardless of the PRF used. Pre-focal cavitation on the vessel wall was occasionally observed when using 50 and 100 Hz PRF, but it appeared weak and infrequently. The 5 Hz PRF showed the best per-pulse fractionation efficiency at the beginning of treatment, but the 50 and 100 Hz PRFs generated larger flow channels with much shorter treatment times over the course of the treatment. In addition, results showed fewer large debris particles were observed with higher PRFs. Overall, the results of this study suggest that 50

or 100 Hz PRF may be a better choice for microtripsy thrombolysis to use clinically due to the larger resulting flow channel, shorter treatment time, and smaller debris particles. Further *in vivo* evaluation of potential vessel damage and treatment efficacy using high PRF for microtripsy thrombolysis is necessary and underway.

## 4.6 References

- [1] X. Zhang, *et al.*, "Noninvasive thrombolysis using microtripsy: a parameter study," *Ultrasonics, Ferroelectrics, and Frequency Control, IEEE Transactions on*, vol. 62, pp. 2092-2105, 2015.
- [2] D. Mozaffarian, *et al.*, "Heart Disease and Stroke Statistics—2015 Update A Report From the American Heart Association," *Circulation*, vol. 131, pp. e29-e322, 2015.
- [3] M. G. Beckman, *et al.*, "Venous thromboembolism: a public health concern," *American journal of preventive medicine*, vol. 38, pp. S495-S501, 2010.
- [4] H. P. Adams, *et al.*, "Guidelines for thrombolytic therapy for acute stroke: a supplement to the guidelines for the management of patients with acute ischemic stroke a statement for healthcare professionals from a special writing group of the stroke council, American heart association," *Circulation*, vol. 94, pp. 1167-1174, 1996.
- [5] S. M. Bates and J. S. Ginsberg, "Treatment of deep-vein thrombosis," *New England Journal of Medicine*, vol. 351, pp. 268-277, 2004.
- [6] H. S. Friedman, *et al.*, "Tissue plasminogen activator for acute ischemic stroke," *N Engl J Med*, vol. 334, p. 1405, 1996.
- [7] M. J. Sharafuddin, *et al.*, "Endovascular management of venous thrombotic and occlusive diseases of the lower extremities," *Journal of vascular and interventional radiology*, vol. 14, pp. 405-423, 2003.
- [8] M. N. Lauw and H. R. Büller, "Treatment of deep vein thrombosis," in *Current Approaches to Deep Vein Thrombosis*, ed: Future Medicine Ltd, 2014, pp. 136-160.
- [9] R. J. Siegel and H. Luo, "Ultrasound thrombolysis," *Ultrasonics*, vol. 48, pp. 312-320, 2008.
- [10] S. Pfaffenberger, *et al.*, "2MHz ultrasound enhances t-PA-mediated thrombolysis: comparison of continuous versus pulsed ultrasound and standing versus travelling acoustic waves," *Thromb Haemost*, vol. 89, pp. 583-589, 2003.



- [11] C. K. Holland, *et al.*, "Ultrasound-enhanced tissue plasminogen activator thrombolysis in an *in vitro* porcine clot model," *Thrombosis research*, vol. 121, pp. 663-673, 2008.
- [12] K. E. Hitchcock, *et al.*, "Ultrasound-enhanced rt-PA thrombolysis in an *ex vivo* porcine carotid artery model," *Ultrasound in medicine & biology*, vol. 37, pp. 1240-1251, 2011.
- [13] J. Larsson, *et al.*, "Ultrasound enhanced thrombolysis in experimental retinal vein occlusion in the rabbit," *British journal of ophthalmology*, vol. 82, pp. 1438-1440, 1998.
- [14] V. Frenkel, *et al.*, "Pulsed High-Intensity Focused Ultrasound Enhances Thrombolysis in an *In Vitro* Model 1," *Radiology*, vol. 239, pp. 86-93, 2006.
- [15] M. J. Stone, *et al.*, "Pulsed-high intensity focused ultrasound enhanced tPA mediated thrombolysis in a novel *in vivo* clot model, a pilot study," *Thrombosis research*, vol. 121, pp. 193-202, 2007.
- [16] A. V. Alexandrov, *et al.*, "Ultrasound-enhanced systemic thrombolysis for acute ischemic stroke," *New England Journal of Medicine*, vol. 351, pp. 2170-2178, 2004.
- [17] C. A. Molina, *et al.*, "Transcranial ultrasound in clinical sonothrombolysis (TUCSON) trial," *Annals of neurology*, vol. 66, pp. 28-38, 2009.
- [18] G. Tsivgoulis, *et al.*, "Safety and efficacy of ultrasound-enhanced thrombolysis a comprehensive review and meta-analysis of randomized and nonrandomized studies," *Stroke*, vol. 41, pp. 280-287, 2010.
- [19] S. Datta, *et al.*, "Ultrasound-enhanced thrombolysis using Definity® as a cavitation nucleation agent," *Ultrasound in medicine & biology*, vol. 34, pp. 1421-1433, 2008.
- [20] A. T. Brown, *et al.*, "Microbubbles improve sonothrombolysis *in vitro* and decrease hemorrhage *in vivo* in a rabbit stroke model," *Investigative radiology*, vol. 46, 2011.
- [21] W. C. Culp, *et al.*, "Successful microbubble sonothrombolysis without tissue-type plasminogen activator in a rabbit model of acute ischemic stroke," *Stroke*, vol. 42, pp. 2280-2285, 2011.
- [22] U. Rosenschein, *et al.*, "Ultrasound Imaging-Guided Noninvasive Ultrasound Thrombolysis Preclinical Results," *Circulation*, vol. 102, pp. 238-245, 2000.
- [23] A. Burgess, *et al.*, "High-intensity focused ultrasound (HIFU) for dissolution of clots in a rabbit model of embolic stroke," *PloS one*, vol. 7, p. e42311, 2012.
- [24] C. Wright, *et al.*, "*In vitro* and *in vivo* high intensity focused ultrasound thrombolysis," *Investigative radiology*, vol. 47, p. 217, 2012.

- [25] A. D. Maxwell, *et al.*, "Noninvasive thrombolysis using pulsed ultrasound cavitation therapy–histotripsy," *Ultrasound in medicine & biology*, vol. 35, pp. 1982-1994, 2009.
- [26] A. D. Maxwell, *et al.*, "Noninvasive treatment of deep venous thrombosis using pulsed ultrasound cavitation therapy (histotripsy) in a porcine model," *Journal of vascular and interventional radiology*, vol. 22, pp. 369-377, 2011.
- [27] X. Zhang, *et al.*, "Noninvasive thrombolysis using histotripsy beyond the intrinsic threshold (microtripsy)," *Ultrasonics, Ferroelectrics, and Frequency Control, IEEE Transactions on*, vol. 62, pp. 1342-1355, 2015.
- [28] Z. Xu, *et al.*, "Effects of acoustic parameters on bubble cloud dynamics in ultrasound tissue erosion (histotripsy)," *The Journal of the Acoustical Society of America*, vol. 122, pp. 229-236, 2007.
- [29] Z. Xu, *et al.*, "Evolution of bubble clouds induced by pulsed cavitation ultrasound therapy-histotripsy," *Ultrasonics, Ferroelectrics, and Frequency Control, IEEE Transactions on*, vol. 55, pp. 1122-1132, 2008.
- [30] Z. Xu, *et al.*, "Noninvasive creation of an atrial septal defect by histotripsy in a canine model," *Circulation*, vol. 121, pp. 742-749, 2010.
- [31] A. D. Maxwell, *et al.*, "Cavitation clouds created by shock scattering from bubbles during histotripsy," *The Journal of the Acoustical Society of America*, vol. 130, pp. 1888-1898, 2011.
- [32] A. D. Maxwell, *et al.*, "Probability of cavitation for single ultrasound pulses applied to tissues and tissue-mimicking materials," *Ultrasound in medicine & biology*, vol. 39, pp. 449-465, 2013.
- [33] K.-W. Lin, *et al.*, "Histotripsy beyond the intrinsic cavitation threshold using very short ultrasound pulses: microtripsy," *Ultrasonics, Ferroelectrics, and Frequency Control, IEEE Transactions on*, vol. 61, pp. 251-265, 2014.
- [34] T.-Y. Wang, *et al.*, "An efficient treatment strategy for histotripsy by removing cavitation memory," *Ultrasound in medicine & biology*, vol. 38, pp. 753-766, 2012.
- [35] A. P. Duryea, *et al.*, "Removal of residual bubble nuclei to enhance histotripsy kidney stone erosion at high rate," *The Journal of the Acoustical Society of America*, vol. 136, pp. 2193-2193, 2014.
- [36] K. Spengos, *et al.*, "Acceleration of thrombolysis with ultrasound through the cranium in a flow model," *Ultrasound in medicine & biology*, vol. 26, pp. 889-895, 2000.

- [37] U. Albrechtsson, *et al.*, "Femoral vein pressure measurements for evaluation of venous function in patients with postthrombotic iliac veins," *Cardiovascular and interventional radiology*, vol. 4, pp. 43-50, 1981.
- [38] D. Negus and F. Cockett, "Femoral vein pressures in post-phlebotic iliac vein obstruction," *British Journal of Surgery*, vol. 54, pp. 522-525, 1967.
- [39] J. Browne, *et al.*, "Assessment of the acoustic properties of common tissue-mimicking test phantoms," *Ultrasound in medicine & biology*, vol. 29, pp. 1053-1060, 2003.
- [40] B. Hertzberg, *et al.*, "Sonographic assessment of lower limb vein diameters: implications for the diagnosis and characterization of deep venous thrombosis," *AJR. American journal of roentgenology*, vol. 168, pp. 1253-1257, 1997.
- [41] S. Park, *et al.*, "Non-invasive embolus trap using histotripsy—an acoustic parameter study," *Ultrasound in medicine & biology*, vol. 39, pp. 611-619, 2013.
- [42] J. E. Parsons, *et al.*, "Cost-effective assembly of a basic fiber-optic hydrophone for measurement of high-amplitude therapeutic ultrasound fields," *The Journal of the Acoustical Society of America*, vol. 119, pp. 1432-1440, 2006.
- [43] Z. Xu, *et al.*, "Controlled ultrasound tissue erosion: The role of dynamic interaction between insonation and microbubble activity," *The Journal of the Acoustical Society of America*, vol. 117, pp. 424-435, 2005.
- [44] E. Vlaisavljevich, *et al.*, "Effects of ultrasound frequency and tissue stiffness on the histotripsy intrinsic threshold for cavitation," *Ultrasound in medicine & biology*, vol. 41, pp. 1651-1667, 2015.
- [45] B. Coulter, "Coulter Counter Multisizer 3 User's Manual," *Hialeah, FL*, 2000.
- [46] E. Vlaisavljevich, *et al.*, "Effects of tissue mechanical properties on susceptibility to histotripsy-induced tissue damage," *Physics in medicine and biology*, vol. 59, p. 253, 2014.
- [47] Z. Xu, *et al.*, "High speed imaging of bubble clouds generated in pulsed ultrasound cavitation therapy-histotripsy," *Ultrasonics, Ferroelectrics, and Frequency Control, IEEE Transactions on*, vol. 54, pp. 2091-2101, 2007.
- [48] M. Delius and W. Brendel, "A model of extracorporeal shock wave action: Tandem action of shock waves," *Ultrasound in medicine & biology*, vol. 14, pp. 515-518, 1988.
- [49] P. Huber, *et al.*, "Control of cavitation activity by different shockwave pulsing regimes," *Physics in medicine and biology*, vol. 44, p. 1427, 1999.
- [50] M. Arora, *et al.*, "Cavitation cluster dynamics in shock-wave lithotripsy: Part 1. Free field," *Ultrasound in medicine & biology*, vol. 31, pp. 827-839, 2005.

- [51] S. Singhal, *et al.*, "Morphometry of the human pulmonary arterial tree," *Circulation Research*, vol. 33, pp. 190-197, 1973.
- [52] K. Yasui, *et al.*, "Recirculation-type Amplatz clot macerator: determination of particle size and distribution," *Journal of vascular and interventional radiology*, vol. 4, pp. 275-278, 1993.
- [53] R. Uflacker, *et al.*, "Treatment of thrombosed dialysis access grafts: randomized trial of surgical thrombectomy versus mechanical thrombectomy with the Amplatz device," *Journal of vascular and interventional radiology*, vol. 7, pp. 185-192, 1996.
- [54] S. MÜLLER-HÜLSBECK, *et al.*, "Mechanical thrombectomy of major and massive pulmonary embolism with use of the Amplatz thrombectomy device," *Investigative radiology*, vol. 36, pp. 317-322, 2001.
- [55] A. Blinc, *et al.*, "Magnetic resonance imaging of retracted and nonretracted blood clots during fibrinolysis *in vitro*," *Pathophysiology of Haemostasis and Thrombosis*, vol. 22, pp. 195-201, 1992.
- [56] J. T. Sutton, *et al.*, "Clot retraction affects the extent of ultrasound-enhanced thrombolysis in an ex vivo porcine thrombosis model," *Ultrasound in medicine & biology*, vol. 39, pp. 813-824, 2013.
- [57] X. Zhang, *et al.*, "Real-Time Feedback of Histotripsy Thrombolysis Using Bubble-Induced Color Doppler," *Ultrasound in medicine & biology*, vol. 41, pp. 1386-1401, 2015.
- [58] R. M. Miller, *et al.*, "Investigation of the mechanism of ARFI-based Color Doppler feedback of histotripsy tissue fractionation," in *Ultrasonics Symposium (IUS), 2013 IEEE International*, 2013, pp. 934-937.
- [59] R. Devanagondi, *et al.*, "Hemodynamic and Hematologic Effects of Histotripsy of Free-Flowing Blood: Implications for US-Mediated Thrombolysis," *Journal of vascular and interventional radiology*, 2015.

## Chapter 5

### Histotripsy Thrombolysis on Retracted Clots

This chapter has been published in *Ultrasound in Medicine and Biology*. 2016; 42(8):1903-1918.  
© UMB. Reprinted, with permission, from [1].

#### 5.1 Introduction

Thrombosis is the formation of a blood clot in the cardiovascular system that prevents blood from circulating. Arterial thrombosis in the cerebral vasculature leads to ischemic stroke, which is a leading cause of disability and death in the United States [2]. The most common form of venous thrombosis is deep vein thrombosis (DVT), which occurs predominantly in the legs and can sometimes lead to lethal pulmonary embolism (PE). DVT/PE (also called venous thromboembolism) affects over 300,000 people and causes deaths of 60,000 to 100,000 each year in the United States [3]. Patients with more extensive thrombosis sometimes require thrombolytic treatments. The current gold standard of thrombolytic treatment involves the infusion of thrombolytic drugs such as tissue plasminogen activator (tPA) [4, 5]. Systemic administration of thrombolytic drugs has limited effectiveness with long treatment time (several hours to days) and is associated with a high risk of major bleeding [6]. Catheter-directed thrombolysis has the advantage over systemic thrombolysis through local application at the thrombosis site, but it is invasive and carries the risks of bleeding, vascular damage, and infections [7, 8].

Ultrasound has been investigated as a tool to enhance or induce thrombolysis for several decades [9]. Significant efforts have been focused on enhancing the efficacy of thrombolytic

drugs using ultrasound [10-15], with several clinical trials showing promising results [16-18]. In addition, ultrasound combined with microbubbles has been demonstrated to successfully augment clot dissolution in the presence or absence of thrombolytic drugs [19-23]. Ultrasound has also been studied as a stand-alone thrombolysis method under approaches utilizing acoustic cavitation [24-30].

Histotripsy is a non-thermal tissue ablation method that mechanically fractionates soft tissue via well-controlled acoustic cavitation generated by microsecond-long, high-pressure ultrasound pulses [31-33]. The potential of using histotripsy as a non-invasive, drug-free, and image-guided thrombolysis method was demonstrated both *in vitro* and *in vivo* by Maxwell *et al.* [27, 28]. Multi-cycle (usually  $\geq 5$  cycles) ultrasound pulses were used in those studies to generate cavitation bubble clouds via a shock scattering mechanism [34]. A new histotripsy approach, termed microtripsy, has been recently investigated for thrombolysis application to improve treatment precision and avoid potential vessel damage [29, 30, 35]. In microtripsy, a cavitation cloud is initiated via a single-cycle ultrasound pulse with only one high, negative pressure phase exceeding a very distinct negative pressure intrinsic threshold of the medium [36, 37]. The location and size of the cavitation cloud generated using microtripsy through the intrinsic threshold mechanism is more reproducible and predictable than the shock scattering mechanism [36, 37]. In those microtripsy thrombolysis studies, cavitation was precisely generated and confined in the vessel lumen without contacting the vessel wall, allowing for a precise flow channel to be created within the clot while minimizing the risk of vessel damage [29].

Previous studies showed that drug-mediated thrombolysis, including ultrasound-enhanced thrombolysis, was difficult to achieve with retracted clots [38-40]. As a clot is formed, clot

retraction initiated by platelets occurs and changes the structure and composition of the clot remarkably as it ages over time [41, 42]. In the clot retraction process, the fibrin network shrinks and effectively increases fibrin density per unit of clot volume and/or decreasing plasminogen concentration, and results in lower porosity and reduced permeability [43-45]. The high resistance of retracted clots to drug-mediated thrombolysis is believed to be due to the reduced permeability of the retracted clot to the thrombolytic agents.

Unlike drug-mediated thrombolysis that depends on the permeation of thrombolytic agents into the clot, microtripsy fractionates clots by controlled cavitation. In the previous microtripsy thrombolysis study, a fast lysis rate was achieved with unretracted clots. Retracted clots are stiffer than unretracted clots and are expected to be more resistant to histotripsy-induced cavitation and fractionation [46, 47]. We hypothesize that microtripsy is effective to treat retracted clots, but with reduced treatment efficacy compared to unretracted clots. We further hypothesize that the treatment efficacy for retracted clots can be enhanced using treatment strategies incorporating electronic focal steering. By using a phased-array transducer with electronic focal steering capability, the treatment focus can be steered to enlarge the flow channel through the retracted clot without additional mechanical movements of the therapy transducer. These hypotheses are tested in this chapter by investigating the treatment efficacy of microtripsy thrombolysis on retracted clots and exploring efficacies of different microtripsy thrombolysis strategies incorporating electrical focal steering. Retracted clots were prepared *in vitro* following a protocol described by Sutton *et al.* [40], and their elasticity was characterized quantitatively. The retracted clots were treated in an *in vitro* flow model using three different strategies: single-focus strategy, electronically-steered multi-focus strategy and a dual-pass multi-focus strategy. After treatments, the generated flow channels were 3D-scanned using a 20

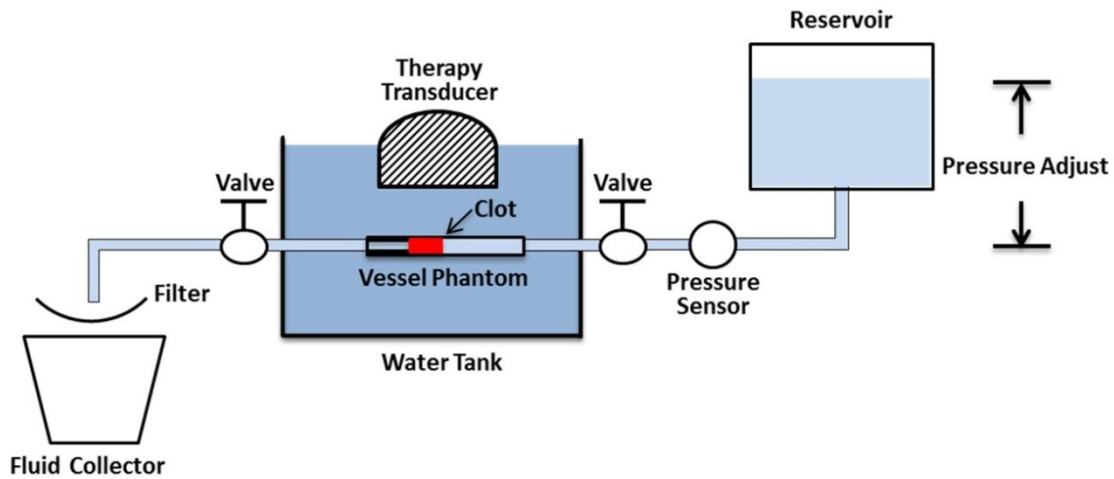
MHz ultrasound imaging probe, and the sizes of the flow channels were quantified. The restored flow and the distribution of generated clot debris particles were also measured. The treatment results of retracted clots were compared with those of the unretracted clots from a previous study. The treatment efficacies using three different microtripsy thrombolysis strategies were also compared side by side.

## **5.2 Materials and Methods**

### **5.2.1 Flow Model**

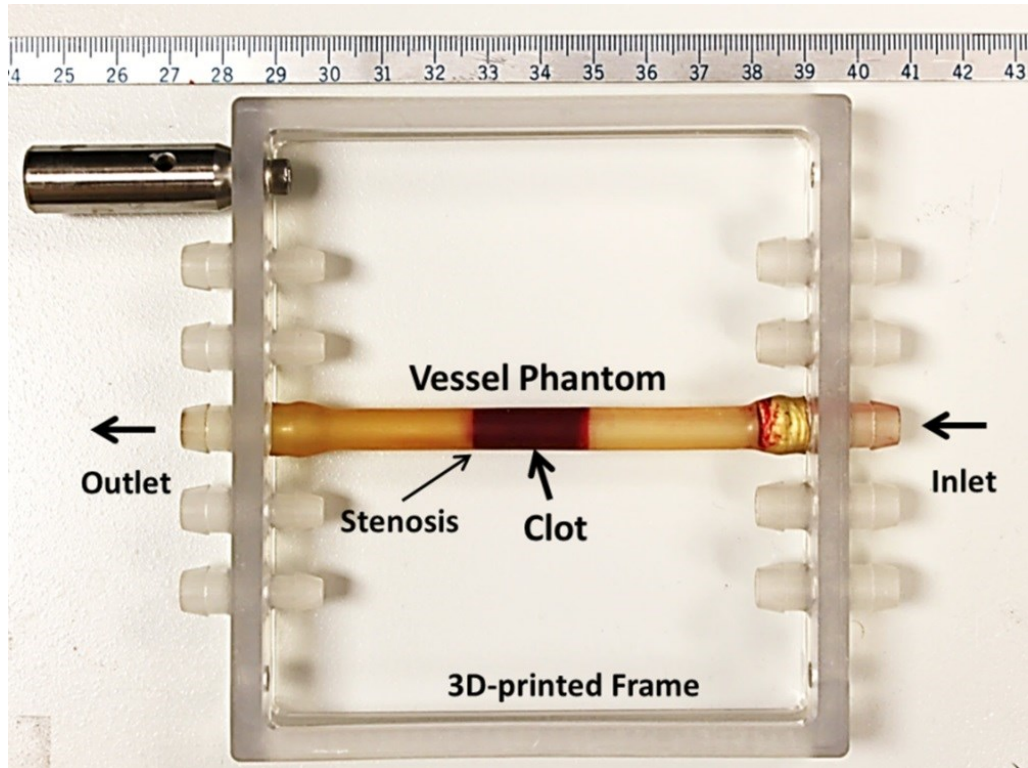
An *in vitro* flow model, which has been described previously [29, 30], was deployed in this study. The flow model was designed to mimic the condition of occlusive venous thrombosis, where blood flow is completely blocked by the thrombus but blood pressure still applies. A saline reservoir, a pressure sensor, a vessel phantom, a filter, and a fluid collector were connected in sequence with silicone tubing (Masterflex L/S 17; Cole-Parmer, Vernon Hills, IL, USA) (**Figure 5.1**). The saline reservoir was placed higher than the rest of the system for perfusion under gravity-driven pressure. With an occlusive thrombus fixed inside, the vessel phantom was mounted horizontally in a tank filled with degassed water. The height difference between the saline level in the reservoir and the vessel phantom was set to apply a constant pressure of 3.7 mm Hg, which was measured by the pressure sensor (MG-9V; SSI Technologies, Janesville, WI, USA). A pressure of 3.7 mm Hg was chosen according to reported femoral vein pressure [48, 49]. The femoral vein in the upper leg is where DVT often occurs. The therapy transducer was positioned inside the tank facing the vessel phantom to conduct the microtripsy recanalization treatment. When a channel was generated through the clot, the restored flow, together with clot debris particles generated from the treatment, was passed through the filter, and the filtered fluid was collected for further small particle analysis.





**Figure 5.1:** Schematic diagram of the *in vitro* flow model.

The vessel phantom was developed in-house to mimic a human femoral vein (**Figure 5.2**). It was made from urethane polymer (Urethane RTV Mold-Making System; Tap Plastics Inc., San Leandro, CA, USA), which has acoustic properties similar to human tissue [50]. The vessel phantom had an 8 mm outer diameter, a 6.5 mm inner diameter on one side, and a 4.2 mm inner diameter (35% stenosis) on the other side. The method of making the vessel phantom has been described previously in detail [29]. The 6.5 mm inner diameter was chosen according to reported DVT vein diameters (5 to 21.7 mm) [51]. The stenosis in this *in vitro* setup stabilized the clot and prevented it from flowing away during the treatment under pressure. The vessel phantom was held by a 3D-printed frame with tube fittings at the two ends to connect the vessel in-line with the rest of the flow model [52].

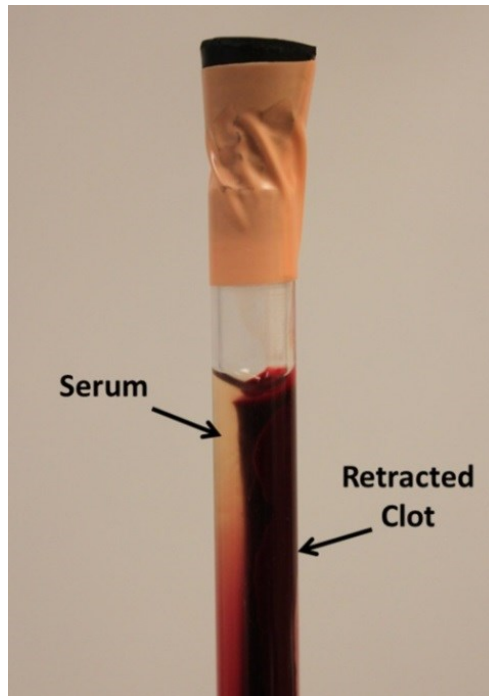


**Figure 5.2:** The vessel phantom was held by a 3D-printed frame and could be easily connected in line with the flow model using tubing fittings. A 35% stenosis in the vessel phantom was used to stabilize the clot so that it did not slip under pressure. The inner diameter was 4.2 mm on the downstream side of the stenosis and 6.5 mm on the upstream side. A clot was inserted to the upstream side of the stenosis as shown in the figure.

### 5.2.2 Retracted Clot Formation

Retracted clots were formed following a protocol similar to that described by Sutton *et al.* [40]. Fresh bovine blood was collected from a local abattoir. A citrate-phosphate-dextrose (CPD) solution (#C7165; Sigma-Aldrich Co., St. Louis, MO, USA) was immediately mixed with fresh bovine blood as an anti-coagulant at a ratio of 1 mL CPD per 9 mL blood. All the blood samples were used within the same day as they were collected. The bovine blood was first warmed up to the normal cow body temperature (38.6 °C). To stimulate the clotting cascade, calcium chloride (#21107; Sigma-Aldrich Co., St. Louis, MO, USA) was injected into the blood to a final concentration of 20 mM/L. To form a retracted clot, the stimulated blood (6.5 mL) was carefully poured into a hydrophilic glass tube (Borosilicate Glass Tubing, GSC International Inc., Nixa,

MO, USA) with an inner diameter of 8.5 mm. After 3 hours in a water bath at 38.6 °C, the tube with newly formed clot inside was moved into refrigeration and stored at 4°C for 7 days to allow for retraction.



**Figure 5.3:** A clot was retracted in a hydrophilic glass tube after 7 days in 4°C incubation. The serum extruded from the clot can be clearly distinguished.

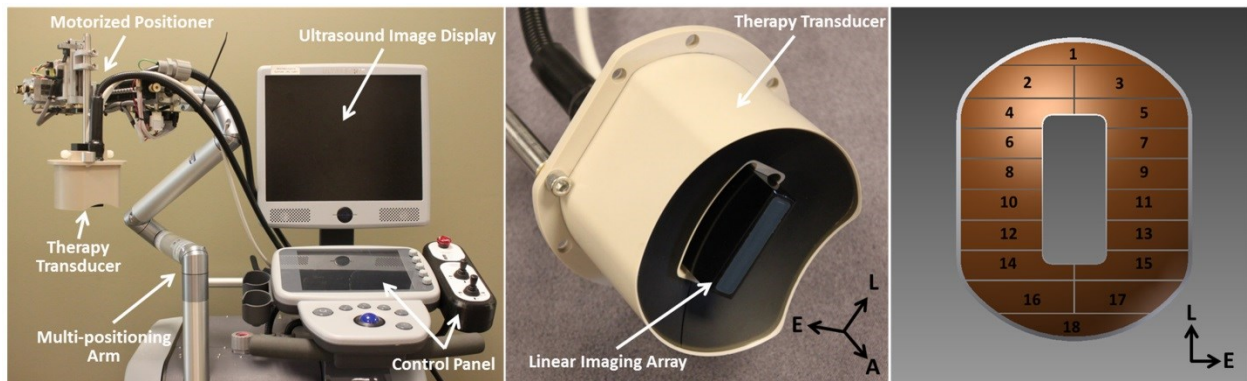
After the 7-day incubation, the clot shrank and translucent serum was separated from the clot (**Figure 5.3**). The degree of clot retraction was quantified by measuring the serum volume left after taking out the retracted clot [53]. To ensure a reasonable consistency in degree of retraction, a retracted clot was selected to use only if its serum volume was within a range from 3 to 3.2 mL. The qualified clot usually had a diameter around 6.5 mm and a length around 10 cm. The 10-cm long clot was cut into 2-cm length clots for individual experiments. Prior to each experiment, three steps were followed to place and fix the clot inside the vessel phantom. First, the clot was warmed up to 38.6 °C in fresh bovine blood. Second, the bovine blood with the clot inside was stimulated by calcium chloride with a final concentration of 20 mM/L. Third, the clot with the stimulated blood coating was inserted into the vessel phantom from the 6.5 mm inner-

diameter side all the way to the stenosis side. The vessel phantom was then placed in a water bath at 38.6 °C, and after 2 hours the blood coating clotted and cross-linked the retracted clot to the interior of the vessel phantom like glue. The vessel phantom with the clot fixed inside was then connected in-line with the rest of the flow model and the connecting tubes were refilled with saline.

### 5.2.3 Therapy System

An integrated, portable, ultrasound image-guided microthrombolysis system was developed in our laboratory (**Figure 5.4**). It includes three subsystems: a microthrombolysis therapy system, an ultrasound imaging system, and a positioning system. The microthrombolysis therapy subsystem used a 1-MHz 18-element therapy transducer manufactured by Imasonic S.A. (Besancon, France) (Figure 5.4). The transducer had an effective 9.8 cm (lateral) x 8 cm (elevational) aperture and a 7 cm focal length. It was driven by a pulse amplifier developed in-house to generate very short ( $< 2$  cycles), high-pressure ultrasound pulses. The focal beam volume ( $-6$  dB) of the transducer was measured to be 6.5 mm (axial) x 1.3 mm (lateral) x 1.5 mm (elevational) at a peak negative pressure of 15 MPa using a fiber-optic probe hydrophone (FOPH) [54]. Peak negative pressures larger than 20 MPa cannot be directly measured and therefore was estimated by linear summation ( $P(-)_{LS}$ ) of the peak negative pressure outputs from 3 separate groups of the transducer elements (6 elements per group). The imaging subsystem was developed based on an Ultrasonix imaging machine (SonixTouch; Analogic Ultrasound, Vancouver, Canada). A custom ultrasound imaging probe with compact rectangular housing (L7.5MHz; Vermon, France) was embedded into the central hole of the therapy transducer to guide and monitor microthrombolysis treatment. The positioning subsystem included a multi-positioning arm and a compact motorized positioner at the end of the arm. The therapy

transducer was mounted on the compact positioner. With 6 degrees of freedom and a range around 1 meter, the multi-positioning arm can be manually moved and held using a press/release lock for coarse target localization. With 3 degrees of freedom and a range of 10 cm x 5 cm x 4 cm, the motorized positioner was controlled by both software and joy sticks for much finer localization with a resolution of 0.1 mm. Control software was developed to manage and coordinate the therapy, imaging, and positioning subsystems.



**Figure 5.4:** The integrated microtripsy thrombolysis system is shown in the left picture. It consists of an ultrasound imaging system, a microtripsy therapy system, and a motorized positioning system. The ultrasound therapy transducer is shown in the middle. A linear imaging probe was embedded at the center of the therapy transducer. The arrangement of the 18 elements in the therapy transducer is illustrated in the right picture. (A = Axial, L = Lateral and E = Elevational)

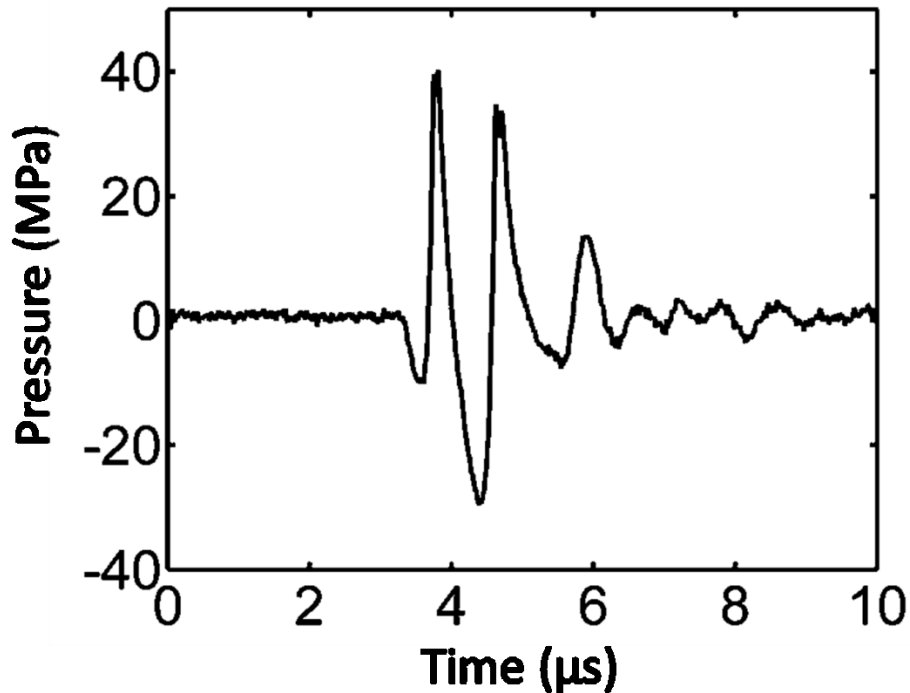
#### 5.2.4 Pre-treatment Planning

Pre-treatment planning was performed prior to each treatment. First, using the multi-positioning arm, the therapy transducer was manually placed above the vessel phantom. The lateral axis of the transducer was oriented perpendicular to the vessel phantom so that the cross section of vessel and clot were imaged during treatment. Second, cavitation was generated in water, and the center of the hyperechoic cavitation region on the ultrasound imaging window was marked as the geometric focus of the transducer. Third, guided by ultrasound imaging, the therapy transducer was moved using the motorized positioner to align the geometric focus at the center of vessel lumen. The transducer was then moved to scan the focus from one end of the

clot (close to the pressure reservoir) to the other end (close to the stenosis side). Several locations (spaced around 3 mm) along the scan path were recorded. Fourth, after these locations registered, the control software linearly interpolated these key locations into a scan path of denser treatment locations with a fixed scan interval (SI).

### **5.2.5 Treatment Strategies**

For each treatment, the treatment zone was scanned following the preset treatment path. The therapy system applied a fixed number of microtripsy pulses (doses) at each scan location before moving automatically to the next location. A 1.5-cycle pulse with only one high negative pressure phase and an estimated peak negative pressure ( $P(-)_{LS}$ ) of 30 MPa was used in this study, as this pressure level was shown to create precise flow channels in our previous microtripsy thrombolysis study [29]. An example waveform of microtripsy pulse is shown in **Figure 5.5**. Real-time B-mode ultrasound imaging was used to monitor microtripsy. The cavitation bubble cloud could be clearly distinguished as a bright dynamic region with ultrasound imaging. The ultrasound therapy transducer was moved by step motors to scan the cavitation bubble cloud along the preset treatment path. If the cavitation cloud was slightly off the center of the vessel lumen during the treatment scan according to the real-time ultrasound B-mode image, the location of cavitation bubble cloud was finely adjusted using joysticks to move it back to the center of the vessel lumen. Three treatment strategies were used: single-focus strategy, electronically-steered multi-focus strategy and dual-pass multi-focus strategy. In the following text, they are termed “single-focus”, “multi-focus” and “dual-pass” for short. A pulse repetition frequency (PRF) of 100 Hz was used in all the three strategies, and therefore the energies delivered per second by the three strategies were the same.



**Figure 5.5:** Pressure waveform of a microtripsy pulse. Because peak negative pressure larger than 20 MPa cannot be directly measured, this waveform was estimated by linearly summing the directly-measured waveforms from 6 separate element groups (3 adjacent elements per group) and the peak negative pressure was 36 MPa.

The single-focus strategy has been used in all the previous microtripsy thrombolysis studies [29, 30]. At each scan location, the treatment zone was only covered by the geometric focus of the therapy transducer (**Figure 5.6**). Five groups were treated using the single-focus strategy: four of them used different doses (100, 200, 600, and 1000 pulses) per scan location with a scan interval of 0.3 mm; the other group used a dose of 500 pulses with a scan interval of 0.15 mm. Four clots were treated in each group. The treatment time of each group can be calculated based on the PRF, dose, and scan interval used. The treatment group with the smaller SI (0.15 mm) and the 500-pulse dose was included in this study to see if a finer scan interval can improve the treatment efficacy compared to the groups with the same treatment time. **Table 5.1** summarizes the parameters used for all treatment groups.

Using the multi-focus strategy, the treatment zone at each scan location was covered with multiple foci by electronically steering the focus of the therapy transducer in the lateral direction (**Figure 5.6**). This multiple foci strategy was expected to widen the generated flow channel. The steering of the focus alternatively at different treatment foci was also designed to reduce cavitation memory effects at each treatment focus to increase the clot fractionation rate per pulse. The previous study shows that residual nuclei from the previous pulse at the same or nearby location can last for a few hundred milliseconds (cavitation memory effects) and may negatively impact the treatment efficacy when the subsequent pulse arrived before the residual nuclei dissolve [55]. Two groups were treated using this strategy: one with 3 treatment foci at each scan location and one with 5 treatment foci. A dose of 200 pulses, a scan interval of 0.3 mm and a separation of 0.5 mm between foci were used for both groups. The dose was defined as the number of microtripsy pulses applied at each treatment focus. The treatment times of the 3 foci and 5 foci multi-focus treatments were the same as those of the single-focus 600-pulse (3.3 min/cm) and 1000-pulse (5.5 min/cm) treatments, respectively. Four clots were treated in each group.

The dual-pass strategy essentially divided the multi-focus treatment into two treatment passes. The dual-pass strategy was developed to further address the concern of the cavitation memory effects. In the first pass, the treatment zone was scanned through the clot and covered by one focus or two foci at each scan location. In the second pass, the treatment zone was scanned through the clot again and covered by two or three additional foci, resulting in effective three or five foci treated at each scan location, respectively (termed “1+2” or “2+3” patterns) (**Figure 5.6**). The foci treated at each scan location within one pass were separated by 1 mm in the lateral direction without any overlapping of the cavitation zones between foci. The same treatment path



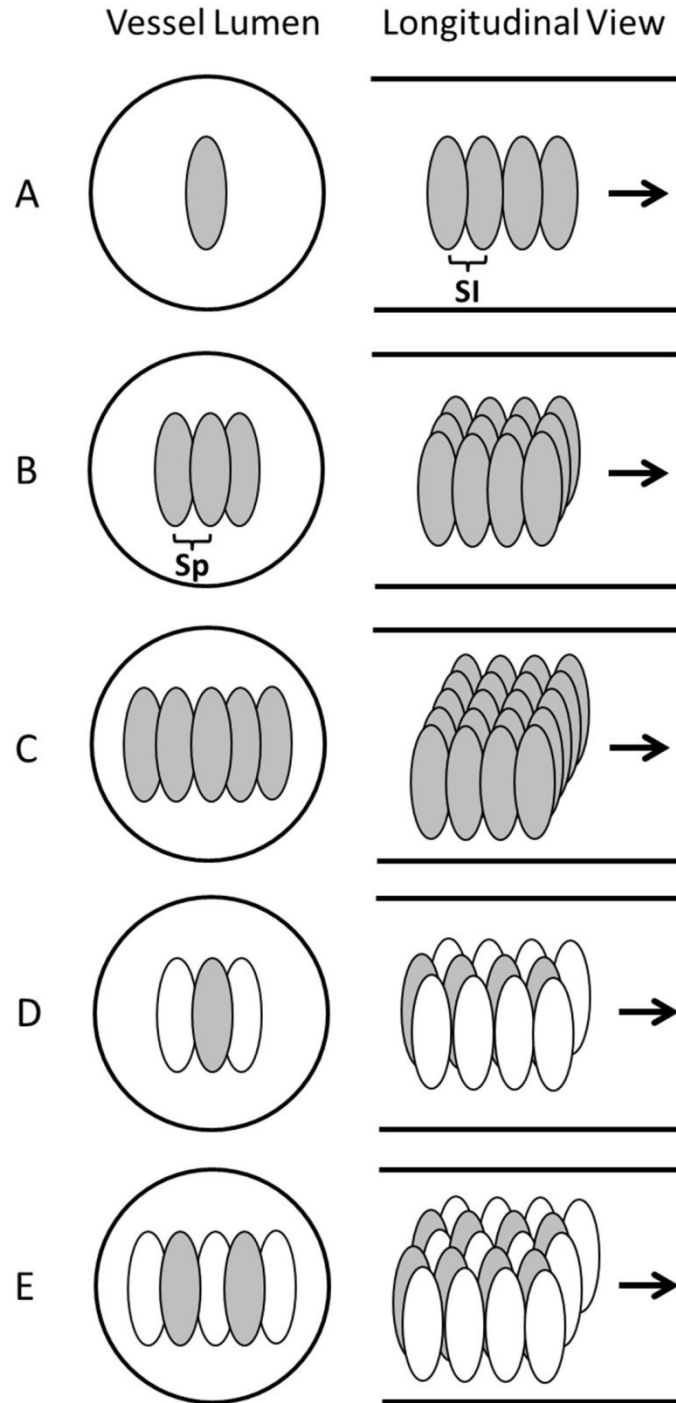
was used for both passes but in the second pass the scan locations were shifted 0.15 mm along the length of the clot. A dose of 200 pulses, a scan interval of 0.3 mm, and a separation of 0.5 mm between the closest foci were used for both 1+2 foci and 2+3 foci dual-pass treatments. Because the motorized movement of the therapy transducer from one end of the clot to the other was very fast, the treatment times of the 1+2 foci and 2+3 foci dual-pass treatments were almost the same as the 3 foci (3.3 min/cm) and 5 foci (5.5 min/cm) multi-focus treatments. Four clots were treated in each group.

**Table 5.1: Treatment Plan**

<b>Group</b>	<b>Strategy</b>	<b># of Foci</b>	<b>PRF (Hz)</b>	<b>Dose (# of pulses)</b>	<b>SI (mm)</b>	<b>Focal Separation (mm)</b>	<b>Treatment Time (min/cm)</b>
<b>1</b>	<b>Single-focus</b>	1	100	100	0.3	/	0.55
<b>2</b>		1	100	200	0.3	/	1.1
<b>3</b>		1	100	600	0.3	/	3.3
<b>4</b>		1	100	1000	0.3	/	5.5
<b>5</b>		1	100	500	0.15	/	5.5
<b>6</b>	<b>Multi-focus</b>	3	100*	200**	0.3	0.5	3.3
<b>7</b>		5	100*	200**	0.3	0.5	5.5
<b>8</b>	<b>Dual-pass</b>	1+2	100*	200**	0.3	0.5	3.3
<b>9</b>		2+3	100*	200**	0.3	0.5	5.5

\* Frequency from pulse to pulse.

\*\* Pulses per focus per treatment location.



**Figure 5.6:** Schematic diagrams of the three treatment strategies in the vessel phantom, with the solid lines outlined the inner vessel lumen. The ellipses in the vessel lumen represent the treatment foci. A illustrates the single-focus strategy. B and C illustrate the 3 foci and 5 foci multi-focus strategies, respectively. D and E illustrate the 1+2 foci and 2+3 foci dual-pass strategies, respectively. In D and E, the gray foci were treated in the first treatment pass and the white foci were treated in the second treatment pass. (SI = Scan Interval, Sp = Separation between foci).

### **5.2.6 Elasticity and Porosity Measurements**

The elasticity of the retracted clots was characterized to estimate its equivalent age *in vivo* and to compare with that of unretracted clots. A direct mechanical measurement method, previously described in detail by Xie [56], was adopted in this study to measure the Young's modulus of retracted and unretracted clots. The measurements were conducted using a desktop device named MicroElastometer (Artann Laboratories, Lambertville, NJ, USA), which measures the displacement vs. force while a test sample is subject to compression, and the Young's modulus of the sample is estimated based on the strain-stress relationship. The device consists of a step motor, a compression stamp, a sample plate, and a strain gauge. The step motor controls the compression stamp moving in the direction normal to the sample plate, and the compression force is measured by the strain gauge under the sample plate. The minimum travel distance of the stamp is 3  $\mu\text{m}$  and the measurable force range is up to 2 N with a precision of 0.1 mN. Before measurement, the retracted clot was warmed up to room temperature (25 °C) after it was stored in 4 °C for 7 days and cut into 2 cm cylindrical samples ( $\sim$  6.5 mm diameter) for the elastic measurements. The axis of the cylindrical sample was positioned perpendicularly to the long side of the stamp. During measurement, the position of the stamp and the force reading was recorded in real-time by its software, and the Young's modulus was estimated right after the measurement. The detailed algorithm and calculation can be found in the paper by Xie [56]. The unretracted clots were prepared following the method described previously [29], and their elasticity were measured using the same protocol as the retracted clots. Ten samples were measured for each clot type. Qualitative and quantitative histological evaluations on porosity (4 samples for each clot type) were conducted following the protocol described by Sutton *et al.* [40].

### **5.2.7 Flow Channel Measurement**

To quantitatively evaluate the flow channels generated using the different microtripsy strategies, each treated clot was scanned using a 20 MHz high-resolution ultrasound probe. The probe was separately mounted onto the motorized positioner before scanning. With the imaging plane perpendicular to the vessel axis, the probe was moved by the positioner from one end to the other end of the clot with a step size of 0.1 mm. One cross-sectional image of the clot was taken after waiting for 2 seconds at each location to allow for image stabilization. 200 scan images were collected in total from each treated clot. Because the fractionated clot region was hypoechoic (low brightness on image) when the flow was restored, in comparison to the hyperechoic (high brightness on image) intact clot region, we applied an intensity threshold to detect the cross section of flow channel on each scan image. Inside the vessel lumen on each scan image, the area with pixel intensity less than 20 (0-255 overall range) was thresholded out as the cross section of the flow channel. The value of 20 was selected according to the intensity histogram of the scan images. To quantify the size of flow channel, the cross-sectional area ( $A_{\text{cross}}$ ) of the flow channel region was calculated.

### **5.2.8 Restored Flow Measurement**

Restored flow rate was measured to evaluate the recanalization effectiveness using the different treatment strategies. After the flow channel was created, the volume of downstream saline in the fluid collector within 1 minute was measured. When the flow was very slow, the restored saline was collected for 5 minutes. The restored volume flow rate was then calculated as the volume of the saline collected divided by the time. Due to the brevity of the time period and the small change in reservoir volume, the pressure was assumed to be constant over this time period. A control measurement with no blockage in the flow system was also conducted to compare with the restored flow rate.

### 5.2.9 Debris Measurement

A method combining macroscopic inspection and Coulter counter analysis was utilized to measure clot debris particle size distribution generated during the treatments. When flow was restored, clot debris was flushed by the restored flow and filtered by a filter sheet with a pore size of 300  $\mu\text{m}$ . Macroscopic inspection was conducted to check for debris particles that may have been trapped on the 300  $\mu\text{m}$  filter. Optical images with a resolution of 20  $\mu\text{m}$  were taken of the filter sheet. The number of distinguishable particles larger than 300  $\mu\text{m}$  was counted and the sizes of individual large debris particles were measured. The filtered fluid with suspended debris particles smaller than 300  $\mu\text{m}$  was then analyzed using a Coulter counter (Multisizer 3; Beckman Coulter, Brea, CA, USA). The measurable range of particles was from 3 to 60  $\mu\text{m}$  using a 100- $\mu\text{m}$  aperture tube and from 60 to 300  $\mu\text{m}$  using a 560- $\mu\text{m}$  aperture tube [57]. The measurements using these two aperture tubes were combined to generate a distribution of debris particles from 3 to 300  $\mu\text{m}$ .

## 5.3 Results

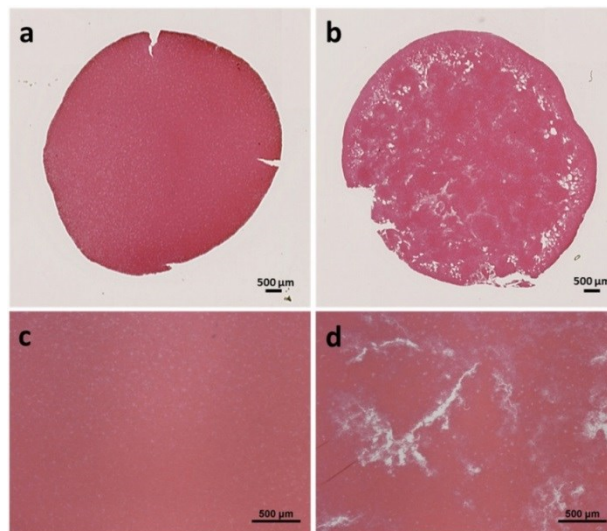
### 5.3.1 Elasticity and Porosity of Retracted and Unretracted Clot

One representative retracted clot after the 7-day incubation is shown in **Figure 5.7**. The unretracted clots and the retracted clots were measured to have Young's moduli of  $2.31 \pm 2.05$  kPa ( $N = 10$ ) and  $11.12 \pm 1.41$  kPa ( $N = 10$ ), respectively. The retracted clots had a much higher stiffness than the unretracted ones. The Young's moduli of clots at different ages in a rat model were measured *ex vivo* using the same mechanical method by Xie [56]. According to their results, the Young's modulus of the retracted clots measured in this study fell between those of the 3-day-old *in vivo* clots ( $9.46 \pm 0.87$  kPa) and the 6-day-old *in vivo* clots ( $17.40 \pm 5.77$  kPa) in the rats, which is when it was expected for the clots to transition from acute phase to chronic

phase. This is similar to human clots of 2 weeks of age [56]. Histology sections showed consistent difference in porosity between the two clot types, similar to those reported by Sutton (Figure 5.8). Intracellular spacing in retracted clots and unretracted clots were measured to be  $0.23 \pm 0.20 \%$  and  $3.31 \pm 1.06 \%$ , respectively. Significant difference was shown by one-sided t-test ( $P < 0.01$ ). The porosity of the retracted clots in this study was lower than what was reported by Sutton *et al.*, indicating that these clots were even more retracted.



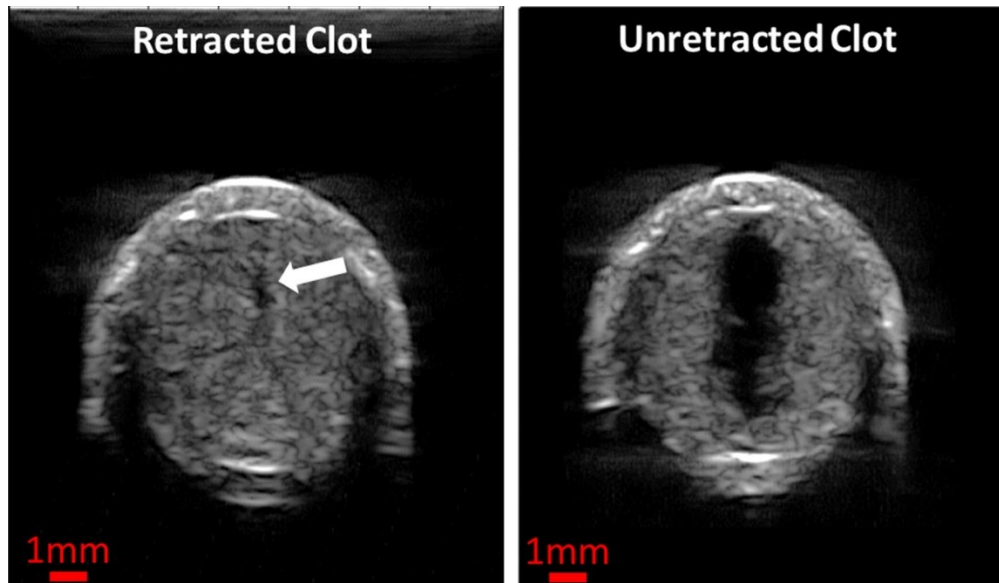
**Figure 5.7:** One long retracted clot separated from the serum before being cut into 2-cm segments.



**Figure 5.8:** Representative histology sections of retracted (left) and unretracted (right) clots showing a cross section (a, b) and 4x magnification (c, d). Stain: Hematoxylin and Eosin.

### 5.3.2 Comparison with Unretracted Clot

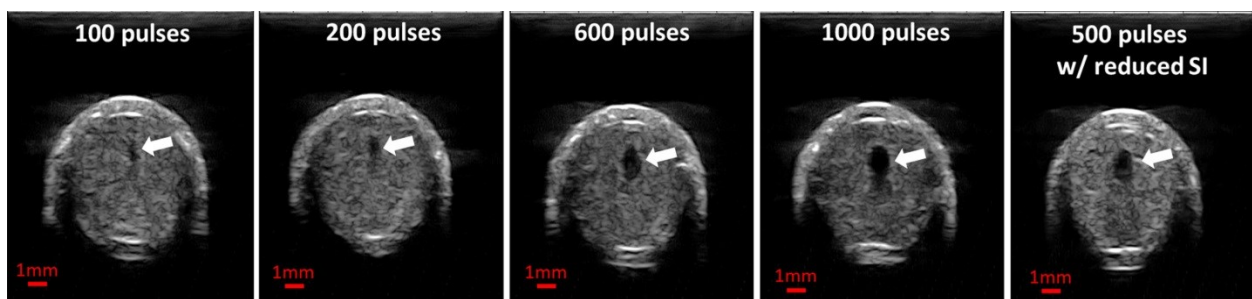
Microtripsy was effective in treating retracted clots, but the flow channel generated using a single-focus method was significantly smaller than the flow channel formed through unretracted clots. A flow channel was generated through the retracted clot using the single-focus strategy even with a 100-pulse dose. **Figure 5.9** shows the representative cross-sectional ultrasound images of a treated, retracted clot in this study on the left and a treated, unretracted clot from a previous study on the right [30]. The unretracted clots were treated using exactly the same treatment parameters as the 100-pulse single-focus treatment used on the retracted clots. The channels generated in the retracted clots were very small and hard to see from the high-resolution ultrasound scan images, whereas the channels in unretracted clots were large and clear. The mean  $A_{\text{cross}}$  of the channels generated in the retracted clots was  $0.0232 \pm 0.0506 \text{ mm}^2$  ( $N = 4 \times 200$ ), which was about 200 times smaller than that in the unretracted clots ( $4.6532 \pm 0.7761 \text{ mm}^2$ ,  $N = 6 \times 67$ ).



**Figure 5.9:** Representative ultrasound images of the cross sections of the flow channels generated using the single-focus strategy in one unretracted clot (left) and one retracted clot (right). The exact same treatment parameters (30 MPa P(-)LS , 0.3 mm Scan Interval and 100 pulses per treatment location) were used in both cases. The generated flow channels show as the hypoechoic zones inside clots (indicated by the block arrow in the left image). Therapeutic ultrasound propagated from the top to the bottom of the images.

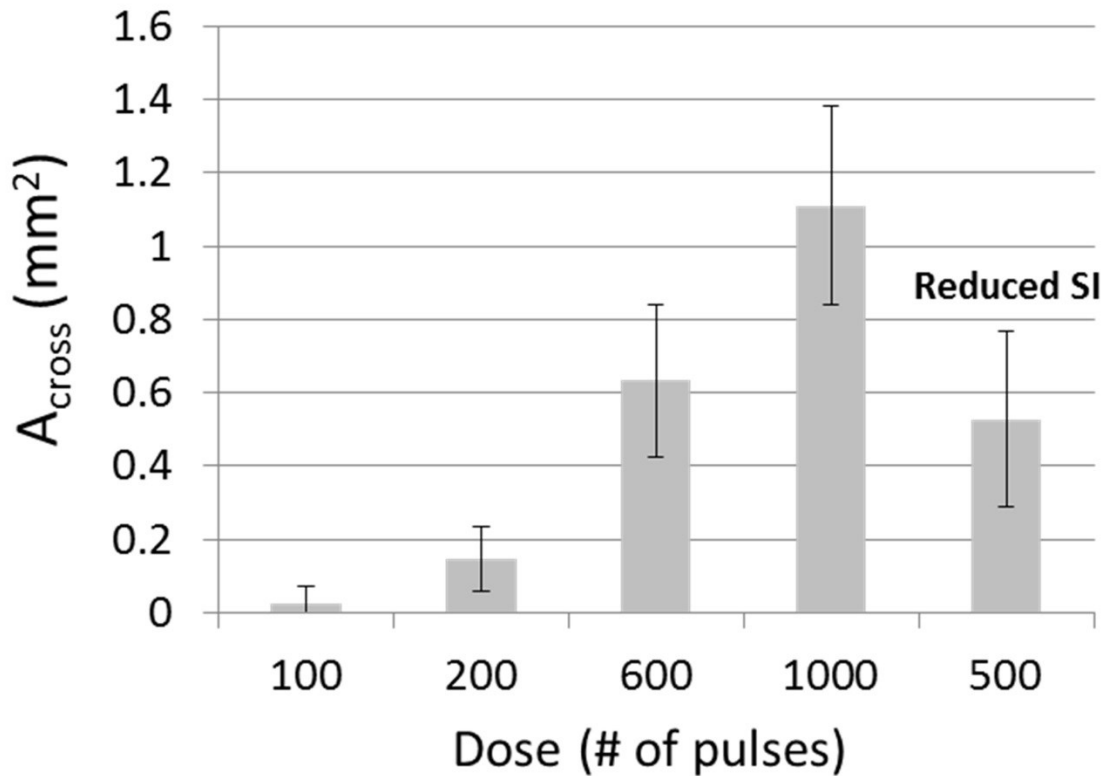
### 5.3.3 Single-focus Treatments

Using the single-focus strategy, a flow channel was successfully generated through retracted clots with all the microtripsy parameters tested. The size of the flow channel increased with increasing dose. The representative scan images of the channels generated by the five treatment groups using the single-focus strategy are shown in **Figure 5.10**. As the dose increased from 100 to 1000 pulses, the channels generated using the same 0.3-mm SI became larger (first four images), and the mean  $A_{\text{cross}}$  of the channels increased from 0.02 to 1.11 mm<sup>2</sup> (**Figure 5.11**). The shape and boundary of the channels became clearer and sharper with the higher doses. The last image of **Figure 5.10** shows a representative channel generated using the smaller 0.15-mm SI and the 500-pulse dose. The channels generated using the 1000-pulse dose and 0.3-mm SI were the largest among the single-focus treatments but the size was still small ( $1.1099 \pm 0.2721$  mm<sup>2</sup>) compared to the 6.5-mm inner-diameter vessel lumen. The  $A_{\text{cross}}$  of channels using the 0.15-mm SI and the 500-pulse dose ( $0.5269 \pm 0.2391$  mm<sup>2</sup>) were only half of those using the 0.3-mm SI and the 1000-pulse dose. This indicates that reducing SI does not improve the treatment efficacy under the same treatment time.



**Figure 5.10:** Representative ultrasound images of the cross sections of the flow channels generated using the single-focus strategy with different doses. The last image shows the flow channel generated with a reduced scan interval (0.15 mm). The generated flow channels show as the hypoechoic zones inside clots (block arrows). Therapeutic ultrasound propagated from the top to the bottom of the images.





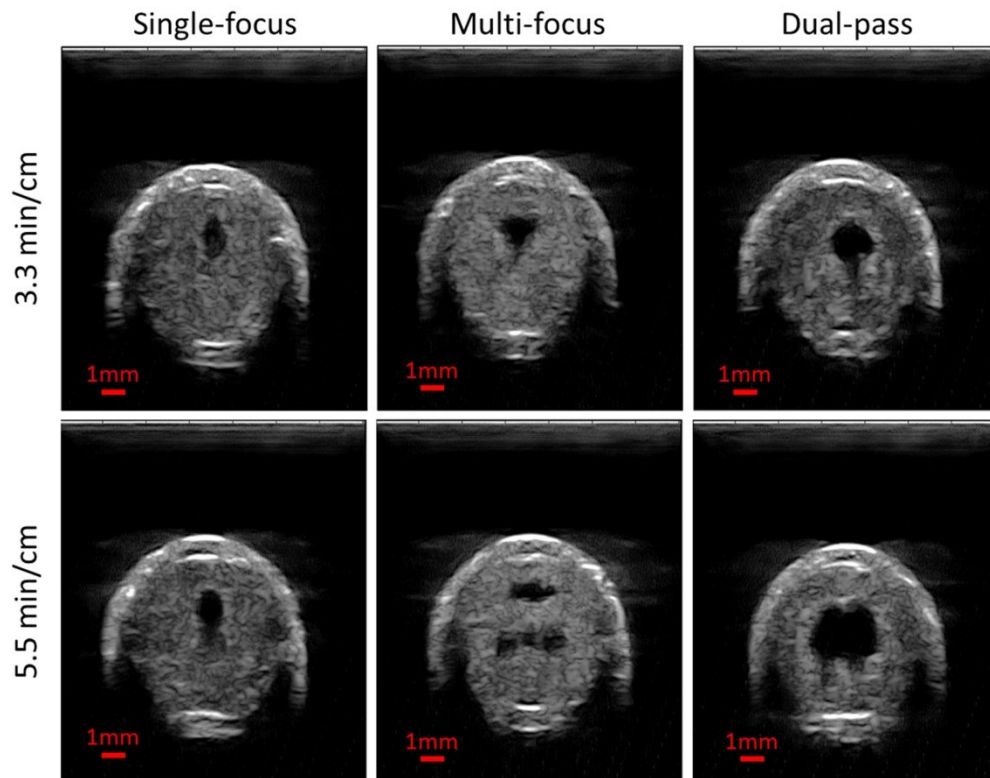
**Figure 5.11:** The mean cross-sectional area ( $A_{\text{cross}}$ ) of the flow channels generated using the single-focus strategy with different doses. The last bar shows the flow channel generated with a reduced scan interval (SI = 0.15 mm). (N = 4 × 200).

### 5.3.4 Comparison of Three Strategies

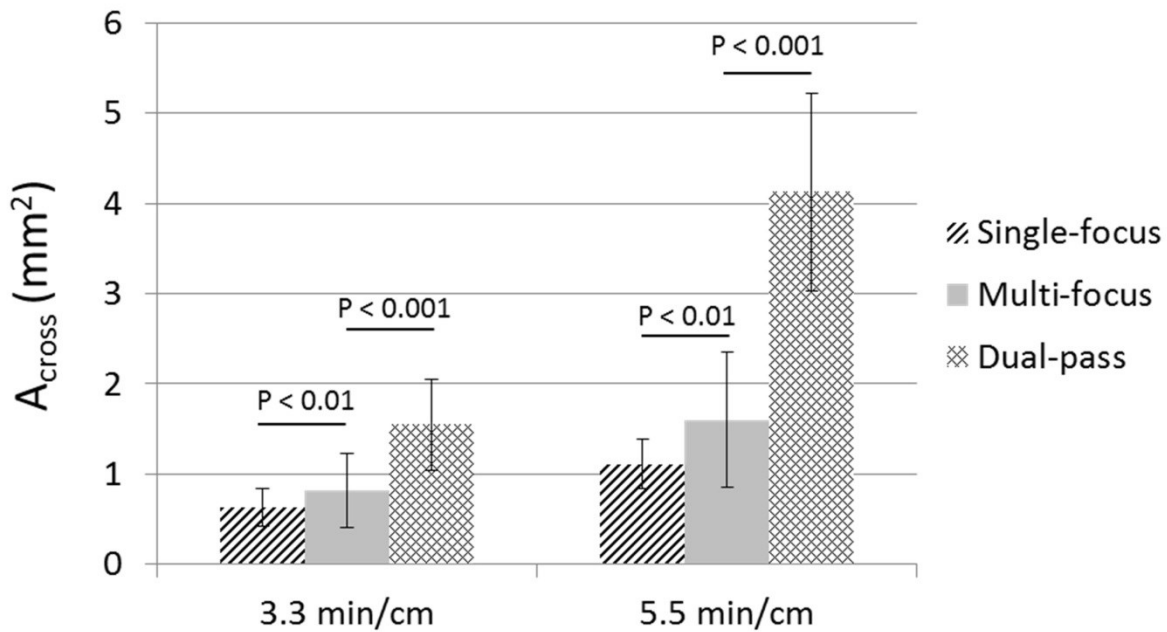
A flow channel was generated through retracted clots using all three strategies tested (**Figure 5.12**). Under the same treatment time, microtripsy thrombolysis generated the largest flow channels using the dual-pass strategy and the smallest channels using the single-focus strategy. When comparing the single-focus strategy to the multi-focus strategy, the channel size was increased by 30% under the same 3.3 min/cm treatment time from  $0.63 \pm 0.21 \text{ mm}^2$  to  $0.82 \pm 0.41 \text{ mm}^2$ , and the increase was 44% under the same 5.5 min/cm treatment time from  $1.11 \pm 0.27 \text{ mm}^2$  to  $1.60 \pm 0.75 \text{ mm}^2$  (**Figure 5.13**). When comparing the multi-focus strategy to the dual-pass strategy, the channel size was increased by 90% under the same 3.3 min/cm treatment time from  $0.82 \pm 0.41 \text{ mm}^2$  to  $1.55 \pm 0.50 \text{ mm}^2$ , and under the same 5.5 min/cm treatment time the channel size increased by 160% from  $1.60 \pm 0.75 \text{ mm}^2$  to  $4.13 \pm 1.09 \text{ mm}^2$ . Statistical

analyses (one-sided Student's t-test) also supported these significant increases of channel size generated using the multi-focus vs. single-focus ( $P < 0.01$ ) and dual-pass vs. multi-focus strategy ( $P < 0.001$ ).

The shapes of the generated flow channels using the three strategies varied. Elliptical-shaped channels were generated using the single-focus strategy. The channels generated using the multi-focus strategy appeared to have two separate lesions with a horizontal orientation, as shown in **Figure 5.12**. When using the dual-pass treatment strategy, the channels had a more circular shape than those generated using the other two treatment strategies. With the 1+2 foci dual-pass treatment, one small tail appeared at one side of the circular channel. With the 2+3 foci dual-pass treatment, two tails appeared.



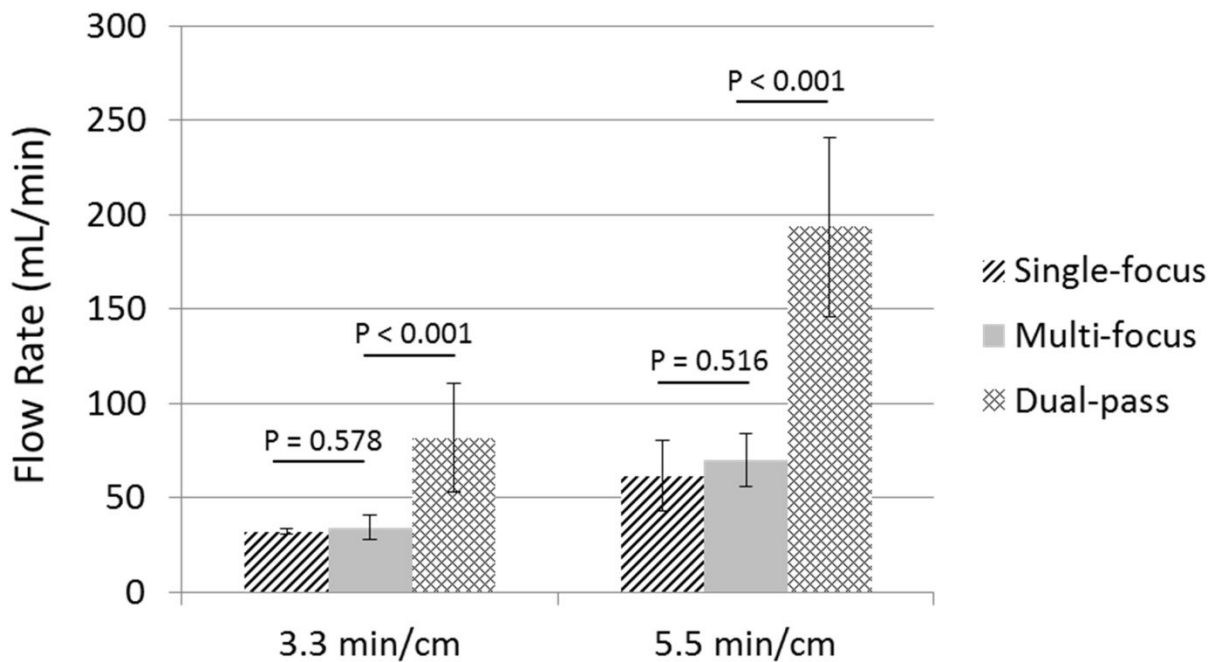
**Figure 5.12:** Representative ultrasound images of the cross sections of the flow channels generated using the single-focus strategy (left column), the multi-focus strategy (middle column) and the dual-pass strategy (right column). The treatment times were 3.3 min/cm in the upper row and 5.5 min/cm in the lower row. The generated flow channels show as the hypochoic zones inside the clot. Therapeutic ultrasound propagated from the top to the bottom of the images.



**Figure 5.13:** The mean cross-sectional area ( $A_{\text{cross}}$ ) of the flow channels generated using the three strategies under the two treatment times (3.3 min/cm and 5.5 min/cm). ( $N = 4 \times 200$ ).

### 5.3.5 Restored Flow

Prior to any treatment, no flow was observed. After each treatment, flow was successfully restored even with the smallest channel created. **Figure 5.14** shows the mean flow rate restored for the treatment groups presented in **Figure 5.12**. With constant pressure (3.7 mm Hg) applied, a larger channel would be expected to permit higher flow rate, which is confirmed by the restored channel cross-sectional area and flow rate results shown in **Figures 5.13** and **5.14**. The restored flow rate was highest when using the dual-pass strategy, while the lowest restored flow rate was generated using the single-focus strategy. The mean flow rate generated by the 2+3 foci treatments was  $193.2 \pm 47.5$  mL/min (maximum at 324 mL/min), which was much higher than the other treatment groups. As a reference, the flow model with no blockage had a flow rate of 640 mL/min under the same 3.7-mmHg pressure.

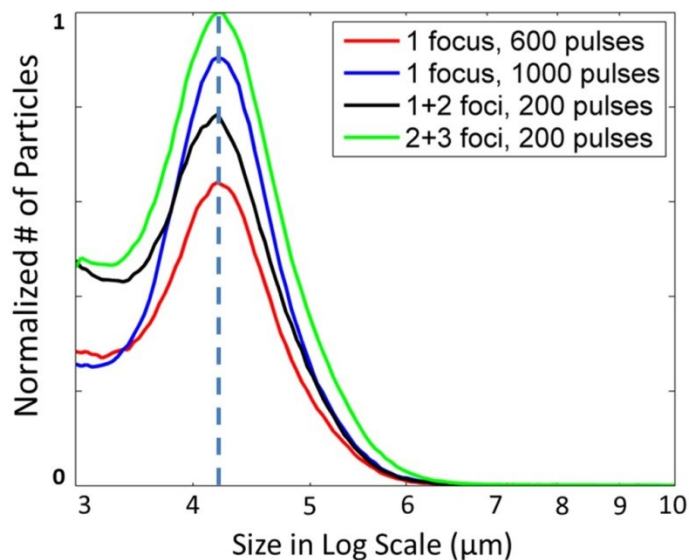


**Figure 5.14:** Restored flow rates of the three strategies under the two treatment times (3.3 min/cm and 5.5 min/cm). (N = 4).

### 5.3.6 Debris

The clot debris distribution was measured in the 600-pulse treatments, the 1000-pulse single-focus treatments, and the 1+2 foci and 2+3 foci dual-pass treatments. The debris size measurement was performed for four selected treatment groups instead of all groups due to the time-consuming nature of the measurement. The dual-pass treatment groups were selected because this strategy achieved the largest flow channel under the same treatment time (i.e., the highest treatment efficacy) among the three strategies. As a comparison and reference, the debris from the single-focus treatments under the same treatment time was measured. Theoretically, the debris generated from the single-focus treatments should be smaller than those using the other two strategies because the single-focus strategy used a three- or five-times higher dose at each treatment focus than the other two strategies, which was expected to break up the clot into smaller particles. For all measured treatments, over 99.9% of the debris particles were less than

10  $\mu\text{m}$ , and the number of debris particles became orders of magnitude less as the size increased from 10  $\mu\text{m}$  to 100  $\mu\text{m}$ . **Figure 5.15** shows the normalized mean distributions of clot debris from the four treatment groups. They all had a similar distributions centered at 4.2  $\mu\text{m}$ , and the only difference was the number of debris particles. The debris particles larger than 100  $\mu\text{m}$  generated using the two different treatment strategies were calculated and summarized in **Table 5.2**. In more than half of the treatments, no debris particles greater than 100  $\mu\text{m}$  were observed. Only one debris particle (453  $\mu\text{m}$ ) was trapped on the 300- $\mu\text{m}$  filter sheet in the total 24 measured treatments, and it was generated using the dual-pass strategy. In the treatments when particles between 100 and 300  $\mu\text{m}$  were observed, only one or two such particles were observed for each treatment. Other than the single 453  $\mu\text{m}$  particle mentioned above, the largest particle observed was 222.85  $\mu\text{m}$  when using the single-focus strategy and 189.75  $\mu\text{m}$  when using the dual-pass strategy.



**Figure 5.15:** The mean distributions of debris particles (3 to 10  $\mu\text{m}$ ) generated using the single-focus and dual-pass strategies ( $N = 4 \times 9$ ). The volumes of the fluids collected from the restored flows were recorded in all the treatments. And the volumes used for Coulter Counter measurements were recorded as well. With this information, the number of the debris particles was first converted to unit volume (mL) for each treatment. Then the mean distributions for each treatment strategy were calculated and normalized by the maximal peak among the mean distributions.

**Table 5.2:** Summary of the generated debris larger than 100  $\mu\text{m}$  using the single-focus and dual-pass strategies

	Single-focus Treatments	Dual-pass Treatments
Treatments with particles $>100 \mu\text{m}$	3 out of 8	4 out of 8
Average No. of particles $>100 \mu\text{m}$	1.67	1.1
Average Size of particles between 100 and 300 $\mu\text{m}$	117.57 $\mu\text{m}$	125.72 $\mu\text{m}$
Maximal Particle Size $<300 \mu\text{m}$	222.85 $\mu\text{m}$	189.75 $\mu\text{m}$
Particles $>300 \mu\text{m}$	None	1 (453 $\mu\text{m}$ )

## 5.4 Discussion

Drug-based thrombolysis methods, including ultrasound-enhanced thrombolysis, have low efficacy for retracted clots or aged clots with low permeability [38-40, 43-45]. The 7-day retracted clots used in this study have Young's moduli similar to the *in vivo* 3-6 day old rat clots, which were believed to turn from acute phase to chronic phase, similar to human clots of 2 weeks of age [56]. The results from this chapter support our hypothesis that microtripsy thrombolysis remains effective for retracted clots, although the treatment efficacy is reduced. Flow channels were generated through all retracted clots when treated using microtripsy and restored flows were consistently observed. The reduced treatment efficacy of microtripsy thrombolysis matched the observations of a previous study by Vlasisavljevich *et al.*, which showed decreased or no histotripsy fractionation for tissues of increased mechanical strength [46]. Vlasisavljevich's study also showed that increasing tissue stiffness results in a significant decrease in cavitation bubble expansion, leading to reduced strain to tissue and increased resistance to histotripsy-induced tissue damage [47]. Our elasticity measurement indicates a 5-times higher Young's modulus for retracted clots compared to unretracted clots. In addition, the

retracted clots have a denser fibrin structure and less water, which increases the time needed for microtripsy to completely fractionate the increased number of fibrin fibers per unit volume.

The results from the multi-focus and dual-pass treatments support the hypothesis that the microtripsy thrombolysis treatment efficacy for retracted clot can be enhanced by electronic focal steering. The multi-focus treatments showed a statistically significant improvement in channel size from the single-focus treatments. With the electronic focal steering, the treatment zone was covered by multiple cavitation foci. A wider flow channel and less required dose per focus were achieved by using the multi-foci strategy. From **Table 5.3**, we can see that the actual widths of channels generated by the multi-focus treatments matched closely with what we expected for both 3 foci and 5 foci cases. For example, with 5 foci side-by-side separated by 0.5 mm and each focus treated with 200 pulses, the flow channel generated by the multi-focus strategy was expected to be 2.45 mm in width (channel width of the 200-pulse single-focus strategy plus 4 times 0.5 mm separation, see Reference in **Table 5.3**). The actual width of the flow channels generated by the 5 foci multi-focus treatments was 2.41 mm, similar to the expected channel width. In comparison, the flow channel generated by the 1000-pulse single-focus strategy was only 1.11 mm wide. The height of the channel generated by multi-focus strategy was 2.00 mm, compared to 1.83 mm channel height generated by the 1000-pulse single-focus strategy. However in some treatments, two separate lesions were generated by the multi-focus strategy. The efficacy of the multi-focus strategy was lowered by this two-lesion pattern. Cavitation memory effects may be associated with the two-lesion pattern. As microtripsy pulses were applied with a 100 Hz PRF, a subsequent pulse arrived before the complete dissolution of the residual bubble nuclei from the previous cavitation. The cavitation bubble cloud generated at the proximal side of the focal region might prevent the incident acoustic energy from delivering

to the zone right below the proximal cavitation site, forming two discontinuous cavitation clouds separated by a “dead” zone resulting in two separate lesions.

**Table 5.3:** Flow channel width and height

	3 Foci			5 Foci		
	Expected*	Multi-focus	Dual-pass	Expected **	Multi-focus	Dual-pass
Channel Width	1.45 ± 0.21	1.39 ± 0.30	1.59 ± 0.32	2.45 ± 0.21	2.41 ± 0.39	2.78 ± 0.32
Channel Height	1.36 ± 0.24	1.66 ± 0.37	2.68 ± 0.36	1.83 ± 0.23	2.00 ± 0.40	2.63 ± 0.34

\* For 3 foci, expected channel width = channel width by 200-pulse single-focus treatments (0.45 mm) + 2 × foci separation (0.5 mm); and expected channel height = channel width by 600-pulse single-focus treatments (1.36 mm).

\*\* For 5 foci, expected channel height = channel height by 200-pulse single-focus treatments (0.45 mm) + 4 × foci separation (0.5 mm); and expected channel height = channel height by 1000-pulse single-focus treatments (1.83 mm).

To further reduce the cavitation memory effects and eliminate the two-lesion pattern encountered in the multi-focus strategy, a dual-pass multi-focus strategy was investigated. With a larger effective separation (1 mm vs. 0.5 mm in the multi-focus strategy) between the steered foci within one treatment pass, the influence of the residual nuclei from the previous focus on the subsequent steered focus was reduced, which, in turn, helps fractionate the dead zone between the two lesions observed in the multi-focus treatments. In addition to reducing the cavitation memory effects, we hypothesize that the key to the dual-pass strategy is that the first treatment pass created “pilot” holes for the second pass. The pilot holes provided empty space and tissue-fluid interfaces for the cavitation in the second pass, and, therefore, resulted in more active cavitation bubble expansions, complete fractionation of the dead zone, and higher fractionation efficacy. The results show that the dual-pass treatments achieved the best thrombolysis outcomes among the three strategies under the same treatment time. The actual widths of channels generated by the dual-pass treatments were even larger than the expected channel width based on the focal separation and size of the lesion generated by the single-focus strategy and those generated by the multi-focus treatments. The mean  $A_{\text{cross}}$  of flow channel generated by the 2+3



foci dual-pass strategy was over two times larger than that by the 5 foci multi-focus strategy, and over three times larger than that by the 1000-pulse single-focus strategy.

The results in this chapter suggest that the dual-pass microtripsy thrombolysis could be an effective treatment option for *in vivo* chronic, retracted clots and possibly for other dense tissues, as the retracted clot is a good model for the chronic clot. Using this advanced treatment strategy, the *in vitro* retracted clots were recanalized successfully with a larger opening. Compared with the other two treatment strategies, the dual-pass treatments achieved much larger openings with the same treatment time. The treatment speed of our noninvasive microtripsy approach is faster compared to current thrombolysis approaches. The current clinical thrombolysis approaches include systemic thrombolytic drug infusion, catheter-directed thrombolysis (CDT), and percutaneous mechanical thrombectomy (PMT). The thrombolytic drug infusion and CDT treatments take from 24 to 56 hours [58, 59] and some PMT treatments can be done within 1 to 3 hours [60]. For our approach, a retracted clot (chronic >14 days) with a length of 10 cm [61] can be treated within 55 min. The treatment can be faster for unretracted clots (acute < 14days) [29] and with parameter optimization for retracted clots.

The debris particles generated from the dual-pass treatments were within the safe range and showed no significant difference from those of the single-focus treatments. The largest particle observed overall was 453  $\mu\text{m}$ . In mechanical thrombectomy procedures, clot particles up to 1000  $\mu\text{m}$  are generated and no severe embolism has been reported from human studies [62-64]. In addition, according to the morphometry of the pulmonary arterial system reported by Singhal *et al.* [65], 500- $\mu\text{m}$ -level particles may only obstruct one arteriole of order 9 which supplies only 0.016% of total capillary beds. The total number of debris particles larger than 100

$\mu\text{m}$  from one dual-pass treatment was less than 20, which would not be expected to cause massive pulmonary embolism.

This chapter shows that microtripsy is effective for retracted clots and that electrical steering can enhance the treatment efficacy. Exploration of the effects of changing acoustic parameters, particularly PRF and pressure, is needed to further improve microtripsy thrombolysis. These parameters were not tested in this paper because our current setup limits the range of PRF and pressure for testing. Future work will be conducted in this direction to further improve the treatment efficacy. For example, increasing the treatment PRF has the potential to further shorten the treatment time under the same treatment dose if the cavitation memory effects can be reduced. Cavitation residual nuclei can be consolidated to reduce cavitation memory effects by interweaving low pressure ultrasound pulses with histotripsy pulses [66]. Another possible investigation to further reduce cavitation memory effects would be to divide the treatment into more than two treatment passes. Increasing the peak negative pressure can enlarge the lesion size [29, 36, 47] and will be investigated with microtripsy.

## **5.5 Conclusion**

After each treatment, regardless of the treatment strategy, a flow channel was successfully generated through the retracted clot and flow was restored. Although the treatment efficacy of the single-focus treatment on retracted clot was reduced, both the multi-focus and the dual-pass treatments incorporating the electronic focal steering showed significant improvements in recanalized channel size when compared to the single-focus treatments. Under the 5.5 min/cm treatment time, the channels generated by the single-focus, multi-focus, and dual-pass treatment had cross-sectional areas of  $1.11 \pm 0.27 \text{ mm}^2$ ,  $1.60 \pm 0.75 \text{ mm}^2$ , and  $4.13 \pm 1.09 \text{ mm}^2$ , respectively. The restored flow rate for the dual-pass treatment was  $193.25 \pm 47.51 \text{ mL/min}$

(max 324 mL/min). The debris generated during the dual-pass treatments remained within a safe range. The results in this chapter show the potential of microtripsy thrombolysis for retracted clot recanalization with the enhancement of electronic focal steering and dual-pass strategy. Due to the much larger flow channels generated with no extra treatment time, the dual-pass treatments were shown to be the most clinically practical and effective among the three strategies.

## 5.6 References

- [1] X. Zhang, *et al.*, "Histotripsy Thrombolysis on Retracted Clots," *Ultrasound in medicine & biology*, 2016.
- [2] D. Mozaffarian, *et al.*, "Heart disease and stroke statistics-2015 update: a report from the american heart association," *Circulation*, vol. 131, p. e29, 2015.
- [3] M. G. Beckman, *et al.*, "Venous thromboembolism: a public health concern," *American journal of preventive medicine*, vol. 38, pp. S495-S501, 2010.
- [4] H. P. Adams, *et al.*, "Guidelines for thrombolytic therapy for acute stroke: a supplement to the guidelines for the management of patients with acute ischemic stroke a statement for healthcare professionals from a special writing group of the stroke council, American heart association," *Circulation*, vol. 94, pp. 1167-1174, 1996.
- [5] S. M. Bates and J. S. Ginsberg, "Treatment of deep-vein thrombosis," *New England Journal of Medicine*, vol. 351, pp. 268-277, 2004.
- [6] H. S. Friedman, *et al.*, "Tissue plasminogen activator for acute ischemic stroke," *N Engl J Med*, vol. 334, p. 1405, 1996.
- [7] M. N. Lauw and H. R. Büller, "Treatment of deep vein thrombosis. ," *In: Current Approaches to Deep Vein Thrombosis. Future Medicine Ltd*, pp. 136-160, 2014.
- [8] M. J. Sharafuddin, *et al.*, "Endovascular management of venous thrombotic and occlusive diseases of the lower extremities," *Journal of vascular and interventional radiology*, vol. 14, pp. 405-423, 2003.
- [9] R. J. Siegel and H. Luo, "Ultrasound thrombolysis," *Ultrasonics*, vol. 48, pp. 312-320, 2008.
- [10] S. Pfaffenberger, *et al.*, "2MHz ultrasound enhances t-PA-mediated thrombolysis: comparison of continuous versus pulsed ultrasound and standing versus travelling acoustic waves," *Thromb Haemost*, vol. 89, pp. 583-589, 2003.

- [11] C. K. Holland, *et al.*, "Ultrasound-enhanced tissue plasminogen activator thrombolysis in an *in vitro* porcine clot model," *Thrombosis research*, vol. 121, pp. 663-673, 2008.
- [12] K. E. Hitchcock, *et al.*, "Ultrasound-enhanced rt-PA thrombolysis in an ex vivo porcine carotid artery model," *Ultrasound in medicine & biology*, vol. 37, pp. 1240-1251, 2011.
- [13] J. Larsson, *et al.*, "Ultrasound enhanced thrombolysis in experimental retinal vein occlusion in the rabbit," *British journal of ophthalmology*, vol. 82, pp. 1438-1440, 1998.
- [14] V. Frenkel, *et al.*, "Pulsed High-Intensity Focused Ultrasound Enhances Thrombolysis in an *In Vitro* Model 1," *Radiology*, vol. 239, pp. 86-93, 2006.
- [15] M. J. Stone, *et al.*, "Pulsed-high intensity focused ultrasound enhanced tPA mediated thrombolysis in a novel *in vivo* clot model, a pilot study," *Thrombosis research*, vol. 121, pp. 193-202, 2007.
- [16] A. V. Alexandrov, *et al.*, "Ultrasound-enhanced systemic thrombolysis for acute ischemic stroke," *New England Journal of Medicine*, vol. 351, pp. 2170-2178, 2004.
- [17] C. A. Molina, *et al.*, "Transcranial ultrasound in clinical sonothrombolysis (TUCSON) trial," *Annals of neurology*, vol. 66, pp. 28-38, 2009.
- [18] G. Tsivgoulis, *et al.*, "Safety and efficacy of ultrasound-enhanced thrombolysis a comprehensive review and meta-analysis of randomized and nonrandomized studies," *Stroke*, vol. 41, pp. 280-287, 2010.
- [19] S. Datta, *et al.*, "Ultrasound-enhanced thrombolysis using Definity® as a cavitation nucleation agent," *Ultrasound in medicine & biology*, vol. 34, pp. 1421-1433, 2008.
- [20] A. T. Brown, *et al.*, "Microbubbles improve sonothrombolysis *in vitro* and decrease hemorrhage *in vivo* in a rabbit stroke model," *Investigative radiology*, vol. 46, 2011.
- [21] W. C. Culp, *et al.*, "Successful microbubble sonothrombolysis without tissue-type plasminogen activator in a rabbit model of acute ischemic stroke," *Stroke*, vol. 42, pp. 2280-2285, 2011.
- [22] S. T. Laing, *et al.*, "Thrombolytic efficacy of tissue plasminogen activator-loaded echogenic liposomes in a rabbit thrombus model," *Thrombosis research*, vol. 130, pp. 629-635, 2012.
- [23] S. Meairs and W. Culp, "Microbubbles for thrombolysis of acute ischemic stroke," *Cerebrovascular diseases*, vol. 27, pp. 55-65, 2009.
- [24] U. Rosenschein, *et al.*, "Ultrasound Imaging-Guided Noninvasive Ultrasound Thrombolysis Preclinical Results," *Circulation*, vol. 102, pp. 238-245, 2000.

- [25] A. Burgess, *et al.*, "High-intensity focused ultrasound (HIFU) for dissolution of clots in a rabbit model of embolic stroke," *PloS one*, vol. 7, p. e42311, 2012.
- [26] C. Wright, *et al.*, "In vitro and in vivo high intensity focused ultrasound thrombolysis," *Investigative radiology*, vol. 47, p. 217, 2012.
- [27] A. D. Maxwell, *et al.*, "Noninvasive thrombolysis using pulsed ultrasound cavitation therapy–histotripsy," *Ultrasound in medicine & biology*, vol. 35, pp. 1982-1994, 2009.
- [28] A. D. Maxwell, *et al.*, "Noninvasive treatment of deep venous thrombosis using pulsed ultrasound cavitation therapy (histotripsy) in a porcine model," *Journal of vascular and interventional radiology*, vol. 22, pp. 369-377, 2011.
- [29] X. Zhang, *et al.*, "Noninvasive thrombolysis using histotripsy beyond the intrinsic threshold (microtripsy)," *Ultrasonics, Ferroelectrics, and Frequency Control, IEEE Transactions on*, vol. 62, pp. 1342-1355, 2015.
- [30] X. Zhang, *et al.*, "Noninvasive thrombolysis using microtripsy: a parameter study," *Ultrasonics, Ferroelectrics, and Frequency Control, IEEE Transactions on*, vol. 62, pp. 2092-2105, 2015.
- [31] Z. Xu, *et al.*, "Effects of acoustic parameters on bubble cloud dynamics in ultrasound tissue erosion (histotripsy)," *The Journal of the Acoustical Society of America*, vol. 122, pp. 229-236, 2007.
- [32] Z. Xu, *et al.*, "Evolution of bubble clouds induced by pulsed cavitation ultrasound therapy-histotripsy," *Ultrasonics, Ferroelectrics, and Frequency Control, IEEE Transactions on*, vol. 55, pp. 1122-1132, 2008.
- [33] Z. Xu, *et al.*, "Noninvasive creation of an atrial septal defect by histotripsy in a canine model," *Circulation*, vol. 121, pp. 742-749, 2010.
- [34] A. D. Maxwell, *et al.*, "Cavitation clouds created by shock scattering from bubbles during histotripsy," *The Journal of the Acoustical Society of America*, vol. 130, pp. 1888-1898, 2011.
- [35] X. Zhang, *et al.*, "Real-Time Feedback of Histotripsy Thrombolysis Using Bubble-Induced Color Doppler," *Ultrasound in medicine & biology*, vol. 41, pp. 1386-1401, 2015.
- [36] K.-W. Lin, *et al.*, "Histotripsy beyond the intrinsic cavitation threshold using very short ultrasound pulses: Microtripsy," *Ultrasonics, Ferroelectrics, and Frequency Control, IEEE Transactions on*, vol. 61, pp. 251-265, 2014.

- [37] A. D. Maxwell, *et al.*, "Probability of cavitation for single ultrasound pulses applied to tissues and tissue-mimicking materials," *Ultrasound in medicine & biology*, vol. 39, pp. 449-465, 2013.
- [38] A. Blinc, *et al.*, "Magnetic resonance imaging of retracted and nonretracted blood clots during fibrinolysis *in vitro*," *Pathophysiology of Haemostasis and Thrombosis*, vol. 22, pp. 195-201, 1992.
- [39] S. Kunitada, *et al.*, "Inhibition of clot lysis and decreased binding of tissue-type plasminogen activator as a consequence of clot retraction," *Blood*, vol. 79, pp. 1420-1427, 1992.
- [40] J. T. Sutton, *et al.*, "Clot retraction affects the extent of ultrasound-enhanced thrombolysis in an *ex vivo* porcine thrombosis model," *Ultrasound in medicine & biology*, vol. 39, pp. 813-824, 2013.
- [41] S. Feghhi and N. J. Sniadecki, "Mechanobiology of platelets: techniques to study the role of fluid flow and platelet retraction forces at the micro-and nano-scale," *International journal of molecular sciences*, vol. 12, pp. 9009-9030, 2011.
- [42] J. Fox and D. Phillips, "Polymerization and organization of actin filaments within platelets," in *Seminars in hematology*, 1983, pp. 243-260.
- [43] K. Kirchhof, *et al.*, "Differentiation of White, Mixed, and Red Thrombi: Value of CT in Estimation of the Prognosis of Thrombolysis—Phantom Study 1," *Radiology*, vol. 228, pp. 126-130, 2003.
- [44] A. Blinc, *et al.*, "Flow through clots determines the rate and pattern of fibrinolysis," *Thrombosis and haemostasis*, vol. 71, pp. 230-235, 1994.
- [45] M. Carr and C. L. Hardin, "Fibrin has larger pores when formed in the presence of erythrocytes," *American Journal of Physiology-Heart and Circulatory Physiology*, vol. 253, pp. H1069-H1073, 1987.
- [46] E. Vlaisavljevich, *et al.*, "Effects of tissue mechanical properties on susceptibility to histotripsy-induced tissue damage," *Physics in medicine and biology*, vol. 59, p. 253, 2014.
- [47] E. Vlaisavljevich, *et al.*, "Effects of tissue stiffness, ultrasound frequency, and pressure on histotripsy-induced cavitation bubble behavior," *Physics in medicine and biology*, vol. 60, p. 2271, 2015.
- [48] U. Albrechtsson, *et al.*, "Femoral vein pressure measurements for evaluation of venous function in patients with postthrombotic iliac veins," *Cardiovascular and interventional radiology*, vol. 4, pp. 43-50, 1981.

- [49] D. Negus and F. Cockett, "Femoral vein pressures in post-phlebitic iliac vein obstruction," *British Journal of Surgery*, vol. 54, pp. 522-525, 1967.
- [50] J. Browne, *et al.*, "Assessment of the acoustic properties of common tissue-mimicking test phantoms," *Ultrasound in medicine & biology*, vol. 29, pp. 1053-1060, 2003.
- [51] B. Hertzberg, *et al.*, "Sonographic assessment of lower limb vein diameters: implications for the diagnosis and characterization of deep venous thrombosis," *AJR. American journal of roentgenology*, vol. 168, pp. 1253-1257, 1997.
- [52] S. Park, *et al.*, "Non-invasive embolus trap using histotripsy—an acoustic parameter study," *Ultrasound in medicine & biology*, vol. 39, pp. 611-619, 2013.
- [53] R. Macfarlane, "A simple method for measuring clot-retraction," *The Lancet*, vol. 233, pp. 1199-1201, 1939.
- [54] J. E. Parsons, *et al.*, "Cost-effective assembly of a basic fiber-optic hydrophone for measurement of high-amplitude therapeutic ultrasound fields," *The Journal of the Acoustical Society of America*, vol. 119, pp. 1432-1440, 2006.
- [55] T.-Y. Wang, *et al.*, "An efficient treatment strategy for histotripsy by removing cavitation memory," *Ultrasound in medicine & biology*, vol. 38, pp. 753-766, 2012.
- [56] H. Xie, *et al.*, "Correspondence of ultrasound elasticity imaging to direct mechanical measurement in aging DVT in rats," *Ultrasound in medicine & biology*, vol. 31, pp. 1351-1359, 2005.
- [57] B. Coulter, "Coulter Counter Multisizer 3 User's Manual," *Hialeah, Florida: Beckman Coulter Incorporated*, 2000.
- [58] S. Z. Goldhaber, *et al.*, "Randomized controlled trial of tissue plasminogen activator in proximal deep venous thrombosis," *The American journal of medicine*, vol. 88, pp. 235-240, 1990.
- [59] H. S. Kim, *et al.*, "Adjunctive percutaneous mechanical thrombectomy for lower-extremity deep vein thrombosis: clinical and economic outcomes," *Journal of vascular and interventional radiology*, vol. 17, pp. 1099-1104, 2006.
- [60] R. K. Popuri and S. Vedantham, "The role of thrombolysis in the clinical management of deep vein thrombosis," *Arteriosclerosis, thrombosis, and vascular biology*, vol. 31, pp. 479-484, 2011.
- [61] G. Y. Lip, *et al.*, "Overview of the treatment of lower extremity deep vein thrombosis (DVT)."

- [62] K. Yasui, *et al.*, "Recirculation-type Amplatz clot macerator: determination of particle size and distribution," *Journal of vascular and interventional radiology*, vol. 4, pp. 275-278, 1993.
- [63] R. Uflacker, *et al.*, "Treatment of thrombosed dialysis access grafts: randomized trial of surgical thrombectomy versus mechanical thrombectomy with the Amplatz device," *Journal of vascular and interventional radiology*, vol. 7, pp. 185-192, 1996.
- [64] S. MÜLLER-HÜLSBECK, *et al.*, "Mechanical thrombectomy of major and massive pulmonary embolism with use of the Amplatz thrombectomy device," *Investigative radiology*, vol. 36, pp. 317-322, 2001.
- [65] S. Singhal, *et al.*, "Morphometry of the human pulmonary arterial tree," *Circulation Research*, vol. 33, pp. 190-197, 1973.
- [66] A. P. Duryea, *et al.*, "Removal of residual nuclei following a cavitation event: a parametric study," *Ultrasonics, Ferroelectrics, and Frequency Control, IEEE Transactions on*, vol. 62, pp. 1605-1614, 2015.



## Chapter 6

### Real-time Feedback of Histotripsy Thrombolysis Using Bubble-induced Color Doppler

This chapter has been published in *Ultrasound in Medicine and Biology*. 2015; 41(5):1386-1401.  
© UMB. Reprinted, with permission, from [1].

#### 6.1 Introduction

Pathological thrombosis is implicated in many cardiovascular diseases. Venous thrombi such as deep vein thrombosis (DVT) can lead to pulmonary embolism (PE) and arterial thrombi can manifest as myocardial infarction (MI) or ischemic stroke. Current clinical thrombolytic methods include the use of thrombolytic drugs [2-4], catheter-based endovascular procedures [5, 6], or a combination of the two [7, 8]. Administering thrombolytic drugs systemically requires long treatment times and has a high risk of major bleeding. Catheter-based methods are site-specific but invasive and associated with frequent complications, such as bleeding, vessel damage, and infection.

Low intensity ultrasound has been shown to enhance the efficacy of thrombolytic agents *in vitro* [9-11], *in vivo* [12], and in clinical trials [13-15]. There are also a number of studies that have successfully demonstrated the use of ultrasound and microbubbles to degrade clot in the presence or absence of thrombolytic agents [16-18]. Studies using microbubbles have suggested that cavitation is correlated with significant enhancement of thrombolysis [19]. High-Intensity Focused Ultrasound (HIFU) has been investigated as a stand-alone thrombolytic approach [20,

21], but the safety and efficiency of this technology still needs further investigation before clinical translation.

Histotripsy fractionates soft tissue by well-controlled acoustic cavitation using microsecond-long, high-intensity and focused ultrasound pulses [22-26]. The feasibility of using histotripsy as a noninvasive, drug-free, and image-guided thrombolysis technique has been demonstrated previously. *In vitro* studies show that histotripsy can completely break down large clots (140-300 mg) within 5 min into particles no larger than 100  $\mu\text{m}$  [27] and *in vivo* studies in a porcine deep vein thrombosis model, showed histotripsy therapy can re-establish blood flow and decrease thrombus burden [28].

Real-time quantitative feedback to monitor the progress of histotripsy clot fractionation would improve treatment efficacy and potentially minimize therapy dose, thereby improving safety. Specifically, as cavitation is known to cause hemolysis and platelet aggregation [29-32], minimizing the therapy dose can mitigate these potential complications of histotripsy thrombolysis treatment. While a number of methods have been investigated to evaluate tissue damage by ultrasound thermal therapies using magnetic resonance imaging (MRI) [33-36] or ultrasound-based measurement of changes in tissue elasticity, sound speed or acoustic attenuation [37-42], none have been incorporated for real-time monitoring of ultrasound thrombolytic therapy.

Cavitation detection has been used to correlate stable and inertial cavitation with the effect of thrombolysis in ultrasound-enhanced thrombolysis [19]. B-mode ultrasound imaging during histotripsy therapy can easily visualize cavitation due to the hyperechogenicity of the bubble cloud and provide precise targeting guidance, but its ability to serve as a quantitative therapy feedback is limited. Thus, we are investigating a modified color Doppler imaging

method to monitor motion induced by histotripsy pulses as a real-time quantitative feedback for histotripsy thrombolysis. This motion is only detectable when a cavitation bubble cloud is formed, and therefore this monitoring method was termed bubble-induced color Doppler (BCD) feedback. The motion itself likely results from a net force exerted by rapid bubble expansion or collapse in the focal region and can last over 10 ms after each pulse. This force generates a variable motion response depending on mechanical properties of the tissue in the focal region. We hypothesize that as the clot is increasingly fractionated and becomes softer and eventually liquefied the change in the bubble-induced motion can be monitored and quantified using BCD feedback as a real-time measure of the degree of clot fractionation.

This chapter evaluates the potential of BCD feedback for histotripsy thrombolysis monitoring in four incremental steps. First, the bubble-induced motion is characterized in transparent fibrin clots using particle image velocimetry (PIV) that serves as the gold standard to compare with BCD. Second, using fibrin clots with a thin layer of embedded red blood cells, the visualized progress of histotripsy thrombolysis is quantitatively compared with its corresponding BCD feedback. Third, the correlation of BCD feedback with clot fractionation is validated in *in vitro* clots by comparing the BCD signal to the change of fractionated debris volume as a function of therapy dose. Finally, a real-time BCD feedback algorithm to predict complete clot fractionation during histotripsy thrombolysis is developed and tested.

## **6.2 Materials and Methods**

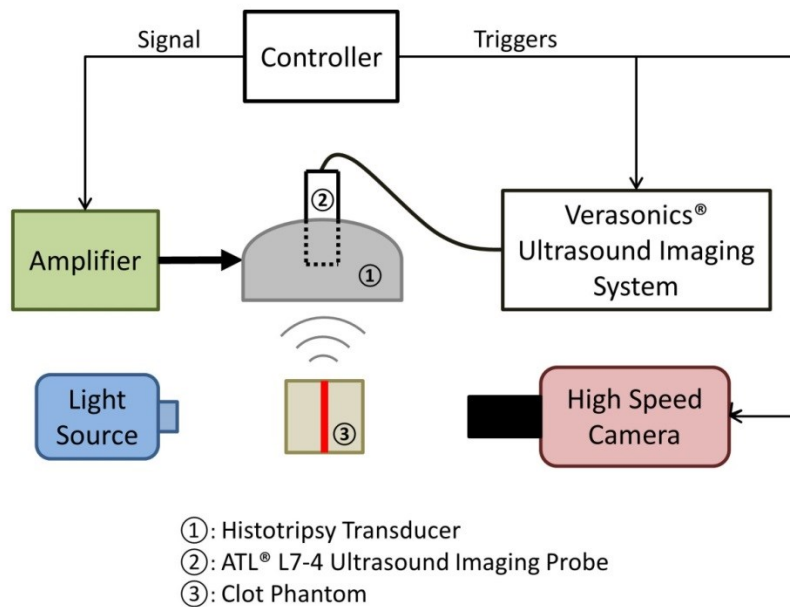
### **6.2.1 Investigation of Bubble-induced Motion**

A transparent fibrin clot was developed to study the bubble-induced motion inside the clot (**Figure 6.1**). Reconstituted plasma was used to form the transparent fibrin clot, following the procedure as previously described [43]. Fresh bovine blood was collected from a local

abattoir. A citrate-phosphate-dextrose (CPD) solution (C7165; Sigma-Aldrich Co., St. Louis, MO, USA) was immediately added and gently mixed in the bovine blood as an anti-coagulant at a ratio of 1 mL CPD per 9 mL blood. The resulting blood sample was stored at 4°C and used within 72 hours. The blood sample was first centrifuged at a relative centrifugal force (RCF) of 1400g for 30 minutes. Then the plasma supernatant was separated from the buffy coat and red blood cell (RBC) pack, and incubated in 55°C water bath for 5 minutes to precipitate the native fibrinogen [44]. The plasma solution was further centrifuged at a RCF of 1400g for 3 minutes to completely separate the precipitated fibrinogen. Bovine fibrinogen (F8630; Sigma-Aldrich Co., St. Louis, MO, USA) was then added to the processed plasma with a concentration of 400 mg/dL. To stimulate the clotting cascade, bovine thrombin (T4648; Sigma-Aldrich Co., St. Louis, MO, USA) and calcium chloride (21107; Sigma-Aldrich Co., St. Louis, MO, USA) were mixed with the reconstituted plasma to a final concentration of 1 IU/mL and 20mM/L respectively [45, 46]. The mixture was then poured into a rectangular mold and incubated in 37°C water bath for 2 hours. The mature clot became a rectangular plate of approximately 30 mm (width) x 50 mm (length) x 5 mm (thickness) and embedded in transparent agarose hydrogel, which helped maintain the shape and position of the clot in water. The transparent fibrin clot allows for direct visualization of the cavitation microbubbles and bubble-induced motion inside the clot.



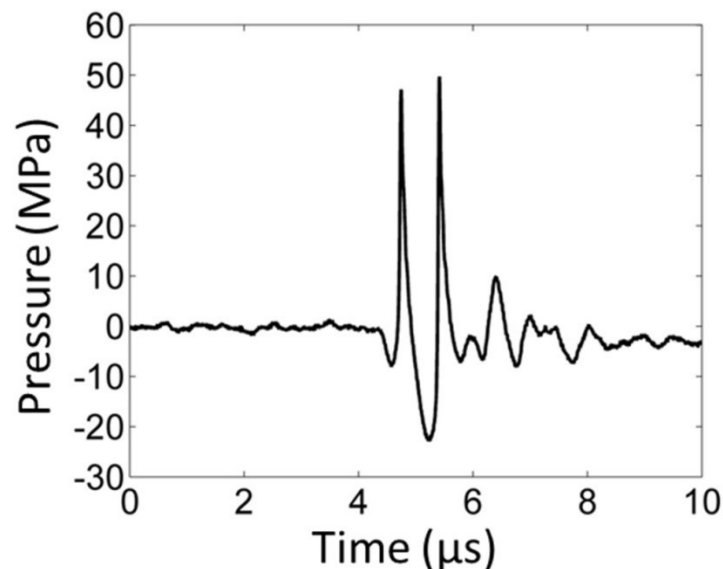
**Figure 6.1:** Transparent fibrin clot embedded in agarose hydrogel. The clot was molded to be rectangular in shape. A ruler segment was placed under the clot to show the transparency.



**Figure 6.2:** A schematic illustration of the experimental setup. A 6-element 1.5-MHz histotripsy transducer was placed facing down in a water tank filled with degassed water. The transducer was driven by a high-voltage amplifier that was connected to a field-programmable gated-array (FPGA) development board specifically programmed for controlling the firing of the transducer. A 5-MHz ultrasound imaging probe was inserted in the central hole of the histotripsy transducer and connected to Verasonics® ultrasound imaging system to image at the transducer focus. A high-speed camera and a continuous-wave light source were placed on the two sides outside the water tank. The FPGA controller sent triggers to the Verasonics® system and the high-speed camera to synchronize them with therapy pulses. The therapy focus was positioned within the transparent fibrin clot phantom. The central plane of the clot plate, the ultrasound imaging plane and the focal plane of the camera were aligned to overlap with each other.

In order to capture the bubble-induced motion following each histotripsy pulse inside the fibrin clot, optical imaging for particle image velocimetry (PIV) and ultrasound imaging for bubble-induced color Doppler (BCD) were applied simultaneously during histotripsy treatment. The experimental setup is illustrated in **Figure 6.2**. The optically and acoustically transparent clot was treated by a 1.5-MHz focused ultrasound transducer with an aperture size of 7.1 cm (lateral) x 8 cm (elevational) and a focal length of 5.5 cm. In the center of the transducer housing is a 6 cm x 2.4 cm rectangular hole for the insertion of imaging probes. The transducer was calibrated using a fiber-optic probe hydrophone (FOPH) adapted from a previously published design [47]. The focal beam volume (-6 dB) of the transducer was measured to be 4.2 mm (axial)

x 1.5 mm (lateral) x 1.9 mm (elevational) at a peak negative pressure of 15 MPa. The histotripsy treatment consisted of 1.5-cycle ultrasound pulses with a pulse repetition frequency (PRF) of 30 Hz, at an estimated peak negative pressure of 36 MPa and a peak positive pressure of 58 MPa at the focus. The focal pressure waveform was measured directly with FOPH up to the peak negative pressure of 25 MPa (**Figure 6.3**). At the peak negative pressure beyond 25 MPa, the pressure cannot be directly measured due to instantaneous cavitation and is estimated by summing the measurable pressure outputs from two sub-groups of the elements. The total exposure at each sample spot was 1000 pulses.



**Figure 6.3:** A representative pressure waveform of the 6-element 1.5-MHz histotripsy transducer taken at the highest pressure (peak negative) level that could be directly measured by the fiber optical hydrophone.

For PIV analysis, optical images of the treatment focal zone were captured by a high-speed camera (Phantom V210; Vision Research, Wayne, NJ) using a 135 mm macro lens. The transparent clot phantom was illuminated by a continuous wave (CW) light source from the opposite side of the phantom from the camera. Each image ( $800 \times 256$  pixels) covered an approximately  $7.3 \text{ mm} \times 2.3 \text{ mm}$  field of view, allowing the observation of the full treatment zone ( $4.2 \text{ mm} \times 1.5 \text{ mm}$ ). The high-speed camera was synchronized to capture images at a frame

rate (FR) of 10 kHz immediately after the delivery of a histotripsy pulse. Limited by the memory size of the high-speed camera, 100 optical images were captured after every 4th histotripsy pulse, covering the first 10 ms after the pulse. A period of 10 ms was sufficiently long to capture the most significant motion.

For BCD imaging, a 5-MHz ultrasound imaging probe (ATL L7-4, Philips, Andover, MA) was placed in the central hole of the therapy transducer and aligned with the transducer focus. The color Doppler acquisitions were realized using a Verasonics<sup>®</sup> imaging system (V-1 Data Acquisition System, Verasonics, Kirkland, WA). The color Doppler field of view was chosen to cover the whole treatment zone. Immediately after the delivery of a histotripsy pulse, the Verasonics<sup>®</sup> system started to transmit color Doppler pulses and acquire echo signals at a PRF of 10 kHz. A total of 100 Doppler acquisitions were collected per histotripsy pulse, covering the first 10 ms.

To estimate the bubble-induced motion in the treatment zone, the captured optical images were analyzed using PIV via a Matlab-based analysis tool (PIVlab, Version 1.32). Dark fragments of broken fibrin fibers resulting from histotripsy fractionation provided contrast to track the motion. Each velocity map at a certain delay after a histotripsy pulse was estimated using the image captured at that delay time and the subsequent image. The image pair was compared using a three-pass Fast Fourier Transformation (FFT) window deformation algorithm to estimate the motions. The interrogation window sizes were chosen to be 64, 32 and 16 pixels respectively, all with 50% interrogation overlap. Since there were 100 images captured after each histotripsy pulse, 99 velocity maps were generated showing velocity information at delay times ranging from 0 to 9.9 ms after the pulse.

The bubble-induced motions were also estimated using color Doppler data. The acquired color Doppler data sets were processed offline using the functions provided by Verasonics software. Each velocity map at a certain delay after a histotripsy pulse was estimated using the color Doppler data acquired at that delay time and 9 subsequent acquisitions. The ensemble length of 10 was chosen as a compromise between the accuracy and the capability of depicting fast change. By processing every set of 10 consecutive acquisitions in a rolling fashion along 100 acquisitions after each histotripsy pulse, 91 velocity maps were generated showing velocity information at different delay times ranging from 0 to 9.1 ms following the pulse.

The mean axial velocity, which was defined as velocity components on the direction of ultrasound propagation, was calculated over the region of interest on each PIV and BCD velocity map. The averaging was applied only over non-zero values within the region of interest. For each histotripsy pulse, a curve of mean axial velocity as a function of time elapsed after the pulse was formed to characterize net axial motion. A full profile of mean axial velocity throughout each treatment was generated by PIV and BCD respectively, with each vertical line representing a mean velocity curve after each pulse. An averaging effect originally existed during color Doppler processing to generate each BCD velocity map because it was estimated using 10 acquisitions collected over a period of 0.9 ms. In order to fairly compare BCD with PIV, 9-point rolling averaging was applied on the mean velocity curves of PIV to simulate the averaging effect on BCD.

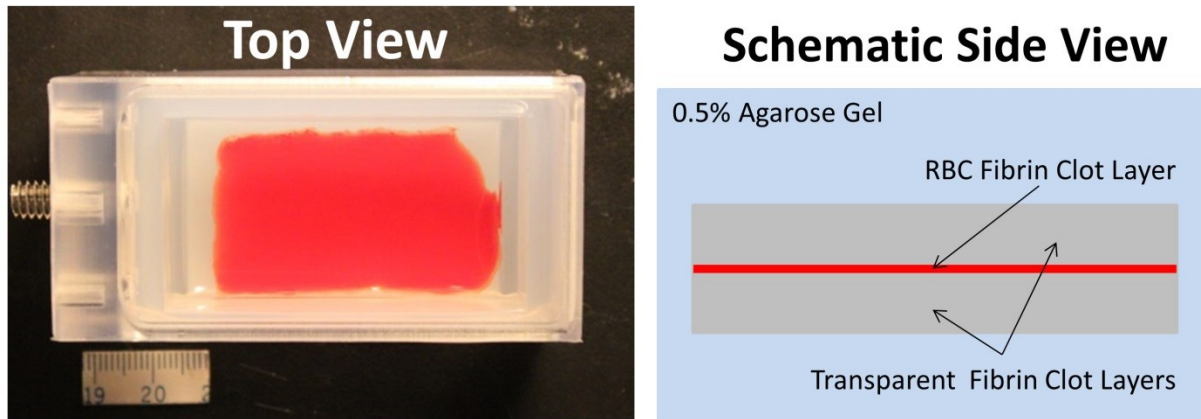
### **6.2.2 Correlation of BCD Feedback and Histotripsy Thrombolysis**

The correlation between the degree of histotripsy thrombolysis and the BCD feedback was investigated using a three-layer fibrin clot, which allowed the direct visualization and quantification of histotripsy fractionation progression. The three-layer fibrin clot constituted of a



thin (~500  $\mu\text{m}$ ) layer of RBC fibrin clot in the center and two thick (~3 mm) layers of transparent fibrin clot on the two sides. As the middle layer embedded with RBC is fractionated, it transitions from opaque to transparent. The degree of fractionation can be quantified as the area of the transparent region within the opaque RBC layer, which is calculated based on the light intensity change in the captured optical images. To evaluate the correlation, the progression of the degree of clot fractionation (lesion progression) in the three-layer clot was compared with two metrics extracted from the corresponding BCD feedback: time of peak rebound velocity ( $t_{\text{PRV}}$ ) and mean velocity of focal zone at a fixed delay ( $V_{\text{f, delay}}$ ) after each pulse.

The three-layer fibrin clot (**Figure 6.4**) was developed to directly visualize the progression of histotripsy thrombolysis. To form a bottom layer (~3 mm thick) of transparent fibrin clot, the reconstituted plasma described above was poured into a rectangular mold right after stimulation and then coagulated at room temperature for 30 minutes. The solution for RBC fibrin clot was made by combining the previously separated RBC pack and the reconstituted plasma to a hematocrit of 30%. The solution was then stimulated and applied on the surface of the bottom layer using blood smearing technique [48] to make an approximate 500  $\mu\text{m}$  thick RBC fibrin clot layer. At last, a top layer (3mm thick) of transparent fibrin clot was made on the coagulated RBC fibrin clot layer. The three-layer clot was then incubated in 37°C water bath for 2 hours. The mature clot was a rectangular plate of approximately 30 mm (wide) x 50 mm (long) x 6.5 mm (thick) and embedded in transparent agarose hydrogel. For all the stimulations, the same concentrations of thrombin (1 IU/mL) and calcium chloride (20 mM/L) were used. Three soft three-layer clot phantoms with a fibrinogen concentration of 400 mg/dL and two hard clot phantoms with doubled fibrinogen concentration were made. All clots were treated within one hour after incubation.

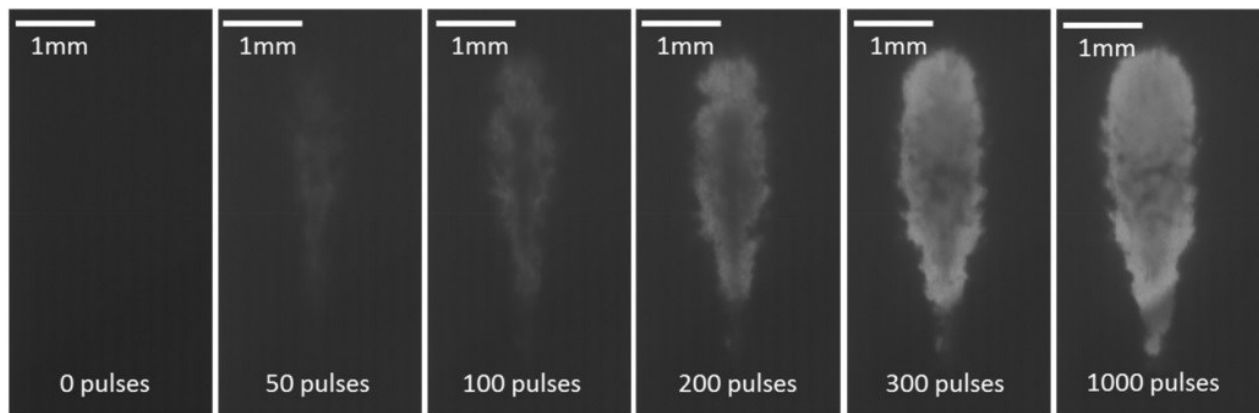


**Figure 6.4:** Three-layer fibrin clot embedded in agarose hydrogel. **(a)** A picture of a three-layer fibrin clot phantom from top view. **(b)** A schematic of the phantom from side view.

The same setup as in the previous section was used for this experiment. The plane of the thin RBC clot layer was positioned perpendicular to the optical axis of the high-speed camera and aligned to the camera's focal plane by visually adjusting the sharpness of the thin RBC layer on the optical images. Since the camera's focal plane was already aligned rigidly with the histotripsy focus and the ultrasound imaging plane, this procedure aligned the thin RBC clot layer onto the therapy focus. The histotripsy treatment was performed by the same transducer and using the same treating parameters (1.5-cycle, 30 Hz PRF and 36 MPa peak negative pressure). When treating a spot, the high-speed camera captured one image of the treatment zone before each histotripsy pulse arrived to record the lesion as a function of the number of applied therapy pulses. The same color Doppler data were acquired and processed using the same settings as that in the previous section. A total of 30 spots were treated in the soft clots (10 in each of the three soft clot phantoms) and 20 spots were treated in the hard clots (10 in each of the two hard clot phantoms) by histotripsy thrombolysis.

The size of the produced lesions was quantified using the acquired optical images. As the targeted volume was increasingly fractionated by the increasing number of applied histotripsy pulses, the treated region within the RBC layer changed gradually from opaque to translucent on

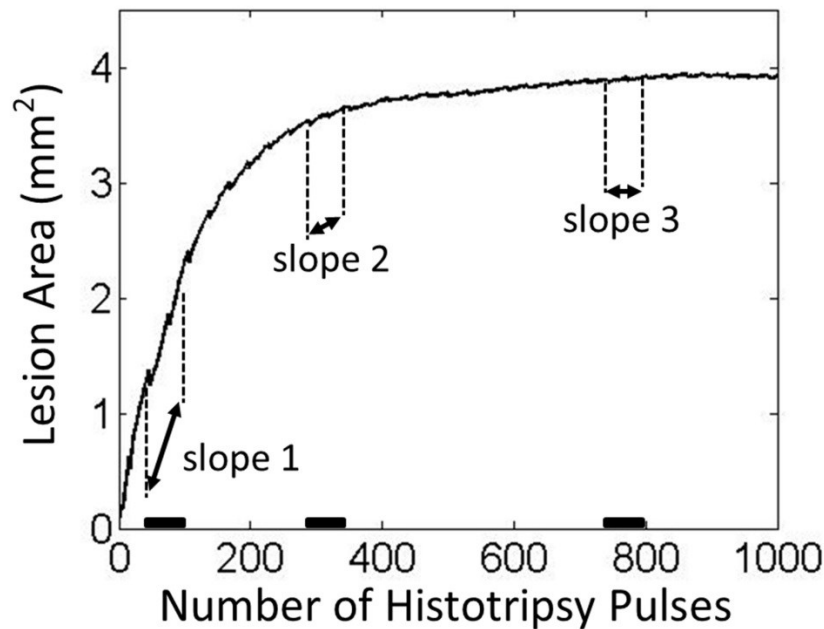
the optical images. Since the clot phantom was back lit with CW light, the captured optical images would appear as shadow graphs in which the untreated region appeared dark and the fractionated region appeared bright (**Figure 6.5**). These optical images were analyzed by Matlab (R2012b, The MathWorks Inc., Natick, MA) using a method similar to those described in previous papers [49-51]. The lesion on each image was detected using a threshold approach. For each spot, a pixel brightness threshold was first chosen and set at 10% above the average pixel brightness of the first image where no damage was done. The grayscale images were converted into binary images using this threshold. The regions with brightness that was higher than the threshold would become 1 (white) in the binary image and be considered fractionated. In contrast, the regions with brightness less than the threshold would become 0 (black) and be considered intact. The lesion area was then plotted as a function of the number of applied therapy pulses to form the lesion progression.



**Figure 6.5:** Representative lesion formation of a treated spot in a soft three-layer fibrin clot. The lesions at different stages (pulse 0, 50, 100, 200, 300 and 1000) are shown here. These images were taken in the axial-lateral plane of the transducer, and the histotripsy pulses propagated from the top to the bottom of the field.

To find the saturation of lesion progression, i.e. the treatment completion, the change rate of the lesion area during each treatment was analyzed by a slope detection algorithm. The slope detection algorithm used a segment-wise approach similar to what was described in a previous study by Turner *et al.* [52]. The mean change rate (slope) of lesion area over a certain time

window (segment) was estimated by fitting a least-square linear model into all lesion area data within this window. The change rate as a function of applied histotripsy pulses during the whole treatment was generated by rolling the time window through the entire treatment period. The algorithm is illustrated in **Figure 6.6**. The saturation dose was determined when the change rate was, for the first time, smaller than 10% of the maximal change rate detected at this treating location. To investigate whether the saturation doses of the metrics extracted from BCD feedback indicate the saturation dose of its corresponding lesion progression, the same algorithm was also applied to analyze the progressions of the BCD metrics using the same parameters.



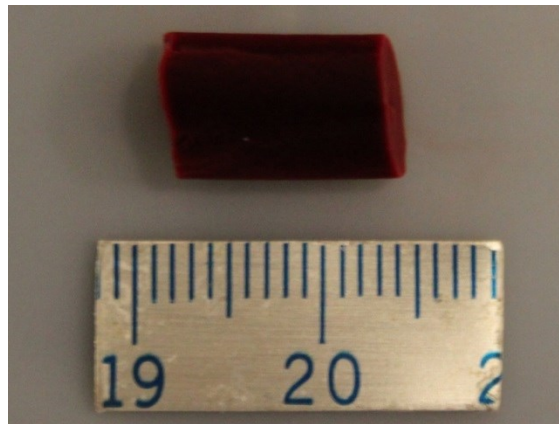
**Figure 6.6:** The illustration of the slope detection algorithm. The lesion progression data shown here is from one treated sample. The slopes over three representative time windows are indicated. The highest change rate appears at the beginning of the treatment around the first time window (slope 1) and the saturation starts to occur around the second time window (slope 2).

### 6.2.3 Validation of BCD Feedback in *In Vitro* Clots

The BCD feedback was validated through histotripsy treatment of *in vitro* clots. The treatment focus was scanned through the length of the clot to create a channel. The volume of clot debris particles generated from histotripsy with different treatment doses was measured to

evaluate the degree of clot fractionation. This metric on degree of clot fractionation was then compared with the BCD feedback.

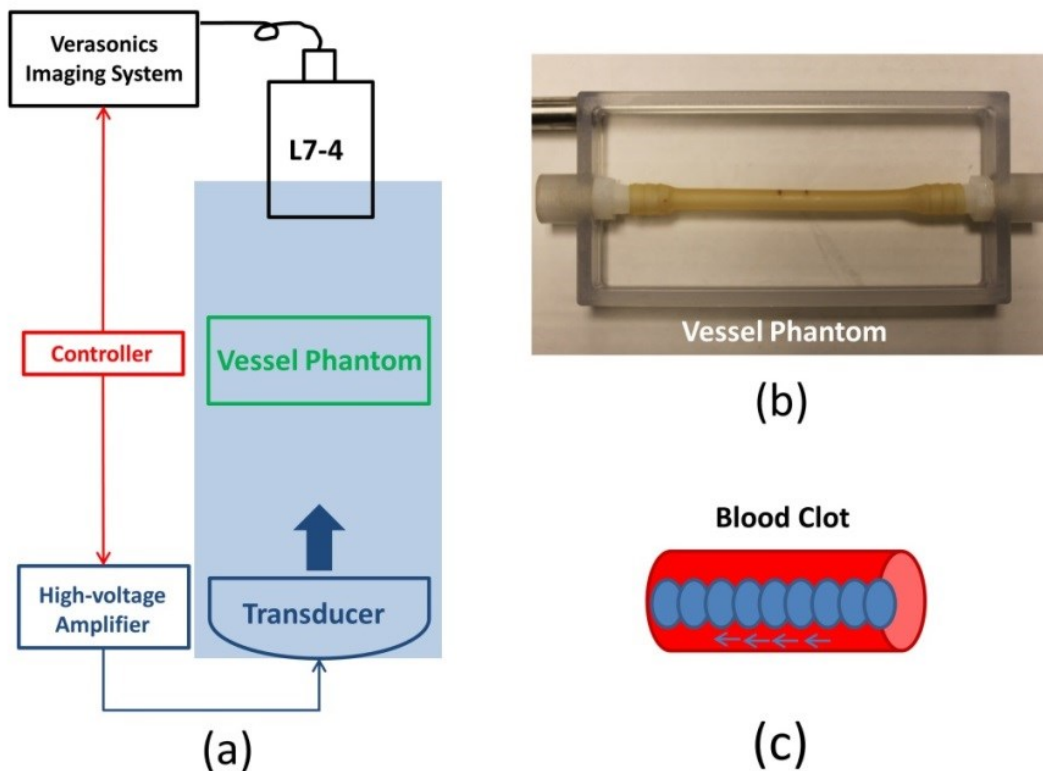
To make *in vitro* clots (**Figure 6.7**), the separated RBC pack and the reconstituted plasma (fibrinogen concentration: 400 mg/dL) described previously were recombined to a hematocrit of 30% [43]. After stimulating with thrombin (1 IU/mL) and calcium chloride (20 mM/L), the mixture was poured into a tube and incubated in 37°C water bath for 2 hours. Each mature clot had a cylinder shape with a diameter of 6.5 mm and a length of 11 mm.



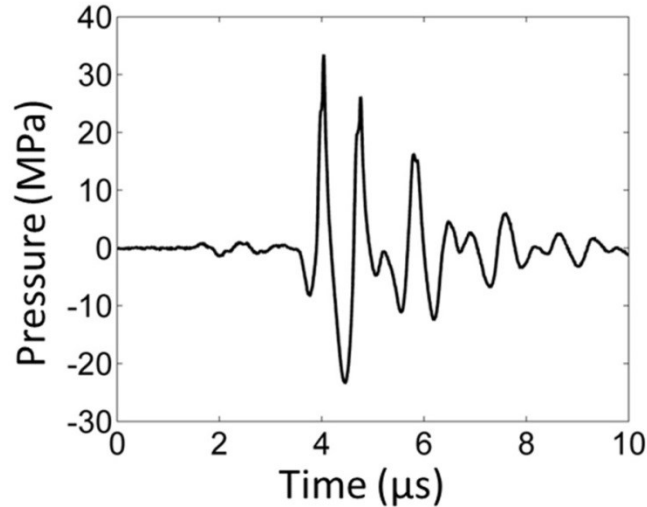
**Figure 6.7:** RBC fibrin clot. The separation between the two adjacent tick marks on the scale ruler is 1 mm.

The experimental setup is illustrated in **Figure 6.8**. The histotripsy recanalization was performed using an 18-element 1.25-MHz focused transducer with an aperture size of 8 cm (lateral) x 8.3 cm (elevational) aperture size and a focal length of 6 cm. This 1.25-MHz transducer was used instead of the 1.5-MHz transducer because its longer working distance makes it easier to operate with this experimental setup and its larger focal volume fits better with the actual vessel. The same calibration method was used here as for the 1.5-MHz transducer in the previous sections. The focal volume ( $-6$  dB beamwidth) was measured as 6.5 mm (axial) x 2 mm (lateral) x 1.5 mm (elevational) at a peak negative pressure of 15 MPa. The histotripsy treatment consists of 1.5-cycle ultrasound pulses with the same PRF (30Hz) and peak negative pressure (36MPa) as using the 1.5MHz transducer. A pressure waveform directly measured by

the fiber optical hydrophone is shown in **Figure 6.9**. The same L7-4 ultrasound imaging probe as in the previous sections was placed opposite to the histotripsy transducer and aligned rigidly with the treatment focus. A vessel phantom (6.5 mm inner diameter and 0.5 mm wall thickness) was made of urethane polymer (TAP Urethane RTV, Tap Plastics Inc., San Leandro, CA) to mimic *in vivo* vessel [53] and placed between the transducer and imaging probe, with the treatment focus targeting at the center of the vessel lumen and the ultrasound imaging plane perpendicular to the longitudinal direction of the vessel.



**Figure 6.8:** (a) A schematic illustration of the *in vitro* experiment setup. An 18-element 1.25-MHz histotripsy transducer was placed facing up in a tank filled with the degassed water. The transducer was driven by a high-voltage amplifier which was connected by an FPGA controller. A 5-MHz ultrasound imaging probe was positioned opposite to the transducer, aligned rigidly to the treatment focus and connected to the Verasonics<sup>®</sup> ultrasound imaging system. The FPGA controller sent triggers to the Verasonics<sup>®</sup> system to synchronize them with therapy pulses. Vessel phantom was placed between the transducer and the ultrasound imaging probe. (b) A picture of the vessel phantom. (c) Strategy of recanalization treatment. Each ellipse represents a treatment focal spot and after the completion of each spot treatment, the focus will move to the adjacent location with a 0.7 mm separation.



**Figure 6.9:** A representative pressure waveform of the 1.25-MHz histotripsy transducer taken at the highest pressure (peak negative) level which can be directly measured by the fiber optical hydrophone.

RBC fibrin clot (6.5 mm in diameter and 11 mm in length) was carefully inserted into the vessel phantom. After being filled with 0.9% saline, the vessel phantom was sealed by rubber plugs. To generate a channel within the clot, the treatment focus was aligned to one end of the clot, and a certain dose of histotripsy pulses were applied at the location. The treatment focus was then moved to the adjacent location with a 0.7 mm separation along the clot length, and the same dose of treatment was conducted. This procedure continued until the focus reached the other end of the clot. Six different histotripsy doses (0, 250, 500, 1000, 1500 and 3000 pulses) were used to canalize *in vitro* clots. Nine clots were treated for each of these histotripsy doses. During the treatment, BCD feedback data were also acquired. An ensemble of 10 color Doppler acquisitions was collected with a PRF of 10 kHz at 0.5 ms delay after each pulse. A delay of 0.5 ms was chosen to capture the first major rebound period of the bubble-induced motion. The mean velocity of focal zone ( $V_{f,0.5ms}$ ) was then estimated as a function of the number of applied histotripsy at each treatment location.

After a clot was treated, the fractionated clot debris was measured accordingly. The saline in the vessel phantom together with the treated clot were carefully moved to a medicine

cup. The treated clot was then cut into 4 cylinder segments and the cup was gently shaken so that clot debris pieces resulting from the histotripsy fractionation could be released to the saline solution. After the large intact clot segments were carefully removed, the solution was diluted with 0.9% saline up to 20 mL. The debris size and volume of a 0.5 mL sample was then measured using a Coulter Counter (Multisizer 3, Beckman Coulter, CA, USA). For the Coulter Counter measurement, a 30- $\mu\text{m}$  aperture tube was used, which allowed measurement of debris sizes between 0.6-18  $\mu\text{m}$  in diameter. Any debris particles larger than 30  $\mu\text{m}$  will block the tube and would be noted and recorded. For each treatment, three measurements were conducted.

#### **6.2.4 Real-time Monitoring of Histotripsy Thrombolysis using BCD Feedback**

The feasibility of using the BCD feedback for real-time monitoring and detection of treatment completion of histotripsy thrombolysis was investigated. The same setup as for the three-layer fibrin clots was used. A three-layer fibrin clot was made with a fibrinogen concentration of 400 mg/dL. The fibrin clot was treated by the same 1.5-MHz transducer using the same parameters (1.5-cycle, 30 Hz PRF and 36 MPa estimated peak negative pressure). The mean velocity of bubble-induced motion within the focal zone at 2 ms delay ( $V_{f,2\text{ms}}$ ) was collected in real time, and the slope saturation of the mean velocity was detected using the real-time version of the slope detection algorithm. A delay of 2 ms was chosen to capture the first major rebound period of the bubble-induced motion. The Verasonics<sup>®</sup> imaging system was synchronized with histotripsy pulses. Starting at 2 ms after each histotripsy pulse, an ensemble of 10 color Doppler acquisitions was captured with a PRF of 10 kHz.  $V_{f,2\text{ms}}$  was estimated from the ensemble real-time and stored as a data point. Every time a new data point was collected, the latest 100 data points were fed into the slope detection function to estimate the current change rate (slope) of  $V_{f,2\text{ms}}$ . The saturation was detected when the current change rate was smaller than



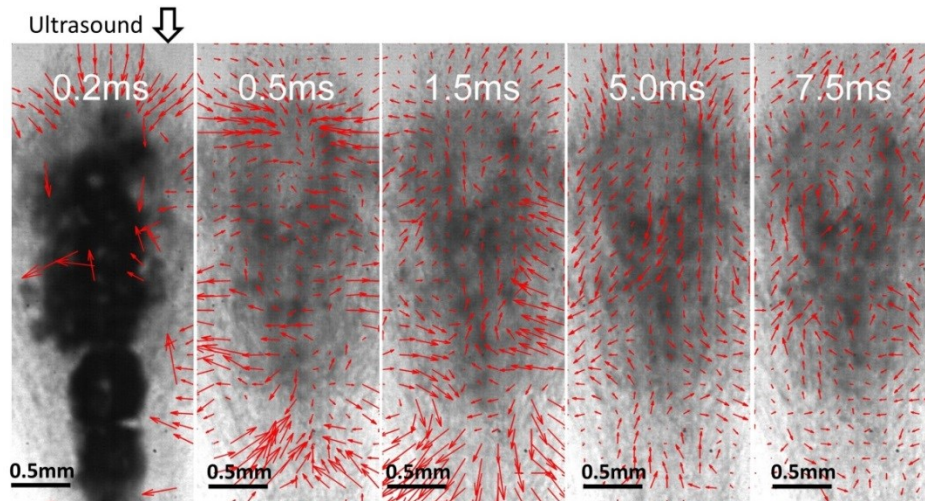
10% of the maximal change rate that appeared previously in this spot. The system would process and determine the saturation dose in real-time but the treatment will continue until 1000 pulses in total were applied. To verify that the saturation of  $V_{f,2ms}$  from BCD feedback indicates treatment completion, high-speed images of the middle RBC clot layer were captured during the treatment, and the lesion progression was quantified using the method described in the previous section. The treatment completion was defined by the detected saturation of the lesion progression (in optical images) and compared with the saturation dose detected in real-time by BCD feedback. Ten locations were treated in total with the real-time BCD monitoring. The difference between real-time detected saturation dose by BCD and the treatment completion dose was calculated.

## **6.3 Results**

### **6.3.1 Investigation of Bubble-induced Motion**

The PIV velocity estimations based on the optical images provided detailed information of bubble-induced motion within the histotripsy focal zone in the transparent fibrin clot. The behaviors of bubble-induced motions observed in all three treated locations were consistent and shared the same trend. Right after the histotripsy pulse, a bubble cloud was created, generating a short period of chaotic motion up to 300  $\mu$ s. Two streams of coherent motions were formed following the chaos. In three-fourths of the focal zone proximal to the histotripsy transducer, the coherent motion was first pushing away from the therapy transducer and then rebounding back. In the rest one-fourth of the focal area distal to the therapy transducer, the coherent motion was observed to be the opposite, first moving toward the transducer and then rebounding away. The rebound oscillations continued in both the proximal and distal areas with decreasing velocity until energy was completely absorbed. The chaotic motion was very short and irregular

compared to the major coherent motion. A representative series of PIV estimations on the corresponding optical images are shown in **Figure 6.10**.

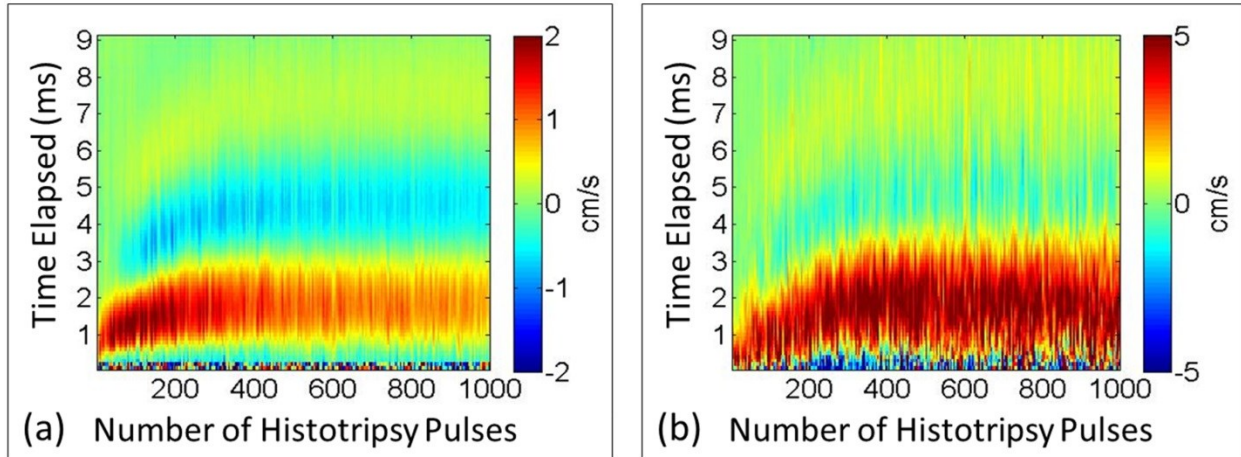


**Figure 6.10:** Representative PIV estimations overlaid with the corresponding optical images taken after the 100<sup>th</sup> histotripsy pulse. These images were taken in the axial-lateral plane of the transducer, and the histotripsy pulses propagated from the top to the bottom of the field. At 0.2 ms after the pulse, the cavitation bubbles show and no coherent motion is detected. At 0.5 ms, coherent motion is forming and pushing away from the transducer in the majority of the focal area proximal to the transducer and another stream of coherent motion at the distal side is moving towards the transducer. At 1.5 ms, the coherent motion at the proximal side is rebounding back and the coherent motion at the distal side is rebounding away. The motions repeat at 5 ms and 7.5 ms as in 0.5 and 1.5 ms.

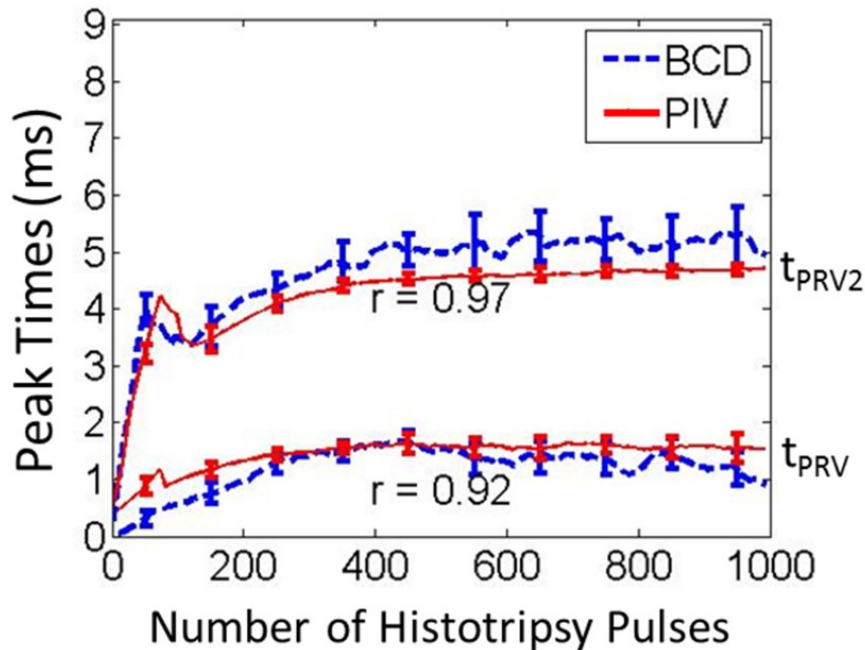
The behavior of the bubble-induced motion estimated by BCD matched that of the proximal-side motion (in the proximal 3/4 of the focal zone) estimated by PIV in all the three treated samples. After the chaotic motion, the motion detected by BCD was coherently pushing away from the therapy transducer and then rebounding back. The same push/rebound cycle was also apparent. As the ultrasound imaging probe was positioned coaxially with the therapy transducer, ultrasound imaging of BCD and therapy beams propagate in the same direction. BCD only detected the motions at the proximal-side of the focal zone, probably because the distal-end of the focal zone was shielded by the bubbles generated in the proximal-side. When placing the ultrasound imaging probe opposite to the histotripsy transducer, the distal-side motions could be captured.

The full profiles of PIV and BCD mean velocity estimations over a representative 1000-pulse treatment are shown in **Figure 6.11**. For both PIV and BCD, the mean axial velocities were calculated over only the proximal three-fourths of the focal zone. For both estimations, the temporal profile of the bubble-induced motion expanded with the increasing number of histotripsy pulses as the clot was increasingly fractionated and saturated around 300 histotripsy pulses when the clot was likely liquefied. The raw data from the three treated samples were analyzed to assess the statistical significance of the posited increasing trend. To account for the correlated nature of the data within each of the experiments, we performed linear regression fit using generalized estimating equations, a well-established approach for repeated measures analysis [54]. We modelled the correlation between measurements within each experiment using an auto-regressive structure, which models higher correlation between points that are temporally closer together. The BCD data was best fit by a cubic polynomial of time ( $BCD=0.81236+1.3356*Time-0.0395*Time^2+0.0003*Time^3$ ). The linear, quadratic, and cubic terms were statistically significant with respective term p-values of  $< 2.0*10^{-16}$ ,  $1.6*10^{-14}$ , and 0.0028. Consistently, the PIV data was best fit by a quadratic polynomial of time ( $PIV=11.3329+0.275*Time-0.004*Time^2$ ). The linear and quadratic terms were statistically significant with respective p-values of 0.011 and 0.006. These analysis results (positive linear coefficients and p-values  $< 0.05$ ) provide strong support that the increasing trend is statically significant. Although the velocity amplitudes estimated from PIV and BCD did not match exactly, the trend of the overall motion had a good agreement. The time period to reach the first peak rebound velocity after each histotripsy pulse increased until it plateaued at  $\sim 1.5$  ms after approximately 300 pulses. The time period to the peak second rebound velocity also had the same trend. In **Figure 6.12**, the times of the peak rebound velocity ( $t_{PRV}$ ) and peak second

rebound velocity ( $t_{PRV2}$ ) were extracted from the same treatment and compared between PIV and BCD estimations, the similarity of which was quantified using the Pearson linear correlation coefficient. The mean correlation coefficient was 92% over all the three treated locations.



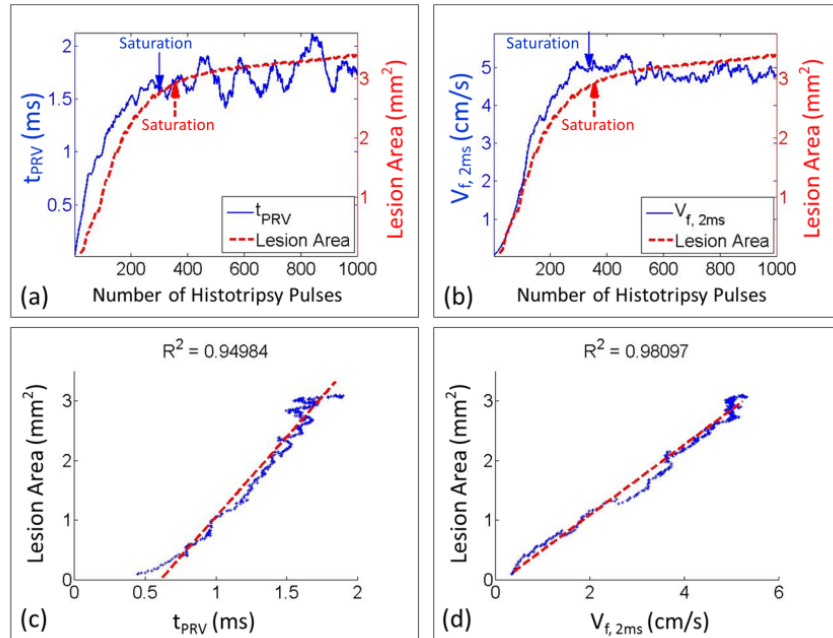
**Figure 6.11:** Representative full profiles of mean axial velocity at the focal zone. **(a)** PIV estimation (only the proximal side). **(b)** BCD estimation. Positive values indicate motion towards the therapy transducer and negative values indicate motion away from the transducer. The horizontal axis shows the number of applied pulses and the vertical axis shows the delay from each histotripsy pulse.



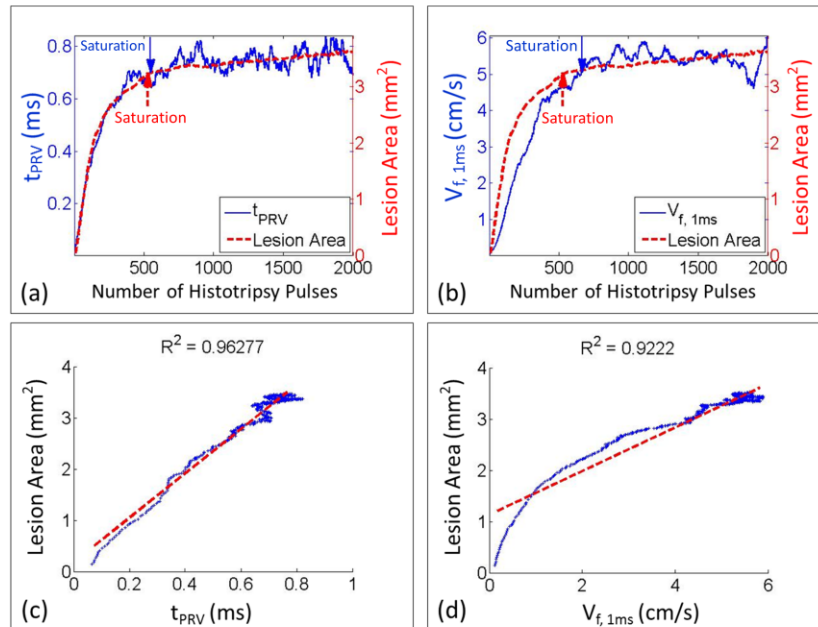
**Figure 6.12:** The times of peak rebound velocity ( $t_{PRV}$ ) and peak second rebound velocity ( $t_{PRV2}$ ) estimated by PIV and BCD as a function of the number of the applied histotripsy pulses from one of the treated locations. The lower curves represent  $t_{PRV}$  and the upper curves represent  $t_{PRV2}$ .

### 6.3.2 Correlation of BCD Feedback and Histotripsy Thrombolysis

The BCD feedback was correlated with the lesion progression measured by the optical images in the three-layer fibrin clots. For each treated spot, a progression curve of lesion area as a function of the number of the applied histotripsy pulses was generated to indicate the degree of thrombolysis and compared with the progression curves (20 points running-averaging) of the two metrics extracted from BCD feedback. For each spot treated in the soft clots, the lesion area increased almost linearly at the beginning and plateaued at around 300 pulses. The progression of the corresponding two BCD feedback metrics ( $t_{PRV}$  and  $V_{f, \text{delay}}$ ) followed a similar trend. They increased rapidly at the beginning and saturated around the same dose. After the saturation, the two BCD metrics fluctuated around the saturation level. A comparison of the lesion progression and the progressions of two BCD metrics from a soft clot spot was illustrated in **Figure 6.13**. For the hard clots, the lesion progression had the same increase-and-saturate pattern as those in the soft clots but saturated later around 600 pulses (**Figure 6.14**). The progressions of the two BCD feedback metrics again followed the same trend.

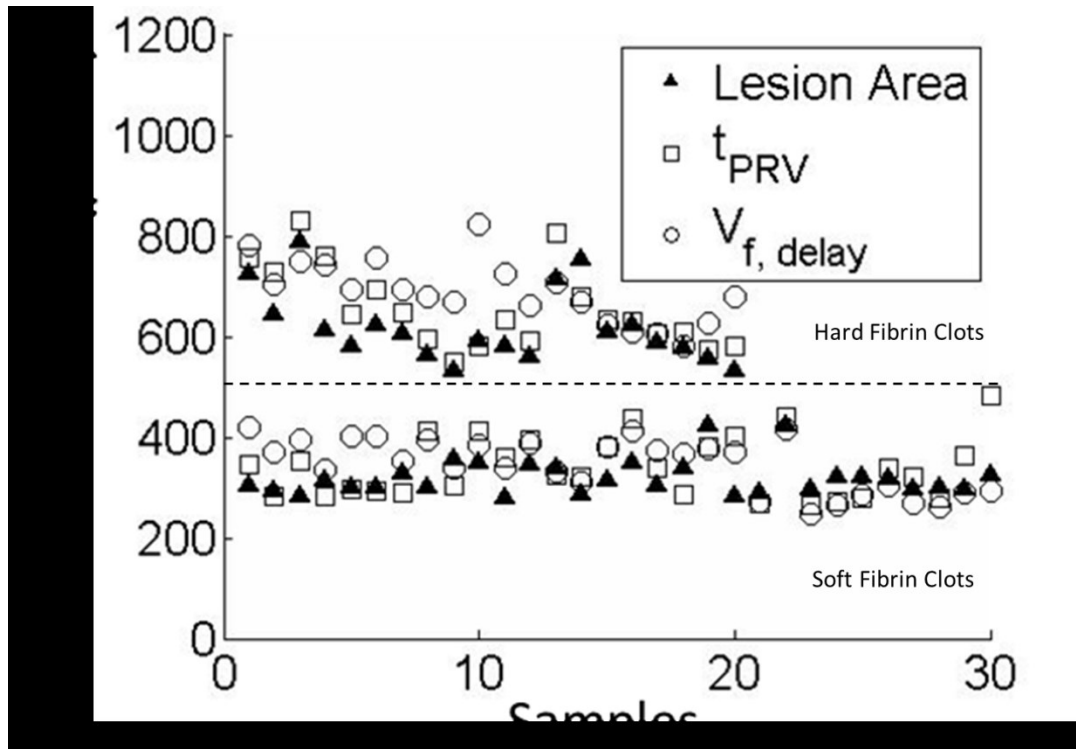


**Figure 6.13:** Comparison between BCD feedback and histotripsy thrombolysis from a representative treated spot in a soft fibrin clot. **(a)** The progression curve of lesion area is compared with the time of peak rebound velocity ( $t_{PRV}$ ) from its BCD feedback. **(b)** The progression curve of lesion area is compared with the mean velocity of the focal zone at 2ms delay ( $V_{f,2ms}$ ) from its BCD feedback. **(c)** The Pearson linear correlation between the progressions of lesion area and  $t_{PRV}$ . **(d)** The Pearson linear correlation between the progressions of lesion area and  $V_{f,2ms}$ . The detected saturation doses were also illustrated.



**Figure 6.14:** Comparison between BCD feedback and histotripsy thrombolysis from a representative treated spot in a hard fibrin clot. **(a)** The progression curve of lesion area is compared with the time of peak rebound time ( $t_{PRV}$ ) from its BCD feedback. **(b)** The progression curve of lesion area is compared with the mean velocity of the focal zone at 1ms delay ( $V_{f,1ms}$ ) from its BCD feedback. **(c)** The Pearson linear correlation between the progressions of lesion area and  $t_{PRV}$ . **(d)** The Pearson linear correlation between the progressions of lesion area and  $V_{f,1ms}$ . The detected saturation doses were also illustrated.

To quantitatively verify the correlation between the lesion progression and the BCD feedback for every treatment spot, their saturation doses were determined using the same slope detection algorithm described in Methods (**Figure 6.15**, **Table 6.1**). The differences of the saturation dose between the lesion progression and each of the two BCD metrics from each treatment were calculated and listed in **Table 6.2**. Using the  $t_{PRV}$  and  $V_{f, delay}$  metrics, the saturation doses detected closely followed the complete clot fractionation analyzed from the lesion optical images, both in soft and hard clots. The  $t_{PRV}$  metrics presented a slightly better accuracy than the  $V_{f, delay}$ . For example, in the soft clots, the mean difference between the saturation doses of  $t_{PRV}$  and clot fractionation was 21 pulses and that of  $V_{f, delay}$  was 25 pulses, while it took 319 pulses (mean) to completely fractionate the clot. In the hard clots, the mean saturation difference between  $t_{PRV}$  and clot fractionation was 38 pulses and that of  $V_{f, delay}$  was 71 pulses, while it took 618 pulses (mean) to completely fractionate the clot. In 17 of 50 treatments, the saturations of the BCD feedback were detected earlier (less than 40 pulses) than that of clot fractionation. The Pearson correlation coefficients among the three progression curves were also calculated. For the Pearson correlation coefficient calculation, the segments covering data points up to 100 data points after the saturation of the clot fractionation curve were first selected from the BCD  $t_{PRV}$  and  $V_{f, delay}$ . These data were then compared with the clot fractionation data. The mean Pearson correlation coefficient over all the treatments ( $N = 50$ ) is 93.2% for  $t_{PRV}$  and 92.6% for  $V_{f, delay}$  (**Table 6.3**).



**Figure 6.15:** The saturation doses of lesion progression, and its corresponding  $t_{PRV}$  and  $V_{f, delay}$ . 50 spots were collected in total, 30 of which were in soft fibrin clots and 20 were in hard fibrin clots. The 20 spots from the hard fibrin clots are all on the top of the ones from soft fibrin clots.

**Table 6.1:** The saturation doses (Mean  $\pm$  SD)

Progressions	Soft Clots (pulses, N=30)	Hard Clots (pulses, N=20)
Lesion	319 $\pm$ 35	617 $\pm$ 72
$t_{PRV}$	341 $\pm$ 59	656 $\pm$ 80
$V_{f, delay}$	344 $\pm$ 52	688 $\pm$ 62

**Table 6.2:** The differences between the BCD detected saturation doses and the corresponding lesion saturation doses.

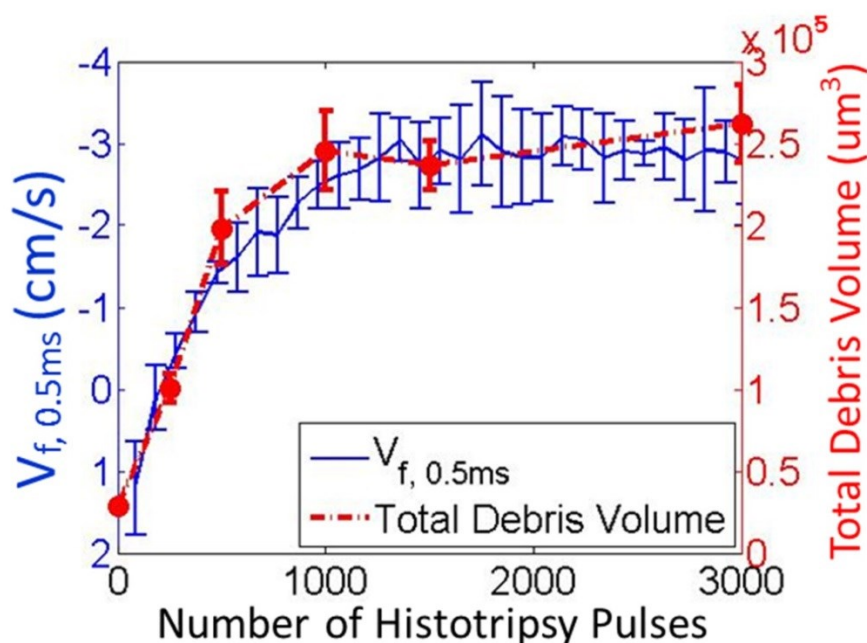
BCD Metrics		Soft Clots (pulses, N=30)	Hard Clots (pulses, N=20)	Total (pulses, N = 50)
$t_{PRV}$	Mean $\pm$ SD	21 $\pm$ 55	38 $\pm$ 43	28 $\pm$ 51
	Median (25%, 75%)	21 (-31, 66)	32 (19, 56)	31 (-13, 65)
$V_{f, delay}$	Mean $\pm$ SD	25 $\pm$ 53	71 $\pm$ 77	43.7 $\pm$ 67
	Median (25%, 75%)	25 (-19, 67)	80 (10, 130)	39 (-14, 101)



**Table 6.3:** The Pearson correlation coefficients (Mean  $\pm$  SD) between the BCD progression curves and their corresponding lesion progression curves

BCD Progressions	Soft Clots (N= 30)	Hard Clots (N= 30)	Total (N= 50)
$t_{PRV}$	93.7 $\pm$ 3.2%	92.4 $\pm$ 3.8%	93.2 $\pm$ 3.5%
$V_{f,delay}$	91.7 $\pm$ 7.9%	94.0 $\pm$ 3.3%	92.6 $\pm$ 6.5%

### 6.3.3 Validation of BCD Feedback in *In Vitro* Clots

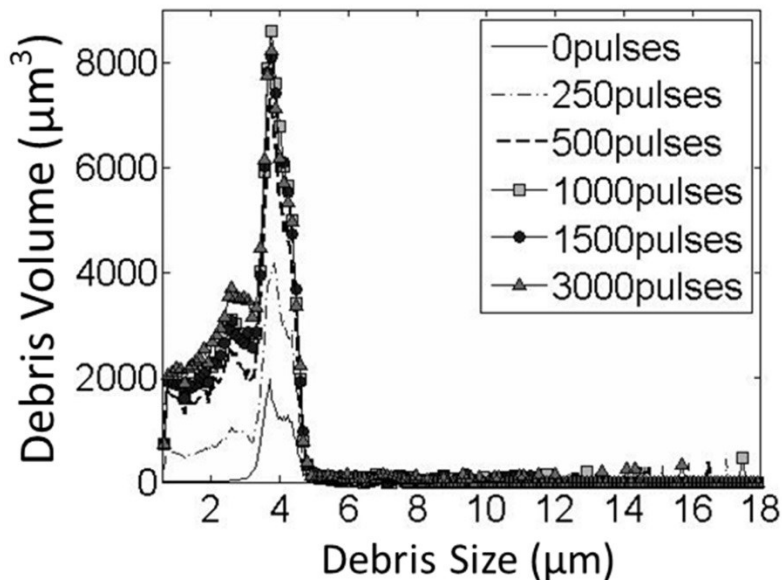


**Figure 6.16:** Comparison between the change of the fractionated debris volume and  $V_{f,0.5ms}$  from the BCD feedback.

The BCD feedback was validated in *in vitro* clots by comparing the progressions of  $V_{f,delay}$  with the change of clot debris volume generated by histotripsy treatment. The increasing and saturation trend of the average BCD feedback over all the 3000-pulse treatments matched well with that of the debris volumes measured at different therapy doses. The mean velocity of focal zone at 0.5ms delay ( $V_{f,0.5ms}$ ) from the BCD feedback was used and the total debris volume was used to characterize the debris distribution. In **Figure 6.16**, the mean of total debris volume

over all samples of each dose was plotted versus its corresponding histotripsy pulses used. The mean of total debris volume kept increasing for the first 1000 pulses and remains around the same level afterwards. The mean progression of  $V_{f,0.5ms}$  over all the treated spots in the 3000-pulse treatments was also plotted versus the number of applied pulses in the same figure. The  $V_{f,0.5ms}$  saturated at 1183 pulses (calculated by the slope detection algorithm) after rapidly increasing, which matched well with the clot debris volume measurement.

The size of the debris pieces generated by the histotripsy thrombolysis treatment was no greater than 30  $\mu\text{m}$ , as no blockage was observed during all the Coulter Counter measurements. The mean debris distribution over all the measurements of each dose is shown in **Figure 6.17**. The debris mainly ranged from 2 $\mu\text{m}$  to 6 $\mu\text{m}$  and 95% of them were smaller than 10 $\mu\text{m}$ .

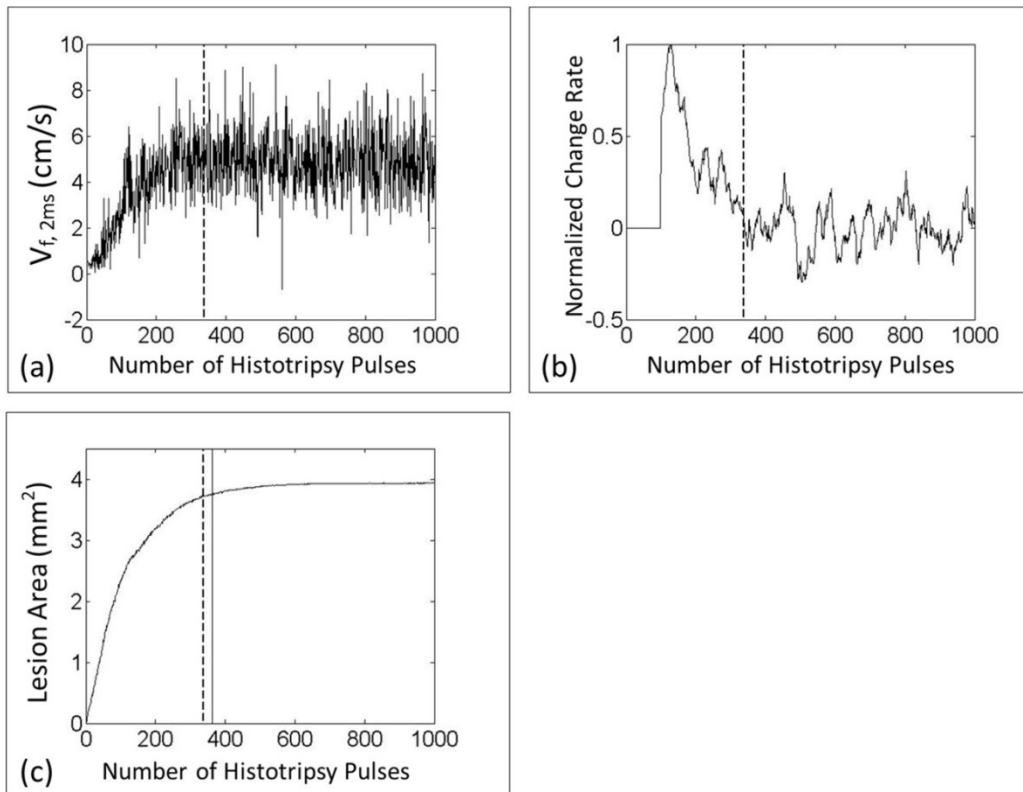


**Figure 6.17:** The debris distributions after histotripsy treatments with different doses. The 1000-pulse, 1500-pulse and 3000-pulse lines almost overlap with each other. The debris volume of the 500-pulse one (dashed line) is a little lower than the three higher-dose groups. The size of the majority of the fractionated debris is smaller than 6  $\mu\text{m}$  in all cases.

### 6.3.4 Real-time Monitoring of Histotripsy Thrombolysis using BCD Feedback

The ability of real-time BCD monitoring was validated in this set of experiment. The saturation dose using BCD feedback  $V_{f,\text{delay}}$  was detected in real time and compared with the saturation dose of its corresponding lesion progression quantified using optical imaging in the three-layer clot. The mean saturation dose detected by the BCD  $V_{f,2\text{ms}}$  was only 39 pulses (N = 10) more than the saturation dose detected by the lesion progression in the clot phantom, with a standard deviation of 55 pulses. On average it took 326 pulses to completely fractionate the clot. The saturations detected by BCD were later than the saturations of the lesion progressions in 6 out of 10 treatments. In the worst case, the difference between the two saturation doses was 61 pulses. The real-time  $V_{f,2\text{ms}}$  and its real-time change rate (slope) data from a spot are shown in

**Figure 6.18.**



**Figure 6.18:** (a) Real-time  $V_{f,2\text{ms}}$  of BCD feedback from one treated spot. (b) The real-time calculated change rate of  $V_{f,2\text{ms}}$ . (c) The corresponding progression of the lesion area. The vertical dashed line indicates the saturation dose real-time detected by the BCD feedback and the vertical solid line indicates the true saturation dose of the lesion progression, which represents the treatment completion.

## 6.4 Discussion

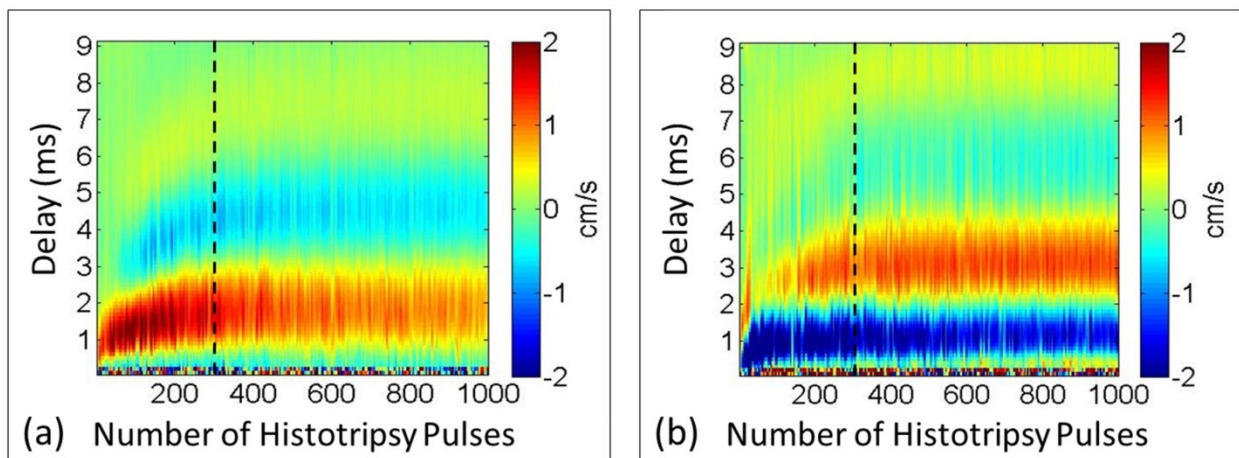
By the results of PIV and BCD estimations, the bubble-induced motions followed the same pattern after each histotripsy pulse: push away, rebound and then repeat, no matter how many pulses have been applied. High-speed images show that this motion is only observable when a bubble cloud is generated, hence called bubble-induced motion. The amplitude mismatch between PIV and BCD estimations may be caused by their resolution difference. PIV using optical images had better resolution and sensitivity which can detect smaller velocity than BCD. Since averaging only applied over non-zero values in the region of interest, PIV with more non-zero but small values led to a smaller mean velocity than BCD.

It is most likely the echoes for BCD primarily originated from the residual bubbles left from cavitation, as bubbles are much stronger reflectors compared to RBC and fibrin fragments. In all of our experiments, a 5MHz linear ultrasound probe was used for BCD. With this imaging frequency, whole blood (bovine, swine and canine) and fibrin clot (w/o RBCs) showed very weak speckles on B-mode images. But when monitoring histotripsy treatment on B-mode using the same probe, a region much brighter than blood and clot was observed even long after the arrival of the therapy pulse, which we used for BCD analysis. This hyperechoic region is thought to be dominated by residual cavitation nuclei.

The exact mechanism behind the bubble-induced motion is still under investigation. It could be caused by asymmetric bubble expansion during the formation of the bubble cloud, violent collapse of the bubble cloud and/or acoustic radiation force. The observed motion may be the result of these factors working on the targeted medium (i.e. tissue and blood clot). And as histotripsy pulses change the mechanical property of the medium, the motion behavior (velocity amplitude, push/rebound timing and duration) is changed accordingly. An important property of

the bubble-induced motion captured by both PIV and BCD is the two-stages of behavior of the coherent motions during each treatment. The first stage is characterized by a rapid changing of the motion behavior and the second stage is characterized by saturated, stable motion behavior. The BCD feedback tracks this change of the motion behavior, which is correlated to the tissue fractionation.

This two-stage phenomenon during histotripsy fractionation occurs for the motions both at the proximal side and the distal side of the focal zone. Although the motion behaviors at the two sides are different, they share the same changing trend and turn from the rapid changing stage into the stable stage at the same time (**Figure 6.19**). The results from the validation of BCD feedback in *in vitro* clots show that the distal-side motions can be also used to monitor the thrombolysis treatment. The distal-side motion is different from the proximal-side probably due to a counterforce formed by untreated tissue outside the distal end of the focal zone. If a larger volume (multiple treatment zones) of tissue is being fractionated simultaneously and BCD is collected only from the center of the focal zone in the absence of surrounding intact tissue, the motions at the proximal and distal sides of the focal zone will be similar in form [55].



**Figure 6.19:** Representative full profiles of mean axial velocity of PIV estimation. **(a)** Proximal side (three fourths of the whole focal zone). **(b)** Distal side. Although the motions at the two sides are different, the changing trends appear the same. To the left of the dashed line (around 300 pulses) is the rapid changing stage and to the right of the dashed line is the stable stage.

Histotripsy thrombolysis treatment can be monitored by BCD feedback via increase and saturation of the  $t_{PRV}$  or  $V_{f, \text{delay}}$ . The treatment completion is indicated by the saturation rather than a specific threshold value of a parameter. Validated using *in vitro* clots, the saturation of  $V_{f, \text{delay}}$  was detected in real-time to indicate treatment completion, and the saturation detection was within 50 pulses of complete clot fractionation. Regardless of different clot stiffnesses, the saturation doses of two BCD metrics are both highly consistent with the completion of clot fractionation. This capability of the BCD feedback to adaptively detect the treatment completion accurately even in clots with different properties is important in clinical situations when clots with different ages exhibit large, varied stiffness and a clot can itself be heterogeneous. The high Pearson correlation coefficient between the clot fractionation progression curve and the corresponding two BCD curves up to the saturation point also supports the feasibility of BCD feedback as a monitor for histotripsy thrombolysis.

The potential explanation for the increased temporal profile and saturation trend of BCD metrics as the clot is increasingly fractionated and eventually liquefied is that the change of bubble-induced motion depends on the change of mechanical properties of the targeted tissue. As the tissue is fractionated by histotripsy, the tissue elasticity is reduced until the tissue is completely liquefied [27, 56, 57]. As a result of the reduced tissue elasticity, the motion induced in the tissue by a given force is expected to exhibit a lower frequency oscillation (i.e. longer  $t_{PRV}$ ), as shown in a simulation study using finite element method (FEM) [58]. When the clot is completely fractionated, the bubble-induced motion reaches the maximum temporal expansion. Based on this principal, the BCD feedback captures the temporal characteristics of the bubble-induced motions in the two metrics ( $t_{PRV}$  and  $V_{f, \text{delay}}$ ) to quantitatively characterize the degree of histotripsy thrombolysis.

It shows that BCD feedback ( $V_{f,\text{delay}}$ ) was achieved real-time using a frame rate of 30 Hz, which is sufficient for real-time monitoring of histotripsy thrombolysis. To monitor  $V_{f,\text{delay}}$ , standard ultrasound color Doppler imaging is sufficient. The color Doppler pulses need to be synchronized with the histotripsy pulses, along with the appropriate pre-set Doppler parameters. No additional hardware is needed and the computation is simple and straightforward. To have the best signal-to-noise ratio and the closest trend representing the expanding temporal profile of the bubble-induced motion, the delay of  $V_{f,\text{delay}}$  with respect to each histotripsy pulse need to be carefully chosen so that the acquisition period can cover the major rebound period of the bubble-induced motion. A delay of 0.5 ms was chosen to capture the major rebound when the imaging probe was placed opposite to the therapy transducer detecting the distal-side motion, whereas a delay of 2 ms was chosen when the imaging probe was detecting the proximal-side motion. In reality, the main rebound period is unknown before treatment and it is a challenge to choose the right delay in the clinical application. Two potential solutions can be used to solve this issue. One is to enlarge the ensemble length of the acquisition from 10 to 20 or 30 frames so that the acquisition period will be wide enough to cover the main rebound period and the rebounding motion features can be reflected through an averaging effect. The other solution is to treat a testing spot in the clot before a full treatment and get the full velocity profile to decide the main rebound period and the appropriate delay. Real-time tracking of  $t_{\text{PRV}}$  is also possible and has the advantages of lower noise level and better match with the overall trend of the motions compared to  $V_{f,\text{delay}}$ . In the future, with a programmable ultrasound imaging system, real-time tracking of  $t_{\text{PRV}}$  may be also achieved.

## 6.5 Conclusion

The results of this chapter show that the potential of using BCD feedback to quantitatively monitor clot fractionation during histotripsy thrombolysis and accurately predict the completion of clot fractionation in real-time. The metrics of BCD,  $t_{PRV}$  and  $V_{f, delay}$ , are both strongly correlated with the degree of clot fractionation. Particularly, the saturation of the increase in  $t_{PRV}$  and  $V_{f, delay}$  coincide with the completion of clot fractionation in both soft and hard clots. This correlation will enable real-time monitoring of histotripsy thrombolysis and detection of treatment completion, which will help improve efficacy and reduce the risks of overtreatment.

## 6.6 References

- [1] X. Zhang, *et al.*, "Real-time feedback of histotripsy thrombolysis using bubble-induced color Doppler," *Ultrasound in medicine & biology*, vol. 41, pp. 1386-1401, 2015.
- [2] H. P. Adams, Jr., *et al.*, "Guidelines for thrombolytic therapy for acute stroke: a supplement to the guidelines for the management of patients with acute ischemic stroke. A statement for healthcare professionals from a Special Writing Group of the Stroke Council, American Heart Association," *Circulation*, vol. 94, pp. 1167-74, Sep 1 1996.
- [3] S. M. Bates and J. S. Ginsberg, "Clinical practice. Treatment of deep-vein thrombosis," *N Engl J Med*, vol. 351, pp. 268-77, Jul 15 2004.
- [4] P. A. Kyrle and S. Eichinger, "Deep vein thrombosis," *Lancet*, vol. 365, pp. 1163-74, Mar 26-Apr 1 2005.
- [5] K. Kasirajan, *et al.*, "Percutaneous AngioJet thrombectomy in the management of extensive deep venous thrombosis," *J Vasc Interv Radiol*, vol. 12, pp. 179-85, Feb 2001.
- [6] H. S. Kim, *et al.*, "Catheter-directed thrombolysis with percutaneous rheolytic thrombectomy versus thrombolysis alone in upper and lower extremity deep vein thrombosis," *Cardiovasc Intervent Radiol*, vol. 29, pp. 1003-7, Nov-Dec 2006.
- [7] R. Verhaeghe, *et al.*, "Catheter-directed lysis of iliofemoral vein thrombosis with use of rt-PA," *Eur Radiol*, vol. 7, pp. 996-1001, 1997.
- [8] M. W. Mewissen, *et al.*, "Catheter-directed thrombolysis for lower extremity deep venous thrombosis: report of a national multicenter registry," *Radiology*, vol. 211, pp. 39-49, Apr 1999.



- [9] S. Pfaffenberger, *et al.*, "2MHz ultrasound enhances t-PA-mediated thrombolysis: comparison of continuous versus pulsed ultrasound and standing versus travelling acoustic waves," *Thromb Haemost*, vol. 89, pp. 583-9, Mar 2003.
- [10] C. K. Holland, *et al.*, "Ultrasound-enhanced tissue plasminogen activator thrombolysis in an *in vitro* porcine clot model," *Thromb Res*, vol. 121, pp. 663-73, 2008.
- [11] K. E. Hitchcock, *et al.*, "Ultrasound-enhanced rt-PA thrombolysis in an *ex vivo* porcine carotid artery model," *Ultrasound Med Biol*, vol. 37, pp. 1240-51, Aug 2011.
- [12] J. Larsson, *et al.*, "Ultrasound enhanced thrombolysis in experimental retinal vein occlusion in the rabbit," *Br J Ophthalmol*, vol. 82, pp. 1438-40, Dec 1998.
- [13] A. V. Alexandrov, *et al.*, "Ultrasound-enhanced systemic thrombolysis for acute ischemic stroke," *N Engl J Med*, vol. 351, pp. 2170-8, Nov 18 2004.
- [14] G. Tsivgoulis, *et al.*, "Ultrasound enhanced thrombolysis in acute arterial ischemia," *Ultrasonics*, vol. 48, pp. 303-11, Aug 2008.
- [15] G. Tsivgoulis, *et al.*, "Safety and efficacy of ultrasound-enhanced thrombolysis: a comprehensive review and meta-analysis of randomized and nonrandomized studies," *Stroke*, vol. 41, pp. 280-7, Feb 2010.
- [16] S. Datta, *et al.*, "Ultrasound-enhanced thrombolysis using Definity as a cavitation nucleation agent," *Ultrasound Med Biol*, vol. 34, pp. 1421-33, Sep 2008.
- [17] A. T. Brown, *et al.*, "Microbubbles improve sonothrombolysis *in vitro* and decrease hemorrhage *in vivo* in a rabbit stroke model," *Invest Radiol*, vol. 46, pp. 202-7, Mar 2011.
- [18] W. C. Culp, *et al.*, "Successful microbubble sonothrombolysis without tissue-type plasminogen activator in a rabbit model of acute ischemic stroke," *Stroke*, vol. 42, pp. 2280-5, Aug 2011.
- [19] S. Datta, *et al.*, "Correlation of cavitation with ultrasound enhancement of thrombolysis," *Ultrasound Med Biol*, vol. 32, pp. 1257-67, Aug 2006.
- [20] C. Wright, *et al.*, "*In vitro* and *in vivo* high-intensity focused ultrasound thrombolysis," *Invest Radiol*, vol. 47, pp. 217-25, Apr 2012.
- [21] A. Burgess, *et al.*, "High-intensity focused ultrasound (HIFU) for dissolution of clots in a rabbit model of embolic stroke," *PLoS One*, vol. 7, p. e42311, 2012.
- [22] Z. Xu, *et al.*, "Controlled ultrasound tissue erosion," *IEEE Trans Ultrason Ferroelectr Freq Control*, vol. 51, pp. 726-36, Jun 2004.

- [23] Z. Xu, *et al.*, "Controlled ultrasound tissue erosion: the role of dynamic interaction between insonation and microbubble activity," *J Acoust Soc Am*, vol. 117, pp. 424-35, Jan 2005.
- [24] Z. Xu, *et al.*, "A new strategy to enhance cavitation tissue erosion using a high-intensity, Initiating sequence," *IEEE Trans Ultrason Ferroelectr Freq Control*, vol. 53, pp. 1412-24, Aug 2006.
- [25] Z. Xu, *et al.*, "Effects of acoustic parameters on bubble cloud dynamics in ultrasound tissue erosion (histotripsy)," *J Acoust Soc Am*, vol. 122, pp. 229-36, Jul 2007.
- [26] Z. Xu, *et al.*, "Evolution of bubble clouds induced by pulsed cavitation ultrasound therapy - histotripsy," *IEEE Trans Ultrason Ferroelectr Freq Control*, vol. 55, pp. 1122-32, May 2008.
- [27] A. D. Maxwell, *et al.*, "Noninvasive thrombolysis using pulsed ultrasound cavitation therapy - histotripsy," *Ultrasound Med Biol*, vol. 35, pp. 1982-94, Dec 2009.
- [28] A. D. Maxwell, *et al.*, "Noninvasive treatment of deep venous thrombosis using pulsed ultrasound cavitation therapy (histotripsy) in a porcine model," *J Vasc Interv Radiol*, vol. 22, pp. 369-77, Mar 2011.
- [29] E. C. Everbach, *et al.*, "Correlation of ultrasound-induced hemolysis with cavitation detector output *in vitro*," *Ultrasound Med Biol*, vol. 23, pp. 619-24, 1997.
- [30] S. L. Poliachik, *et al.*, "Effect of high-intensity focused ultrasound on whole blood with and without microbubble contrast agent," *Ultrasound Med Biol*, vol. 25, pp. 991-8, Jul 1999.
- [31] S. L. Poliachik, *et al.*, "Activation, aggregation and adhesion of platelets exposed to high-intensity focused ultrasound," *Ultrasound Med Biol*, vol. 27, pp. 1567-76, Nov 2001.
- [32] S. L. Poliachik, *et al.*, "The relation between cavitation and platelet aggregation during exposure to high-intensity focused ultrasound," *Ultrasound Med Biol*, vol. 30, pp. 261-9, Feb 2004.
- [33] A. Vanne and K. Hynynen, "MRI feedback temperature control for focused ultrasound surgery," *Phys Med Biol*, vol. 48, pp. 31-43, Jan 7 2003.
- [34] D. Arora, *et al.*, "MR thermometry-based feedback control of efficacy and safety in minimum-time thermal therapies: phantom and in-vivo evaluations," *Int J Hyperthermia*, vol. 22, pp. 29-42, Feb 2006.
- [35] F. A. Jolesz, "MRI-guided focused ultrasound surgery," *Annu Rev Med*, vol. 60, pp. 417-30, 2009.

- [36] K. Hynynen, "MRI-guided focused ultrasound treatments," *Ultrasonics*, vol. 50, pp. 221-9, Feb 2010.
- [37] N. L. Bush, *et al.*, "Acoustic properties of lesions generated with an ultrasound therapy system," *Ultrasound Med Biol*, vol. 19, pp. 789-801, 1993.
- [38] C. A. Damianou, *et al.*, "Dependence of ultrasonic attenuation and absorption in dog soft tissues on temperature and thermal dose," *J Acoust Soc Am*, vol. 102, pp. 628-34, Jul 1997.
- [39] N. R. Miller, *et al.*, "Imaging of temperature-induced echo strain: preliminary *in vitro* study to assess feasibility for guiding focused ultrasound surgery," *Ultrasound Med Biol*, vol. 30, pp. 345-56, Mar 2004.
- [40] A. N. Amini, *et al.*, "Noninvasive estimation of tissue temperature via high-resolution spectral analysis techniques," *IEEE Trans Biomed Eng*, vol. 52, pp. 221-8, Feb 2005.
- [41] R. Souchon, *et al.*, "Visualisation of HIFU lesions using elastography of the human prostate *in vivo*: preliminary results," *Ultrasound Med Biol*, vol. 29, pp. 1007-15, Jul 2003.
- [42] J. Bercoff, *et al.*, "Monitoring thermally-induced lesions with supersonic shear imaging," *Ultrason Imaging*, vol. 26, pp. 71-84, Apr 2004.
- [43] A. D. Janis, *et al.*, "A reconstituted *in vitro* clot model for evaluating laser thrombolysis," *J Thromb Thrombolysis*, vol. 13, pp. 167-75, Jun 2002.
- [44] H. Luo, *et al.*, "Effect of External Ultrasound Frequency on Thrombus Disruption *In Vitro*," *J Thromb Thrombolysis*, vol. 3, pp. 63-66, 1996.
- [45] E. A. Ryan, *et al.*, "Structural origins of fibrin clot rheology," *Biophys J*, vol. 77, pp. 2813-26, Nov 1999.
- [46] R. M. Bateman, *et al.*, "The Effect of Thrombin Concentration on Fibrin Clot Structure Imaged by Multiphoton Microscopy and Quantified by Fractal Analysis " *Microscopy and Microanalysis*, vol. 11, pp. 1018-1019, 2005.
- [47] J. E. Parsons, *et al.*, "Cost-effective assembly of a basic fiber-optic hydrophone for measurement of high-amplitude therapeutic ultrasound fields," *J Acoust Soc Am*, vol. 119, pp. 1432-40, Mar 2006.
- [48] M. H. Ross, *et al.*, *Histology: a text and atlas*, 2nd edition ed.: Williams & Wilkins (Baltimore), 1989.

- [49] A. D. Maxwell, *et al.*, "A tissue phantom for visualization and measurement of ultrasound-induced cavitation damage," *Ultrasound Med Biol*, vol. 36, pp. 2132-43, Dec 2010.
- [50] T. Y. Wang, *et al.*, "An efficient treatment strategy for histotripsy by removing cavitation memory," *Ultrasound Med Biol*, vol. 38, pp. 753-66, May 2012.
- [51] K. W. Lin, *et al.*, "Histotripsy beyond the intrinsic cavitation threshold using very short ultrasound pulses: microtriopsy," *IEEE Trans Ultrason Ferroelectr Freq Control*, vol. 61, pp. 251-65, Feb 2014.
- [52] C. S. Turner, "Slope Filtering: An FIR Approach to Linear Regression," *Ieee Signal Processing Magazine*, vol. 25, pp. 159-+, Nov 2008.
- [53] J. E. Browne, *et al.*, "Assessment of the acoustic properties of common tissue-mimicking test phantoms," *Ultrasound Med Biol*, vol. 29, pp. 1053-60, Jul 2003.
- [54] S. L. Zeger and K.-Y. Liang, "Longitudinal data analysis for discrete and continuous outcomes," *Biometrics*, pp. 121-130, 1986.
- [55] R. M. Miller, *et al.*, "Investigation of the mechanism of ARFI-based Color Doppler feedback of histotripsy tissue fractionation," in *Ultrasonics Symposium (IUS), 2013 IEEE International*, Prague, 2013, pp. 934 - 937.
- [56] T. Y. Wang, *et al.*, "Imaging feedback of histotripsy treatments using ultrasound shear wave elastography," *IEEE Trans Ultrason Ferroelectr Freq Control*, vol. 59, pp. 1167-81, Jun 2012.
- [57] T. Y. Wang, *et al.*, "Imaging feedback for histotripsy by characterizing dynamics of acoustic radiation force impulse (ARFI)-induced shear waves excited in a treated volume," *IEEE Trans Ultrason Ferroelectr Freq Control*, vol. 61, pp. 1137-51, Jul 2014.
- [58] M. L. Palmeri, *et al.*, "Dynamic mechanical response of elastic spherical inclusions to impulsive acoustic radiation force excitation," *IEEE Trans Ultrason Ferroelectr Freq Control*, vol. 53, pp. 2065-79, Nov 2006.

## Chapter 7

### Noninvasive Thrombolysis using Microtripsy in a Porcine Deep Vein Thrombosis Model

A majority component of this chapter has been submitted to Journal of Vascular and Interventional Radiology.

#### 7.1 Introduction

Deep vein thrombosis (DVT) is the most common form of venous thrombosis and can lead to pulmonary embolism (PE). DVT/PE affects over 300,000 people and results in the deaths of 60,000 to 100,000 people each year in the United States [1]. In addition to anticoagulation, some DVT patients, especially those with severe symptoms, may require thrombolytic treatments, including systemic administration of thrombolytic drugs [2, 3], catheter-directed infusion of thrombolytic drugs, or mechanical thrombectomy. Systemic administration of thrombolytic drugs has limited effectiveness and requires prolonged time for affect (several hours to days) [4]. Catheter-directed thrombolysis can deliver drugs locally at the thrombosis site, but it is invasive and carries risks of bleeding, vascular damage, clot detachment, and infection [5]. In more severe cases, such as phlegmasia cerulea dolens, surgical or percutaneous mechanical thrombectomy may be performed [6].

Histotripsy is a noninvasive tissue ablation method that mechanically fractionates soft tissue using ultrasound [7-9]. High-intensity, microsecond-long ultrasound pulses are focused to generate well-controlled acoustic cavitation to fractionate target tissue without thermal necrosis. The feasibility of using histotripsy as a noninvasive and image-guided thrombolysis method was first shown by Maxwell *et al.* [10, 11]. Histotripsy was used to fractionate blood clots into

acellular debris using ultrasound alone both *in vitro* and in an *in vivo* porcine DVT model. The safety concerns (primarily hemolysis) of histotripsy in circulating blood were also addressed by Devanagondi *et al.* [12]. In the previous studies, multi-cycle (usually  $\geq 5$  cycle) ultrasound pulses were used to generate acoustic cavitation via a shock scattering mechanism [13]. Using the shock scattering mechanism, a shock front scatters from individual sparse bubbles formed from weak nuclei resulting in an inverted shockwave. This inverted shockwave combines with the incoming negative pressure phase to create very high negative pressures exceeding the cavitation threshold and generates a cavitation cloud. Because the shock scattering approach relies on the weak nuclei which often reside in the vessel wall, cavitation generated by this approach is usually less-confined and forms near the vessel wall. This poor localization within the clot can result in vessel damage and hemolysis.

Microtripsy is a new histotripsy approach that has recently been evaluated for its use in thrombolysis [14-16]. Microtripsy uses the intrinsic threshold mechanism where acoustic cavitation is generated via single-cycle ultrasound pulses with the negative pressure phase directly exceeding the cavitation threshold intrinsic to the media. The intrinsic threshold mechanism does not rely on pre-existing weak nuclei and is more reproducible and predictable than the shock scattering mechanism [17, 18]. Our *in vitro* microtripsy thrombolysis study showed that cavitation can be precisely generated and confined to the vessel lumen without contacting the vessel wall, which allows for creation of a precise flow channel within the clot while minimizing the risk of vessel damage [14].

This *in vivo* study investigated the safety and efficacy of microtripsy-mediated thrombolysis in a porcine DVT model. Thrombi were created in the femoral veins of juvenile pigs and then treated using an integrated, portable microtripsy thrombolysis system. Ultrasound

images were used to guide and monitor the treatment. Ultrasound cross-sectional scans of the femoral vein were acquired before and after each thrombolysis treatment for qualitative and quantitative assessments of treatment efficacy. To evaluate the treatment safety, vessel damage was examined by histology. Blood samples were collected to evaluate the degree of hemolysis induced during microtripsy thrombolysis. In addition to acute pigs, which were euthanized right after therapy, four pigs were survived for two weeks to assess the subacute extent of any vessel damage and/or hemolysis.

## **7.2 Materials and Methods**

### **7.2.1 Animal Preparation and Thrombus Formation**

The protocols involved in this study have been approved by the University Committee on Use and Care of Animals at our university. A porcine DVT model, previously described by Maxwell *et al.* [11], was used in this study. Juvenile pigs (mixed breed) weighing approximately 35 kg were selected as the subjects of the study. The animal was first sedated with 6 mg/kg tiletamine + zolazepam (Telazol, Fort Dodge Animal Health, Fort Dodge, Iowa, USA) and 2.2 mg/kg xylazine (Lloyd Laboratories, Shenandoah, Iowa, USA). The animal was then endotracheally intubated and rotated to a supine position onto a medical grade, water-filled heating pad to maintain body temperature. 0.5%–3.5% isoflurane (Vet-One, Meridian, Idaho, USA) was administered through the endotracheal tube for anesthesia. The animal was attached to monitoring equipment for continuous monitoring of core body temperature, pulse, SpO<sub>2</sub> levels, and respiratory rate throughout the procedure. A chemical depilatory (Nair, Church & Dwight Co, Princeton, New Jersey, USA) was applied on the legs and the lower quadrant for 10 minutes, followed by a surgical preparation consisting of three applications of betadine scrub followed by a sterile saline rinse and an application of iodine. The area was then draped with a sterile drape.

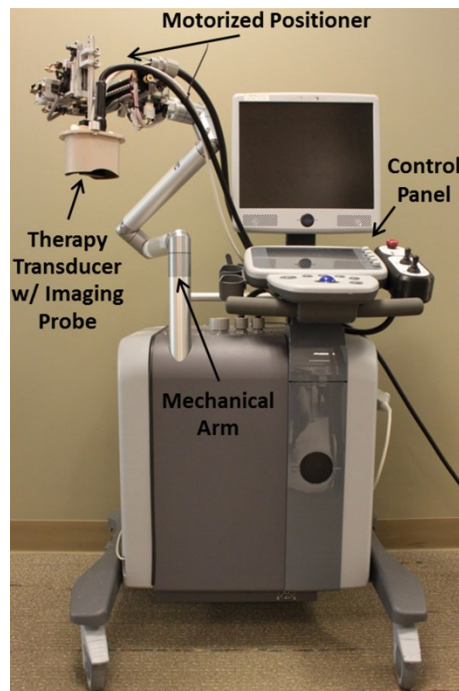
Two 5-Fr wedge occlusion balloon catheters (AI-07124, Arrow International, Reading, Pennsylvania, USA) were introduced percutaneously into the left femoral vein from the distal side of the desired location for thrombus formation [11]. The two balloons were positioned and inflated to occlude a 1.5-cm segment at the desired location in the vein. 0.5 mL thrombin (1000 IU/mL) was then infused through the distal catheter into the occluded region in the vein to stimulate thrombus formation. Heparin (200 U/kg, IV) was administered systemically through an ear-vein catheter immediately after thrombin infusion to prevent blood coagulation outside the occluded region. The balloons remained inflated for two hours to allow the thrombus to become fully formed [19]. The balloons were then deflated and the catheters were removed from the vein. Blood pressure was continuously monitored from the carotid artery. Additional heparin (200 U/kg, IV) was administered every hour from the start of thrombus formation to the end of treatment to maintain an activated clotting time (ACT) of blood greater than 200 seconds. For the animals to be euthanized right after treatment, high dose pentobarbital (140-160 mg/kg, IV) was given. For the animals that were euthanized at two weeks after treatment, carprofen (2-4 mg/kg, SC) was given before treatment for pain relief, and protamine (0.5 mg/kg, IV) was given at the end of treatment to lower the ACT. The animals were continuously monitored until they were recovered from anesthesia and returned to the housing facility when they were fully mobile. Animals were observed twice daily for 48 hours for pain levels, activity levels, feeding activity, and any evidence of bleeding. Carprofen (2-4 mg/kg, PO) was given every 12-24 hours as needed until the animal returned to baseline activity levels.

### **7.2.2 Microtripsy Thrombolysis System and Setup**

Thrombolysis treatments were performed with an integrated and portable microtripsy system, which was developed in-house for this specific application [14]. It consisted of three



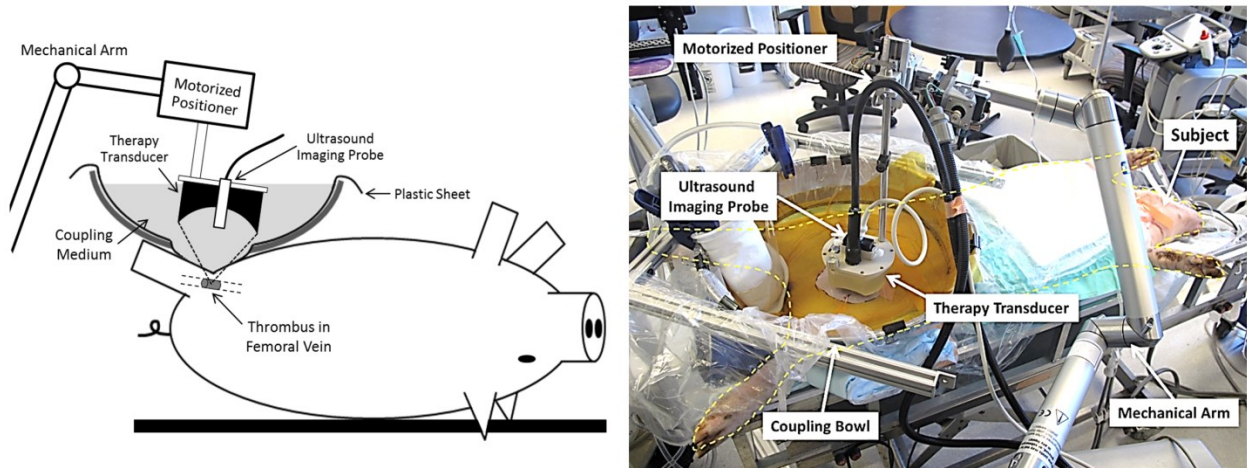
subsystems: a microthrombolysis therapy system, an ultrasound imaging system, and a positioning system (**Figure 7.1**). Microthrombolysis pulses were generated by a 1-MHz, 18-element therapy transducer (Imasonic, Besancon, France) with an effective 10×8-cm aperture and a 7-cm focal length. A 7.5-MHz ultrasound imaging probe (Vermon, Tours, France) was embedded in the rectangular central hole of the therapy transducer to guide and monitor microthrombolysis treatment. The positioning system, including a compact motorized positioner and a multi-degree-of-freedom mechanical arm, provided high-resolution and large-range mobility for the therapy transducer. Control software with a clinician-friendly interface was developed to manage treatments.



**Figure 7.1:** The integrated microthrombolysis system. It consists of an ultrasound imaging system, a microthrombolysis therapy system, and a motorized positioning system. A linear imaging probe was embedded at the center of the therapy transducer. The therapy transducer is mounted on the top of the positioning system. Treatment is controlled using touch screen interface and physical buttons on the control panel.

To enable direct ultrasound transmission between the therapy transducer and the subject, an Ioban<sup>®</sup> sheet (3M, St Paul, Minnesota, USA) was first pasted onto a larger polyethylene sheet from which a 25-cm-diameter circular piece was previously removed. The Ioban<sup>®</sup>, exposed by

the central hole, was then pasted on to the subject's skin. The Ioban<sup>®</sup> sheet was then cut away around the area of treatment. A bottomless bowl was placed around the combined sheet and was then filled with a water-based coupling medium developed in-house that was set to body-temperature and degassed overnight. This provided a clear acoustic window while still maintaining a water-tight seal that prevented the coupling medium from leaking. The experimental setup is shown in **Figure 7.2**.



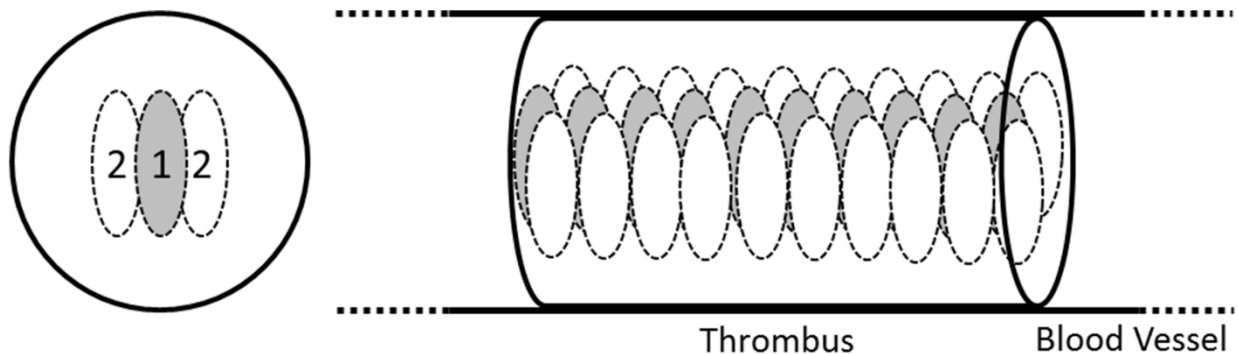
**Figure 7.2:** Schematic experimental setup (Left) and a picture of the actual setup during one thrombolysis treatment (Right).

### 7.2.3 Pre-treatment Planning

The focus of the therapy transducer was first calibrated in the coupling bath. Cavitation was generated by firing microtripsy pulses in the coupling media, and the cavitation bubble cloud was shown as a bright (hyperechoic), dynamic region on the ultrasound image. The center of the cavitation region was then marked as the therapy focus on the ultrasound imaging window. The therapy transducer was re-positioned to align the therapy focus within the left femoral vein where the thrombus was formed. The therapy focus, aiming at the center of the vessel lumen, was moved from the distal end to the proximal end of the thrombus. The moving path was linearly interpolated into a treatment path with treatment locations spaced by 0.3 mm.

### 7.2.4 Treatments

A dual-pass strategy, previously developed in our lab [16], was used for the thrombolysis treatments in this study. The thrombus was treated with microtripsy in two passes (**Figure 7.3**). In the first pass, the treatment zone was covered by one focus (the original therapy focus) at each treatment location and scanned through the thrombus following the preset treatment path. In the second pass, the treatment zone followed the preset treatment path and scanned through the thrombus again but was covered by two foci electronically steered to the lateral sides of the first-pass focus. A pulse repetition frequency (PRF) of 100 Hz and a dose of 1000 pulses (10 seconds) at each focus was used for microtripsy treatments. The treatment time for each two-pass treatment was 16 min per cm length clot. With 1.5 to 2 cm overlying tissue and 0.5 dB/cm-MHz acoustic attenuation of the overlying tissue, the in situ peak negative pressure (P-) of the microtripsy pulses was estimated to be 34 to 35 MPa. In total, fourteen pigs were treated with microtripsy. Ten pigs were euthanized (Pentobarbital, 140-160 mg/kg, IV) within one hour after treatment (acute) and four pigs were recovered and euthanized two weeks later (subacute).



**Figure 7.3:** Illustration of the dual-pass treatment. Each ellipse represents a focal zone with the number of the treatment pass. The gray foci were treated in the first treatment pass and the white foci were treated in the second treatment pass.

In 8 acute pigs, microtripsy treatment was also applied to the right femoral vein with no thrombi. Exposure of microtripsy in free blood flow in the femoral vein was considered to be the worst scenario test to evaluate the safety of microtripsy thrombolysis treatment, as it maximized the potential contact between cavitation and vessel wall (without the clot barrier between the two) and thus would lead to maximal vessel damage. In addition, the maximal volume blood would be exposed to cavitation that could induce increased hemolysis without the thrombus barrier [11, 12]. The same dual-pass strategy and microtripsy parameters used in the thrombolysis treatment in the left femoral vein were used in the free-flow treatments in the right femoral vein. An 18-mm segment of the right femoral vein was treated for each pig (30 minutes).

#### **7.2.5 Measurements and Evaluations**

To qualitatively evaluate the efficacy of the microtripsy thrombolysis treatments, ultrasound B-mode and color Doppler images of the left femoral vein were collected before, right after and two weeks after the treatments to compare the volumes of the thrombi and the blood flows in the veins. A 10-MHz linear imaging probe (L14-5, Ultrasonix, Vancouver, Canada) was placed directly on the skin to image the thrombi and the veins. For quantitative analysis, the thrombi were 3D-scanned before and right after the treatments. Before each treatment, the 10-MHz imaging probe was mounted to a positioning system and positioned in the coupling bath to image the cross sections of the thrombus. A path was set to scan the imaging probe through the thrombus, acquiring a scan image every 0.2 mm. There was no direct contact between the imaging probe and the skin to avoid tissue movements during the scanning. After treatment, the imaging probe was scanned through the thrombus using the exact same path. The contours of the thrombus and the vessel lumen on each scan image were depicted manually in

Matlab (The Mathworks, Natick, MA, USA). The diameter of the generated flow channel was quantified as the diameter of a circle with equivalent cross-sectional area on scan images.

Blood samples were collected before and after the thrombolysis treatments, after the free-flow treatments, and two weeks later for the subacute pigs. Serum laboratory studies and hemodynamic values were reported from each sample. Since the free-flow treatments always followed the thrombolysis treatments, the post-thrombolysis data were also used as the baseline data for the free-flow treatments. Carotid artery pressure was obtained at the start of each treatment and every 10 minutes during the treatment for all subjects.

The left femoral bundles, where the thrombolysis treatments were conducted, were harvested together with surrounding tissue from the 4 subacute pigs. The right femoral bundles, where the free-flow treatments were conducted, were harvested with surrounding tissue from the 8 acute pigs. Since the catheter and balloon procedures for thrombus formation caused significant vessel damage and would confound the data [11], the left femoral veins of all the acute pigs were not collected for evaluation of vessel damage. The harvested tissues were immersed in 10% buffered formalin for fixation. The cross sections of the femoral bundles were then embedded in paraffin, sectioned, stained with hematoxylin and eosin and examined with a light microscope for signs of damage. The lungs from one acute pig and one subacute pig were fixed with 10% formalin and grossly examined for emboli.

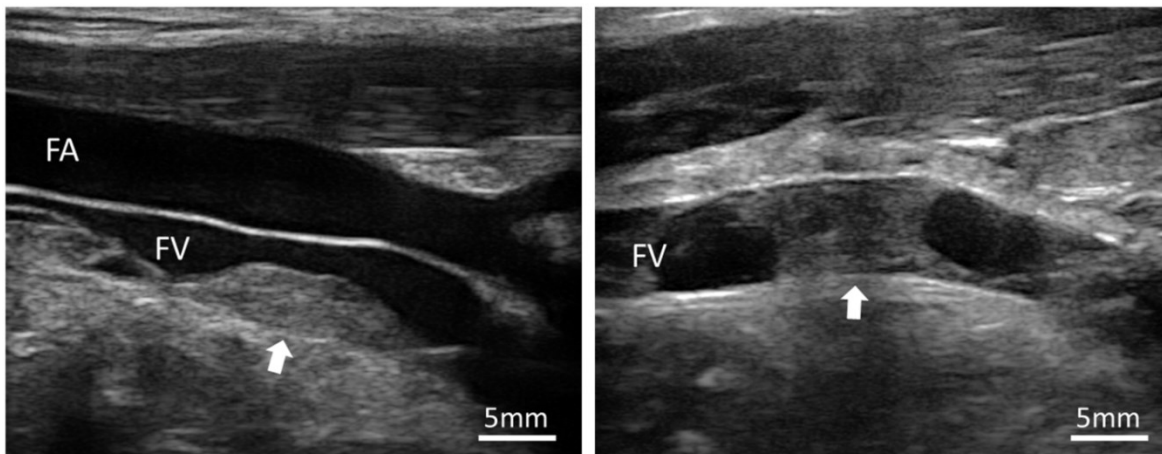
### **7.2.5 Statistical Analysis**

All statistical comparisons in this study were performed using Student's t-test. P-values < 0.01 were considered significant. Numerical data are expressed as mean  $\pm$  standard deviation.

## **7.3 Results**

### **7.3.1 Thrombus**

Thrombi were formed in the left femoral veins of the 14 subjects at a depth of 16 to 22 mm from skin (**Figure 7.4**). The lengths of the thrombi ranged from 7.5 to 28.6 mm, with an average length of 16.0 mm. The diameters of the veins where the thrombi were formed had a mean of 6.7 mm and a standard deviation (SD) of 1.1 mm. Nine thrombi were completely occlusive and five were partially occlusive with an occlusion percentage of  $81.9 \pm 12.2$  % (mean  $\pm$  SD). The morphological characteristics of the thrombi are summarized in **Table 7.1**.



**Figure 7.4:** Partially and fully occlusive thrombi (Arrow) formed in femoral veins. FV: Femoral Vein; FA: Femoral Artery.

**Table 7.1:** Summary of Thrombus Formations and Treatment Outcomes

	<b>Partial</b>	<b>Occlusive</b>	<b>Total</b>
No. of Treatments	5	9	14
Thrombus Length (mm)	$15.3 \pm 1.9$	$16.3 \pm 6.9$	$16.0 \pm 5.6$
Vessel Inner Diameter (mm)	$7.5 \pm 1.2$	$6.2 \pm 0.8$	$6.7 \pm 1.1$
Vessel Occlusion (Area %)*	$81.9 \pm 12.2$	100	$93.5 \pm 11.3$
No. of Treatments with Flow Improved	5	8	13
Increase in Channel Diameter (mm)	$2.8 \pm 1.2$	$3.6 \pm 0.8$	$3.3 \pm 1.0$
Occlusion Reduction (Area %)**	$13.3 \pm 4.7$	$32.6 \pm 6.1$	$26.7 \pm 10.8$
Channel Opening (Diameter %)***	$34.4 \pm 12.8$	$56.2 \pm 9.4$	$50.0 \pm 14.4$

\* Vessel Occlusion = occluded cross-sectional area / total vessel lumen area  $\times$  100%

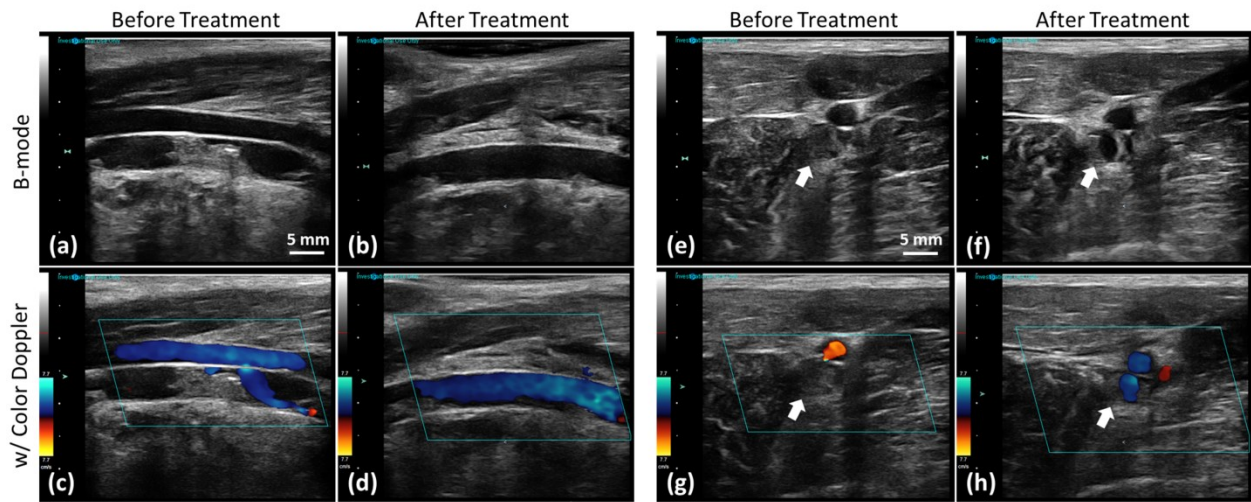
\*\* Occlusion Reduction (Area %) = (pre-treatment vessel occlusion - post-treatment vessel occlusion) / pre-treatment vessel occlusion  $\times$  100%

\*\*\* Channel Opening (Diameter %) = generated channel diameter / vessel diameter  $\times$  100%

### 7.3.2 Cavitation

In all 14 subjects, during the thrombolysis treatments, cavitation bubble clouds were generated at the marked therapy focus without any spatial shift and were well confined within the target thrombi without contacting the femoral veins (Video). There was no pre-focal or post-focal cavitation observed on the vessel walls or surrounding tissues. The cavitation bubble cloud remained at the therapy focus when it scanned through thrombus. During the free-flow treatments, cavitation behaved differently. Although the therapy focus was targeted at the center of the vessel lumen, the cavitation bubble clouds were only sporadically visible on the B-mode image but occurred in both the free blood flow and on the post-focal vessel walls and tissues.

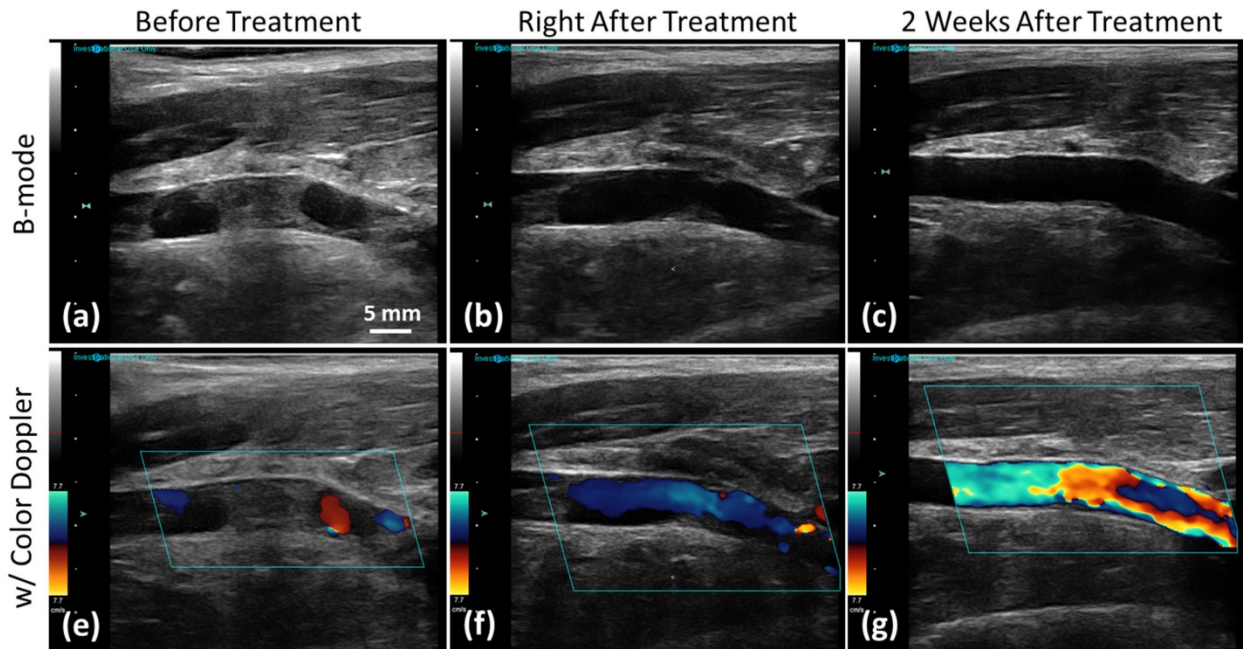
### 7.3.3 Recanalization



**Figure 7.5:** Representative US B-mode images (first row) and color Doppler images (second row) taken before and right after microtripsy thrombolysis treatment in an acute pig. (a)-(d): Longitudinal sections of the femoral vein. (e)-(h): Cross sections of the femoral veins (indicated by the black arrows).

As shown by color Doppler imaging, blood flow was restored or significantly improved by the microtripsy treatments in 13 of the 14 subjects (**Figure 7.5 and 7.6**). In the one treatment where no flow was restored, the thrombus could not be completely scanned through by microtripsy due to the extension of the thrombus to regions (deep into abdomen) with limited

acoustic access. Thrombus volume reductions, indicated by brightness decrease on B-mode imaging, were observed in all treatments. **Figure 7.5** shows ultrasound images of the femoral vein taken before and right after one thrombolysis treatment in an acute pig.

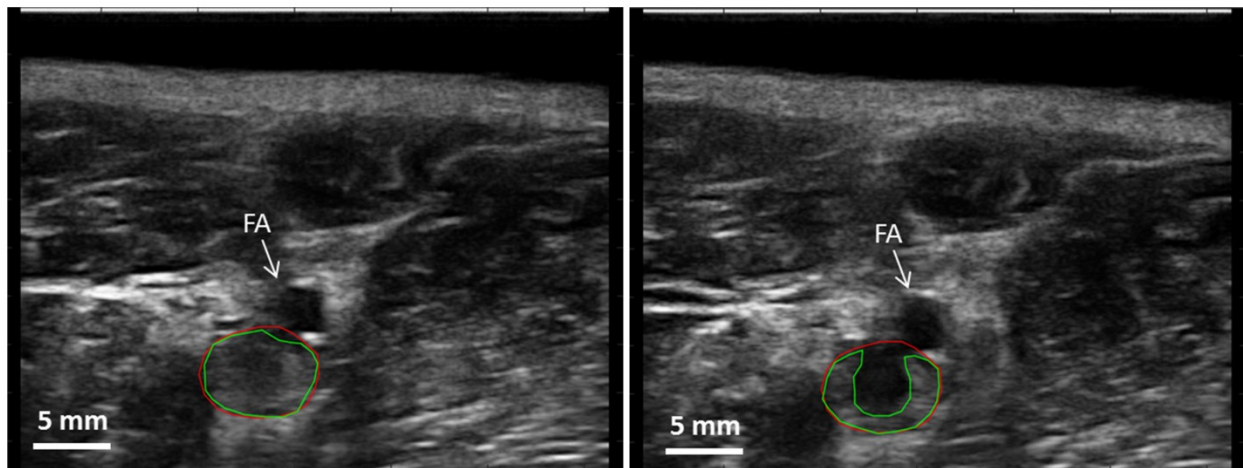


**Figure 7.6:** Representative US B-mode images (first row) and color Doppler images (second row) taken before, right after and two weeks after microtripsy thrombolysis treatment in a subacute pig. Blood flow was increased after two weeks of recovery compared to that right after the treatment. Since a relatively smaller velocity scale was chosen to be consistent throughout all the color Doppler images, velocity aliasing occurred on the two-week color Doppler image (g) with an increased blood flow.

**Figure 7.6** shows ultrasound images of the femoral vein taken before, right after and two weeks after one thrombolysis treatment in a subacute pig. For the subacute pigs, no remaining thrombus was observed in the femoral veins on ultrasound B-mode or color Doppler images after two weeks of recovery. The femoral veins appeared normal on the B-mode images. As shown on the color Doppler images of **Figure 7.6(g)** and **(f)**, the blood flow after two weeks of recovery was further increased compared to the blood flow right after treatment, which was due to dissolution of both the remaining thrombus at the treatment site and the untreated thrombus outside the treatment site over two weeks.



Quantitative evaluation of the thrombolysis efficacy was conducted using the pre- and post-treatment scan images of the thrombi (**Figure 7.7**). Cross sections of the flow channels generated in thrombi were distinguished as regions with significant echogenicity reduction between the pre- and post-treatment scan images. The flow channels generated in the fully occlusive thrombi had a diameter of  $3.6 \pm 0.8$  mm, in comparison to a mean vessel diameter of 6.2 mm. The increase in channel diameter in the partially occlusive thrombi was  $2.8 \pm 1.2$  mm. Occlusion (percent of cross-sectional area) was reduced by  $32.6 \pm 6.1\%$  and  $13.3 \pm 4.7\%$  in the fully and partially occlusive thrombi, respectively. The vessels were opened by  $56.2 \pm 9.4\%$  and  $34.4 \pm 12.8\%$  (generated channel diameter vs. vessel diameter) in the fully and partially occlusive thrombi, respectively. The average treatment time was 16 minutes per cm-long thrombus. The quantitative results are also presented in **Table 7.1**.



**Figure 7.7:** Quantification of flow channel generated by microtripsy. On the left is the ultrasound image taken before treatment. On the right is the ultrasound image taken at the exact same location right after treatment. Green lines indicate the boundaries of the thrombi and red lines indicate the vessel lumen.

### 7.3.4 Blood

**Table 7.2:** Blood Contents Change. “\*” indicates significant difference.

	Thrombolysis Treatments (N = 14)		Free-flow Treatments (N = 8)		Two Weeks of Recovery (N = 4)	
	Baseline <sup>1</sup>	Post	Baseline <sup>2</sup>	Post	Baseline <sup>3</sup>	Two weeks later
Free Hgb (mg/dL)	3.8 ± 3.4	63.2 ± 21.6*	56.7 ± 25.1	78.1 ± 13.9	2.3 ± 0.8	2.1 ± 1.0
LDH (U/L)	404.4 ± 104.3	524.6 ± 130.1*	554.1 ± 132.0	608.4 ± 164.5	355.0 ± 78.0	334.5 ± 67.0
K (mmol/L)	4.1 ± 0.2	4.9 ± 0.5*	4.7 ± 0.4	4.9 ± 0.5	4.0 ± 0.3	3.6 ± 0.2
Serum Hematocrit (%PCV)	26.6 ± 2.5	27.1 ± 3.2	27.3 ± 3.9	27.3 ± 3.1	28.3 ± 1.0	25.3 ± 3.6
pH	7.3 ± 0.1	7.3 ± 0.1	7.4 ± 0.1	7.4 ± 0.1	7.3 ± 0.1	7.4 ± 0.03
SBP (mmHg)	81.4 ± 11.2	86.6 ± 10.8	84.5 ± 9.2	86.0 ± 11.3	NA	NA
HR (BPM)	79.8 ± 11.2	79.9 ± 12.5	76.6 ± 13.6	78.4 ± 14.5	NA	NA

<sup>1</sup> The baselines are the measurements before any treatments and calculated using all 14 samples.

<sup>2</sup> The baselines are the measurements after the thrombolysis treatments and before the free-flow treatments and calculated only using the corresponding 8 samples.

<sup>3</sup> The baselines are the measurements before any treatments and calculated only using the corresponding 4 samples.

Hemodynamic and hematological effects of the microtripsy treatments are shown in **Table 7.2**. Over the 14 thrombolysis treatments, there were significant increases in free hemoglobin ( $3.8 \pm 3.4$  mg/dL baseline vs  $63.2 \pm 21.6$  mg/dL after treatment,  $P < 0.0001$ ) and lactate dehydrogenase (LDH) ( $404.4 \pm 104.3$  U/L baseline vs  $524.6 \pm 130.1$  U/L after treatment,  $P < 0.01$ ). There was a small but statistically significant increase ( $P < 0.0001$ ) in serum potassium ( $4.1 \pm 0.2$  mmol/L baseline vs  $4.9 \pm 0.5$  mmol/L after treatment). No significant difference was shown in serum hematocrit ( $P = 0.32$ ) between the baseline ( $26.6 \pm 2.5\%$ ) and post-treatment ( $27.1 \pm 3.2\%$ ). With regard to hemodynamic responses, there were no significant changes in system systolic blood pressure ( $81.4 \pm 11.2$  mmHg vs  $86.6 \pm 10.8$  mmHg,  $P = 0.11$ ) or heart rate ( $79.8 \pm 11.2$  BPM vs  $79.9 \pm 12.5$  BPM,  $P = 0.49$ ).

After two weeks of recovery for the 4 subacute pigs, all the parameters returned back to the pre-treatment baseline. Free hemoglobin decreased back to  $2.1 \pm 1.0$  mg/dL, which showed

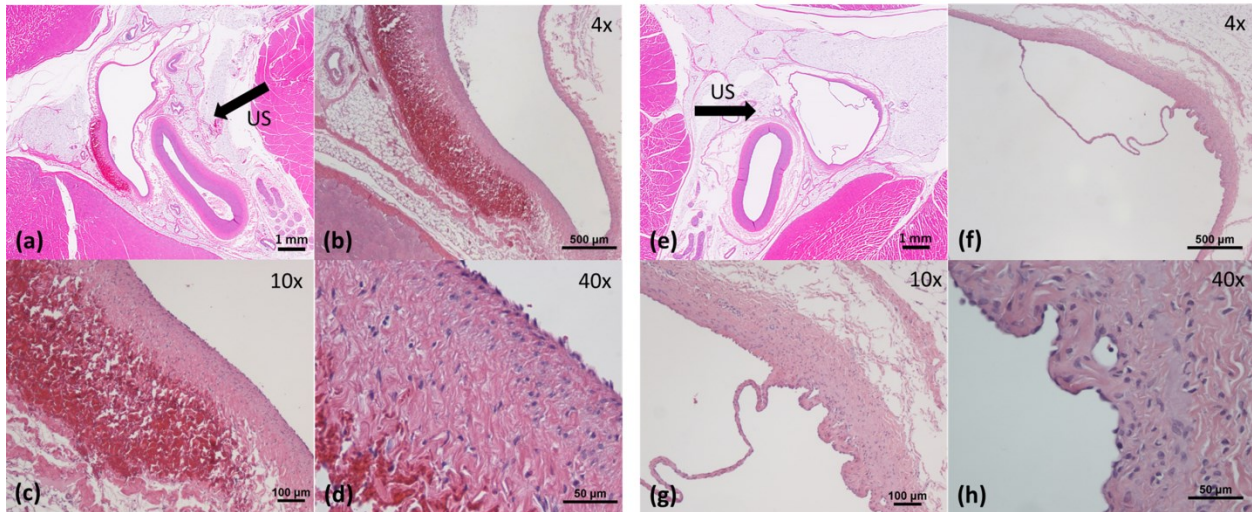
no significant difference from its baseline ( $P = 0.41$ ). LDH decreased to  $334.5 \pm 67.0$  U/L and showed no difference from its baseline ( $P = 0.35$ ). There was also no significant difference in serum potassium ( $P = 0.035$ ) and serum hematocrit ( $P = 0.08$ ) between the recoveries and their baselines.

For the 8 free-flow treatments, there was no significant change in all variables compared to the pre-free-flow treatment baselines: free hemoglobin ( $P = 0.027$ ), LDH ( $P = 0.24$ ), serum potassium ( $P = 0.18$ ), system systolic blood pressure ( $P = 0.39$ ), hear rate ( $P = 0.40$ ) and serum hematocrit ( $P = 0.50$ ).

### **7.3.5 Gross and Histology Evaluation**

The hematoxylin and eosin stained sections of the femoral bundles were examined to assess vessel damage caused by microtripsy. Acute vessel damage was evaluated on the right femoral veins harvested right after the free-flow treatments, and subacute vessel damage was evaluated on the left femoral veins recovered after two weeks from the thrombolysis treatments. In the acute vessel samples, there was focal venular wall thickening with corresponding hemorrhage in the tunica adventitia and thickening of the tunica media distal to the ultrasound source, as shown in **Figure 7.8(a)-(d)**. Most of the tunica intima of the femoral veins was intact, with no evidence of perforation through vessel walls. In rare cases, there was tunica intima and media injury with hemorrhage into the tunica adventitia. No thrombus was noted in the lumen. No injury was found in or around the femoral arteries. In the subacute vessel samples, there was a mild thickening of the tunica media with granulation tissue composed of small vascular channels and inflammatory cells, presumably secondary to the microtripsy injury, otherwise there was no other significant abnormalities (**Figure 7.8(e)-(h)**). There was no hemorrhage or evidence of tunica intima injury. No injury to the femoral arteries and surrounding tissues as

well. Valves in the femoral veins were preserved from the thrombolysis treatments as shown in **Figure 7.8(f)-(g)**. Grossly, there is no pulmonary embolus or infarct in the lung parenchyma.



**Figure 7.8:** Histology of Femoral Veins. (a)-(d): Right after a free-flow treatment. (e)-(h): Two weeks after a thrombolysis treatment.

### 7.3.5 Animal Behavior and Symptom Monitoring

During anesthesia, none of the animals showed clinical signs of distress due to the clot formation or the thrombolysis treatment. All recovery animals showed no significant pain levels post-treatment and returned to normal activity levels and feeding activity upon full recovery from anesthesia. No evidence of abnormal bleeding was observed in any of the recovered animals. No change in general behavior was observed during the course of two weeks.

## 7.4 Discussion

This study demonstrated the efficacy and safety of microtripsy-mediated thrombolysis in a porcine DVT model. Microtripsy reliably generated well-controlled acoustic cavitation in the pig femoral vein to perform thrombolysis treatments. In 13 out of the 14 thrombolysis treatments conducted in this study, a flow channel was generated through the completely occlusive or partially occlusive clot by microtripsy and blood flows were successfully restored or

significantly improved. The flow channel diameters generated were increased by an average of  $3.3 \pm 1.0$  mm, in comparison to an average vessel diameter of 6.7 mm. The average treatment time was 16.6 minutes per cm-long thrombus. Only mild intravascular hemolysis was induced during microtripsy thrombolysis. No damage was observed on vessel walls after two weeks of recovery, venous valves were preserved, and there was no sign of pulmonary embolism.

The efficacy of microtripsy-mediated thrombolysis was shown to be significantly improved from the previous histotripsy-mediated thrombolysis using the shock scattering mechanism. Using a similar porcine DVT model, microtripsy achieved 13 successful recanalizations in the total 14 treatments, whereas the shock-scattering histotripsy only achieved successful recanalizations in 7 out of 12 treatments [11]. Only one microtripsy treatment in this study was unable to restore flow, due to the unintentional extension of the thrombus to ultrasound-inaccessible regions. The difference in treatment efficacy is likely related to the different mechanisms that the two approaches use to generate cavitation. Microtripsy uses the intrinsic threshold mechanism where acoustic cavitation is generated when the negative pressure phase of a single-cycle ultrasound pulse directly exceeds a cavitation threshold intrinsic to the media, and shock-scattering histotripsy uses multi-cycle ultrasound pulses and relies on pre-existing weak nuclei to reflect and invert positive pressure phases to combine with the incident negative pressure phases to generate acoustic cavitation. Weak nuclei often reside on tissue interfaces, such as vessel walls, so cavitation generated by shock-scattering histotripsy is easily formed on vessel walls instead of at target thrombus inside the vessels. In contrast, cavitation generated by microtripsy is more confined at its desired focus and less affected by surrounding tissue interfaces than shock-scattering histotripsy, resulting in more reliable and continuous fractionations in target thrombi.

The safety of microtripsy thrombolysis was also shown to be improved from the previous shock-scattering histotripsy. Hemolysis and vessel damage were both greatly reduced using microtripsy. Only minor hemolysis was observed during microtripsy thrombolysis treatments in this study. In the free-flow treatments, hemolysis induced by microtripsy was about 15 times less than that induced by shock-scattering histotripsy [12]. The lower PRF used in microtripsy thrombolysis is expected to play an important role in reducing hemolysis. In microtripsy thrombolysis, a higher pressure (~30 MPa P-) and a lower PRF (100 Hz) was used in comparison to the previous shock-scattering histotripsy study (~17 MPa P- and 500 Hz PRF). With relatively slow blood flow, the same volume of blood is exposed to cavitation more times using a higher PRF, resulting in the rupturing of more erythrocytes using the shock-scatter approach. The natures of the two cavitation mechanisms may also make a difference in hemolysis. The less-confined, larger cavitation bubble clouds generated by shock-scattering histotripsy may affect a larger volume of blood in the flow than the better-confined, smaller cavitation generated by microtripsy. In addition, no vessel damage was observed after two weeks of recovery from the microtripsy-mediated thrombolysis treatments. There was no damage observed in the endothelial cells of the targeted femoral veins or adjacent femoral arteries. Focal hemorrhage observed in the tunica adventitia disappeared completely after two weeks of recovery. This improvement was attributed to the better-confined cavitation in the vessel lumen generated by microtripsy, as shock-scattering histotripsy tends to generate cavitation on vessel walls where weak nuclei reside and therefore cause damage. Microtripsy generates more reproducible and predictable cavitation at the desired target without contacting the vessel walls so that vessel damage can be minimized. In addition, the new design of the therapy transducer also contributed to the reduced vessel damage. The therapy transducer used in this study was designed for DVT treatment to have the

focal zone smaller than the lumen of the femoral vein, while the therapy transducer used in the previous study had a focal zone larger than the femoral vein.

Exposure of microtripsy in free blood flow in the femoral vein was considered to be the worst case test to further evaluate the safety of microtripsy-mediated thrombolysis treatment, as it maximized the potential contact between cavitation and vessel wall without a thrombus barrier, thus resulting in maximal vessel damage. In addition, without the thrombus barrier, a higher volume of free blood was expected to be exposed to cavitation in the flow, leading to a greater risk of hemolysis. The histological results showed no vessel perforation or major endothelial damage in any samples treated in free blood flow, and there was only microscopic hemorrhage located in the tunica adventitia of the target femoral veins. The hematological results also showed no statistically significant increase in free Hgb, LDH, potassium, or serum hematocrit in blood before and after the free flow treatments, suggesting that only slight hemolysis was induced during the free-flow treatments. All of these results from the free-flow scenario provide further evidence to support the safety of microtripsy thrombolysis treatment. A surprising result was that a lesser degree of hemolysis was observed in the free-flow treatments than that induced during the thrombolysis treatments with clots. One explanation is that in the thrombolysis treatment, cavitation was reliably and robustly generated in the targeted clots, and dissolving the targeted clots mostly consisting of red blood cells would lead to an increase in free hemoglobin. Another reason is associated with the different behavior of acoustic cavitation generated in free blood flow than in static tissue. Although the therapy system was consistently targeted at the center of vessel lumen, the cavitation tended to form at the bottom of the vessel wall in the flowing environment. Therefore, blood cells passing through the target may not get full cavitation exposure to be fractionated. Cavitation also appeared smaller and sparser in the free flow

environment than in the thrombus on the ultrasound images, which could further reduce the blood cell lysis. In the flow environment, residual bubble nuclei from cavitation bubble collapse are immediately flushed away with blood flow and cannot serve as “seeds” to enhance the following cavitation generation. Therefore the cavitation observed in the free-flow veins was smaller and sparser and lysed less blood cells.

There are notable differences between this porcine DVT model and a human DVT: available acoustic access, thrombi age, thrombi length and localization of thrombi. There is better acoustic access to DVT sites in human legs than in pig legs. Pig legs are short and the femoral veins are very close to the abdomen, leaving us with a limited acoustic window for ultrasound to transmit to the target in the veins. Human legs are longer, and DVT sites are usually accessible from more angles and locations. Therefore, thrombolysis treatments in human legs could potentially be more effective with a therapy transducer with a larger aperture and more transmitting area than the transducer used in this study. Another consideration about this study is that the age of thrombi in human femoral veins varies from several days to weeks, but we were only able to form and treat very acute thrombi using this porcine model in this study. We are currently working on developing a new porcine model to form chronic thrombi inside femoral veins. We are also developing a real-time thrombolysis monitoring algorithm to adaptively adjust therapy doses and strategies for thrombi with different ages [16, 20]. In some cases, the thrombi formed in human legs can be extended to over 10 cm long, whereas the thrombi formed in our study were less than 3 cm. Treating a long thrombus may be challenging because re-clotting may occur before complete recanalization is achieved. Localization of thrombi in humans may also be a challenge. In some cases, the thrombi (especially in the chronic phase) are not easily visualized on ultrasound images due to the lack of red blood cells inside the



thrombi. Pre-treatment planning based on other thrombus localization methods, such as angiography or magnetic resonance imaging, may be needed. We believe the potential issues from these differences are solvable, and the application of microtripsy-mediated thrombolysis for human DVT therapy is promising.

## 7.5 References

- [1] M. G. Beckman, *et al.*, "Venous thromboembolism: a public health concern," *American journal of preventive medicine*, vol. 38, pp. S495-S501, 2010.
- [2] H. P. Adams, *et al.*, "Guidelines for thrombolytic therapy for acute stroke: a supplement to the guidelines for the management of patients with acute ischemic stroke a statement for healthcare professionals from a special writing group of the stroke council, American heart association," *Circulation*, vol. 94, pp. 1167-1174, 1996.
- [3] S. M. Bates and J. S. Ginsberg, "Treatment of deep-vein thrombosis," *New England Journal of Medicine*, vol. 351, pp. 268-277, 2004.
- [4] H. S. Friedman, *et al.*, "Tissue plasminogen activator for acute ischemic stroke," *N Engl J Med*, vol. 334, p. 1405, 1996.
- [5] M. J. Sharafuddin, *et al.*, "Endovascular management of venous thrombotic and occlusive diseases of the lower extremities," *Journal of vascular and interventional radiology*, vol. 14, pp. 405-423, 2003.
- [6] A. Karthikesalingam, *et al.*, "A systematic review of percutaneous mechanical thrombectomy in the treatment of deep venous thrombosis," *European Journal of Vascular and Endovascular Surgery*, vol. 41, pp. 554-565, 2011.
- [7] Z. Xu, *et al.*, "Effects of acoustic parameters on bubble cloud dynamics in ultrasound tissue erosion (histotripsy)," *The Journal of the Acoustical Society of America*, vol. 122, pp. 229-236, 2007.
- [8] Z. Xu, *et al.*, "Evolution of bubble clouds induced by pulsed cavitation ultrasound therapy-histotripsy," *Ultrasonics, Ferroelectrics, and Frequency Control, IEEE Transactions on*, vol. 55, pp. 1122-1132, 2008.
- [9] Z. Xu, *et al.*, "Noninvasive creation of an atrial septal defect by histotripsy in a canine model," *Circulation*, vol. 121, pp. 742-749, 2010.
- [10] A. D. Maxwell, *et al.*, "Noninvasive thrombolysis using pulsed ultrasound cavitation therapy-histotripsy," *Ultrasound in medicine & biology*, vol. 35, pp. 1982-1994, 2009.

- [11] A. D. Maxwell, *et al.*, "Noninvasive treatment of deep venous thrombosis using pulsed ultrasound cavitation therapy (histotripsy) in a porcine model," *Journal of vascular and interventional radiology*, vol. 22, pp. 369-377, 2011.
- [12] R. Devanagondi, *et al.*, "Hemodynamic and Hematologic Effects of Histotripsy of Free-Flowing Blood: Implications for Ultrasound-Mediated Thrombolysis," *Journal of vascular and interventional radiology*, vol. 26, pp. 1559-1565, 2015.
- [13] A. D. Maxwell, *et al.*, "Cavitation clouds created by shock scattering from bubbles during histotripsy," *The Journal of the Acoustical Society of America*, vol. 130, pp. 1888-1898, 2011.
- [14] X. Zhang, *et al.*, "Noninvasive thrombolysis using histotripsy beyond the intrinsic threshold (microtripsy)," *Ultrasonics, Ferroelectrics, and Frequency Control, IEEE Transactions on*, vol. 62, pp. 1342-1355, 2015.
- [15] X. Zhang, *et al.*, "Noninvasive thrombolysis using microtripsy: a parameter study," *Ultrasonics, Ferroelectrics, and Frequency Control, IEEE Transactions on*, vol. 62, pp. 2092-2105, 2015.
- [16] X. Zhang, *et al.*, "Histotripsy Thrombolysis on Retracted Clot," *Ultrasound in Medicine & Biology*, 2016.
- [17] A. D. Maxwell, *et al.*, "Probability of cavitation for single ultrasound pulses applied to tissues and tissue-mimicking materials," *Ultrasound in medicine & biology*, vol. 39, pp. 449-465, 2013.
- [18] K.-W. Lin, *et al.*, "Histotripsy beyond the intrinsic cavitation threshold using very short ultrasound pulses: microtripsy," *Ultrasonics, Ferroelectrics, and Frequency Control, IEEE Transactions on*, vol. 61, pp. 251-265, 2014.
- [19] E. A. Ryan, *et al.*, "Structural origins of fibrin clot rheology," *Biophysical journal*, vol. 77, pp. 2813-2826, 1999.
- [20] X. Zhang, *et al.*, "Real-time feedback of histotripsy thrombolysis using bubble-induced color Doppler," *Ultrasound in medicine & biology*, vol. 41, pp. 1386-1401, 2015.

## Chapter 8

### Summary and Future Work

#### 8.1 Summary

This dissertation demonstrates the efficacy and safety of microtripsy for thrombolysis application through a series of *in vitro* and *in vivo* studies. The work follows a step-by-step approach that first develops a system platform, then researches new therapy and monitoring methods, and finally validates in a large animal model. More specifically, an integrated, portable, and image-guided histotripsy thrombolysis system is first designed and developed for both research and clinical uses. Two technical innovations, microtripsy and bubble-induced color Doppler feedback, are then investigated *in vitro* to augment histotripsy thrombolysis. Finally, the histotripsy thrombolysis system with the new technical enhancements is validated by a comprehensive pre-clinical study in an *in vivo* porcine DVT model. It is our hope that this work will provide enough scientific and engineering bases for clinical translation of histotripsy thrombolysis technology.

**1) Development:** The histotripsy thrombolysis system was designed and developed for both research and clinical use, and incorporated all the necessary hardware and software components for potential technology implementations. It served as a platform where microtripsy parameters and bubble-induced color Doppler feedback could be implemented and investigated, and also served as an integrated therapy device for pre-clinical validations. This prototype system can also provide design and engineering guidance for future product commercialization.

Such a clinically designed integrated system is an important milestone to advance the research and clinical translation of the histotripsy thrombolysis technology.

**2) Research:** Technical innovations for both therapy and therapy monitoring were systematically investigated *in vitro* for thrombolysis application. A new histotripsy approach, microtripsy, was first investigated for therapy enhancements. Microtripsy approach was demonstrated to improve both the safety and efficacy of histotripsy thrombolysis [1]. Cavitation was reliably generated by microtripsy and consistently confined within targeted vessel lumen, resulting in precise, effective recanalization and significantly lowered risk of collateral vessel damage. Flow channels could be quickly and precisely established by microtripsy treatments, followed by significant flow improvements. The debris particles generated by microtripsy were measured with over 99.9% smaller than 10  $\mu\text{m}$  and the largest particle was less than 200  $\mu\text{m}$ . Under the microtripsy approach, acoustic parameters and treatment strategy were then further optimized in an *in vitro* setting. The different pulse repetition frequencies (PRF) of microtripsy were explored and evaluated, and an optimal PRF under current technical limits was identified [2]. Different treatment strategies were also investigated on different blood clot types. It was found that treatment efficacy differed under different treatment strategies and electronically focal-steering and multiple treatment passes can significantly improve the thrombolysis efficacy [3]. Bubble-induced color Doppler was also developed and investigated to enable advanced therapy monitoring [4, 5]. It was verified that BCD can monitor the tissue motion induced by histotripsy pulses. It was further demonstrated that BCD feedback can be used to quantitatively monitor clot fractionation during histotripsy thrombolysis and accurately predict the completion of clot fractionation in real-time. These *in vitro* research studies demonstrated the capabilities of

microtripsy and bubble-induced color Doppler to improve histotripsy thrombolysis and provided optimized solutions for later large animal validation studies.

**3) Validation:** The safety and efficacy of the histotripsy thrombolysis system incorporated with the newly-developed technical enhancements was demonstrated in an *in vivo* porcine DVT model. Comprehensive evaluations were conducted during this study to assess the thrombolysis performance. Microtripsy reliably generated well-controlled acoustic cavitation in the pigs' femoral veins to perform thrombolysis treatments. In 13 out of the 14 thrombolysis treatments conducted in this study, a flow channel was generated through the completely occlusive or partially occlusive clot by microtripsy and blood flows were successfully restored or significantly improved. In the one treatment where no flow was restored, the thrombus could not be completely scanned through by microtripsy due to the extension of the thrombus to regions (deep into abdomen) with limited acoustic access. The flow channel diameters generated were increased by an average of  $3.3 \pm 1.0$  mm, in comparison to an average vessel diameter of 6.7 mm. The average treatment time was 16.6 minutes per cm-long thrombus. Only mild intravascular hemolysis was induced during microtripsy thrombolysis. No damage was observed on vessel walls after two weeks of recovery, and there was no sign of any pulmonary embolism.

While this dissertation demonstrated the improved safety and efficacy of microtripsy thrombolysis and provided a real-time therapy monitoring method using BCD, much work remains to facilitate the successful clinical translation of this assembly of the technologies and designs. The remainder of this chapter details the key components of our future work that will permit the continued development of the therapy and the monitoring technologies for histotripsy thrombolysis.

## **8.2 Future Work**

### 8.2.1 Further Investigation of Bubble-induced Color Doppler Feedback

The feasibility of using BCD for real-time quantitative therapy monitoring was demonstrated in Chapter 6 of this dissertation. Most of the work involved verifying the BCD feedback *in vitro*, where the accuracy of BCD to detect tissue motion was established by high-speed optical images in transparent fibrin clots. The strong correlation of the BCD feedback with clot fractionation was verified in three-layer fibrin clots and in *in vitro* clots in vessel environment. However, limited work was done to directly use BCD feedback to guide histotripsy thrombolysis treatments and validate the treatment outcomes.

In order to further demonstrate the capability of BCD feedback and to apply it directly during histotripsy thrombolysis treatments, a software development project and two sets of studies should be conducted. For the development project, the BCD feedback pathway and algorithms should be integrated into the control software of the histotripsy thrombolysis system (see details in Chapter 2). The BCD feedback was previously realized in Matlab (The Mathworks, Natick, MA, USA) based on Verasonics<sup>®</sup> system (Kirkland, WA, USA), which was completely separate from positioning and therapy systems and could not implement BCD-guided thrombolysis treatments. In order to increase the processing speed of the real-time BCD feedback and directly control treatment according to the feedback, the histotripsy thrombolysis system with a better Ultrasonix<sup>®</sup> (Vancouver, Canada) imaging core should be used. The control software will be able to use the BCD feedback to real-time monitor clot fractionation, detect the completion at each treatment location and automatically manage the positioning and therapy systems to move to the next treatment location and start fractionation.

An *in vitro* study should be conducted first with the BCD-embedded histotripsy thrombolysis system to validate its efficacy and tune the BCD parameters. The flow model setup

described in Chapter 3, 4, and 5 should be used to mimic the clinical thrombosis environment. BCD-guided thrombolysis treatments should be performed on blood clots formed in the flow model. Treatment outcomes should be compared to over-dosed treatments to support our hypothesis that BCD-guided treatment can achieve the same recanalization outcomes as over-dosed treatments with less treatment time. Different BCD parameters, such as delay for velocity detection and Doppler ensemble length, should be also tested to identify the optimal values. Blood clots with different ages and stiffness should be treated using BCD-guided thrombolysis to show the capability of adaptive dosing of BCD feedback.

An *in vivo* study should be also conducted to validate the BCD feedback in the porcine DVT model described in Chapter 7. With the fully optimized settings, BCD-guided thrombolysis treatments should be performed on blood clots formed in pigs' femoral veins. Comprehensive evaluations of the safety and efficacy of the BCD-guided treatments should be included in this study, such as recanalization time, recanalized channel size, degree of hemolysis and collateral damage. The results from this study should conclude the investigation of BCD feedback for thrombolysis application.

### **8.2.2 Microtripsy PRF Study**

The parameter space of microtripsy PRF was explored for thrombolysis treatments in Chapter 4 of this dissertation. But with the technical limitation, the tested PRF did not exceed 100 Hz. It was found that within this tested range ( $\leq 100$  Hz) higher PRF could achieve a better treatment outcome with less time. This led us to think about the potential of even higher PRF. A follow-up study should be conducted to investigate higher microtripsy PRF ( $> 100$  Hz). Hardware should be first updated to allow output of higher microtripsy PRF. A new therapy transducer and the corresponding amplifier should be developed. The limits of the hardware

should be carefully tested and verified. An extended range of output PRF from 100 Hz to 500 Hz should be feasible according to the current-available technical improvements. An *in vitro* study, the same to the study described in Chapter 4, should be conducted using the microtripsy PRFs higher than 100 Hz. Our hypothesis is that as PRF increases, the benefit from the cavitation memory effects on clot fractionation will be reduced or canceled by the pre-focal cavitation on vessel walls induced by high PRF. In addition to verify our hypothesis, finding the optimal PRF which can maximize the clot fractionation with no or minimal pre-focal cavitation should be another primary goal of this study.

### **8.2.3 Retracted Clots in the Porcine DVT Model**

Microtripsy thrombolysis treatments were conducted and validated in an *in vivo* porcine DVT model, as described in Chapter 7 of this dissertation. In that porcine DVT model, blood clots were freshly formed and matured for only two hours inside the femoral veins. The blood clots treated in that study were only considered as acute clots in clinical circumstances. There are still a large portion of patients with subacute (retracted) blood clots need to be treated. In order to investigate the efficacy of microtripsy on subacute retracted clots, additional work should be conducted to develop a new porcine DVT model with the capability to form subacute retracted clots inside of femoral veins. Preliminary experiments have been done to form a blood clot inside the vein and wait for several days for the clot to retract. But the clots usually dissolved or detached after the period. One possible alternative approach is to pre-form retracted clots *ex vivo* and then inject back into femoral veins. Studies have shown that retracted clots can be prepared in an *in vitro* environment [6]. It may be possible to inject the pre-formed retracted clots into the femoral vein using a big catheter and let it re-form inside of the vein for several hours before treatment. If it works, microtripsy thrombolysis treatments should be performed and evaluated in



a similar manner as described in Chapter 7. These results should be used to provide additional data to back up the clinical translation of histotripsy thrombolysis.

#### **8.2.4 Further Investigation of Multi-pass Treatment Strategy**

Different treatment strategies were explored in Chapter 6 of this dissertation. It was found that electronically focal-steering and multiple treatment passes could significantly improve the microtripsy thrombolysis efficacy. In that study, dual-pass strategy was investigated. One of the hypotheses for this dual-pass enhancement is that cavitation at different lateral locations were more separated both temporally and spatially. Therefore, more treatment passes may have the potential to further improve the thrombolysis efficacy. An *in vitro* study using the same setup as in Chapter 6 should be conducted and microtripsy treatments should be performed with different number of treatment passes. The thrombolysis efficacy of different passes on the same treatment path should be compared to that of single pass with the same accumulated dose. The treatment efficacy of different passes on different laterally-shifted treatment paths should be compared to that of single pass with therapy focus electronically steered at different lateral locations. The influence of different number of passes on thrombolysis efficacy should be also investigated. With the series of experiments, a better idea about the mechanism of multi-pass enhancement may be obtained and the optimal treatment solution can be identified for histotripsy thrombolysis.

### **8.3 References**

- [1] X. Zhang, *et al.*, "Noninvasive thrombolysis using histotripsy beyond the intrinsic threshold (microtripsy)," *Ultrasonics, Ferroelectrics, and Frequency Control, IEEE Transactions on*, vol. 62, pp. 1342-1355, 2015.
- [2] X. Zhang, *et al.*, "Noninvasive thrombolysis using microtripsy: a parameter study," *Ultrasonics, Ferroelectrics, and Frequency Control, IEEE Transactions on*, vol. 62, pp. 2092-2105, 2015.

- [3] X. Zhang, *et al.*, "Histotripsy Thrombolysis on Retracted Clots," *Ultrasound in medicine & biology*, 2016.
- [4] X. Zhang, *et al.*, "Real-Time Feedback of Histotripsy Thrombolysis Using Bubble-Induced Color Doppler," *Ultrasound in medicine & biology*, 2015.
- [5] R. M. Miller, *et al.*, "Investigation of the mechanism of ARFI-based Color Doppler feedback of histotripsy tissue fractionation," in *Ultrasonics Symposium (IUS), 2013 IEEE International*, 2013, pp. 934-937.
- [6] J. T. Sutton, *et al.*, "Clot retraction affects the extent of ultrasound-enhanced thrombolysis in an ex vivo porcine thrombosis model," *Ultrasound in medicine & biology*, vol. 39, pp. 813-824, 2013.